

**REDESIGN AND EVALUATION OF A
COMBUSTION CHAMBER FOR A
TURBOSHAFT ENGINE**

**RECONCEPTION ET ÉVALUATION D'UNE
CHAMBRE À COMBUSTION D'UN
TURBOMOTEUR**

A Thesis Submitted to the Division of Graduate Studies
of the Royal Military College of Canada
by

Curtis Richard Kaatz

In Partial Fulfillment of the Requirements for the Degree of
Master of Applied Science in Aeronautical Engineering

June, 2019

© This thesis may be used within the Department of National Defence but
copyright for open publication remains the property of the author.

Acknowledgements

I would like to acknowledge my thesis supervisor, Dr. Marc LaViolette, who introduced me to combustion and guided me in several areas throughout my studies. His knowledge of several engineering fields allowed me to learn more about topics outside of combustion than I ever thought I would. These valuable lessons will be carried throughout my career.

I'm extremely grateful to Dr. Billy Allan for providing me the opportunity to come to RMC and complete my Master's degree. His advice during my time at RMC was always welcomed. I would also like to thank StandardAero and the Natural Science and Engineering Research Council for funding this research.

This project involved nearly all of the technical staff within the Department of Mechanical and Aerospace Engineering and would not have been possible without their excellent and timely work. Specifically, Mr. Brendan Freeman and Mr. Pierre Bissonnette deserve tremendous appreciation for their dedication to the project.

I would like to thank my fellow graduate students who helped me during the testing phase of this project. My gratitude goes to Satpreet, Alexi, Crystal, George, and Stewart for not turning me away when I asked for assistance.

I am also thankful for all of the friends I have made at RMC. This includes students, professors, and technical staff in the department. There are far too many to list but you know who you are and I am glad to have met all of you.

The most sincere thanks must be given to my family and friends back home who encouraged me to pursue this, most importantly Rachel. Her patience and support through the hard times was greatly appreciated and I could not have achieved this without her.

Abstract

The two inlets to the reverse flow combustion chamber of the Rolls-Royce (Allison) Model 250 turboshaft gas turbine produce a non-uniform temperature profile that is exacerbated by inlet flow distortion caused by the compressor. A new combustion chamber was designed to improve the exit temperature profile even with distorted inlet mass flow rate conditions. This liner includes a swirl-stabilized recirculation region, a smaller diameter, improved cooling devices and air distribution but is the same length as the original design. The new design's exhaust temperature profile was measured on a test rig composed of mostly original engine parts and simulated a 3000 m altitude cruise condition by matching Mach number, fuel-to-air equivalence ratio, and fuel droplet Sauter mean diameter. The average non-dimensional temperature rise using the new liner was lower than the original, 0.906 compared to 0.931 and the pattern factor increased from 0.256 for the original to 0.379 for the new design. However both of these values were hardly influenced by inlet distortion when using the redesigned liner.

Keywords: Allison 250, Combustion, Combustion Chamber, Gas Turbine Engine, Pattern Factor, Rolls-Royce M250, Temperature Profile

Résumé

Les deux entrées de la chambre à combustion du moteur Rolls-Royce (Allison) Model 250, produisent un champ de température non-uniforme qui est exacerbé par un écoulement inégal provenant du compresseur. Une nouvelle chambre fut conçue dans le but d'améliorer le champ de température même lors d'inégalité de débit à son entrée. Cette chambre inclus une zone de recirculation, un plus petit diamètre, un système de refroidissement et de distribution d'air améliorer mais est de la même longueur que l'originale. Le champ de températures de la nouvelle chambre fut évalué sur un montage composé presque entièrement de pièces du moteur originale et simulant une croisière à 3000 m d'altitude en assurant la similitude du nombre de Mach, de la richesse et du diamètre moyen de Sauter des gouttelettes de carburant. Le champ de température à la sortie de la nouvelle chambre est similaire à celle originale mais n'est pas influencé par l'écoulement inégal du compresseur. La moyenne de l'augmentation de la température adimensionnelle produite par la nouvelle chambre est plus petite que celle originale, 0.906 comparé à 0.931, et le pattern factor est plus grand, passant de 0.256 du design original à 0.379 pour la nouvelle chambre. Par contre, ces deux paramètres demeurent presque inchangés par un écoulement inégal à l'entrée.

Contents

Acknowledgements	ii
Abstract	iii
Résumé	iv
List of Tables	viii
List of Figures	ix
Nomenclature	xi
1 Introduction	1
1.1 Objectives	2
1.2 Thesis Outline	3
2 Theory	4
2.1 Gas Turbine Thermodynamic Cycle	4
2.1.1 Combustion Chamber Objectives	6
2.2 Combustion Reactions	7
2.2.1 Equivalence Ratio	7
2.2.2 Chemical Equilibrium	8
2.2.3 Adiabatic Flame Temperature	10
2.2.4 Reaction Rates	10
2.3 Airflow Partitioning	11
2.3.1 Primary Zone	12
2.3.2 Secondary Zone	12
2.3.3 Dilution Zone	12
2.4 Combustion Chamber Description	13
2.4.1 Combustion Chamber Types	13
2.4.2 Airflow Configurations	14
2.4.3 Components	15
2.5 Combustion Chamber Design	16
2.5.1 Sizing	17
2.5.1.1 Chemical Kinetics	17
2.5.1.2 Mach Number Correlation	17
2.5.1.3 Bragg Correlation	18
2.5.1.4 Aerodynamic Groups	18
2.5.1.5 Greenhough-Lefebvre Correlation	19
2.5.1.6 Length	19

2.5.1.7	Casing	20
2.5.2	Diffuser Design	20
2.5.3	Dome Design	21
2.5.4	Liner Wall Cooling	24
2.5.5	Air Admission Holes	28
2.6	Exit Temperature Profile	31
2.6.1	Quantifying Exit Temperature Profile	31
2.6.2	Contributors to Pattern Factor	33
2.7	Atmospheric Rig Testing	35
3	Rolls-Royce M250	37
3.1	M250 Research	38
4	Combustion Chamber Redesign	42
4.1	Design Constraints and Assumptions	42
4.2	Calculation of Operating Conditions	43
4.2.1	Engine Operating Points	43
4.2.2	Operating Conditions	43
4.3	Combustion Chamber Air Distribution	49
4.3.1	Primary Zone	49
4.3.2	Secondary Zone	51
4.4	Calculation of Combustion Chamber Dimensions	52
4.5	Dome Design	55
4.5.1	Swirler	55
4.6	Film Cooling Devices	58
4.6.1	Film Cooling Device Placement	60
4.7	Air Admission Holes	61
4.8	Design Summary	64
5	Experimental Rig and Validation	67
5.1	Atmospheric Combustion Chamber Test Rig	68
5.2	Temperature Profiles	71
5.3	Average Temperature and Pattern Factor	77
6	Discussion	79
6.1	Temperature Profiles	79
6.1.1	Performance Comparison	82
6.1.2	Effects of Inlet Distortion	88
6.2	Combustion Chamber Design Comparison	89
6.2.1	Geometry	89
6.2.2	Air Distribution	91
6.3	Effects on Engine	94
7	Conclusions and Recommendations	96
7.1	Conclusions	96
7.2	Recommendations	98
	References	100
A	Calculations	104
A.1	Diameter Calculations	104

A.1.1	Chemical Kinetics	104
A.1.2	Mach Number Correlation	105
A.1.3	Bragg Correlation	105
A.1.4	Aerodynamic Groups	106
A.1.5	Greenhough-Lefebvre Correlation	107
A.2	Dome Angle Equation Derivation	108
A.3	Filming Cooling Device Placement	110
B	Engineering Drawings	117

List of Tables

2.1	Types of Fuel-Air Mixtures	8
2.2	Typical Values Used in Eqn. 2.14.	18
4.1	Engine Operating Points At Sea Level Static Conditions Unless Indicated Otherwise.	43
4.2	Combustion Chamber Operating Conditions	49
4.3	Lean and Rich Limits	49
4.4	Primary Zone Limit Ratios	50
4.5	Primary Zone Conditions	51
4.6	Secondary Zone Conditions	52
4.7	Summary of Primary Zone Diameters	53
4.8	Liner Dimension Summary	54
4.9	Film Cooling Device Locations and Flow Rates	60
4.10	Liner Wall Temperature for All Conditions Immediately Upstream of the Next Film Cooling Device.	61
4.11	Liner Hole Summary	64
5.1	Engine and Test Rig Operating Conditions	69
5.2	Test Cases	70
5.3	Average Non-dimensional Temperature Rise and Pattern Factor	77
6.1	Average Non-dimensional Temperature Rise and Pattern Factor Comparison to Tests by Maqsood [30].	86
6.2	Liner Hole Comparison	91
A.1	Typical Values Used in Eqn. A.16.	106
A.2	Operating Conditions for Condition 1	110

List of Figures

2.1	Schematic of a Gas Turbine Engine.	5
2.2	Ideal Brayton Cycle for a Gas Turbine Engine.	5
2.3	Effect of Equivalence Ratio, Temperature, and Pressure on Adiabatic Flame Temperature Rise for Kerosine, adapted from [6].	11
2.4	Cross Sectional Views Looking Downstream of the Types of Combustion Chambers, (a) Can, (b) Can Annular, (c) Annular.	14
2.5	Cross Section of a Combustion Chamber, adapted from [6].	15
2.6	A Reverse Flow Combustion Chamber, taken from [6].	15
2.7	Flow in the Primary Zone, taken from [6].	21
2.8	Dimensions of the Magic Circle and Dome.	22
2.9	Axial and Radial Swirlers [6].	23
2.10	Four Types of Cooling Devices, (a) Transpiration, (b) Effusion Cooling, (c) Impingement Cooling, (d) Film Cooling, adapted from [14].	25
2.11	Diagram of a Wiggle Strip [6].	26
2.12	A Representation of a Film Cooling Device	26
2.13	Cooling Efficiency for a Wiggle Strip taken from [10].	28
2.14	Jet in a Crossflow taken from [18].	30
2.15	Explanation of Exit Temperature Profile Parameters on a Sample Radial Temperature Profile, from Lefebvre [6].	33
2.16	Contributors to Pattern Factor [21].	34
3.1	M250 Engine Cutaway.	38
3.2	M250-C20B Combustion Liner.	38
3.3	Turbine Inlet Temperature Profiles at (a) 80 % and (b) 100 % Compressor Speed, adapted from [22].	39
3.4	Exit Temperature Profile for (a) Even Inlet Mass Flow Rate, (b) 4 % Higher Left Inlet Mass Flow Rate, from Maqsood [30].	40
4.1	Compressor Map, taken from [32].	44
4.2	Compressor Efficiency Map, taken from [32].	44
4.3	Gas Generator Turbine Map, taken from [32].	45
4.4	Gas Generator Turbine Efficiency Map, taken from [32].	45
4.5	(a) Swirler With Too Few Blades, (b) Swirler With the Correct Number of Blades.	58
4.6	Axial Temperature Profiles for Each Condition.	59
4.7	View of the Swirler and Dome.	64
4.8	View of the Holes and Film Cooling Devices.	65
4.9	Sumamry of Air Flow in the Redesigned Combustion Chamber.	66
5.1	Atmospheric Combustion Chamber Test Rig, from Maqsood [30].	67

5.2	Restriction Screen used to Reduce Airflow at Combustion Chamber Inlet. . .	70
5.3	Nozzle Guide Vane Shield Sketch.	71
5.4	Exit Temperature Profile for (a) Maqsood Even [30], (b) Baseline Even. . .	73
5.5	Change in Exit Temperature Profile Between Maqsood Test and Baseline Test, Even.	73
5.6	Exit Temperature Profile for the New Combustion Chamber, Even.	74
5.7	Exit Temperature Profile for the New Combustion Chamber for (a) Even, (b) +4% LD.	75
5.8	Change in Exit Temperature Profile, Even and +4% LD.	75
5.9	Exit Temperature Profile for the New Combustion Chamber for (a) Even, (b) +4% RD.	76
5.10	Change in Exit Temperature Profile, Even and +4% RD.	76
6.1	Sketch of Casing Inner Wall.	80
6.2	Plot of Temperature Rise as a Function of Equivalence Ratio.	81
6.3	Soot Deposit on Splash Strip After Test.	82
6.4	Exit Temperature Profile for +4% LD with (a) Original Liner from Maq- sood [30], (b) New Liner.	83
6.5	Change in Exit Temperature Profile - New and Original Liners, +4% LD. . .	83
6.6	Exit Temperature Profile for Even Inlet Flow with (a) Original Liner from Maqsood [30], (b) New Liner.	84
6.7	Change in Exit Temperature Profile - New and Original Liners, Even. . . .	84
6.8	Exit Temperature Profile for +4% RD with (a) Original Combustion Cham- ber from Maqsood [30], (b) New Combustion Chamber.	85
6.9	Change in Exit Temperature Profile - New and Original Liners, +4% RD. . .	85
6.10	(a) Outer Gap Around the NGV Shield, (b) Liner Lip.	87
6.11	Hole Size and Placement (a) New Liner, (b) Original Liner.	92
A.1	Primary Zone Dimensions.	108
A.2	Cooling Efficiency for a Wiggle Strip [10].	113

Nomenclature

Latin Symbols

A	Area	m^2
C	Coefficient	—
D	Casing Diameter	m
G	Gibbs Free Energy	$\frac{\text{J}}{\text{mol}}$
K	Constant	
Lu	Luminosity Factor	—
M	Molar Mass	$\frac{\text{g}}{\text{mol}}$
Ma	Mach Number	—
\tilde{Ma}	Quasi-non-dimensional Mach Number	$\frac{\text{kg K}^{0.5}}{\text{Pa s}}$
N	Rotational Speed	$\frac{\text{rev}}{\text{min}}$
PF	Bruan Profile Factor	—
Q	Pattern Factor	—
R	Mass Specific Gas Constant	$\frac{\text{J}}{\text{kg K}}$
\bar{R}	Universal Gas Constant	$\frac{\text{J}}{\text{mol K}}$
S	Swirl Number	—
T	Temperature	K
V	Volume	m^3

X	Axial Position Parameter	$\frac{1}{\text{m}^{0.2}}$
a	Number of Carbon Atoms	mol
b	Number of Hydrogen Atoms	mol
c	Speed of Sound	$\frac{\text{m}}{\text{s}}$
d	Liner Diameter	m
f	Fuel-air Ratio	—
m	Mass	kg
n	Reaction Order	—
q	Heat Transfer	$\frac{\text{J}}{\text{m}^2}$
u	Uncertainty	—
v	Velocity	$\frac{\text{m}}{\text{s}}$
w	Film Cooling Device Width	m
y	Jet Penetration	m

Greek Symbols

θ	Temperature Ratio	—
Φ	Combustion Efficiency Parameter	$\frac{\text{Pa}^{1.75} \text{m}^{2.25} \text{s}}{\text{kg}}$
β	Angle	°
γ	Heat Capacity Ratio	—
δ	Pressure Ratio	—
ϵ	Emissivity	—
η	Efficiency	—
θ	Non-dimensional Temperature Rise	—
κ	Surface Tension	$\frac{\text{N}}{\text{m}}$
λ	Thermal Conductivity	$\frac{\text{W}}{\text{mK}}$
μ	Viscosity	Pa s
ν	Number of Moles	mol
ρ	Density	$\frac{\text{kg}}{\text{m}^3}$
σ	Stefan-Boltzmann Constant	$\frac{\text{W}}{\text{m}^2 \text{K}^4}$
ϕ	Equivalence Ratio	—
ψ	Dome Angle	°

Subscripts

1	Gas Generator
3	Station 3
32	Sauter Mean Diameter
4	Station 4
5	Station 5
B	Blockage
D	Discharge
DZ	Dilution Zone
L	Liner
PZ	Primary Zone
RZ	Recirculation Zone
SZ	Secondary Zone
X	Axial Velocity Parameter
adia	Adiabatic
atm	Atmospheric Condition
avg	Average
c	Film Cooling Flow
coll	Collision Theory
cond	Conduction
conv	Convection
corr	Corrected
eff	Effective
f	Fuel

g Combustion Gas
max Maximum
o Outlet Condition
rad Radiation
stoic Stoichiometric
sw Swirler
w Liner Wall

Abbreviations

CEA Chemical Equilibrium with Applications

NGV Nozzle Guide Vane

1 Introduction

The method of designing combustion chambers for gas turbine engines is one that is not well-known. Gas turbine engines operate at multiple design points, resulting in combustion chambers designed to satisfy several turbine inlet requirements for a variety of combustion chamber inlet conditions. The temperature of highest importance to designers of combustion chambers is the exit temperature. The combustion chamber should provide the appropriate exit temperature, but also provide a nearly uniform exit temperature profile. High exit temperatures and non-uniform exit temperature profiles may cause turbine components to experience high thermal stresses and fatigue leading to premature failure if not detected.

The damage of hot section components is a major factor in the service life of gas turbine engines. Non-uniform combustion chamber outlet temperature profiles can result in temperatures above the design specifications leading to performance degradation in turbines, as well as damage to turbine vanes and blades. The result of damage caused by excessive combustion chamber outlet temperatures is increased down-time due to engine maintenance. This problem can be solved by improving the high temperature properties of turbine materials or improving the outlet temperature profile of combustion chambers.

In gas turbine engines, the behaviour of upstream components can have a significant impact of the performance and life of downstream components. Abnormal operation of the compressor may result in poor performance in the combustion chamber, affecting the turbine which powers the compressor. The cyclical operation of the gas turbine

engines means that the performance of components can have consequences on the rest. This necessitates the understanding of flow characteristics throughout the engine to identify problems reducing performance.

The dual-entry, reverse flow combustion chamber is a can-type design common to the Rolls-Royce (Allison) Model 250 turboshaft widely used in civil and military aviation. It produces a non-uniform temperature profile at the outlet, which is known to lead to localized damage of nozzle guide vanes reducing engine performance and increasing maintenance costs.

The Model 250 is a perfect example of an engine where upstream components affect downstream performance. The compressor is known to provide unevenly distributed airflow to the combustion chamber. This imbalance of air at the two inlets of the combustion chamber leads to increasingly non-uniform outlet temperature profiles with higher maximum temperatures at the inlet of the turbine. The result of the uneven air distribution prompts further damage to the downstream hot section components.

1.1 Objectives

The objective of this project is to design and evaluate a new combustion liner for the Rolls-Royce M250-C20B engine to reduce the non-uniform temperature profile found at the exit of the combustion chamber due to uneven inlet mass flow rate conditions. This will be accomplished by following present-day design practices to design the liner. The performance of the new liner will be tested with an atmospheric test rig to measure the exit temperature profile. The new combustion chamber will be tested with even inlet flow and conditions with uneven inlet flow rate to determine the change in outlet temperature profile due to inlet flow conditions.

1.2 Thesis Outline

Chapter 1 provides an introduction to the project. Chapter 2 discusses the theory of gas turbine engines and the design of gas turbine combustion chambers. Chapter 3 provides a review of the M250 and relevant research on the engine. Chapter 4 presents the design methodology of the new combustion chamber. Chapter 5 presents experimental setup, the test procedures, and the results of the experiment. The results are then discussed in Chapter 6. Chapter 7 contains conclusions of the research and recommendations for future work.

2 Theory

This chapter presents the basic theory behind the thermodynamic cycle of a gas turbine engine and the theory drawn from thermodynamics, chemical kinetics, and aerodynamics required to design combustion chambers of gas turbines. A review of combustion chamber design method is then presented.

2.1 Gas Turbine Thermodynamic Cycle

A gas turbine engine is made up of a compressor, a combustion chamber, and a turbine, with a shaft connecting the turbine and compressor. The gas turbine engine can be modeled as a real Brayton cycle with air as the working fluid as presented by Saravanan *et al.* [1]. Air enters the compressor before being delivered to the combustion chamber. Heat is added in the combustion chamber. The products of combustion expand in the turbine which produces the work to drive the compressor. The excess energy not needed by the compressor is transformed into thrust or work depending on the configuration of the engine. An exhaust nozzle may provide thrust as in turbojet engines and turbofan engines or the use of a free turbine may provide shaft work in turboshaft and turboprop engines. Turbofan engines are a mix of these two. Schematics of a basic gas turbine and the ideal Brayton cycle are shown in Figs. 2.1 and 2.2.

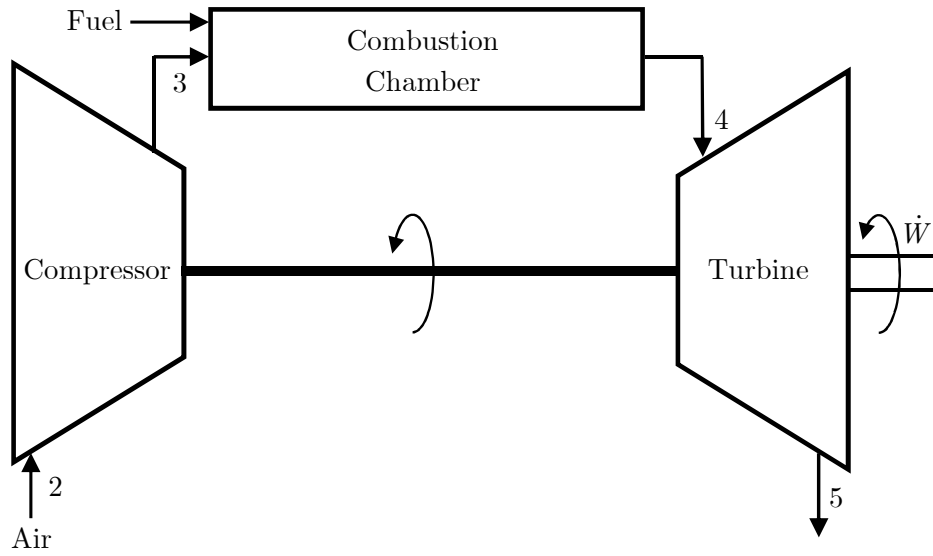


Figure 2.1: Schematic of a Gas Turbine Engine.

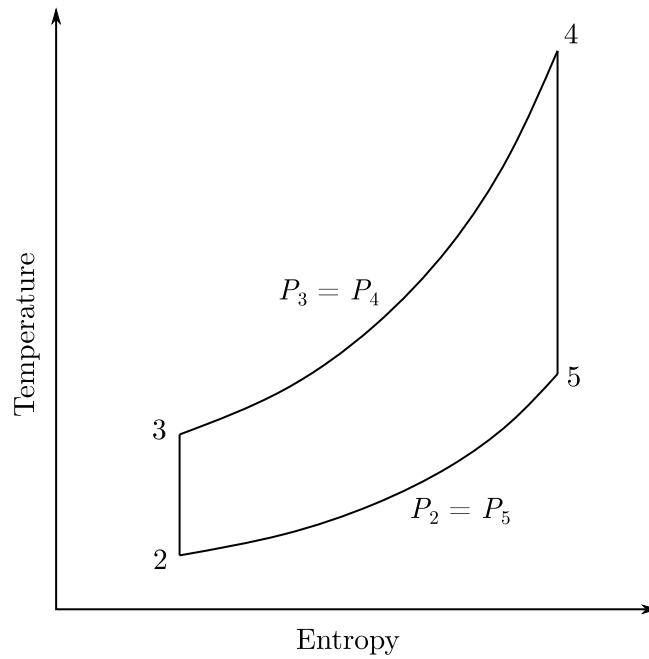


Figure 2.2: Ideal Brayton Cycle for a Gas Turbine Engine.

2.1.1 Combustion Chamber Objectives

A combustion chamber contains no moving parts and must be designed to accommodate all operating conditions in one configuration. Although the combustion chamber is a seemingly simple component of the gas turbine, the method in which they operate and are designed is much more complex. The process of combustion involves the atomization of fuel, evaporation of fuel, mixing of fuel and air, and burning of the fuel-air mixture. The purpose of a combustion chamber is to increase the enthalpy of the air from the compressor and deliver it at the design temperature to the turbine. Blazowski and Henderson [2] presented 10 general requirements of combustion chambers regarding design and performance objectives.

Performance Objectives:

- high combustion efficiency at all operating conditions;
- low overall system total pressure loss;
- stable combustion at all operating conditions; and
- reliable ground-level ignition and altitude relight capability.

Design Objectives:

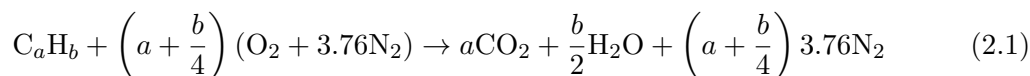
- minimum size, weight, and cost;
- combustion chamber exit temperature profile consistent with turbine design requirements;
- low stressed structure;
- effective hot parts cooling for long life;
- good maintainability and reliability; and
- minimum exhaust emissions consistent with current specified limitations and regulations.

The temperature at the outlet of a combustion chamber is limited by the maximum operating temperature of the turbine blades. Since the turbine inlet temperature is critical, the combustion process of a gas turbine engine must be controlled. The temperature increase in the combustion chamber is the result of a chemical reaction

between air and fuel. The ratio of fuel to air and combustion efficiency determines the temperature of the products of combustion and, hence, the combustion chamber exit temperature.

2.2 Combustion Reactions

Combustion is an exothermic reaction of fuel and air. In complete combustion of hydrocarbons, fuel reacts with the oxygen in the air to produce water and carbon dioxide like in the stoichiometric reaction shown in Eqn. 2.1. Nitrogen in the air does not react and is in the products. In real combustion processes a multitude of chemical reactions take place between various species as described by Kanury [3, p. 379].



2.2.1 Equivalence Ratio

A stoichiometric fuel-air mixture is a mixture that has the ideal amount of fuel and air for a combustion reaction to occur. When dealing with mixtures not at the stoichiometric ratio, the fuel to air equivalence ratio, ϕ , is used. The equivalence ratio describes the proportions of fuel and air in a mixture, f , with respect to the stoichiometric ratio, f_{stoic} . Equations 2.2 and 2.3 show the fuel-air ratio and fuel to air equivalence ratio. Table 2.1 explains the terms used to describe proportions of air and fuel with regards to the equivalence ratio.

$$f = \frac{\dot{m}_f}{\dot{m}_{\text{air}}} \quad (2.2)$$

$$\phi = \frac{f}{f_{\text{stoic}}} \quad (2.3)$$

In the combustion chamber, reactions can only occur within certain equivalence ratio limits, known as the flame stability limits. For most fuels, the flame will extinguish if the reaction temperature is less than 1600 K [4]. Mixtures that are too lean or too rich will result in a flame temperature below the flame stability limit. The lean and rich

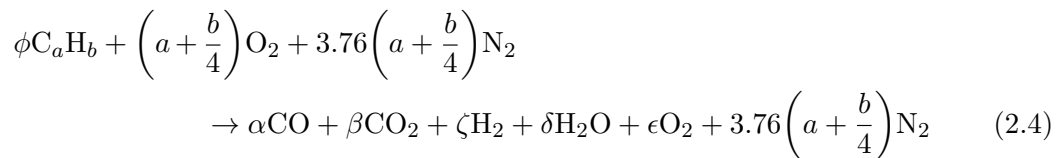
Table 2.1: Types of Fuel-Air Mixtures

	Condition
$\phi < 1$	Lean
$\phi = 1$	Stoichiometric
$\phi > 1$	Rich

limits that produce a temperature of 1600 K vary greatly with the operating conditions in the combustion chamber.

2.2.2 Chemical Equilibrium

To determine the reaction temperature of a real combustion reaction, the composition of the reactants and products must be known when the reaction is at equilibrium. Complete combustion cannot occur in practice according to the second law of thermodynamics, as explained by Kanury [3, p. 357]. When reactions take place at high temperatures, such as in gas turbine combustion chambers, dissociation of molecules occurs, changing the composition of the products from those in Eqn. 2.1. A simplified combustion reaction for a lean mixture is shown in Eqn. 2.4. Here, the equivalence ratio is used to describe the amount of air and fuel reactants.



In reality there are additional products due to dissociation of molecules but their amounts are negligible compared to those present in Eqn. 2.4. The prediction of the composition of the products of combustion requires the simultaneous solution of a set of equations. These include the first law of thermodynamics, the stoichiometric chemical reaction equation, and additional chemical equilibrium relationships [2]. The equilibrium relationships allow for the composition of the products in Eqn. 2.4 to be predicted.

If the composition of the products is known, the First Law of Thermodynamics will allow the prediction of the temperature of the products. Dissociation of CO_2 and H_2O

results in the formation of CO, H₂ and O₂. These relationships at equilibrium can be represented by Eqns. 2.5 and 2.6.



These equilibrium relations are used to determine the equilibrium constants aiding in the calculation of the composition of the products of combustion. The partial pressures are a function of the number of moles so the equilibrium constants can be written in moles rather than partial pressures.

$$K_{p,\text{CO}_2} = \frac{P_{\text{CO}_2}}{P_{\text{CO}} P_{\text{O}_2}^{\frac{1}{2}}} = \frac{\nu_{\text{CO}_2}}{\nu_{\text{CO}} \left(P_{\text{total}} \frac{\nu_{\text{O}_2}}{\nu_{\text{total}}} \right)^{\frac{1}{2}}} \quad (2.7)$$

$$K_{p,\text{H}_2\text{O}} = \frac{P_{\text{H}_2\text{O}}}{P_{\text{H}_2} P_{\text{O}_2}^{\frac{1}{2}}} = \frac{\nu_{\text{H}_2\text{O}}}{\nu_{\text{H}_2} \left(P_{\text{total}} \frac{\nu_{\text{O}_2}}{\nu_{\text{total}}} \right)^{\frac{1}{2}}} \quad (2.8)$$

The equilibrium constants are functions of temperature and can be solved with the Gibbs function and Gibbs free energy G , which is a function of temperature, enthalpy, and entropy. Equation. 2.9 shows the Gibbs function.

$$\ln K_p = \frac{-\Delta G}{RT} \quad (2.9)$$

Molar balances with Eqn. 2.4 and some additional algebra with the equilibrium constant expressions will reduce the number of unknowns in Eqn. 2.4 leading to the composition of the products, shown further in Law [5]. The equations used to determine the product composition is highly non-linear, therefore, iterative techniques are used to solve them. This is done by assuming a temperature for the products, T_{flame} , calculating the equilibrium constants at the assumed temperature, and determining the composition of the products. The first law is then used to determine the temperature of the products. If the sum of the enthalpy of the reactants and the sum of the enthalpy of the products are equal, Eqn. 2.4 is balanced and the temperature of the products

is T_{flame} . This is a simplified approach, however, programs like *NASA Chemical Equilibrium with Applications (CEA)*, calculate the equilibrium conditions with additional products and higher accuracy.

2.2.3 Adiabatic Flame Temperature

The adiabatic flame temperature is the temperature of the products of a mixture that has reached equilibrium. It is the maximum temperature a combustion reaction that has reached equilibrium can produce for a given equivalence ratio. Although it is seldom reached in practice, the actual temperature is very close. The predicted adiabatic temperature is used to determine combustion efficiency, establish flammability limits, and calculate heat transfer within the combustion chamber.

Because of dissociation, the adiabatic temperature is a function of the fuel to air equivalence ratio, along with the initial pressure and temperature of the air. The maximum temperature rise occurs for an equivalence ratio of approximately 1.05 [2]. The temperature rise for various initial conditions is shown in Fig. 2.3.

The final temperature of a reaction increases with increased initial temperature, however, as shown in Fig. 2.3, the temperature rise is not as significant at higher initial temperatures. This is due to increased effects of dissociation at higher product temperature. At increased pressure, the product temperature also increases and the maximum temperature rise is shifted closer to the stoichiometric equivalence ratio.

2.2.4 Reaction Rates

As stated by Blazowski and Henderson, combustion should occur in a minimal volume due to space requirements in the engine [2], requiring it to take place in a short time. The time required for combustion to take place is dependent on three factors: the time for the fuel to evaporate, the time for the evaporated fuel to mix with air, and the time for the chemical reaction to complete described by Odgers and Kretschmer [4]. Due to

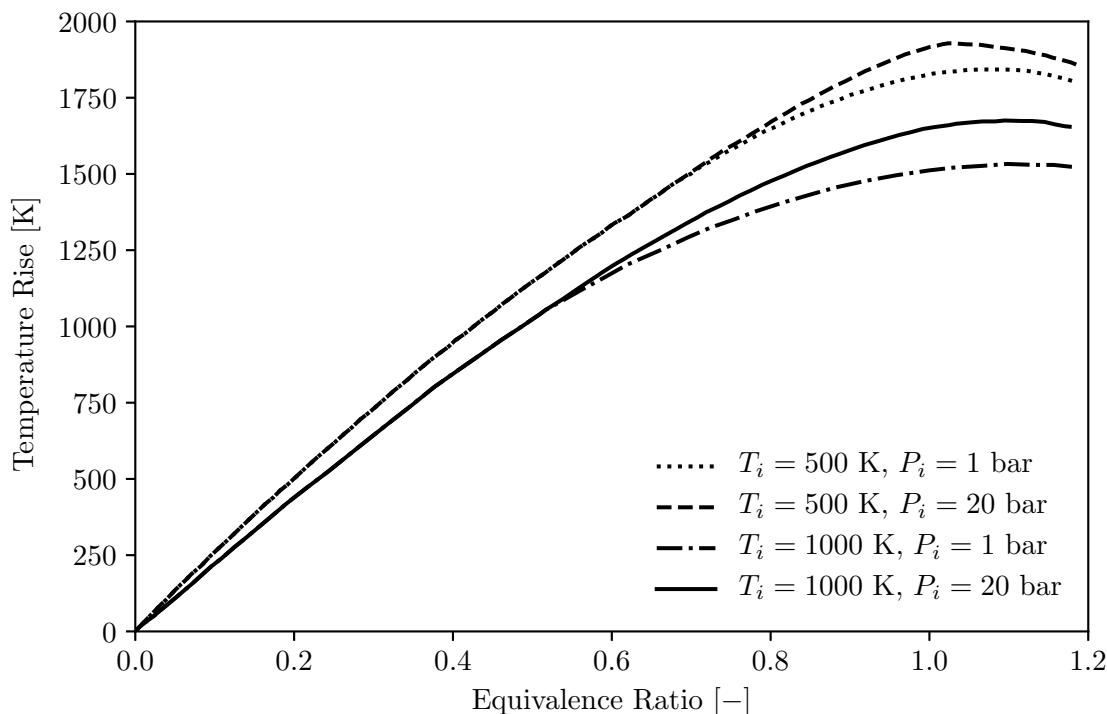


Figure 2.3: Effect of Equivalence Ratio, Temperature, and Pressure on Adiabatic Flame Temperature Rise for Kerosine, adapted from [6].

high rates of reaction in combustion chambers, the time for the reaction to take place is negligible when compared to the time required for evaporation and mixing.

2.3 Airflow Partitioning

The required overall equivalence ratio for a gas turbine is lean and lower than the lean flammability limit for all operating points. Therefore, the air in the combustion chamber is divided into three zones with each zone having a local equivalence ratio suitable to the objective of the given zone. These zones are the primary zone, the secondary zone, and the dilution zone.

Proper distribution of air in the combustion chamber will result in stable operation at all operating conditions and sufficient mixing leading to desired exit temperatures and exit temperature profiles. The chosen temperature in each zone determines the equivalence ratio needed. Using Eqns. 2.2 and 2.3 the required local equivalence ratio,

ϕ_i , is calculated with Eqn. 2.10.

$$\frac{\dot{m}_{\text{air},i}}{\dot{m}_{\text{air}}} = \frac{\dot{m}_{\text{f}}}{\dot{m}_{\text{air}}} = \frac{\frac{\dot{m}_{\text{f}}}{\dot{m}_{\text{air}}}}{\left(\frac{\dot{m}_{\text{f}}}{\dot{m}_{\text{air}}}\right)_{\text{stoic}}} = \frac{\phi}{\phi_i} \quad (2.10)$$

Since the flow in the combustion chamber is incompressible, $Ma < 0.3$, at all operating conditions but at different mass flow rates, it is convenient to express the flows as fraction of the total flow, \dot{m}_3 . These mass flow rate fractions are then true for all operating conditions.

2.3.1 Primary Zone

In the primary zone the fuel is prepared by evaporating, mixing with air, followed by partial combustion. The amount of air introduced into the primary zone is such that the zone is always slightly rich, $1 < \phi < 1.5$, ensuring the mixture is within the flammability limits. The higher temperatures produced with slightly fuel rich mixtures ensure high reaction rates and rapid evaporation, reducing the time required for the combustion reaction to occur.

2.3.2 Secondary Zone

The fuel that is not burned in the primary zone does so in the secondary zone. The amount of air introduced in the secondary zone produces a slightly lean mixture, $0.8 < \phi < 1$, so that combustion is complete at the exit of the secondary zone.

2.3.3 Dilution Zone

In the dilution zone, the chemical reaction has stopped. The purpose of the dilution zone is to add the remaining air required to reduce the temperature of the products of combustion in the liner after combustion is complete. This addition of air lowers the equivalence ratio to the desired equivalence ratio, typically below 0.5. The air is

mixed with the combustion gases to provide the correct outlet temperature as well as an acceptable temperature distribution.

2.4 Combustion Chamber Description

The most common types and configurations of combustion chambers are presented in this section. The various components that are used in combustion chambers are also presented.

2.4.1 Combustion Chamber Types

There are three main types of combustion chamber configurations as outlined by Blazowski and Henderson [2]: can, can-annular, and annular, shown in Fig. 2.4. The configuration selected is based on the overall design of the engine.

The first type is the can combustion chamber, Fig. 2.4(a). A single can may be used in small combustion chambers or several cans may be arranged around the shaft connecting the turbine and compressor with each can having its own concentric outer casing. In this type, the air is split into several streams, one for each can. Each can also has its own fuel injector. The can type was popular in early aircraft engines due to its compatibility with centrifugal compressors, where the air is divided into several streams in the diffuser [1]. Their relatively high weight and the resulting high frontal area have meant a decrease in usage in more recent engines.

The second type of combustion chamber is the can annular type, Fig. 2.4(b). In this type, several cans are arranged uniformly in an annular casing. This type replaced the can type combustion systems of early engines as the most common due to its more compact design.

The third type of combustion chamber is the annular type, Fig. 2.4(c). An annular casing houses a single annular combustion chamber. This type is now the most common in modern aircraft engines. The annular combustion chamber is the ideal type due to

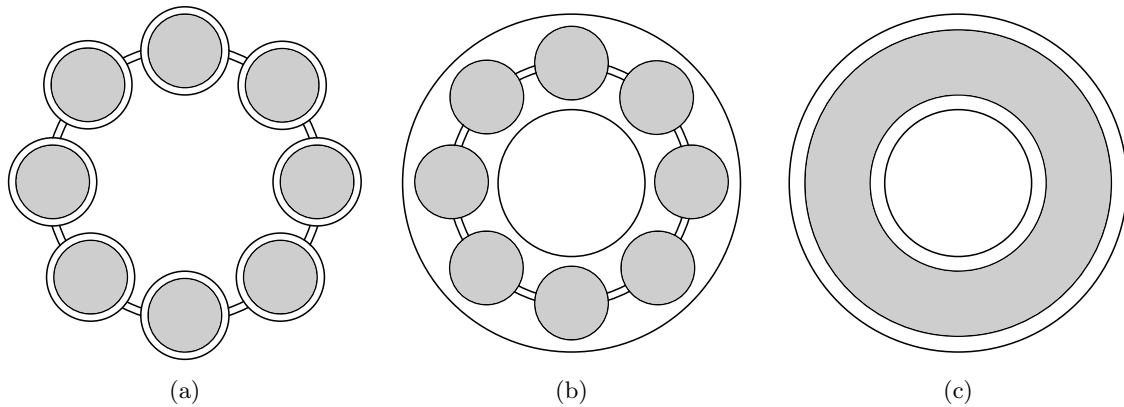


Figure 2.4: Cross Sectional Views Looking Downstream of the Types of Combustion Chambers, (a) Can, (b) Can Annular, (c) Annular.

its reduced surface area, length, and frontal area [7]. Although it is the most common type, there are some disadvantages to annular combustion chamber systems including the complexity in development, difficulty to obtain an even temperature distribution, and structural weakness [1].

2.4.2 Airflow Configurations

For each type there is also an airflow configuration that can be chosen. There are two airflow configurations: axial flow and reverse flow. The name of each configuration refers to the direction of airflow relative to the axis of the engine. In the axial flow configuration, air flows approximately parallel to the axis of the engine from compressor to turbine as shown in Fig. 2.5. This is the most common flow configuration [2].

In a reverse flow configuration the air is directed towards the outlet end of the combustion chamber before turning 180° and passing back along the outside of the combustion chamber. The air then makes another 180° turn through the combustion chamber to the outlet. This configuration can be used to minimize the length of the shaft between the compressor and turbine and is well suited for engines with centrifugal compressors as described by Blazowski and Henderson [2]. An example is shown in Fig. 2.6.

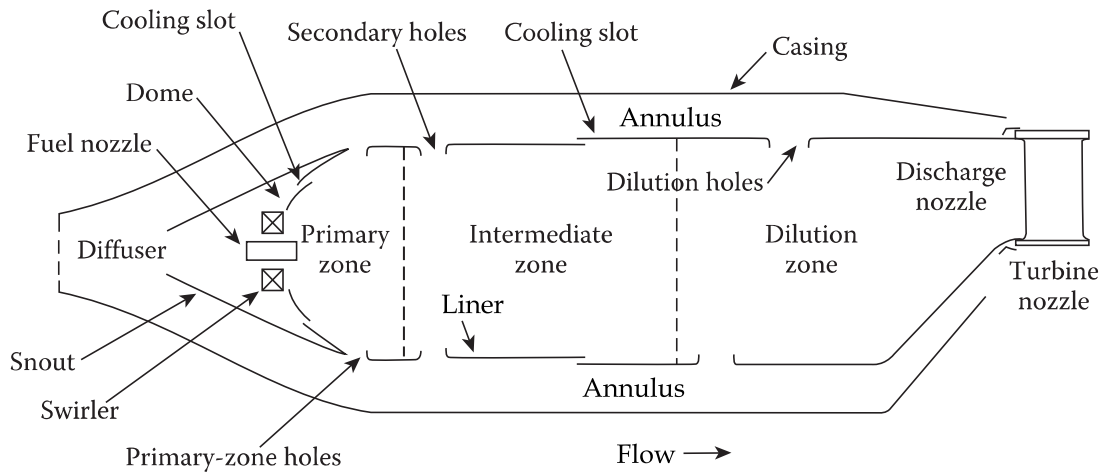


Figure 2.5: Cross Section of a Combustion Chamber, adapted from [6].

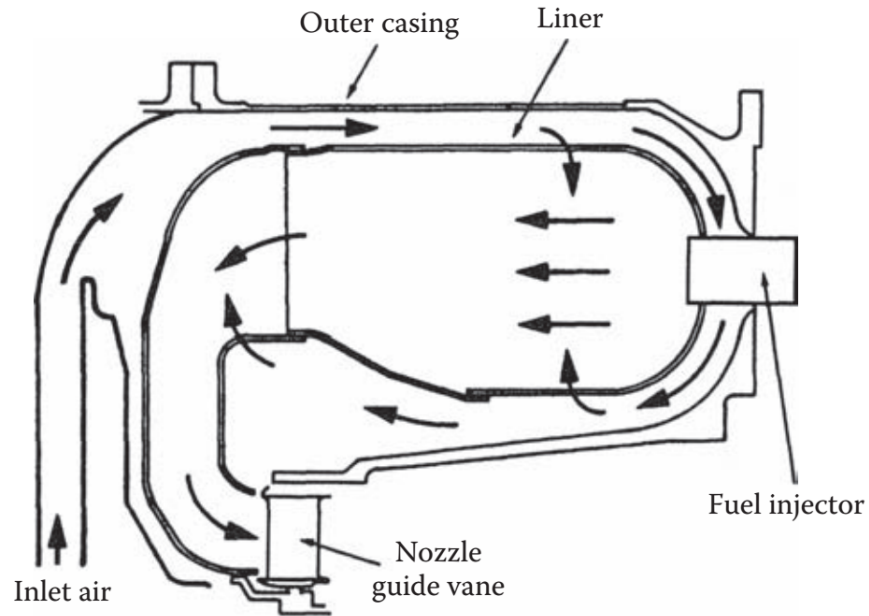


Figure 2.6: A Reverse Flow Combustion Chamber, taken from [6].

2.4.3 Components

The fuel in the combustion chamber is supplied by the fuel injector. The fuel is supplied at high pressure and is atomized and sprayed in a conical pattern into the liner. Well atomized fuel droplets evaporate quickly, decreasing the time required for a combustion reaction to take place.

Air travels from the compressor to the combustion chamber through a diffuser. The velocity of the air at the exit of the compressor often exceeds $150 \frac{\text{m}}{\text{s}}$. This is too fast for the reaction to occur within the combustion chamber, as laminar flame speeds are rarely higher than $5 \frac{\text{m}}{\text{s}}$ [6, 8]. To ensure combustion is completed within the combustion chamber, and to avoid excessive pressure losses, the air velocity must be reduced. This is accomplished with a diffuser.

Downstream of the diffuser are the snout and dome. The dome houses the fuel injector, swirler, and in most cases the igniter. The snout divides the air from the diffuser into two streams. The first stream, which is the majority of the air, enters an annulus between the casing and the liner going around the snout. The angle between the snout and casing wall provide the increase in area to diffuse the air. The second stream is directed to the dome, where it is introduced into the liner through the swirler and dome cooling slot.

Relatively cold air introduced through cooling slots keep the liner from overheating. The temperature of the combustion gases can exceed 2500 K, however, the cooling slots are placed such that the liner wall temperature does not exceed the materials maximum temperature limit. Modern liners are often constructed using alloys of nickel due to their desirable properties at high temperatures. The liner must be made to withstand continuous and cyclical high temperature operation.

The casing is the outer shell that surrounds the liner. The casing provides the outer wall that creates the annulus around the liner. Like the liner, the casing must be able to withstand high pressures, high temperatures, and high cyclic loading.

2.5 Combustion Chamber Design

The following section describes the combustion chamber design method taken from Odgers and Kretschmer [4].

2.5.1 Sizing

The size of the combustion chamber is dictated by two factors: the reaction rate of the mixture and the allowable pressure loss in the liner [4]. To determine the size of the combustion chamber, the diameter of the primary zone must be determined. The volume of the primary zone can be estimated with several methods. Methods have been derived for both chemical kinetics and aerodynamics.

The diameter of the primary zone determines the size of the entire combustion chamber. The diameter of the liner is proportional to the length of each of the zones. Therefore, the calculation of the diameter of the primary zone is a critical procedure in the design of a combustion chamber.

2.5.1.1 Chemical Kinetics

A correlation to determine the primary zone volume based on reaction rate is given in Kretschmer and Odgers [9]. The correlation was derived for propane, Eqn. 2.11, and may be assumed valid for most fuels. The diameter can be determined by assuming that the volume of the primary zone is a cylinder of equal length and diameter. The values for the variables in Eqn. 2.11 are given in Kretschmer and Odgers [9]. This equation does not take into account the evaporation of fuel droplets.

$$\frac{\dot{M}}{VP_3^n} = \frac{4.76 K_{\text{coll}}}{\bar{R}^n} \frac{e^{-\frac{E}{\bar{R}(T_3 + \epsilon \Delta T_{\text{PZ}})}}}{(T_3 + \epsilon \Delta T_{\text{PZ}})^{n-0.5}} \frac{1}{y\epsilon} \frac{[5(1 - y\epsilon)]^\alpha [\phi - y\epsilon]^{n-\alpha}}{[23.8 + \phi + y\epsilon]^n} \quad (2.11)$$

2.5.1.2 Mach Number Correlation

The size of the combustion chamber can be estimated with a reference Mach number. Some methods estimate the diameter of the casing, while others estimate the diameter of the liner. The ratio of the casing diameter, D , and liner diameter, d , is recommended to be between 1.39 and 1.54 [4]. The reference Mach number for a typical combustion chamber is approximately equal to the allowable pressure loss. The pressure loss is

normally 5% of the inlet pressure [4], therefore, the reference Mach number is 0.05. An equation to approximate the Mach number is given in Eqn. 2.12 [10].

$$Ma = \left(14.31 \frac{\text{m}}{\text{s K}^{0.5}}\right) \frac{\dot{m}_3 \sqrt{T_3}}{A_D P_3} \leq 0.05 \quad (2.12)$$

2.5.1.3 Bragg Correlation

Another aerodynamic relationship to determine the primary zone diameter comes from a correlation by Bragg [10] in Eqn. 2.13. With this correlation the mass flow rate of fuel is used to determine the appropriate area of the primary zone.

$$A_d = \left(0.0162 \frac{\text{m}^2 \text{s}}{\text{kg K}^{0.5}}\right) \frac{\dot{m}_f \sqrt{T_3}}{\left(\frac{P_3}{P_2}\right)} \sqrt{\frac{1}{\left(\frac{\Delta P_{3-4}}{P_3}\right)}} \quad (2.13)$$

2.5.1.4 Aerodynamic Groups

A third method uses aerodynamic groups based on the Mach number for each combustion chamber type. The area of the casing is calculated with Eqn. 2.14.

$$A_D = \frac{\dot{m}_3}{P_3} \sqrt{\frac{RT_3}{2}} \sqrt{\frac{\Delta P_{3-4}}{q_{\text{ref}}}} \frac{P_3}{\Delta P_{3-4}} \quad (2.14)$$

Table 2.2: Typical Values Used in Eqn. 2.14.

Type	$\frac{\Delta P_{3-4}}{q_{\text{ref}}}$	$\frac{\Delta P_{3-4}}{P_3}$	$\frac{\dot{m} \sqrt{T_3}}{A_D P_3}$
Can	40	0.053	0.0030
Can-annular	30	0.054	0.0035
Annular	20	0.060	0.0030

The overall pressure loss, $\frac{\Delta P_{3-4}}{P_3}$, is the pressure loss from the compressor outlet to the turbine inlet. The pressure loss factor, $\frac{\Delta P_{3-4}}{q_{\text{ref}}}$, is a coefficient of pressure loss with respect to a reference dynamic pressure. In practice, two of the values in Tab. 2.2 are selected and the third value is then calculated. Substituting the calculated values back into Eqn. 2.14 along with the operating conditions, allows for the size of the combustion chamber to be determined.

2.5.1.5 Greenhough-Lefebvre Correlation

The Greenhough-Lefebvre correlation [4] is the another method used to determine the size of the combustion chamber. The correlation is shown in Eqn. 2.15. The volume is assumed to be a cylinder with length equal to the casing diameter.

$$\phi = \frac{V^{0.75} P_3^{1.75}}{\dot{m}} e^{\frac{T_3}{260\text{K}}} \quad (2.15)$$

2.5.1.6 Length

The diameters calculated vary with each method, therefore, the selected diameter is typically determined by the engine geometry constraints. The length of each zone in the combustion chamber is proportional to the diameter of the primary zone as shown in Eqs. 2.16, 2.17, and 2.18.

$$0.66d_{\text{PZ}} \leq L_{\text{PZ}} \leq 0.75d_{\text{PZ}} \quad (2.16)$$

$$L_{\text{SZ}} = 0.5d_{\text{PZ}} \quad (2.17)$$

$$L_{\text{DZ}} = \left[\frac{20}{Q \left(\frac{\Delta P_{3-4}}{q_{\text{ref}}} \right)} \right]^{0.4} d_{\text{PZ}} \quad (2.18)$$

Where Q is the maximum pattern factor, also called traverse quality. The pattern factor represents the maximum outlet temperature deviation from the mean outlet temperature. The pattern factor is calculated with Eqn. 2.19.

$$Q = \frac{T_{\text{max}} - T_4}{T_4 - T_3} \quad (2.19)$$

An even temperature profile can be obtained by lengthening the dilution zone, however, as stated by Lefebvre [6], the additional length required to achieve such a temperature profile would result in an unacceptable increase in weight of the engine and pressure loss in the combustion chamber. Therefore, the length of the dilution zone is limited to reduce these negative aspects of a longer combustion chamber.

2.5.1.7 Casing

The diameter of the casing, D , is also based on the diameter of the primary zone. Equation 2.20 is used to calculate the diameter of the casing.

$$1.39 d_{PZ} < D < 1.54 d_{PZ} \quad (2.20)$$

2.5.2 Diffuser Design

Diffuser design can vary greatly depending on engine configuration. One type is the faired diffuser where the velocity of the air is reduced gradually through multiple diffusing passages. The first passage is located upstream of the combustion chamber, another in the annular region around the liner, and inside the snout [6]. A second diffuser type is the dump diffuser where the velocity of the air is reduced in a conventional diffuser before being dumped in front of the liner dome. The faired diffuser offers lower pressure drop compared to the dump diffuser, however, the length and weight is higher when compared to the dump diffuser.

The purpose of the diffuser is to effectively reduce the velocity of the air with the smallest possible pressure drop, often approximately 1% of the inlet pressure. The air exiting the diffuser should also have a minimal amount of flow distortion, therefore, the angle at which the passage diverges must not be too great. If the angle is too great, flow separation on the diffuser wall will result in distorted flow and higher pressure losses.

The diffuser pressure loss factor, $\frac{\Delta P_{\text{diff}}}{q_{\text{ref}}}$, contributes to the pressure loss factor for the entire combustion chamber along with the snout and swirler pressure loss, as shown in Eqn. 2.21. The pressure loss factor is calculated with Eqn. 2.22.

$$\frac{\Delta P_{3-4}}{q_{\text{ref}}} = \frac{\Delta P_{\text{diff}}}{q_{\text{ref}}} + \frac{\Delta P_{\text{sn}}}{q_{\text{ref}}} + \frac{\Delta P_{\text{sw}}}{q_{\text{ref}}} \quad (2.21)$$

$$\frac{\Delta P_{\text{diff}}}{q_{\text{ref}}} = \frac{\Delta P_{\text{diff}}}{P_3} \frac{\Delta P_{3-4}}{q_{\text{ref}}} \frac{P_3}{\Delta P_{3-4}} \quad (2.22)$$

The velocity of the air in the snout is further reduced before entering the liner. The velocity of the air at the inlet of the snout and the velocity of the air around the snout

should be equal, therefore the area of the snout, A_{sn} , is determined by the conservation of mass. The area around the snout is known as the annulus. The mass flow rate of air through the snout is selected based on swirler flow rate and dome cooling requirements. A good estimation of this flow rate is half of the airflow in the primary zone.

2.5.3 Dome Design

The dome houses the fuel injector and the swirler. The fuel injected into the primary zone requires time to evaporate and mix with air. To allow the fuel droplets adequate time in this zone, a recirculation region is created, keeping the fuel droplets in the primary zone. This flow structure is created by a swirler, shown in Fig. 2.7.

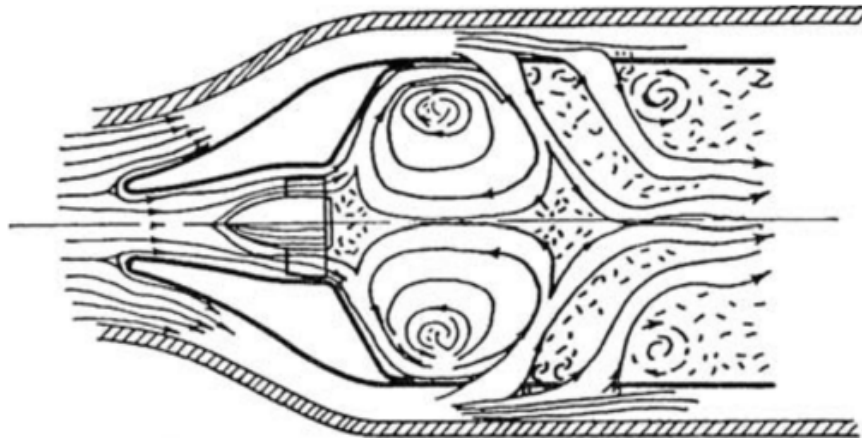


Figure 2.7: Flow in the Primary Zone, taken from [6].

The swirler stabilizes the flame by creating a low pressure region just downstream of the swirler promoting a recirculation flow to form. The diameter of the swirler is smaller than the liner, therefore, the air expands radially outward once it enters the liner due to the tangential velocity of the flow. This results in axial and radial pressure gradients in the primary zone. A low pressure region can be found in front of the fuel injector. If the swirl is strong and the fuel droplets are small enough, these pressure gradients are large enough to cause flow reversal and entrain the fuel droplets [11]. The flow pattern is assisted by incoming air from the primary zone hole jets and forms a

toroidal vortex. The resulting flow pattern is a toroid with edges tangent to the liner wall, the dome wall, the liner centerline, and the primary zone hole jets. The toroidal vortex can be simplified to a circle in two dimensions, and is known as the magic circle. The approximate dimensions of the magic circle are shown in Fig. 2.8.

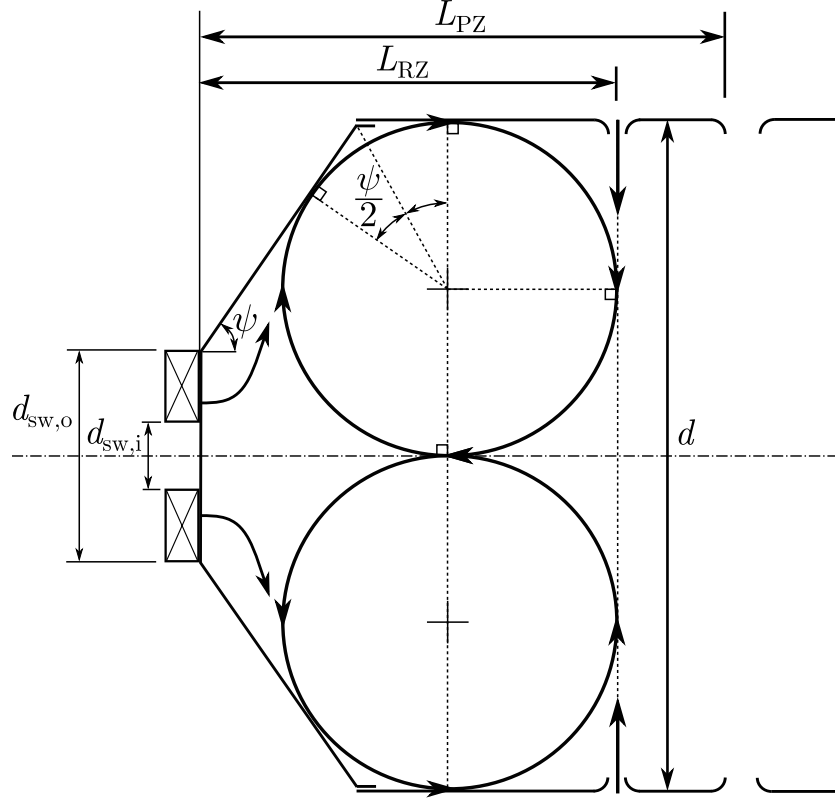


Figure 2.8: Dimensions of the Magic Circle and Dome.

The angle of the dome relative to the centerline of the liner, ψ , is calculated such that this circle occupies approximately 80% of the primary zone by volume [4]. The angle of the dome, ψ , must be calculated by iteratively solving Eqn. 2.23. The derivation of this equation is given in Appendix A.2.

$$L_{RZ} = 0.8L_{PZ} = \frac{1}{2} \left[\frac{d - d_{sw,o}}{\tan \psi} + \frac{d}{2} \tan \left(\frac{\psi}{2} \right) + \frac{d}{2} \right] \quad (2.23)$$

Another useful method of determining the angle of the dome is by estimating the length of the recirculation zone, L_{RZ} , with the swirl number, S , as suggested by Mat-

tingly [12, p. 354]. Equation 2.24 is used to calculate the length of the recirculation zone. The swirl number is defined in Eqn. 2.25.

$$L_{\text{RZ}} = S d_{\text{sw},o} \quad (2.24)$$

$$S = \frac{2}{3} \tan \beta_{\text{sw}} \left[\frac{1 - \left(\frac{d_{\text{sw},i}}{d_{\text{sw},o}} \right)^3}{1 - \left(\frac{d_{\text{sw},i}}{d_{\text{sw},o}} \right)^2} \right] \quad (2.25)$$

Swirlers are typically placed around the fuel injector at the center of the dome. The purpose of the swirler is to add a tangential component to the velocity of the flow with a set of angled blades resulting in air flowing radially outward at the exit of the swirler. There are two main types of swirlers: axial swirlers and radial swirlers as shown in Fig. 2.9.

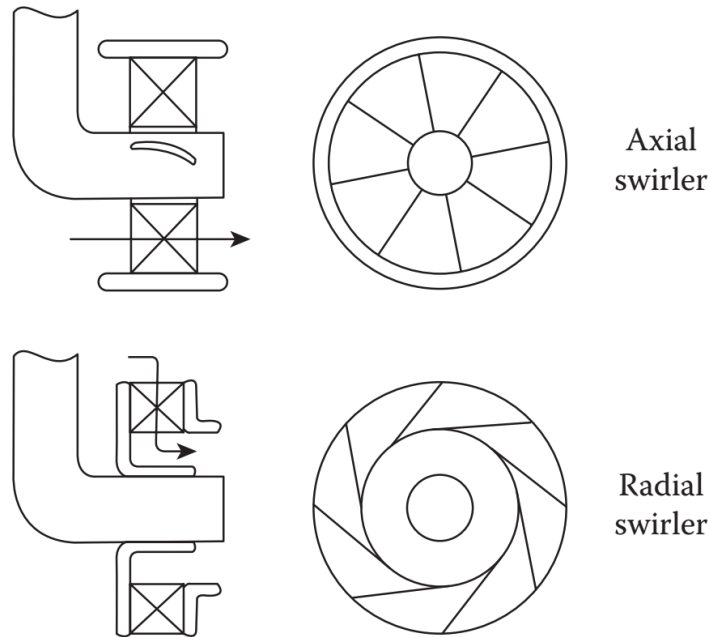


Figure 2.9: Axial and Radial Swirlers [6].

The size of the swirler is determined by the swirler pressure loss factor, which is calculated by rearranging Eqn. 2.21, the angle of the blades, and the mass flow rate of air through the swirler. The fraction of the total flow rate through the swirler is typically

between 3% and 10%. The cross sectional area of an axial swirler is calculated with Eqn. 2.26.

$$A_{sw} = \frac{A_D}{\cos \beta_{sw}} \sqrt{\frac{K_{sw}}{\frac{\Delta P_{sw}}{q_{ref}} \left(\frac{m_3}{m_{sw}}\right)^2 + K_{sw} \left(\frac{A_D}{A_d}\right)^2}} \quad (2.26)$$

Where K_{sw} is a swirler constant, which is dependent on the type of blade used, $K_{sw} = 1.15$ for curved blades and $K_{sw} = 1.3$ for straight blades. The angle of the blades is between 45° and 70° . The area of the swirler calculated with Eqn. 2.26 is then increased by 50% to account for the blockage of the blades [4]. The inner diameter of the swirler, $d_{sw,i}$, is the diameter of the injector, therefore, the outer diameter of the swirler, $d_{sw,o}$ can be calculated using Eqn. 2.27.

$$d_{sw,o} = \sqrt{\frac{4(1.5 A_{sw})}{\pi} + d_{sw,i}^2} \quad (2.27)$$

2.5.4 Liner Wall Cooling

The liner wall is heated by the combustion gas through radiation and convection resulting in situations where the liner may deform due to extreme heat. Therefore, cooling devices are used to inject air along the liner wall to maintain acceptable liner temperatures.

On present day engines approximately 20% of the air is used for wall cooling [6], however, prior to advancements in wall cooling techniques, the proportion of air required for cooling was as much as 60% [13]. Air can be introduced in many ways, a variety of cooling devices are shown in Fig. 2.10.

Transpiration cooling (Fig. 2.10(a)) uses specially manufactured materials to pass air through small pores in the wall [14, 15]. Effusion cooling (Fig. 2.10(b)) uses several holes in the liner wall to add air and create a film along the liner wall. Impingement cooling involves directing air onto the outside of the liner, cooling the liner by convection as shown in Fig. 2.10(c). Machined ring cooling and wiggle strip cooling are examples

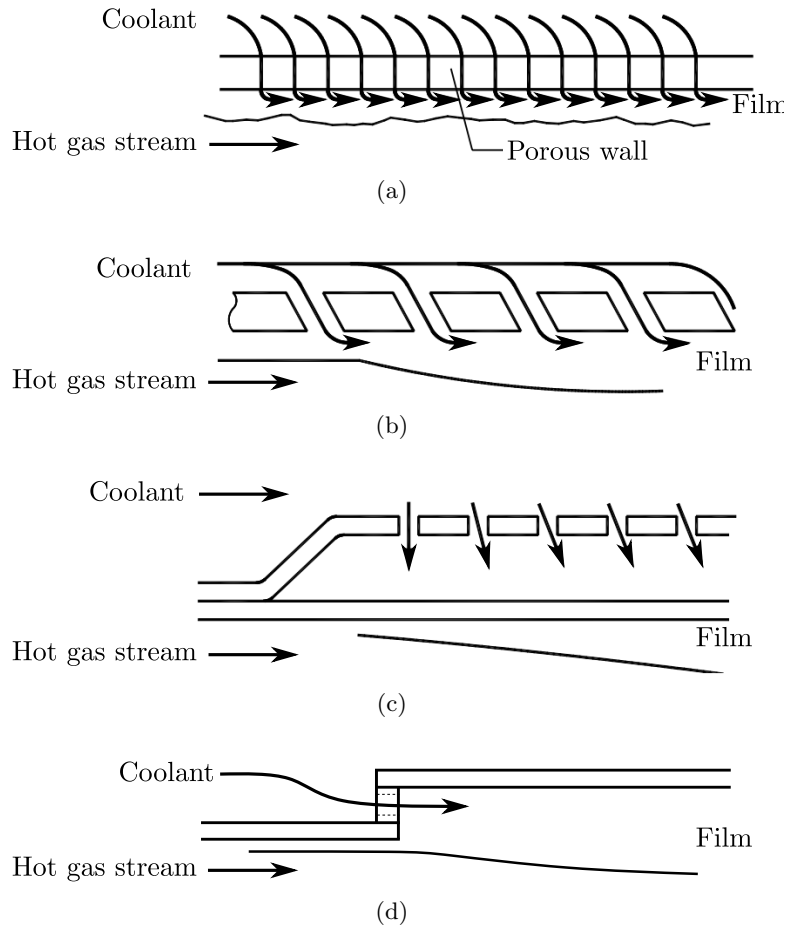


Figure 2.10: Four Types of Cooling Devices, (a) Transpiration, (b) Effusion Cooling, (c) Impingement Cooling, (d) Film Cooling, adapted from [14].

of film cooling techniques. Some cooling devices simply introduce a film of cool air parallel to the liner wall through slots, as shown in Fig. 2.10(d). Air passes along the outside of the upstream wall before passing through the wiggle strip to the inner side of the downstream wall as shown in Fig. 2.11. The wiggle strip acts as a joint between the two walls.

It is important to maintain a uniform film along the liner to avoid overheating of the liner. Film cooling air injected upstream of holes is blocked by the jets produced by the holes, leaving a region behind the jets without cooling air. Therefore, film cooling slots should be placed downstream but reasonably close to the holes.

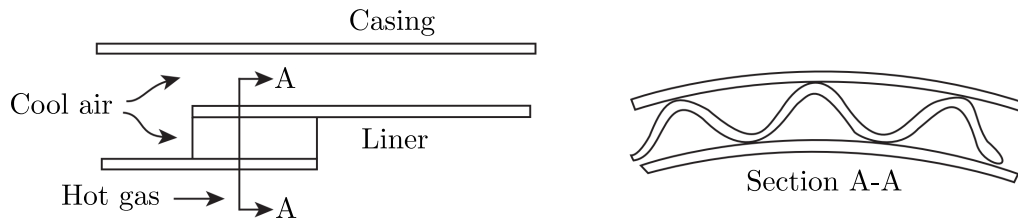


Figure 2.11: Diagram of a Wiggle Strip [6].

The placement of the film cooling devices is determined by calculating the wall temperature of the combustion liner and placing a new film cooling device when the wall temperature exceeds the allowable temperature of the material. This process is continued until the end of the combustion chamber. This requires the calculation of the mass flow rate inside and outside of the liner, as well the mass flow rate of the cooling film. The temperatures of the cooling air, annulus air, and combustion gas are also required. Figure 2.12 shows a representation of a film cooling device.

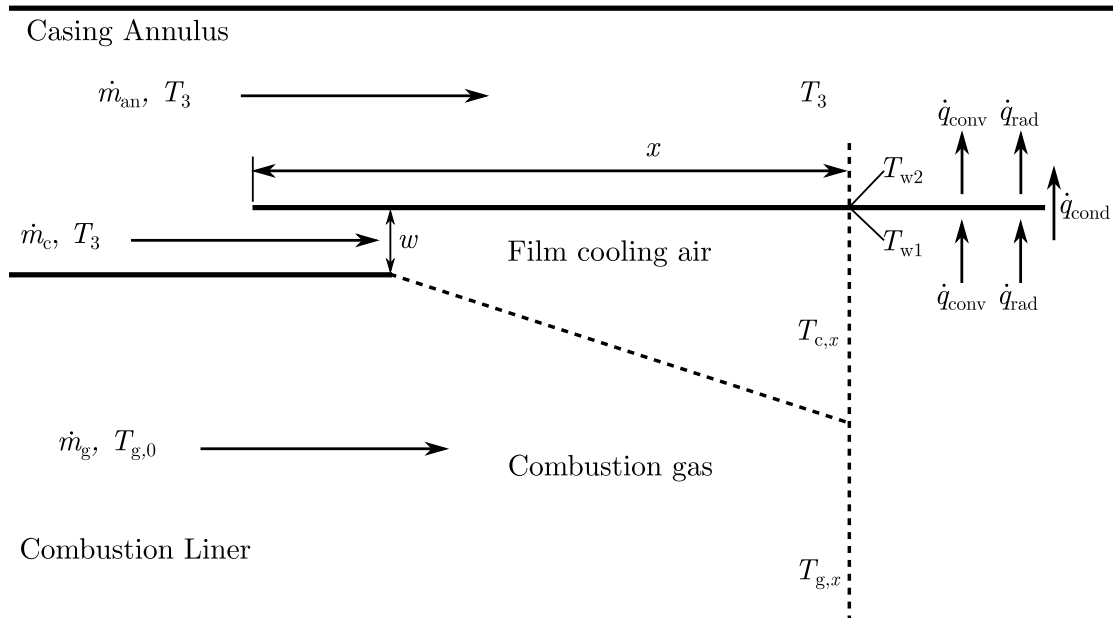


Figure 2.12: A Representation of a Film Cooling Device

To determine the wall temperature, the combustion gas temperature at any given point, $T_{g,x}$, through the combustion chamber must be known. Each region of the com-

bustion chamber has a different temperature change based on the equivalence ratio at the given location. For the purposes of calculating the wall temperature for film cooling device placement, the temperature changes in each zone are considered to be linear. Odgers and Kretschmer [4] provide a method to determine the axial temperature profile along the length of the combustion chamber.

The temperature of the liner is determined by the radiation and convective heat transfer into the liner and the convection to the air in the annulus and the radiation to the casing. The wall temperature is calculated through an energy balance defined by the convection and radiation from the hot gas inside the liner to the liner wall, $\dot{q}_{\text{conv,w1}}$ and $\dot{q}_{\text{rad,w1}}$, the conduction of heat through the liner wall, \dot{q}_{cond} , and the convection and radiation away from the liner to the air in the annulus and casing wall, $\dot{q}_{\text{conv,w2}}$ and $\dot{q}_{\text{rad,w2}}$. Again, the equations to predict the magnitude of each type of heat transfer are found in Odgers and Kretschmer [4]. The energy balance is shown in Eqn. 2.28.

$$\dot{q}_{\text{conv,w1}} + \dot{q}_{\text{rad,w1}} = \dot{q}_{\text{cond}} = \dot{q}_{\text{conv,w2}} + \dot{q}_{\text{rad,w2}} \quad (2.28)$$

The difference in temperature on the inside and outside of the the liner wall is small if the wall is sufficiently thin (1-2 mm). Therefore, the temperature difference does not need to be calculated and the energy balance can be simplified to only consider convection and radiation to and from the wall.

The temperature of the cooling air near the wall increases and the efficiency of the cooling air on the the liner wall decreases further away from the cooling device. The cooling efficiency varies for the different types of cooling devices and is used to calculate the convective heat transfer to the inner wall of the liner. The cooling efficiency for a wiggly strip decreases as the distance from the film cooling device increases, as shown in Fig. 2.13.

The mass flow rate of air through each cooling device is a function of the cooling air temperature and pressure, the pressure loss across the cooling device, and the area of the air passage. Each cooling device is designed such that the pressure loss is equal to that

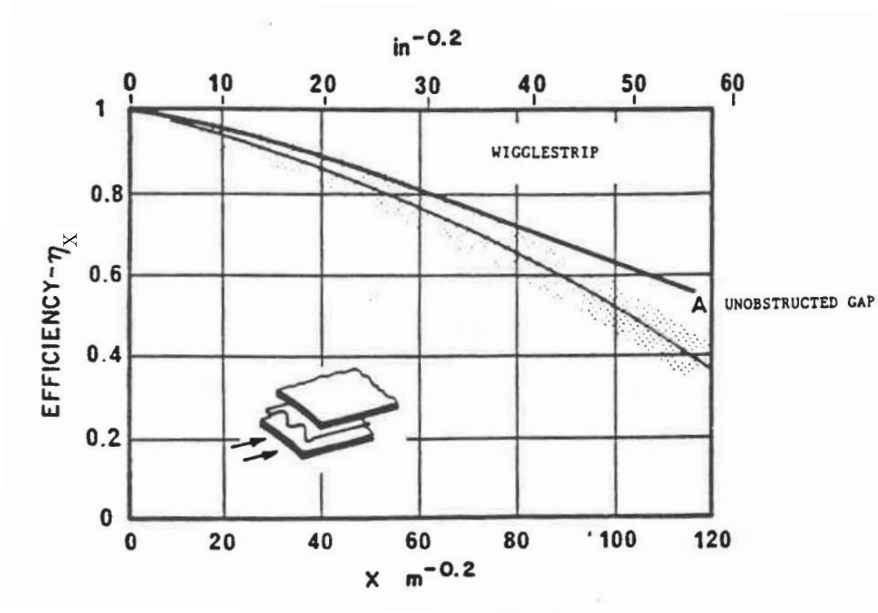


Figure 2.13: Cooling Efficiency for a Wiggle Strip taken from [10].

of the swirler. The pressure loss through the slot is equal to the pressure loss through the swirler resulting in an even pressure distribution between the two. The pressure loss is calculated with Eqn. 2.29. The mass flow rate is calculated with Eqn. 2.30.

$$\frac{\Delta P_c}{P_3} = \frac{\Delta P_{sw}}{P_3} = \left(\frac{\Delta P_{sw}}{q_{ref}} \right) \left(\frac{q_{ref}}{\Delta P_{3-4}} \right) \left(\frac{\Delta P_{3-4}}{P_3} \right) \quad (2.29)$$

$$\dot{m}_c = \sqrt{\frac{2 P_3^2 A_{c,eff} \Delta P_c}{R T_3 P_3}} \quad (2.30)$$

2.5.5 Air Admission Holes

Mixing of air with combustion gases in the combustion chamber has significant effects on the exit temperature profile. Mixing is dependent on the geometry of the combustion chamber as well as the geometry of the holes in the liner that the air is admitted through. The quality of mixing, is dependent on the size of the hole, pressure loss through the hole, the flow conditions around the hole, and the type of hole [6].

The design of holes in the liner begins with the calculation of airflow through each set of holes. The air in the primary zone is supplied by the swirler, the air from cooling devices that end in the primary zone, and the primary zone holes. It is assumed that half of the air from the primary zone holes supplies the recirculation zone and the other half continues downstream into the primary zone towards the secondary zone. The air in the recirculation zone contributes to the total air in the primary zone and is supplied by the swirler and the air from cooling devices in the recirculation zone. Equations 2.31 and 2.32 describe the sources of air in the recirculation zone and primary zone. Substituting Eqn. 2.31 into Eqn. 2.32 yields Eqn. 2.33, which is used to calculate the required flow rate through the primary zone holes.

$$\dot{m}_{\text{RZ}} = \dot{m}_{\text{sw}} + \sum \dot{m}_{\text{c,RZ}} + \frac{\dot{m}_{\text{PZ,hole}}}{2} \quad (2.31)$$

$$\dot{m}_{\text{PZ}} = \dot{m}_{\text{RZ}} + \frac{\dot{m}_{\text{PZ,hole}}}{2} \quad (2.32)$$

$$\dot{m}_{\text{PZ,hole}} = \dot{m}_{\text{PZ}} - \dot{m}_{\text{sw}} - \sum \dot{m}_{\text{c,PZ}} \quad (2.33)$$

Air through the secondary and dilution zone holes are defined in a similar manner. Air from upstream in the liner supply a portion of the air and the holes make up the remainder to achieve the required air proportion in the zone. Equations 2.34 and 2.35 define the flow rate through the secondary and dilution zone holes.

$$\dot{m}_{\text{SZ,hole}} = \dot{m}_{\text{SZ}} - \dot{m}_{\text{PZ}} - \sum \dot{m}_{\text{c,SZ}} \quad (2.34)$$

$$\dot{m}_{\text{DZ,hole}} = \dot{m}_3 - \dot{m}_{\text{SZ}} - \sum \dot{m}_{\text{c,DZ}} \quad (2.35)$$

The total area of the holes is a function of the condition of the air, the mass flow rate of the air, and the allowable pressure loss through the holes. The allowable pressure loss through the holes is determined with Eqn. 2.36. The area of the holes is calculated with Eqn. 2.37. This is the total area for a set of holes. Once the number of holes is determined, the diameter of each hole is calculated.

$$\frac{\Delta P_{\text{hole}}}{P_3} = \frac{\Delta P_{3-4}}{P_3} - \frac{\Delta P_{\text{diff}}}{P_3} \quad (2.36)$$

$$A_{\text{hole}} = \frac{\dot{m}_{\text{hole}}}{P_3 C_D} \sqrt{\frac{RT_3}{2} \frac{P_3}{\Delta P_{\text{hole}}}} \quad (2.37)$$

The primary zone holes are placed at the end of the recirculation zone to assist with the formation of the toroidal vortex. The secondary holes are placed at the beginning of the secondary zone. The dilution zone holes are placed at the beginning of the dilution zone. Holes are normally arranged symmetrically around the liner in a single row.

The penetration of the jets issuing from the liner holes is influenced most significantly by the jet to cross-flow momentum flux ratio [16] which is the ratio of the momentum of the jet from the liner hole to the momentum of the flow inside the liner. Ideal jet penetration occurs when the jet reaches the centerline of the liner. Over-penetration of the jets results in higher pressure losses within the liner, while under-penetration will result in a hot core stream due to insufficient mixing at the centerline of the liner. Therefore, it is important to attain satisfactory jet penetration. Pressure gradients caused by the blockage of the jet provides the force required to deform the jet, as shown in Fig. 2.14 [17, 18]. The penetration of the jet is estimated using Eqn. 2.38.

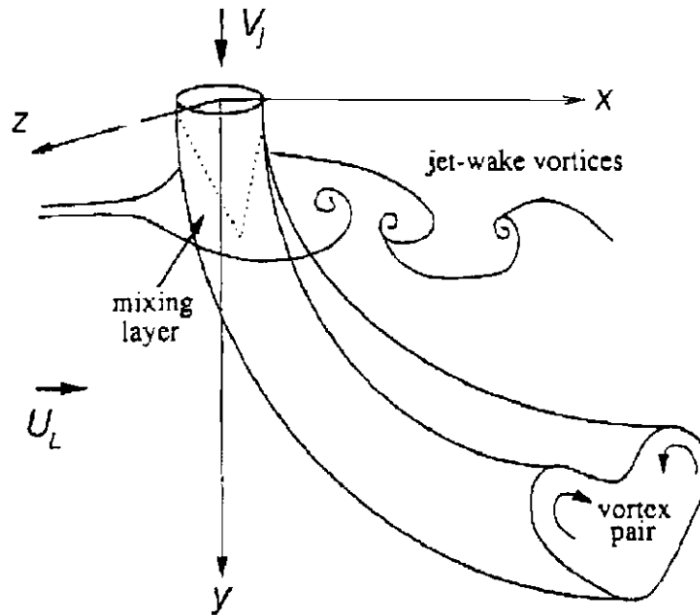


Figure 2.14: Jet in a Crossflow taken from [18].

$$\frac{y}{d} = 0.365 \log \left[\left(\frac{\rho_g A_d^2 \dot{m}_{\text{hole}}^2}{\rho_{\text{hole}} A_{\text{hole}}^2 \dot{m}_g^2} \right)^{0.5} \left(\frac{2d_{\text{hole}}}{d} \right) \left(\frac{\dot{m}_{\text{hole}} + \dot{m}_g}{\dot{m}_g} \right) \sin \theta_{\text{hole}} \right] + 0.485 \quad (2.38)$$

2.6 Exit Temperature Profile

As mentioned in Saravanamuttoo *et al.* [1, p. 84] the temperature of highest importance in a gas turbine engine is the combustion chamber exit temperature. The combustion chamber exit temperature affects the total power output of the engine as well as the cycle efficiency but also limits the life of the hot section components. The exit of a combustion chamber may have hot streaks or uneven temperatures, therefore, hot section components should be designed to withstand temperatures above the average exit temperature.

The quality of the exit temperature profile is one of the major challenges in the development of gas turbine combustion chambers. The temperatures at the outlet of the combustion chamber must be within the design limitations of the turbine. Failure to remain within these limits can prematurely degrade nozzle guide vanes and turbine blades, leading to decreased service duration.

2.6.1 Quantifying Exit Temperature Profile

Lefebvre [6] outlines three methods used in industry to describe the exit temperature of the a combustion chamber: the pattern factor, profile factor, and turbine profile factor. Pattern factor represents the maximum temperature deviation from the mass flow weighted mean temperature at the exit of the combustion chamber. Since a measure of the maximum temperature deviation is given, nozzle guide vanes can be designed to operate in the most extreme conditions. Pattern factor is defined as:

$$\text{Pattern Factor} = \frac{T_{\text{max}} - T_4}{T_4 - T_3} \quad (2.39)$$

Pattern factor can be calculated using either the mass-flow weighted or area average temperature. Both methods yield similar results, however, mass-weighted averages are rarely used. In general, mean temperatures are expressed as area averages due to their relatively simplicity [19]. Ideally, to maximize turbine component life, the pattern factor should be below 0.2. Variations may occur but the pattern factor should not be higher than 0.5 [20].

The exit temperature profile can be characterized by its radial temperature profile which is described by profile factor. Profile factor describes the temperature distribution on a turbine blade from hub to tip. The profile factor is the ratio of the difference between the maximum circumferential mean temperature and the mean exit temperature and the difference between the mean exit temperature and the inlet temperature. Profile factor is calculated with Eqn. 2.40.

$$\text{Profile Factor} = \frac{\max(T_{\text{mean,r}}) - T_4}{T_4 - T_3} \quad (2.40)$$

Both the pattern factor and profile factor compare temperature differences to a mean temperature and are best suited for situations where the exit temperature distribution is perfectly uniform. The desired temperature profile is rarely flat. The radial temperature profile is typically tailored to provide low temperatures at the blade root where mechanical stresses are high and at the blade tip where cooling is difficult [6]. The turbine profile factor takes the design temperature profile into account as is defined by Eqn. 2.41.

$$\text{Turbine Profile Factor} = \frac{\max(T_{4,r} - T_{4,\text{des}})}{T_4 - T_3} \quad (2.41)$$

The maximum temperature difference, $\max(T_{4,r} - T_{4,\text{des}})$, compares the average temperature and the design temperature at the same given radius. Profile factor offers a very detailed measure of the exit temperature profile in relation to the turbines operating limits, however, the design profile is not always available, and therefore, is less common. Pattern factor remains the most common parameter when quantifying the exit temperature profile of a combustion chamber [21]. An example of an actual and a

design radial temperature profile with exit temperature profile parameters is shown in Fig. 2.15.

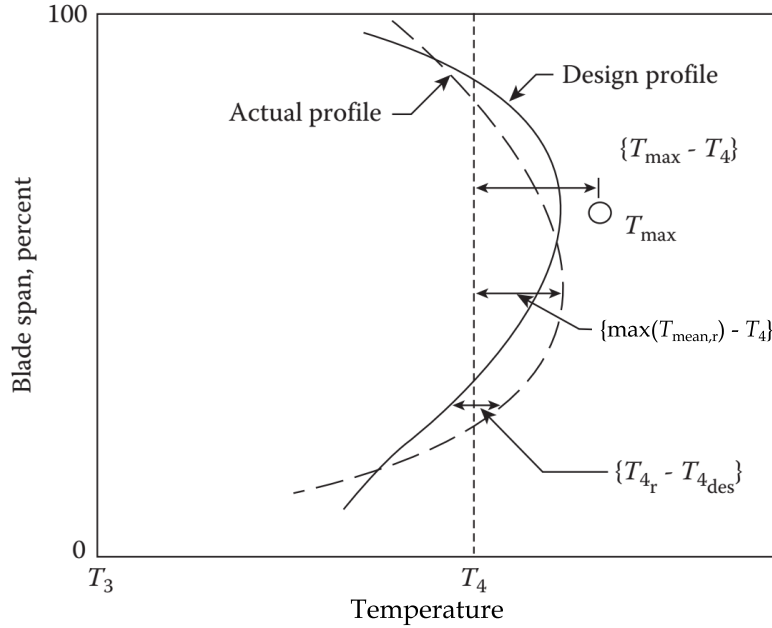


Figure 2.15: Explanation of Exit Temperature Profile Parameters on a Sample Radial Temperature Profile, from Lefebvre [6].

Another method to quantify the outlet temperature field was presented by Bruan [22]. With this factor, the measured temperature is compared to the maximum and minimum measured temperatures. The Bruan profile factor is defined in Eqn. 2.42.

$$\text{Bruan Profile Factor} = \frac{T - T_{\min}}{T_{\max} - T_{\min}} \quad (2.42)$$

2.6.2 Contributors to Pattern Factor

The temperature distribution at the exit of the combustion chamber is influenced by several factors. The most significant contributors are dilution, cooling, primary zone temperature, and combustion chamber geometry. Each of these factors have several dependencies of their own, as shown in Fig. 2.16.

Cooling air flows may not mix sufficiently with the combustion gases before reaching the outlet of the combustion chamber leading to temperature profiles diverging from the

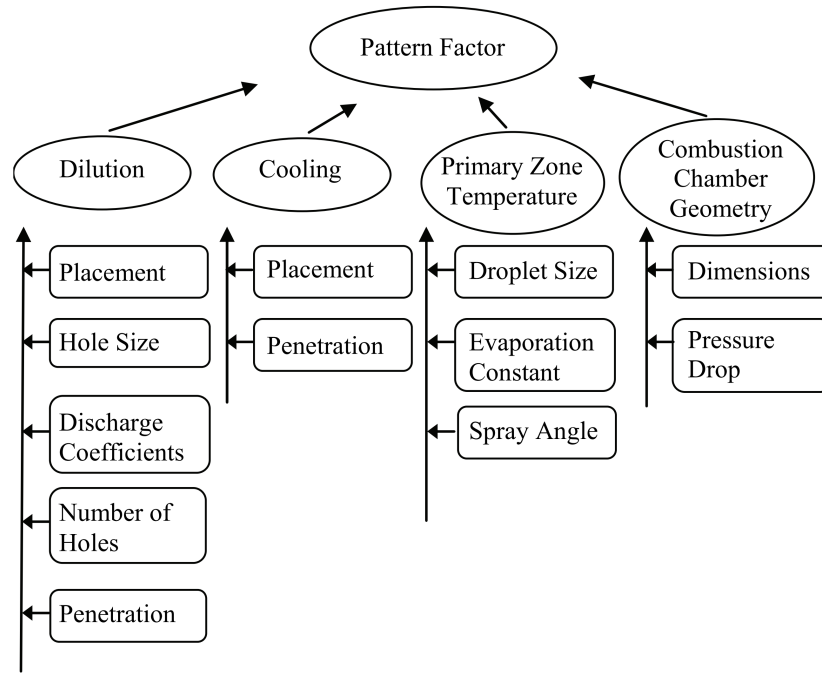


Figure 2.16: Contributors to Pattern Factor [21].

design profile. As Sjöblom [23] states, cooling air tends to make the temperature profile more peaked due to the accumulation of cooling air near the walls. This problem is worsened for higher turbine inlet temperatures, where increased cooling air is required.

Lefebvre proposed a correlation between pattern factor, pressure loss, and liner length [24]. The correlation for can and can annular combustion chambers is shown in Eqn. 2.43.

$$\frac{T_{\max} - T_4}{T_4 - T_3} = 1 - \exp \left[\frac{1}{-0.07 \frac{L}{d} \left(\frac{\Delta P_{sn}}{q_{ref}} + \frac{\Delta P_{sw}}{q_{ref}} \right)} \right] \quad (2.43)$$

With increased pressure drop or increased length, pattern factor is reduced. The pressure drop in the liner dictates the penetration in the dilution zone, while the length of the liner controls the time and volume in which the jets have to mix with the combustion gases.

2.7 Atmospheric Rig Testing

Testing gas turbine engine components at engine operating conditions is difficult as it often requires a tremendous amount of energy. Therefore, to perform preliminary testing of engine components, scaled tests can be performed. This involves scaling operating conditions by matching dimensionless groups. An explanation of the dimensionless groups used to achieve similarity is provided in White [25]. In general, combustion depends on mixing, energy transfer, and fuel spray characteristics.

Consistent airflow between operating and test conditions is ensured by matching the Mach number. The Mach number is calculated with Eqn. 2.44.

$$Ma = \frac{v}{c} \quad (2.44)$$

The velocity, v , and speed of sound, c , can then be defined using mass flow rate, pressure, temperature, and gas properties to define the Mach number with Eqn. 2.48.

$$v = \frac{\dot{m}}{\rho A} \quad (2.45)$$

$$\rho = \frac{P}{RT} \quad (2.46)$$

$$c = \sqrt{\gamma RT} \quad (2.47)$$

$$Ma = \frac{\dot{m}\sqrt{RT}}{PA\sqrt{\gamma}} \quad (2.48)$$

Since the areas are constant for the combustion chamber, and R and γ are approximately equal between the engine and test rig, they can be disregarded. This allows the quasi-non-dimensional Mach number, \widetilde{Ma} , to be used in place of the Mach number. The quasi-non-dimensional Mach number is calculated with Eqn. 2.49.

$$\widetilde{Ma}_{\text{rig}} = \widetilde{Ma}_{\text{engine}} = \frac{\dot{m}\sqrt{T}}{P} \quad (2.49)$$

The enthalpy increase in the combustion chamber is determined by the chemical reaction between the air and fuel. The efficiency of combustion is rarely lower than 99%, therefore, only the fuel flow rate needed to be scaled from the cruise condition

to the test condition to achieve the correct temperature rise. This is done by matching the equivalence ratio, ϕ .

$$\phi_{\text{rig}} = \phi_{\text{engine}} \quad (2.50)$$

In addition to supplying the fuel at the correct flow rate, the fuel spray characteristics must also be equivalent. Odgers *et al.* [26] showed that for fuel sprays with mean fuel droplet diameter below 120 μm the difference in evaporation time is negligible. The mean fuel droplet diameter is known as the Sauter mean diameter, D_{32} , as is defined as the diameter of a drop in a spray that has the same ratio of volume to surface area for the particle of interest [24] as shown in Eqn. 2.51.

$$D_{32} = \frac{\sum_n \frac{4}{3}\pi r_n^3}{\sum_n 4\pi r_n^2} \quad (2.51)$$

For pressure swirl fuel nozzles the Sauter mean diameter is calculated with Eqn. 2.52 [6].

$$D_{32} = 2.25 \left(\frac{\kappa_f \mu_f \dot{m}_f}{\rho_a} \right)^{0.25} \left(\frac{1}{\Delta P_f} \right)^{0.5} \quad (2.52)$$

The surface tension of the fuel is denoted by κ_f . Fuel pressure during flight conditions is often high enough that $D_{32,\text{engine}}$ is less than 120 μm , therefore, to produce equivalent evaporation characteristics $D_{32,\text{rig}}$ must also be less than 120 μm .

The two dimensionless groups, \widetilde{Ma} and ϕ , are used to match the airflow and fuel flow conditions for a real engine operating condition. A sufficiently low Sauter mean diameter will offer equivalent fuel spray characteristics to real engine operation. By controlling these three values, a test simulating a real engine operating condition can be performed at atmospheric conditions.

3 Rolls-Royce M250

The Rolls-Royce M250, originally known as the Allison 250, was introduced in the 1960's. The M250 is an extremely popular and uniquely designed turboshaft engine spawning several variants possessing a wide range of power ratings. The compressor consists of six axial stages and one centrifugal stage. The discharge air from the centrifugal stage is delivered to two diffuser tubes on either side of the engine. The air enters the combustion chamber through the diffuser tubes, with a dual entry design. A reverse-flow combustion chamber with a single can liner is located at the rear of the engine allowing the compressor and turbine to be closer, reducing the length of the shaft connecting the two. The outlet of the combustion chamber is an annulus at the inlet of the turbine section. The first turbine, the gas generator turbine, contains two stages and powers the compressor. The second turbine, the power turbine, also contains two stages and powers an external load. A display cutaway of the engine is shown in Fig. 3.1. The arrows indicate the direction of airflow.

Air from the diffuser tubes turns 180° and enters the casing through two inlets. The air enters the liner through a set of dome swirlers, holes, and wiggle strips. The swirlers create counter rotating flow to assist with mixing of fuel and air in the primary zone. Since there is no radial expansion out of the swirler, no significant pressure gradients are setup to form a strong toroidal vortex. The recirculation zone is set up by the jets in the primary zone. The liner is shown in Fig. 3.2.

The M250 uses a dual orifice pressure swirl nozzle. At low fuel pressure, the primary fuel nozzle is used. Above a certain pressure, the secondary nozzle is activated. In

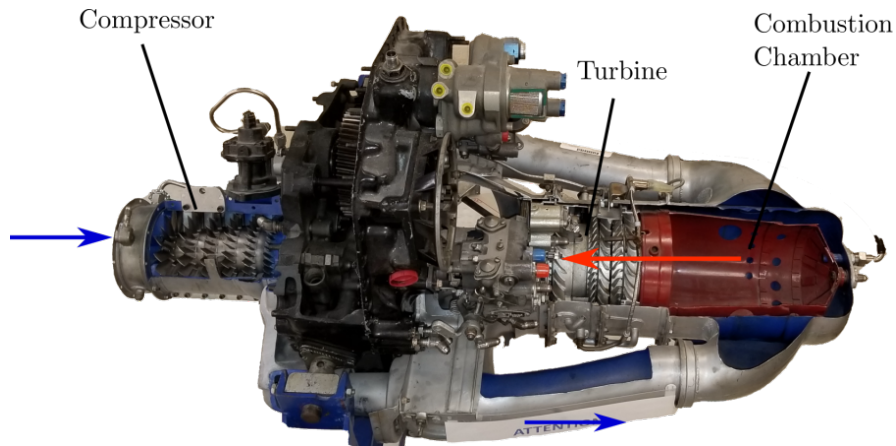


Figure 3.1: M250 Engine Cutaway.



Figure 3.2: M250-C20B Combustion Liner.

normal engine operation, both the primary and secondary nozzles are used.

3.1 M250 Research

A series of studies was performed on the military version of the M250, the T63-A-700, by Eckerle [27], Haas [28], and Bruan [22]. Eckerle built the original test rig with Haas improving on the design by adding additional monitoring systems. Bruan measured the temperature profile at the outlet of the combustion chamber. The temperature profile was measured by installing a thermocouple array consisting of 48 thermocouples at 3 radii and 16 equally spaced locations around the exit annulus. The profile had

a non-uniform temperature distribution and was non-symmetrical with one side being significantly hotter than the other. Temperature profiles using the Bruan profile factor are shown in Fig. 3.3.

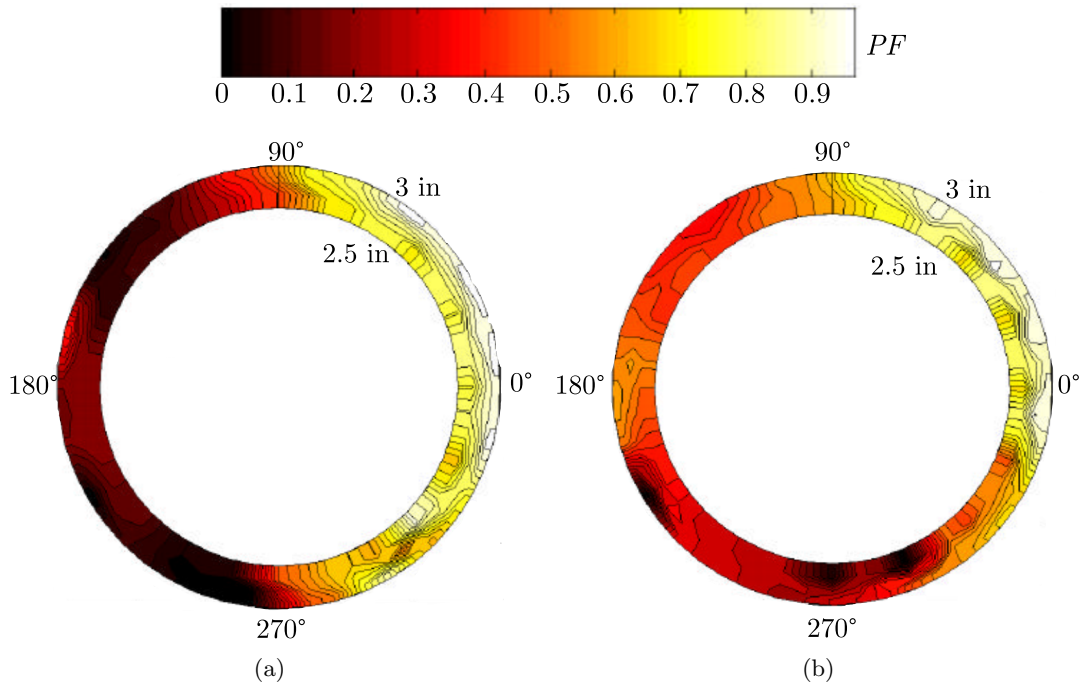


Figure 3.3: Turbine Inlet Temperature Profiles at (a) 80% and (b) 100% Compressor Speed, adapted from [22].

Bruan found that there was a difference in pressure in the two diffuser tubes. It was suspected that the non-symmetric temperature profile was caused by an uneven mass flow rate between the two diffuser tubes. It was concluded that the uneven air flow directed the flame towards one side of the exit. The side with the higher temperature was the side of the engine with the lower pressure diffuser tube.

The difference in flow condition in the two diffuser tubes was studied by Ilott [29], who developed a rig to power and measure the performance of the compressor. The mass flow rate in each of the discharge ports of the centrifugal compressor was measured using venturi type flow meters. It was found that there was up to 3.9% variation in mass flow rate between the two compressor outlet ports at 80% of the design speed

verifying the observations of Bruan.

Ilott [29] also found the Mach number profile at the inlet of the diffuser tubes was highly non-uniform. This non-uniformity would have significant influence the performance of the diffuser tubes upstream of the combustion chamber. Therefore, the quality of the compressor exit profile would have an influence on the combustion chamber performance.

Maqsood [30] continued research on the M250 by investigating the effect of inlet distortion on the combustion chamber exit temperature profile. A test rig was constructed to scale the operating conditions of the M250 to simulate combustion chamber inlet airflow distortion and measure the exit temperature profile. Conclusions of the study were that inlet distortion did have an effect on the exit temperature profile. Regions of relatively high and low temperatures were found for even inlet conditions but were exacerbated and shifted with distorted inlet flow, shown in Fig. 3.4.

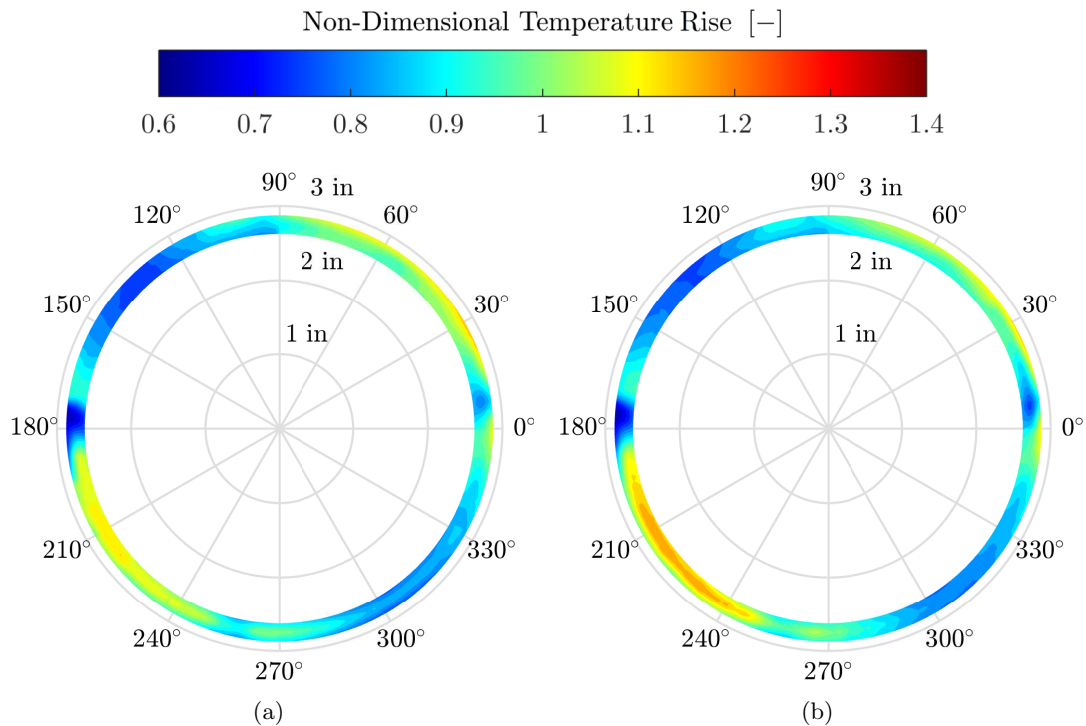


Figure 3.4: Exit Temperature Profile for (a) Even Inlet Mass Flow Rate, (b) 4% Higher Left Inlet Mass Flow Rate, from Maqsood [30].

Maqsood [30] concluded that the two low and two high temperature regions were from incomplete mixing in the dilution zone from the two dilution zone holes. Another conclusion was that when the inlet mass flow rate was higher on one side, the regions of high and low temperature were still present, however, the high temperature region on the side with higher inlet mass flow rate would increase in temperature, thus increasing the pattern factor.

4 Combustion Chamber Redesign

A design process described by Odgers and Kretschmer [4] was followed to develop the new combustion chamber for the Rolls Royce M250-C20B. The design of the combustion chamber is provided in this chapter. First the design constraints and assumptions are stated. Then the operating conditions for the combustion chamber are presented, followed by the air distribution in the zones of the combustion chamber. The calculation of the dimensions of the new combustion chamber is then presented. Next is the dimensioning of the dome followed by the design of the cooling devices. Finally, the sizing of the holes is shown. The dimensions of the newly designed combustion chamber can be found in a set of engineering drawings in Appendix B.

4.1 Design Constraints and Assumptions

The design of the new combustion chamber is intended to be compatible with the current engine configuration, therefore, an unusual set of constraints are placed on the design. The casing and diffuser tubes will remain the same. The new design must have an outlet diameter matching the dimensions of the existing combustion chamber so as to avoid alteration of the turbine section. The new liner must fit into the current casing and must be compatible with the fuel injector and igniter that are currently installed on the engine. It is assumed that the pressure drop across the combustion chamber from compressor outlet to turbine inlet will be 5% of the compressor outlet pressure for all operating points.

4.2 Calculation of Operating Conditions

To begin the design of the combustion chamber, the engine operating conditions are required. These conditions include the compressor exit temperature and pressure, the turbine inlet temperature, and the mass flow rate of air and fuel. The required fuel-to-air equivalence ratio for each operating condition can then be determined.

4.2.1 Engine Operating Points

Seven operating points were obtained from the Allison 250 Engine Installation Manual [31]. When designing a combustion chamber for a gas turbine engine, many more operating points would be used to design the combustion chamber. The operating points used for this design represent typical flight conditions and include the extreme conditions experienced by the engine. The operating points are shown in Tab. 4.1.

Table 4.1: Engine Operating Points At Sea Level Static Conditions Unless Indicated Otherwise.

Condition	Rotor Speed	Fuel Flow Rate	Temperature	
	N_1 [$\frac{\text{rev}}{\text{min}}$]	\dot{m}_f [$\frac{\text{g}}{\text{s}}$]	T_{atm} [K]	T_5 [K]
1 Takeoff	53 000	34.4	288	1 083
2 Max. Continuous	52 220	32.7	288	1 050
3 Max. Cruise	51 200	30.3	288	1 011
4 Cruise A	50 160	27.9	288	970
5 Cruise B	48 800	24.8	288	920
6 Ground Idle	33 000	8.82	288	700 ± 38
7 Takeoff (1 892 m)	52 640	25.5	308	1 083

4.2.2 Operating Conditions

The operating conditions for each operating point were calculated with a set of compressor and turbine maps from Palmer [32] and measured test data from StandardAero [33]. This involved matching the compressor and gas generator turbine so that the conditions of compatibility of mass flow, work, and rotational speed were met. Saravanamuttoo *et*

al. [1] and El-Sayed [34] provide an in-depth explanation of this process. The compressor and gas generator turbine maps from Palmer are shown in Figs. 4.1 through 4.4.

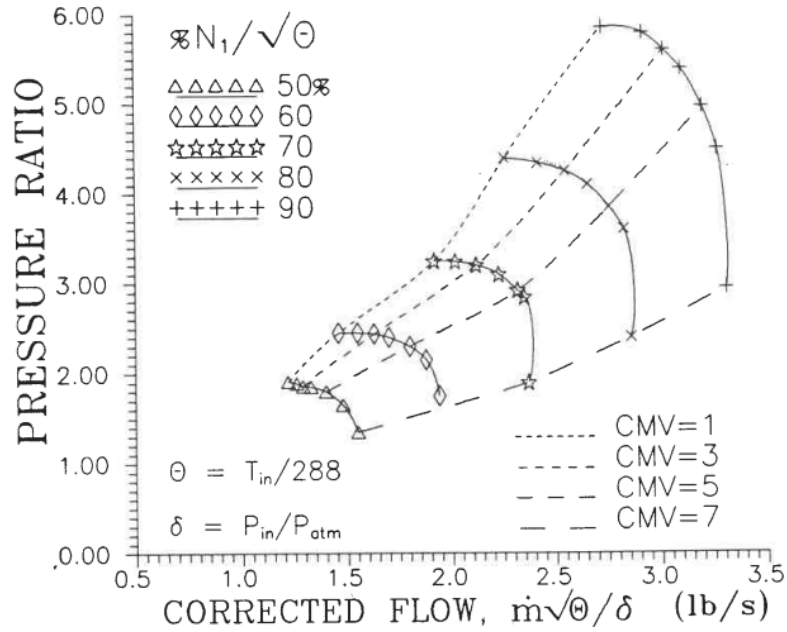


Figure 4.1: Compressor Map, taken from [32].

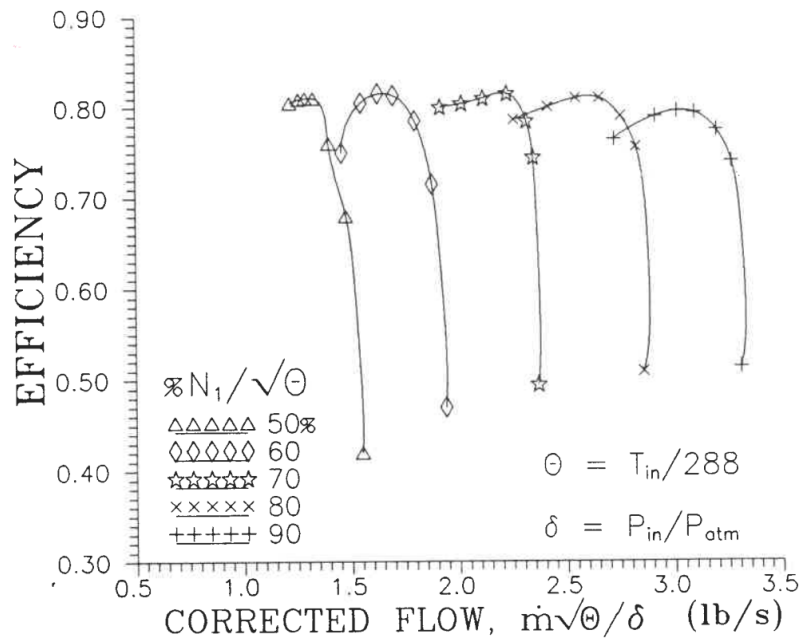


Figure 4.2: Compressor Efficiency Map, taken from [32].

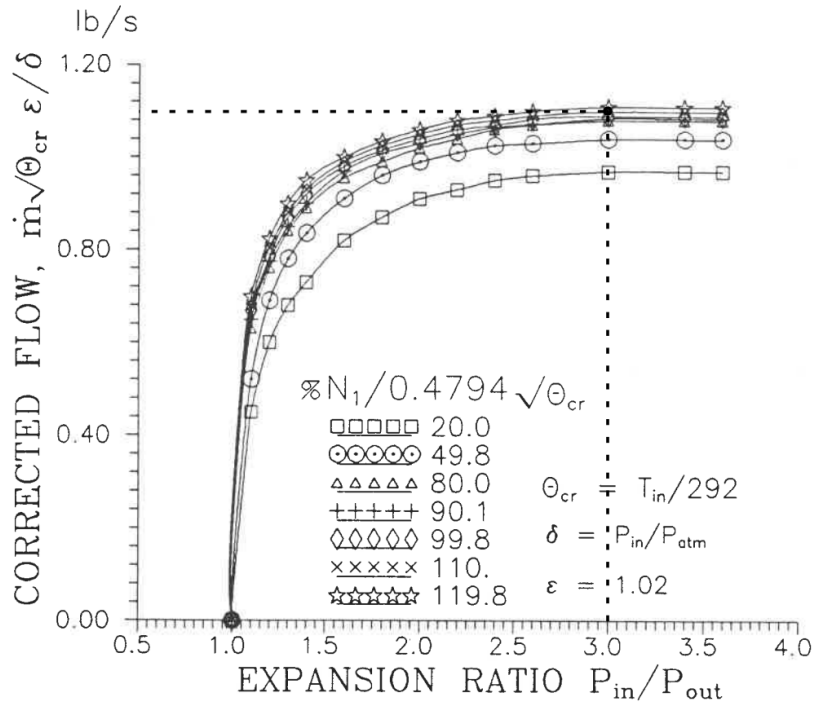


Figure 4.3: Gas Generator Turbine Map, taken from [32].

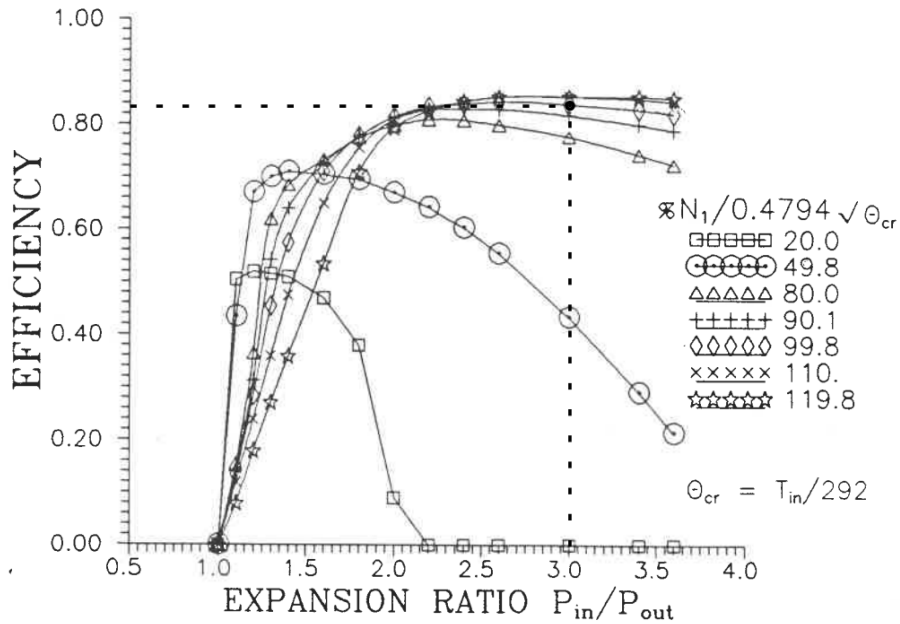


Figure 4.4: Gas Generator Turbine Efficiency Map, taken from [32].

The calculations to determine the operating conditions for condition 1 are shown. The calculation process is iterative until the mass flow rate, rotor speed, and work

across the engine are compatible. For the calculations shown, the final iteration values have been selected for demonstration purposes. For simplicity, the isentropic relations are shown here assuming constant specific heat. The actual operating conditions were calculated using varying specific heat with methods by McBride et. al. [35].

The compressor maps by Palmer [32] do not provide data above $\frac{N_1}{\sqrt{\Theta}} = 90\%$ which is below the rotor speed of many of the operating points in tab. 4.1, therefore, the compressor conditions are taken from StandardAero test data [33] which are not shown. The operating point for condition 1 is shown only on the turbine maps, as it can not be shown on the compressor maps. The corrected rotor speed N_1 is calculated with Eqn. 4.3. The rotor speed is corrected with the compressor inlet temperature which is calculated with Eqn. 4.1. The inlet total pressure is then calculated. The Mach number through the engine is 0.468. This was calculated through component matching iterations.

$$T_{02} = T_{\text{atm}} \left(1 + \frac{\gamma - 1}{2} Ma^2 \right) = 288 \text{ K} \left(1 + \frac{1.4 - 1}{2} (0.468)^2 \right) = 301 \text{ K} \quad (4.1)$$

$$\frac{P_{02}}{P_{\text{atm}}} = \left(\frac{T_{02}}{T_{\text{atm}}} \right)^{\frac{\gamma}{\gamma-1}} = \left(\frac{301 \text{ K}}{288 \text{ K}} \right)^{\frac{1.4}{1.4-1}} = 1.17 \quad (4.2)$$

$$N_{1,\text{corr}} = \frac{\frac{N_1}{50970 \frac{\text{rev}}{\text{min}}}}{\sqrt{\Theta}} = \frac{53000 \frac{\text{rev}}{\text{min}}}{50970 \frac{\text{rev}}{\text{min}}} = \frac{53000 \frac{\text{rev}}{\text{min}}}{\sqrt{\frac{301 \text{ K}}{288 \text{ K}}}} = 101.8\% \quad (4.3)$$

The rotor speed results in a compressor efficiency of 76%. An efficiency of 76% results in a corrected mass flow rate of $3.52 \frac{\text{lb}}{\text{s}}$, which corresponds to a compressor pressure ratio of 7.37. The actual mass flow rate is calculated with Eqn. 4.4. It is assumed 2% will be bled for secondary air systems as suggested by Saravanamuttoo *et al.* [1]. The temperature at the outlet of the compressor is calculated with Eqns. 4.7 and 4.8.

$$\dot{m}_3 = 0.98 \left(\frac{\dot{m}\sqrt{\Theta}}{\delta} \right) \left(\frac{\delta}{\sqrt{\Theta}} \right) \quad (4.4)$$

$$\dot{m}_3 = 0.98 \left(3.52 \frac{\text{lb}}{\text{s}} \right) \left(\frac{1.17}{\sqrt{\frac{301\text{K}}{288\text{K}}}} \right) \left(\frac{1\text{kg}}{2.205\text{lb}} \right) = 1.78 \frac{\text{kg}}{\text{s}} \quad (4.5)$$

$$T_{03} = T_{02} + \frac{T_{02}}{\eta_{\text{comp}}} \left(\left(\frac{P_3}{P_2} \right)^{\frac{\gamma-1}{\gamma}} - 1 \right) \quad (4.6)$$

$$T_{03} = 301\text{K} + \frac{301\text{K}}{0.76} \left((7.37)^{\frac{1.4-1}{1.4}} - 1 \right) = 606\text{K} \quad (4.7)$$

$$T_3 = \frac{T_{03}}{\left(1 + \frac{\gamma-1}{2} Ma^2 \right)} = \frac{605\text{K}}{\left(1 + \frac{1.4-1}{2} (0.468)^2 \right)} = 580\text{K} \quad (4.8)$$

With varying specific heat $T_3 = 575\text{K}$. The power needed to drive the compressor is calculated with Eqn. 4.9. The mechanical efficiency for engines of the era according to Mattingly [36, p. 382] is 0.95.

$$\dot{W}_{\text{comp}} = \frac{\dot{m}_3}{\eta_{\text{mech}}} C_p (T_{03} - T_{02}) \quad (4.9)$$

$$\dot{W}_{\text{comp}} = \frac{1.78 \frac{\text{kg}}{\text{s}}}{0.95} \left(1.005 \frac{\text{kJ}}{\text{kg K}} \right) (605\text{K} - 301\text{K}) = 572\text{kW} \quad (4.10)$$

The turbine outlet temperature is 1083 K. The total temperature is calculated with Eqn. 4.11.

$$T_{05} = T_5 \left(1 + \frac{\gamma-1}{2} Ma^2 \right) = 1083\text{K} \left(1 + \frac{1.33-1}{2} (0.468)^2 \right) = 1122\text{K} \quad (4.11)$$

The turbine expansion ratio is first estimated to be 3. Using Fig. 4.4, this corresponds to a turbine efficiency of 0.83. The turbine inlet total temperature can then be calculated with Eqn. 4.12.

$$T_{04} = \frac{T_{05}}{1 - \eta_{\text{turb}} \left(1 - \frac{P_5}{P_4} \right)^{\frac{\gamma-1}{\gamma}}} = \frac{1122\text{K}}{1 - 0.83 \left(1 - \left(\frac{1}{3} \right)^{\frac{1.33-1}{1.33}} \right)} = 1400\text{K} \quad (4.12)$$

The mass flow rate through the turbine is the air flow rate and the fuel flow rate. The corrected mass flow rate, as defined by Palmer [32] in Fig. 4.3, can then be calculated

with Eqn. 4.13. The relative pressure loss through the combustion chamber is 0.05.

$$\frac{1.02 \dot{m} \sqrt{\Theta}}{\delta} = \frac{1.02 (\dot{m}_3 + \dot{m}_f) \sqrt{\frac{T_{04}}{292 \text{ K}}}}{0.95 \left(\frac{P_{02}}{P_{\text{atm}}} \right) \left(\frac{P_3}{P_2} \right)} \quad (4.13)$$

$$\frac{1.02 \dot{m} \sqrt{\Theta}}{\delta} = \frac{1.02 \left(1.78 \frac{\text{kg}}{\text{s}} + 0.0344 \frac{\text{kg}}{\text{s}} \right) \sqrt{\frac{1402 \text{ K}}{292 \text{ K}}}}{0.95 (1.16) (7.37)} = 1.10 \frac{\text{lb}}{\text{s}} \quad (4.14)$$

Figure 4.3 is used to determine the turbine expansion ratio. The corrected flow rate of $1.10 \frac{\text{lb}}{\text{s}}$ validates the estimation for the turbine expansion ratio of 3. The turbine inlet temperature is calculated with Eqn. 4.15.

$$T_4 = \frac{T_{04}}{\left(1 + \frac{\gamma-1}{2} Ma^2 \right)} = \frac{1400 \text{ K}}{\left(1 + \frac{1.33-1}{2} (0.468)^2 \right)} = 1353 \text{ K} \quad (4.15)$$

With varying specific heat $T_4 = 1345 \text{ K}$. The power produced by the gas generator turbine is calculated with Eqn. 4.16.

$$\dot{W}_{\text{turb}} = (\dot{m}_3 + \dot{m}_f) C_p (T_{04} - T_{05}) \quad (4.16)$$

$$\dot{W}_{\text{turb}} = \left(1.78 \frac{\text{kg}}{\text{s}} + 0.0344 \frac{\text{kg}}{\text{s}} \right) \left(1.148 \frac{\text{kJ}}{\text{kg K}} \right) (1402 \text{ K} - 1122 \text{ K}) = 574 \text{ kW} \quad (4.17)$$

The power produced by the gas generator turbine is equal to the power required to drive the compressor. The mass flow rate is also conserved, therefore, the operating condition calculation is complete.

The equivalence ratio, ϕ , for each combustion chamber condition, was determined using the chemical equilibrium program *CEA* [37]. In this program, the chemical equilibrium conditions were calculated for the combustion reaction for each operating condition. Therefore, the operating conditions of the combustion chamber for each operating point are shown in Tab. 4.2.

The equivalence ratio for each condition is very lean, lower than the stable flammability limit. Therefore, the air must be distributed such that stable combustion is produced within the combustion chamber.

Table 4.2: Combustion Chamber Operating Conditions

Condition	Mass Flow Rate	Temperature		Pressure	Equivalence Ratio
	\dot{m}_3 [$\frac{\text{kg}}{\text{s}}$]	T_3 [K]	T_4 [K]	P_3 [bar]	ϕ [-]
1	1.78	575	1345	7.47	0.311
2	1.75	569	1305	7.34	0.295
3	1.69	559	1259	6.94	0.279
4	1.64	547	1216	6.63	0.264
5	1.54	536	1149	6.22	0.239
6	0.746	407	860	2.82	0.167
7	1.30	596	1345	5.70	0.303

4.3 Combustion Chamber Air Distribution

The airflow through the combustion chamber is split into three zones. To ensure stable operation of the combustion chamber, the proper proportion of air must be added to each zone. Distributing the air correctly allows for the equivalence ratio to be controlled in each zone and ensure a stable flame at all operating points.

4.3.1 Primary Zone

The chemical equilibrium program *CEA* [37] was used to determine the lean and rich limits resulting in a flame temperature of 1600 K. The limits are shown in Tab. 4.3.

Table 4.3: Lean and Rich Limits

Condition	Temperature	Pressure	Temperature Rise	Equivalence Ratio	
	T_3 [K]	P_3 [bar]	$1600 \text{ K} - T_3$ [K]	ϕ_{lean} [-]	ϕ_{rich} [-]
1	575	7.47	1025	0.432	2.41
2	569	7.34	1031	0.432	2.40
3	559	6.94	1043	0.437	2.39
4	547	6.63	1053	0.443	2.37
5	536	6.22	1064	0.448	2.34
6	407	2.82	1193	0.500	2.19
7	596	5.70	1004	0.423	2.45

To determine the air flow limits in the primary zone, the limits of flammability must

first be calculated. The ratio of the overall equivalence ratio to the lean limit and ratio of the overall equivalence ratio to the rich limit must be calculated with Eqn. 2.10.

The range of required fraction of air flow in the primary zone can be determined with Eqn. 2.10 using the ratios of $\frac{\phi}{\phi_{\text{lean}}}$ and $\frac{\phi}{\phi_{\text{rich}}}$. These fractions represent the fraction of total airflow to produce a reaction with temperatures above 1600 K. These fractions are calculated with values from Tab. 4.3 for condition 1 in Eqns. 4.18 and 4.19.

$$\frac{\dot{m}_{\text{air,lean}}}{\dot{m}_3} = \frac{\phi}{\phi_{\text{lean}}} = \frac{0.311}{0.432} = 0.720 \quad (4.18)$$

$$\frac{\dot{m}_{\text{air,rich}}}{\dot{m}_3} = \frac{\phi}{\phi_{\text{rich}}} = \frac{0.311}{2.41} = 0.129 \quad (4.19)$$

Choosing the minimum of $\frac{\phi}{\phi_{\text{lean}}}$ will ensure that there is not an excess of air so the flame stays lit for all lean conditions. Choosing the maximum of $\frac{\phi}{\phi_{\text{rich}}}$ will ensure that there is not an excess of fuel so the flame stays lit for all rich conditions. This will maintain an equivalence ratio that results in a flame temperature higher than the extinction temperature for all conditions. The limits are in bold in Tab. 4.4.

Table 4.4: Primary Zone Limit Ratios

Condition	ϕ [-]	ϕ_{lean} [-]	ϕ_{rich} [-]	$\frac{\dot{m}_{\text{air,lean}}}{\dot{m}_3} = \frac{\phi}{\phi_{\text{lean}}}$ [-]	$\frac{\dot{m}_{\text{air,rich}}}{\dot{m}_3} = \frac{\phi}{\phi_{\text{rich}}}$ [-]
1	0.311	0.432	2.41	0.720	0.129
2	0.295	0.432	2.40	0.683	0.123
3	0.279	0.437	2.39	0.638	0.117
4	0.264	0.443	2.37	0.596	0.112
5	0.239	0.448	2.34	0.534	0.102
6	0.167	0.500	2.19	0.334	0.0764
7	0.303	0.423	2.45	0.716	0.124

The fraction of air in the primary zone is chosen to be between these two ratios to satisfy all of the lean and rich constraints, therefore, a good value for the primary zone air flow is the average of the two highlighted values. The required proportion of air in the primary zone can be calculated from equivalence ratio limits with Eqn. 4.20.

$$\frac{\dot{m}_{\text{air,PZ}}}{\dot{m}_3} = \frac{0.129 + 0.334}{2} = 0.232 \quad (4.20)$$

The local equivalence ratio in the primary zone for each condition is calculated with Eqn. 2.10, shown for condition 1 in Eqn. 4.21. The temperature was then calculated with *CEA* [37]. The equivalence ratios and temperatures in the primary zone are shown in Tab. 4.5.

$$\phi_{\text{PZ}} = \frac{\phi}{\frac{\dot{m}_{\text{air,PZ}}}{\dot{m}_3}} = \frac{0.311}{0.232} = 1.34 \quad (4.21)$$

Table 4.5: Primary Zone Conditions

Condition	Equivalence Ratio		Temperature	
	ϕ [-]	ϕ_{PZ} [-]	T_3 [K]	T_{PZ} [K]
1	0.311	1.34	575	2320
2	0.295	1.27	569	2366
3	0.279	1.20	559	2410
4	0.264	1.14	547	2442
5	0.239	1.03	536	2458
6	0.167	0.721	407	2006
7	0.303	1.31	596	2360

All conditions have temperatures above 1600 K in the primary zone. The airflow fraction of 23.2% is acceptable. The temperatures produced at these conditions are very high which will result in fast reaction rates in the primary zone.

4.3.2 Secondary Zone

Combustion must be completed before the exit of the secondary zone. To do this, the maximum equivalence ratio in the secondary zone must be lean, which will ensure that the fuel is fully burned at this stage. It is suggested by Odgers and Kretschmer [4] that $\phi_{\text{SZ,max}} \leq 0.9$. A value of $\phi_{\text{SZ,max}} = 0.85$ was selected. This was chosen to increase the amount of air entering through the secondary zone holes to enhance jet penetration and mixing. To determine the airflow in the secondary zone, $\phi_{\text{SZ,max}}$ is applied to the richest condition, which is condition 1. The secondary zone airflow is calculated with Eqn. 4.22.

$$\frac{\dot{m}_{\text{air,SZ}}}{\dot{m}_3} = \frac{\phi}{\phi_{\text{SZ,max}}} = \frac{0.310}{0.85} = 0.365 \quad (4.22)$$

With an airflow fraction of 36.5%, the equivalence ratio for the other operating conditions can be calculated using Eqn. 4.23. The equivalence ratio in the secondary zone for condition 2 is given as an example. A summary of the secondary zone conditions are shown in Tab. 4.6.

$$\phi_{SZ} = \frac{\phi}{\frac{\dot{m}_{air,SZ}}{\dot{m}_3}} = \frac{0.295}{0.365} = 0.808 \quad (4.23)$$

Table 4.6: Secondary Zone Conditions

Condition	Equivalence Ratio		Temperature	
	ϕ	ϕ_{SZ}	T_3	T_{SZ}
	[-]	[-]	[K]	[K]
1	0.311	0.850	575	2327
2	0.295	0.808	569	2264
3	0.279	0.763	559	2189
4	0.264	0.723	547	2115
5	0.239	0.654	536	1991
6	0.167	0.457	407	1514
7	0.303	0.828	596	2308

The equivalence ratio for the most lean mixture, condition 6, is 0.457. This results in a secondary zone temperature of 1514 K. This is less than 1600 K, however, the fuel is burned first in the primary zone. Combustion should be completed before the end of the primary zone for this condition because the condition is lean in the primary zone. Hence, this airflow will be acceptable.

The exit of the dilution zone represents the desired conditions at the exit of the combustion chamber, therefore, all temperatures in the combustion chamber are known.

4.4 Calculation of Combustion Chamber Dimensions

The geometry of the primary zone determines the geometry of the entire combustion chamber as discussed in Section 2.5.1. The calculation of the diameter of the primary zone is a critical procedure in the design of a combustion chamber. The calculations

for condition 1 with each correlation, Eqns. 2.11 to 2.15 are shown in Appendix A.1. Table 4.7 shows the results of each method.

Table 4.7: Summary of Primary Zone Diameters

Condition	Chemical Kinetics	Mach	Bragg	Non-dimensional Groups	Greenhough-Lefebvre
	Eqn. 2.11 [mm]	Eqn. 2.12 [mm]	Eqn. 2.13 [mm]	Eqn. 2.14 [mm]	Eqn. 2.15 [mm]
1	42.4	101	102	109	161
2	37.2	101	100	109	164
3	33.9	101	98.3	109	171
4	33.4	102	96.0	110	178
5	47.6	101	93.0	109	186
6	74.1	97.7	76.9	105	311
7	40.2	100	91.0	96.8	141

The calculated liner diameters range from 33.4 mm to 311 mm. Therefore, these results must be analyzed further to determine a diameter. The chemical kinetics correlation suggests the minimum required volume and diameter required for a well stirred reactor, without taking evaporation time into account so it underestimates the primary zone diameter with regards to the other four methods. The Greenhough-Lefebvre correlation has an estimate that is relatively high. The value for condition 6 which is the ground idle condition is considered an outlier because it is an idle condition and will be dismissed. The average diameter when the chemical kinetic method and outlier are not considered is 115 mm. The length of each zone are calculated using Eqns. 2.16, 2.17, and 2.18. The dimensions of the combustion chamber are shown in Tab. 4.8.

$$L_{PZ} = \frac{2}{3} d_{PZ} = \frac{2}{3}(115 \text{ mm}) = 76.7 \text{ mm} \quad (2.16)$$

$$L_{SZ} = 0.5 d_{PZ} = 0.5(115 \text{ mm}) = 58.5 \text{ mm} \quad (2.17)$$

$$L_{DZ} = \left(\frac{20}{Q \frac{\Delta P_{3-4}}{q_{\text{ref}}}} \right)^{0.4} d_{PZ} = \left(\frac{20}{0.32(41.0)} \right)^{0.4} d_{PZ} = 136 \text{ mm} \quad (2.18)$$

$$L = L_{PZ} + L_{SZ} + L_{DZ} = 76.7 \text{ mm} + 58.5 \text{ mm} + 136 \text{ mm} = 271 \text{ mm} \quad (4.24)$$

$$1.39 d_{PZ} < D < 1.54 d_{PZ} \quad (4.25)$$

$$160 \text{ mm} < D < 177 \text{ mm} \quad (4.26)$$

Table 4.8: Liner Dimension Summary

	Iteration 1 $d_{PZ} = 115 \text{ mm}$	Iteration 2 $d_{PZ} = 100 \text{ mm}$
L_{PZ}	76.7 mm	66.7 mm
L_{PZ}	58.5 mm	50.0 mm
L_{PZ}	136 mm	118 mm
L	271 mm	235 mm
D	160 mm – 172 mm	139 mm – 153 mm

The suggested casing diameter for a 115 mm diameter liner is between 160 mm, and 177 mm, which is comparable to the 180 mm of the existing casing. The average diameter of the redesigned liner is smaller than the existing can, 145 mm, however the resulting length of the redesigned liner is longer than the existing liner’s length of 242 mm.

The preferred design of the new combustion chamber is one that is longer than the existing chamber, however, increasing the length would result in changes to the casing and possibly the diffuser tubes. To avoid increasing the complexity of the redesign, the diameter of the liner was decreased in order to match the length of the existing combustion chamber. For the second iteration, a diameter of 100 mm was chosen with a corresponding length of 235 mm, allowing for a 7 mm axial swirler giving a total length of 242 mm. The length of each zone was calculated with Eqns. 2.16, 2.17, and 2.18, and determined to be 66.7 mm, 50.0 mm, and 118 mm, respectively.

The chosen diameter of 100 mm is within the range of suggested diameters in Tab. 4.7, and is also within the suggested diameters according to Eqns. 2.12 and 2.13, therefore, should be taken as a valid choice.

The diameter of the redesigned liner is smaller than the existing liner, therefore, the outlet must be adapted to the existing geometry of the turbine inlet on the engine. A

conical section was used for the dilution zone to increase the diameter of the liner to achieve the desired outlet diameter.

The calculation of the size of the combustion chamber normally includes the sizing of the casing and diffuser, however, the casing and diffuser will remain unchanged. Any design choices based on the diffuser and casing are made with the existing component geometries.

4.5 Dome Design

For the redesigned liner, the igniter and fuel injector must be in the same position as the existing liner so that the casing does not require modification. For this combustion chamber, the fuel injector is positioned in the center of the dome surrounded by the swirler.

The recirculation zone will occupy 80% of the primary zone length. The limit of 80% is an acceptable recirculation zone size as suggested by Odgers and Kretschmer [4] and Mattingly [12]. Figure 2.8 shows dimensions to define the geometry of the dome. The angle of the dome, ψ , is calculated with Eqn. 2.23, however, this requires the dimensions of the swirler.

4.5.1 Swirler

An axial swirler will be implemented for this combustion chamber. The portion of the pressure drop contributed by the swirler is determined by the pressure drop from the diffuser, snout, and allowable pressure drop in the combustion chamber. Since the diffuser and snout properties are not known, they will be calculated as if they were being redesigned to determine an appropriate pressure loss associated for each component. These values are used to calculate the pressure loss through the swirler. The swirler pressure loss factor is determined by rearranging Eqn. 2.21 to obtain Eqn. 4.27.

$$\frac{\Delta P_{sw}}{q_{ref}} = \frac{\Delta P_{3-4}}{q_{ref}} - \frac{\Delta P_{sn}}{q_{ref}} - \frac{\Delta P_{diff}}{q_{ref}} \quad (4.27)$$

The combustion chamber pressure loss factor, $\frac{\Delta P_{3-4}}{q_{\text{ref}}}$ is already defined in Tab. 2.2. The overall pressure loss in the combustion chamber, $\frac{\Delta P_{3-4}}{P_3}$, is 5% and it is assumed that the diffuser pressure loss, $\frac{\Delta P_{\text{diff}}}{P_3}$, is 1%. The diffuser pressure loss factor can then be calculated with Eqn. 2.22.

$$\frac{\Delta P_{\text{diff}}}{q_{\text{ref}}} = \frac{\Delta P_{\text{diff}}}{P_3} \frac{\Delta P_{3-4}}{q_{\text{ref}}} \frac{P_3}{\Delta P_{3-4}} = 0.01 (41.0) \left(\frac{1}{0.05} \right) = 8.21 \quad (4.28)$$

For combustion chambers with a snout, air for the swirler and dome cooling devices enters through the snout. There is a small pressure loss associated with this. The air that does not enter the snout is directed into an annulus between the casing and liner where it is then distributed into the rest of the liner. The velocity of the air that enters the snout and the velocity of the air going around the snout should be equal, therefore the area of the snout, A_{sn} , is determined by the conservation of mass. Although there is no snout in this combustion chamber based on the liner and casing configuration, the values for the snout should be estimated to help with calculation of the swirler. For now, it is assumed that 15% of the air will enter through snout and 85% will enter the annulus.

$$\dot{m}_3 = \rho v A_3 \quad (4.29)$$

$$\dot{m}_{\text{an}} = \rho v A_{\text{an}} \quad (4.30)$$

$$\frac{\dot{m}_{\text{an}}}{\dot{m}_3} = \frac{\dot{m}_{\text{an}}}{\dot{m}_{\text{an}} + \dot{m}_{\text{sn}}} = \frac{A_{\text{an}}}{A_{\text{an}} + A_{\text{sn}}} \quad (4.31)$$

$$A_{\text{sn}} = A_{\text{an}} \left(\frac{\dot{m}_{\text{an}} + \dot{m}_{\text{sn}}}{\dot{m}_{\text{an}}} - 1 \right) \quad (4.32)$$

$$A_{\text{sn}} = \frac{\pi}{4} (D^2 - d^2) \left(\frac{\frac{\dot{m}_{\text{an}}}{\dot{m}_3} + \frac{\dot{m}_{\text{sn}}}{\dot{m}_3}}{\frac{\dot{m}_{\text{an}}}{\dot{m}_3}} - 1 \right) \quad (4.33)$$

$$A_{\text{sn}} = \frac{\pi}{4} ((180 \text{ mm})^2 - (100 \text{ mm})^2) \left(\frac{0.85 + 0.15}{0.85} - 1 \right) = 3100 \text{ mm}^2 \quad (4.34)$$

The mass flow rate through the snout, \dot{m}_{sn} , is equal to the swirler flow rate plus the flow rate of any film cooling devices starting at the dome. It was assumed that the snout will receive 15% of the total mass flow rate. This can be recalculated later

if the estimated flow changes. The pressure loss factor of the snout is calculated with Eqn. 4.36.

$$\frac{\Delta P_{\text{sn}}}{q_{\text{ref}}} = 0.25 \left(\frac{A_{\text{D}}}{A_{\text{sn}} + A_{\text{an}}} \right)^2 \quad (4.35)$$

$$\frac{\Delta P_{\text{sn}}}{q_{\text{ref}}} = 0.25 \left(\frac{\frac{\pi}{4} D^2}{A_{\text{sn}} + A_{\text{an}}} \right)^2 \quad (4.36)$$

$$\frac{\Delta P_{\text{sn}}}{q_{\text{ref}}} = 0.25 \left(\frac{\frac{\pi}{4} (180 \text{ mm})^2}{3100 \text{ mm}^2 + \frac{\pi}{4} ((180 \text{ mm})^2 - (100 \text{ mm})^2)} \right)^2 = 0.378 \quad (4.37)$$

The swirler pressure loss factor can now be calculated.

$$\frac{\Delta P_{\text{sw}}}{q_{\text{ref}}} = 41.0 - 8.21 - 0.378 = 32.4 \quad (4.38)$$

The pressure loss factor is used to determine the area of the swirler with Eqn. 2.26. This equation does not account for the blockage of the blades so the area is increased by 50 %. Straight blades will be used at an angle of 60° .

$$A_{\text{sw}} = 1.5 \frac{A_{\text{D}}}{\cos \beta_{\text{sw}}} \sqrt{\frac{K_{\text{sw}}}{\frac{\Delta P_{\text{sw}}}{q_{\text{ref}}} \left(\frac{m_{\text{g}}}{m_{\text{sw}}} \right)^2 + K_{\text{sw}} \left(\frac{A_{\text{D}}}{A_{\text{d}}} \right)^2}} \quad (4.39)$$

$$A_{\text{sw}} = 1.5 \frac{\frac{\pi}{4} (180 \text{ mm})^2}{\cos 60^\circ} \sqrt{\frac{1.3}{32.4 \left(\frac{1}{0.06} \right)^2 + 1.3 \left(\frac{\frac{\pi}{4} (180 \text{ mm})^2}{\frac{\pi}{4} (100 \text{ mm})^2} \right)^2}} \quad (4.40)$$

$$A_{\text{sw}} = 9160 \text{ mm} \quad (4.41)$$

The inner diameter of the swirler, which is 19 mm, is based on the diameter of the fuel injector. The outer diameter of the swirler is calculated with Eqn. 4.43.

$$d_{\text{sw,o}} = \sqrt{\frac{4 A_{\text{sw}}}{\pi} + d_{\text{sw,i}}^2} \quad (4.42)$$

$$d_{\text{sw,o}} = \sqrt{\frac{4 (9160 \text{ mm}^2)}{\pi} + (19 \text{ mm})^2} = 39.6 \text{ mm} \quad (4.43)$$

With the swirler dimensions known, the angle of the dome can be calculated. Solving Eqn. 2.23 gives an angle of 69° . To provide strong swirl at the exit of the swirler, there

must be no spaces where air can pass straight through, however, this should be done without an excessive number of blades. Figure 4.5 shows two swirlers with a different number of blades.

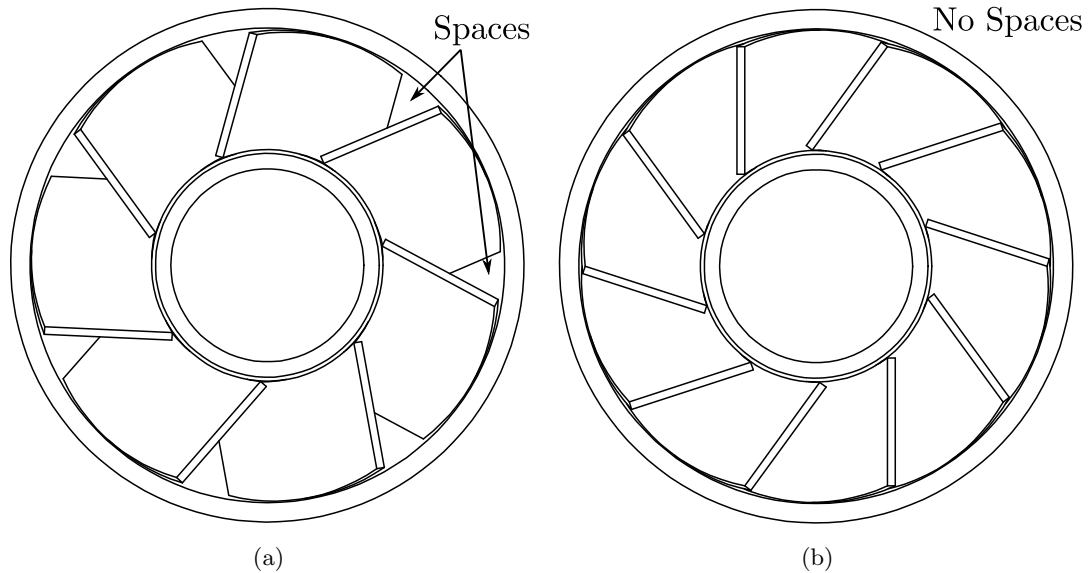


Figure 4.5: (a) Swirler With Too Few Blades, (b) Swirler With the Correct Number of Blades.

Figure 4.5(a) has too few blades resulting in spaces where air can pass in a straight line through the swirler without turning. The correct number of blades is an amount which contains no straight passages as shown in Fig. 4.5(b). Ten straight blades at an angle of 60° have been selected for this swirler.

4.6 Film Cooling Devices

The walls of the liner require methods to prevent overheating resulting in mechanical failure, therefore, film cooling devices will be designed for the liner. The liner is made of 316L stainless steel, thus, the maximum allowable wall temperature is 1100 K [6]. The liner wall temperature at any given point can be determined if the operating conditions are known, allowing the film cooling devices to be placed accordingly. Using the method proposed by Kretschmer and Odgers [38], the temperatures throughout the combustion

chamber were determined. The full procedure for determining the temperature in the liner and the wall temperature is presented in Appendix A.3, where an example using condition 1 is shown. The temperature through the combustion chamber for each condition is presented in Fig. 4.6

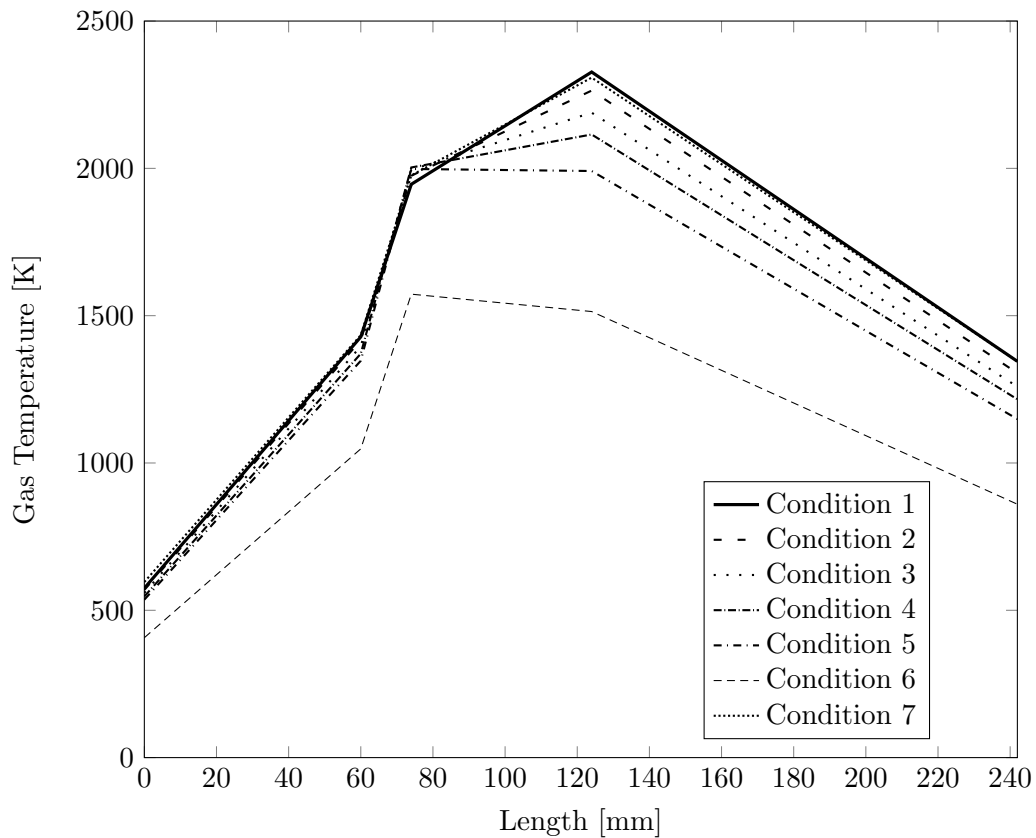


Figure 4.6: Axial Temperature Profiles for Each Condition.

Based on Fig. 4.6, conditions 1 and 7 have the most extreme temperature profile. It is likely that the placement of the film cooling slots will be dictated by these two operating conditions, however, the wall temperature for each condition must be checked. Once the temperature profile is known, the liner temperature can be calculated.

4.6.1 Film Cooling Device Placement

To determine the location of each film cooling device on the liner, the first was placed at the end of the dome and the wall temperature was calculated along the wall for each condition until the maximum temperature (1100 K) was exceeded, at which point a new film cooling device was placed. The energy balance described by Eqn. 2.28 is used to determine the wall temperature. The radiation and convective heat transfer to and from the wall were calculated and the wall temperature was determined.

Wiggle strips were selected for the film cooling devices on the liner wall. To install them, the liner wall must be made in segments of concentric cylinders with increasing diameter. A wiggle strip with a width of 2 mm was selected, and designed to block 65% of the slot area, A_c . A wider slot with high area of blockage, A_B , was selected to increase the change in diameter of the liner from one cylinder to the next. This reduced the angle of the conical section of the dilution zone, while still maintaining an appropriate mass flow rate through each slot.

A splash cooling device was placed in the dome to prevent the dome from over heating. A strip of metal was placed in the inner wall of the dome which directs air from a set of holes in the dome, outwards along the wall. The length of this wall is not long, therefore, only a small portion of the total mass flow was used for this. The location of each film cooling device is indicated in Tab. 4.9 along with the the mass flow rate through each slot.

Table 4.9: Film Cooling Device Locations and Flow Rates

Film Cooling Device	Distance from Swirler Exit	Flow Rate
	L_c [mm]	$\frac{\dot{m}_c}{\dot{m}_3}$ [—]
Dome	0	0.036
1	12	0.052
2	38	0.055
3	104	0.059
4	146	0.063

Four film cooling devices were placed on the liner wall after the dome. Film cooling device 2 was placed well before it is needed to allow the primary and secondary holes to be positioned in the correct locations. If film cooling device 2 was placed at the calculated location it would interfere with the secondary zone holes. The solution to this was to place the film cooling device upstream of the holes. Film cooling device 3 is then placed between the secondary zone holes and the dilution zone holes. The final film cooling device is placed immediately after the dilution zone holes. The temperature of the liner wall before each film cooling device is shown in Tab. 4.10.

Table 4.10: Liner Wall Temperature for All Conditions Immediately Upstream of the Next Film Cooling Device.

Condition	Wall Temperature [K]			
	$L = 38 \text{ mm}$	$L = 104 \text{ mm}$	$L = 146 \text{ mm}$	$L = 235 \text{ mm}$
1	681	1093	1099	821
2	673	1078	1078	798
3	659	1042	1043	775
4	643	1005	1008	751
5	627	946	944	714
6	459	640	682	525
7	710	1094	1082	818

4.7 Air Admission Holes

With the air distribution in each zone determined and cooling air allocated, the air admission holes can be designed. To design the holes, the airflow through each set of holes must be determined. Air from the first two film cooling devices are added to the primary zone air. The flow rate of the two film cooling devices, the swirler, and the total flow rate in the primary zone are known, therefore, the required airflow is calculated with Eqn 4.44.

$$\frac{\dot{m}_{\text{PZ,hole}}}{\dot{m}_3} = \frac{\dot{m}_{\text{PZ}} - \dot{m}_{\text{sw}} - \sum \dot{m}_{\text{c,PZ}}}{\dot{m}_3} = 0.232 - 0.06 - (0.036 + 0.052) = 0.084 \quad (4.44)$$

The air for the secondary zone is supplied by the primary zone, any film cooling devices in the zone, and the secondary zone holes. There are no film cooling devices that supply air in this region so the required flow rate is simply the difference in flow rate between the primary and secondary zones. The required flow rate through the secondary zones holes is calculated with Eqn. 4.45.

$$\frac{\dot{m}_{SZ, \text{hole}}}{\dot{m}_3} = \frac{\dot{m}_{SZ} - \dot{m}_{PZ} - \sum \dot{m}_{c, SZ}}{\dot{m}_3} = 0.365 - 0.232 - 0 = 0.133 \quad (4.45)$$

The flow rate through the dilution zone holes is the remaining air left after the secondary zone and final film cooling devices. A small portion of the air, 1% - 2%, is assumed to bypass the combustion chamber for turbine cooling and must be taken into account when calculating the air flow in the dilution zone. Equation 4.46 is used to calculate the air flow through the dilution zone holes.

$$\frac{\dot{m}_{DZ, \text{hole}}}{\dot{m}_3} = \frac{\dot{m}_3 - \dot{m}_{SZ} - \sum \dot{m}_{c, DZ}}{\dot{m}_3} \quad (4.46)$$

$$\frac{\dot{m}_{DZ, \text{hole}}}{\dot{m}_3} = 1 - 0.365 - (0.055 + 0.059 + 0.063) - 0.015 = 0.443 \quad (4.47)$$

With the flow rate of the holes known, the size of the holes can be determined. The area of the holes is calculated with Eqn. 2.37. The calculations of the area for the primary zone holes are shown in Eqn. 4.48. The C_D for circular plain holes in the liner is 0.55 as stated by Odgers and Kretschmer [4]. The pressure loss through the holes is calculated with Eqn. 2.36 and is 0.04.

$$A_{PZ, \text{hole}} = \frac{\dot{m}_{PZ, \text{hole}}}{P_3 C_D} \sqrt{\frac{RT_3}{2} \frac{P_3}{\Delta P_{\text{hole}}}} \quad (4.48)$$

$$A_{PZ, \text{hole}} = \frac{0.084 \left(1.78 \frac{\text{kg}}{\text{s}}\right)}{747000 \text{Pa} (0.55)} \sqrt{\frac{287 \frac{\text{J}}{\text{kgK}} (575 \text{K})}{2} \left(\frac{1}{0.04}\right)} = 523 \text{mm}^2 \quad (4.49)$$

The secondary zone hole and dilution zone hole areas are 828 mm and 2730 mm, respectively. The calculated area is the combined area for all of the holes for a given zone. The diameter and number of holes may vary in each zone are chosen based on mixing and jet penetration objectives. The diameter of each hole is determined by the

number of holes selected. For each set of holes, a greater number of smaller holes can be selected to promote mixing, however, a smaller number of larger holes offers better jet penetration.

Eight holes were selected for the primary zone, six holes were selected for the secondary zone, and eight holes were selected in the dilution zone based on the jet penetration for each set of holes. The diameter of the holes is calculated with Eqn. 4.50, shown for the primary zone holes.

$$d_{\text{PZ,hole}} = \sqrt{\frac{4 \left(\frac{A_{\text{PZ,hole}}}{8} \right)}{\pi}} = \sqrt{\frac{4 \left(\frac{523 \text{ mm}^2}{8} \right)}{\pi}} = 9.1 \text{ mm} \quad (4.50)$$

Ideally the penetration of the jets should reach the centerline of the liner or half way through the diameter, $\frac{y}{d} = 0.5$. The penetration of the jets is calculated with Eqn. 2.38, shown for the primary zone holes. The density of the air is calculated with the ideal gas law.

$$\frac{y}{d} = 0.365 \log \left[\left(\frac{\rho_{\text{RZ}} A_{\text{d}}^2 \dot{m}_{\text{hole}}^2}{\rho_{\text{hole}} A_{\text{hole}}^2 \dot{m}_{\text{RZ}}^2} \right)^{0.5} \left(\frac{2d_{\text{hole}}}{d} \right) \times \left(\frac{\dot{m}_{\text{hole}} + \dot{m}_{\text{RZ}}}{\dot{m}_{\text{RZ}}} \right) \sin \theta_{\text{hole}} \right] + 0.485 \quad (4.51)$$

$$\frac{y}{d} = 0.365 \log \left[\left(\frac{1.82 \frac{\text{kg}}{\text{m}^3} (7850 \text{ mm}^2)^2 (0.084)^2}{4.52 \frac{\text{kg}}{\text{m}^3} (523 \text{ mm}^2)^2 (0.19)^2} \right)^{0.5} \left(\frac{2(9.1 \text{ mm})}{100 \text{ mm}} \right) \times \left(\frac{0.084 + 0.19}{0.19} \right) \sin(90^\circ) \right] + 0.485 = 0.498 \quad (4.52)$$

The axial locations of the holes along the liner are at the end of the recirculation zone, the start of the secondary zone, and the start of the dilution zone. The size of the holes, the corresponding number of holes, and jet penetration for each set on the liner are shown in Tab. 4.11.

The jet penetration for the dilution zone holes is slightly higher than 0.5, however, the number of holes was chosen based on the number of primary zone holes. Eight dilution zone holes were chosen so that they could be staggered with the primary zone holes. This resulted in higher jet penetration than desired but was acceptable.

Table 4.11: Liner Hole Summary

Zone	Flow Rate	Diameter	Jet Penetration	
	$\frac{\dot{m}_{\text{hole}}}{\dot{m}_3}$ [—]	d_{hole} [mm]	Number of Holes	$\frac{y}{d}$ [—]
Primary	0.084	9.1	8	0.498
Secondary	0.133	13.2	6	0.470
Dilution	0.443	21.0	8	0.519

4.8 Design Summary

The liner was designed using the methods outlined by Odgers and Kretschmer [4] leading to a result with very different geometry from the original liner. The liner was made of rolled sheets of 316L stainless steel and welded at the seams to form cylinders. The sheets were 1.27 mm (18 gauge) thick. The cylinders were then welded together with wiggle strips between. The new liner is shown in Figs. 4.7 and 4.8. The air flow distribution for the redesign is shown in Fig. 4.9. Detailed design and assembly drawings are provided in Appendix B.



Figure 4.7: View of the Swirler and Dome.



Figure 4.8: View of the Holes and Film Cooling Devices.

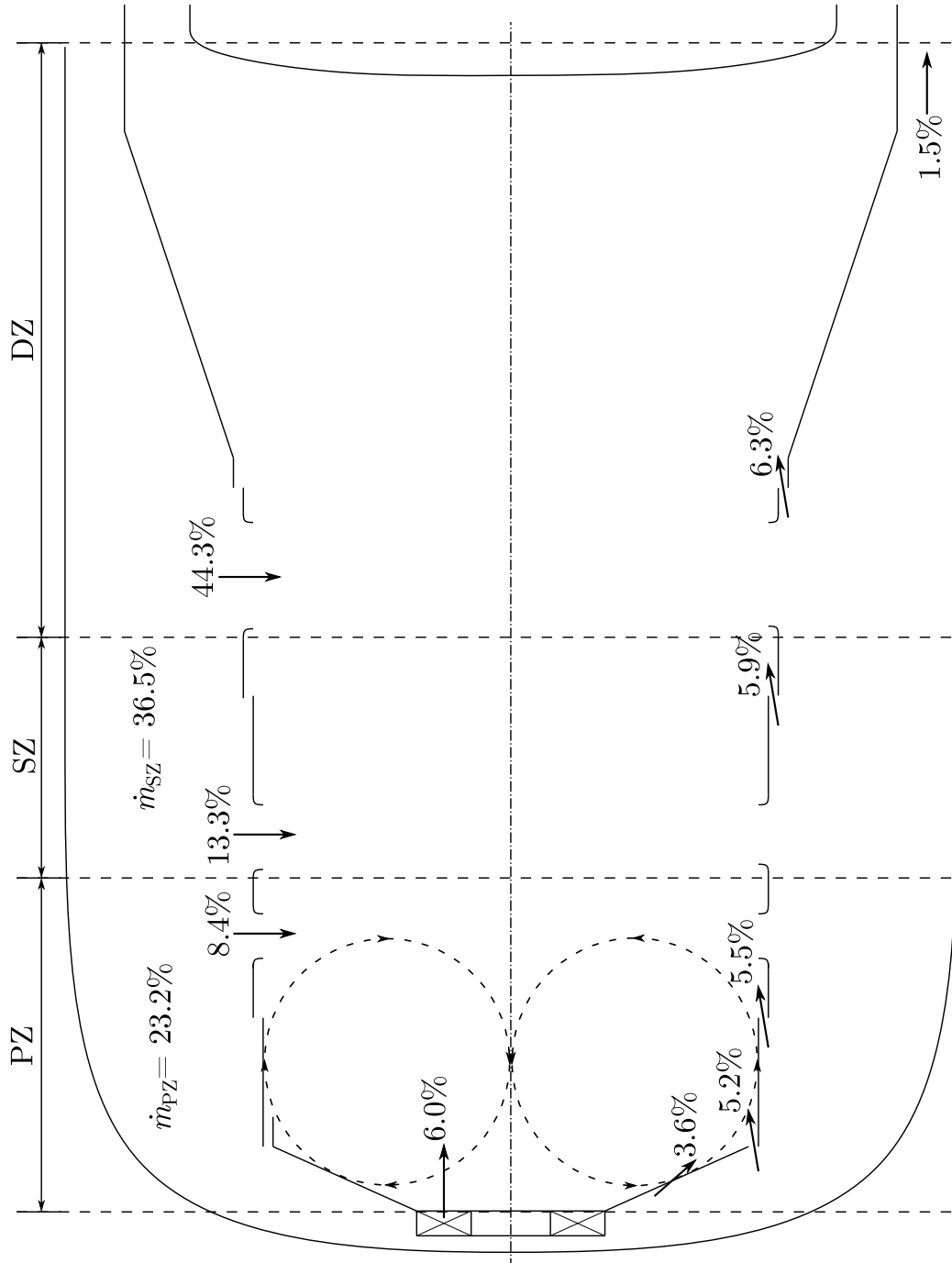


Figure 4.9: Summary of Air Flow in the Redesigned Combustion Chamber.

5 Experimental Rig and Validation

To test the new combustion chamber, the atmospheric combustion chamber test rig developed by Maqsood [30] was used. The test rig is constructed with, as much as possible, engine parts including the left and right diffuser tubes, combustion casing, fuel injector, igniter, and nozzle guide vane (NGV) shield. The test rig is shown in Fig 5.1.

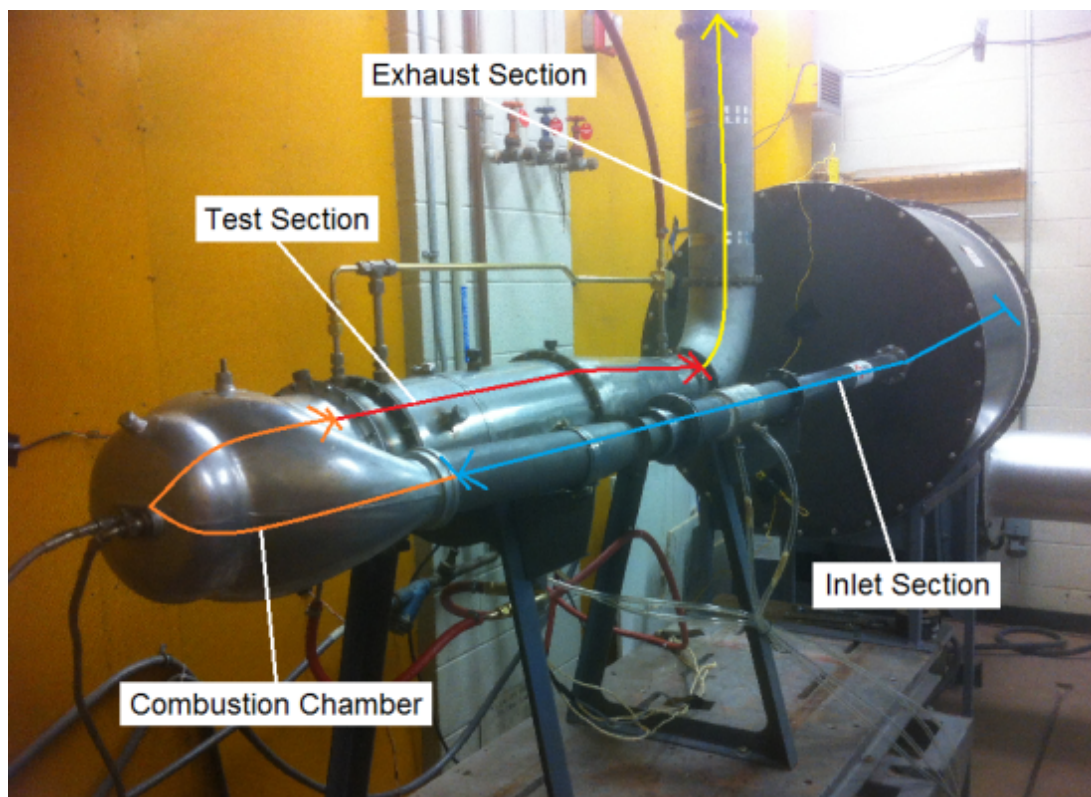


Figure 5.1: Atmospheric Combustion Chamber Test Rig, from Maqsood [30].

A centrifugal blower delivers air to a plenum which is used to provide a uniform and steady flow to the combustion chamber. The air exits the plenum through two bell mouth intakes, one for each side of the combustion chamber inlet, into two pipes. The air travels through a venturi flow meter followed by a restriction screen. These screens are used to modulate the inlet airflow distribution for the various test cases. The air passes through the diffuser tubes and enters the combustion chamber. At the outlet of the combustion chamber is the NGV shield from an M250-C20B. After the NGV shield is the test section which contains a thermocouple rake rotating 3 K-type thermocouples 360° to measure the temperature profile at the exit annulus. The thermocouple rake is positioned by a stepper motor, housed within a water cooled chamber. Once the air passes through the test section it enters the exhaust pipe, mixes with atomized outlet cooling water, and exits the test cell.

The temperature was recorded at 250 equally spaced circumferential locations at three radial locations. The three radial locations, measured from the centerline of the combustion chamber, are 67 mm (2.625 in), 70 mm (2.75 in), 73 mm (2.875 in). Once the test rig was operating at steady state, temperature data was recorded. The data at each position was sampled for 2.5 s at 4 Hz and the thermocouples were given a 3 s stabilization time after moving to a new circumferential position. This was repeated for all 250 positions. Further details of the test rig can be found in Maqsood [30].

5.1 Atmospheric Combustion Chamber Test Rig

The test rig was operated at the same conditions used by Maqsood [30] in the original liner testing. A 3000 m cruise condition was simulated by matching the Mach number, the equivalence ratio, and minimizing the Sauter mean diameter of fuel droplets at ambient conditions inside the combustion chamber. The rig operating conditions are shown in Tab. 5.1.

The fuel nozzle used by Maqsood [30] was tested prior to being used in the com-

Table 5.1: Engine and Test Rig Operating Conditions

	Operating Conditions				Matched Properties		
	P_3	T_3	\dot{m}_3	\dot{m}_f	\widetilde{Ma}	ϕ_{3-4}	D_{32}
	[kPa]	[K]	$\left[\frac{\text{kg}}{\text{s}}\right]$	$\left[\frac{\text{g}}{\text{s}}\right]$	$\left[\frac{\text{kg K}^{0.5}}{\text{kPa s}}\right]$	[—]	[μm]
Cruise at 3000 m	427	501	1.01	15.9	52.9	0.231	47.2
Test Rig	101	293	0.314	4.93	52.9	0.231	63.4

bustion chamber. In previous tests the fuel pressure was 552 kPa resulting in 4.93 $\frac{\text{g}}{\text{s}}$, however, to achieve the same flow rate, a fuel pressure of 780 kPa was required. Streaks were also visible in the spray pattern meaning some regions of the spray pattern had a higher concentration of fuel droplets than others, which would result in invalid test data. A second M250 nozzle was obtained and similar conditions to those reported by Maqsood [30] were achieved at the desired operating condition. No streaks were visible in the spray pattern from the second nozzle.

A compressed air line was added to the test rig to keep the stepper motor from over heating. It was found that the water jacket around the stepper motor was not enough to keep the motor housing cool. To keep the exhaust air from heating this chamber, an external supply of compressed air was delivered to pressurize the housing and fill it with room temperature air. This chamber is downstream of the exit temperature measurement plane so it did not affect the flow field at the exit of the combustion chamber. This cooling air, in addition to the water jacket proved to be sufficient in keeping the housing cool. Other changes to the test rig included re-machining O-ring grooves to provide a better seal for the cooling water and adding a fuel pressure regulator to the fuel supply line. The fuel pressure regulator resulted in a steady delivery pressure to the fuel nozzle.

Tests were conducted for the 3 cases shown in Tab. 5.2. These test cases were performed by Maqsood on the original combustion chamber [30], based on the 4% difference in mass flow rate in the diffuser tubes measured by Ilott [29].

For the test cases, left diffuser and right diffuser refer to the side when looking down-

Table 5.2: Test Cases

Test Case	Description
+4% LD	4 % Higher Left Diffuser Mass Flow Rate
Even	Even Mass Flow Rate
+4% RD	4 % Higher Right Diffuser Mass Flow Rate

stream of the combustion chamber to the exit temperature measurement plane, shown in Fig. 5.3. The change in flow rate was done with a restriction screen decreasing the flow area in the corresponding diffuser tube by 4%. The difference in flow rate between the two diffuser tubes was experimentally verified by Maqsood [30] and reproduced for the current tests. For even flow cases, identical screens were used. When reducing the flow on one side, one screen was replaced with another of reduced cross sectional area. The restriction screen was 3D printed and is shown in Fig. 5.2. The scale at the side of the figure is in inches.



Figure 5.2: Restriction Screen used to Reduce Airflow at Combustion Chamber Inlet.

The air exiting the combustion chamber passes through the annulus of the NGV shield and the temperature was measured at the exit temperature measurement plane. The central dome of the NGV shield is held in place by five struts which block small

portions of the flow through the annulus resulting in colder regions on the temperature profiles at the locations shown in Fig. 5.3. The temperature profiles are presented as if the viewer is looking downstream to the turbine from NGV shield.

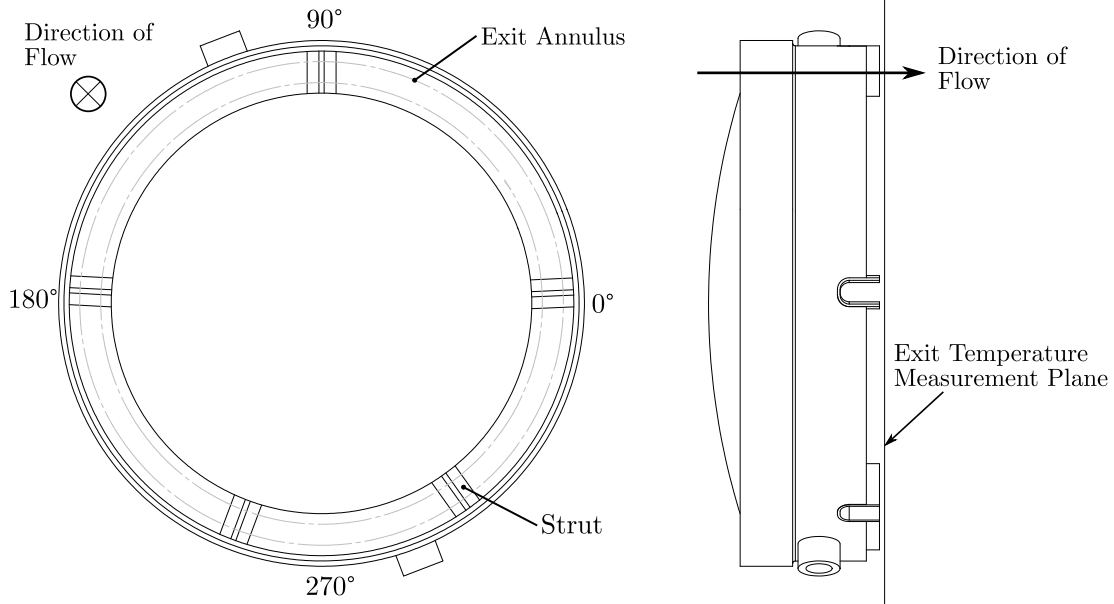


Figure 5.3: Nozzle Guide Vane Shield Sketch.

5.2 Temperature Profiles

The temperature profiles are presented as contour plots with each contour representing the non-dimensional temperature rise which is the ratio of the measured temperature rise to the adiabatic temperature rise. The adiabatic flame temperature was calculated with *CEA* based on the operating conditions of each test. Equation 5.1 was used to calculate the non-dimensional temperature rise for each measurement point.

$$\theta_{(x,y)} = \frac{T_{(x,y)} - T_3}{T_{\text{adia}} - T_3} \quad (5.1)$$

The *MATLAB*TM routine, written by De Freitas [39] and used by Maqsood [30], was used to create the contour plots that represent the exit temperature profile. The data was measured in polar coordinates, converted to non-dimensional temperature rise,

interpolated onto a uniformly spaced rectangular grid using the `griddata` function with cubic interpolation, and then presented as an annular temperature profile.

The average non-dimensional temperature rise is calculated as an area weighted average over the measurement area, as shown in Eqn. 5.2. The test rig was not instrumented to collect flow field data, therefore, a mass-weighted average was not used. The average exit temperature, T_4 , is calculated with Eqn. 5.3. The average temperature, the maximum measured temperature, and the inlet temperature are used to calculate the pattern factor with Eqn. 2.39.

$$\theta_{\text{avg}} = \frac{\sum_{n=1}^{750} (\theta \Delta A)}{A} \quad (5.2)$$

$$T_4 = \theta_{\text{avg}} (T_{\text{adia}} - T_3) + T_3 \quad (5.3)$$

To compare temperature profiles from similar tests, the change in non-dimensional temperature rise between respective tests was used, calculated with Eqn. 5.4.

$$\Delta\theta_{(x,y)} = \theta_{(x,y),2} - \theta_{(x,y),1} \quad (5.4)$$

The original combustion chamber was tested for an even inlet flow rate condition and compared to the previous tests by Maqsood [30] to ensure the rig was operating correctly. The tests by Maqsood were shown to be repeatable, therefore, only one test case needed to be reproduced before proceeding to the new combustion chamber test phase. Two baseline tests were performed for the even flow rate test case. The baseline test average temperature profile is shown in Fig. 5.4(b) and the temperature difference between the test by Maqsood and the baseline test is shown in Fig. 5.5.

The temperature profile in Fig. 5.4(b) and the comparison in Fig. 5.5 show that the results recorded by Maqsood [30] were reproduced by the test rig based on a qualitative inspection of the temperature profiles. The hot spots and cold spots were in the same locations and of similar magnitudes, therefore, the next phase of testing could be carried out. The exit temperature profile of the new combustion chamber with even inlet flow was then measured. The temperature profile for even inlet flow rate is shown in Fig. 5.6.

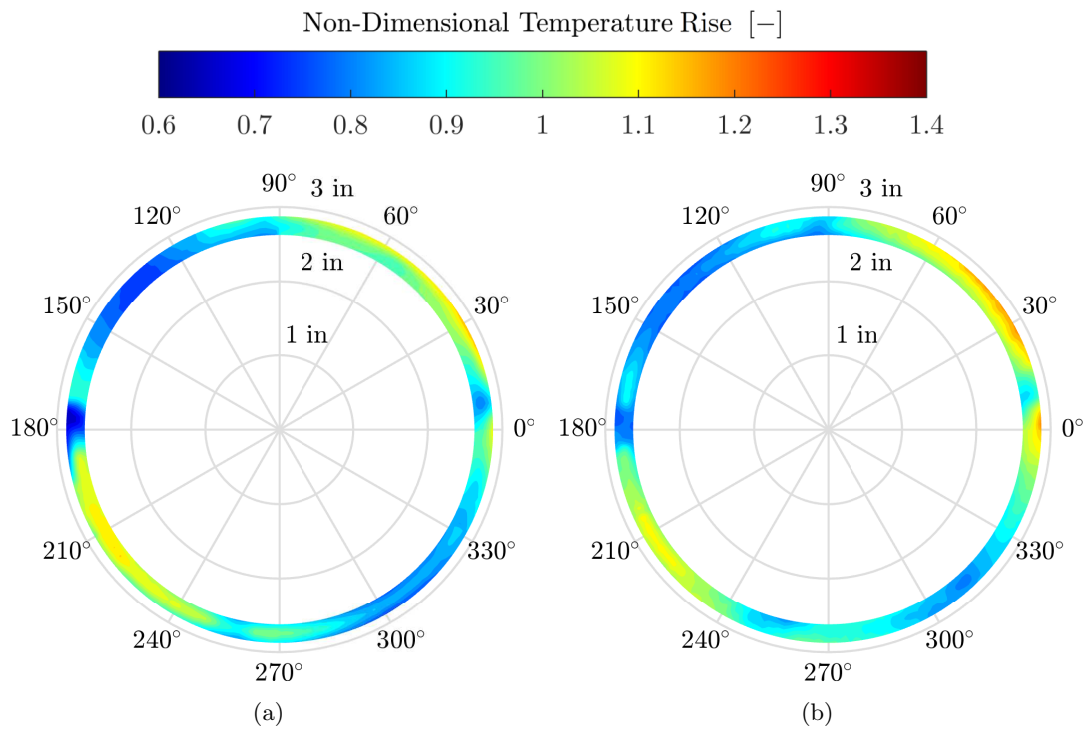


Figure 5.4: Exit Temperature Profile for (a) Maqsood Even [30], (b) Baseline Even.

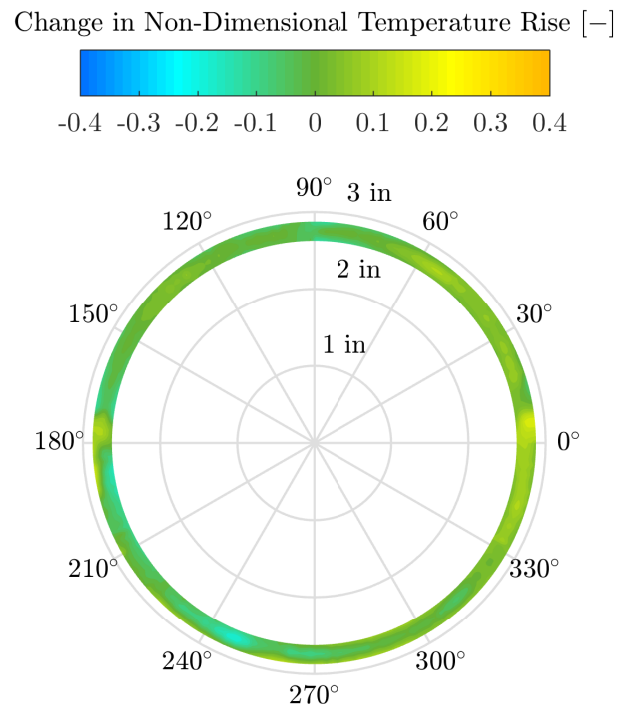


Figure 5.5: Change in Exit Temperature Profile Between Maqsood Test and Baseline Test, Even.

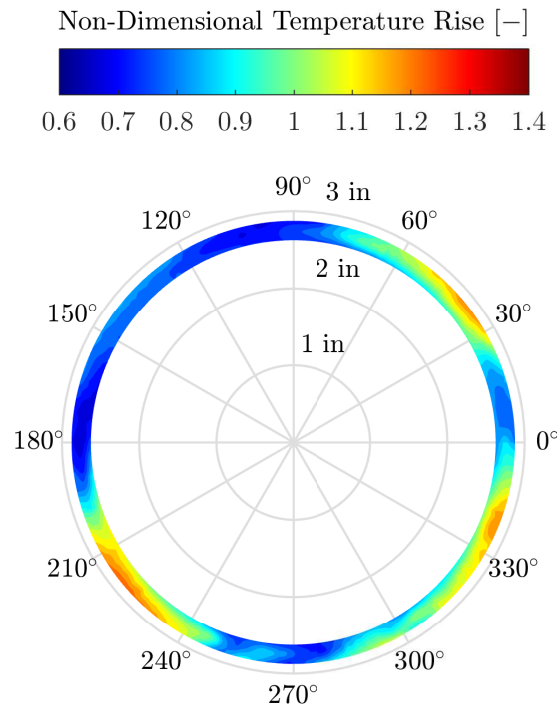


Figure 5.6: Exit Temperature Profile for the New Combustion Chamber, Even.

The mass flow rate of air in the right diffuser tube was modified to be 4% lower than the left diffuser tube using the restriction screen in Fig. 5.2. The temperature profile for 4% higher left diffuser flow rate is shown in Fig. 5.7(b) where the effect of inlet distortion can be seen. With the increased flow rate on the left side, the regions at 150° and 220° have increased in temperature and expanded in area when compared to the even flow rate case. The most significant increase can be seen along the inner radius at 230° , as well as the region between 150° and 180° .

The mass flow rate of air in the left diffuser tube was modified with the previously described restriction screen to be 4% lower than the right diffuser tube. The temperature profile for 4% higher right diffuser flow rate is shown in Fig. 5.9(b). With increased flow on the right side, the hot spots at 40° and 330° expanded in area, however, there was no significant increase in temperature. The regions near 150° and 220° also decreased in temperature and area. The change in non-dimensional temperature rise due to inlet distortion is shown in Figs. 5.8 and 5.10.

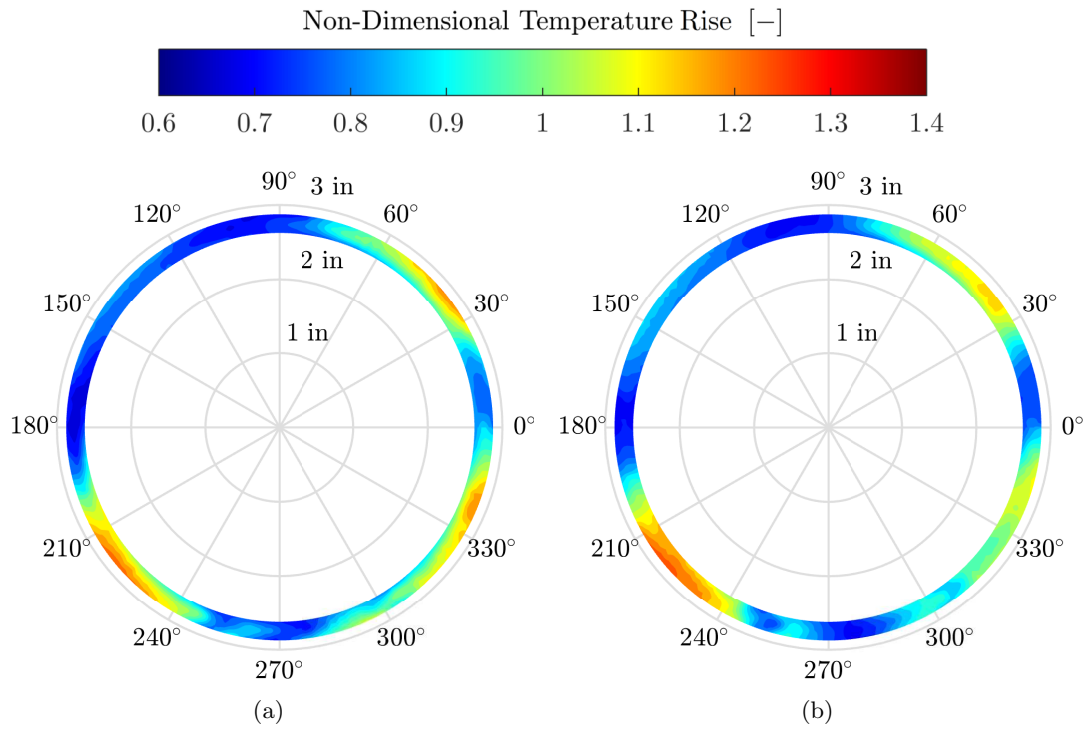


Figure 5.7: Exit Temperature Profile for the New Combustion Chamber for (a) Even, (b) +4% LD.

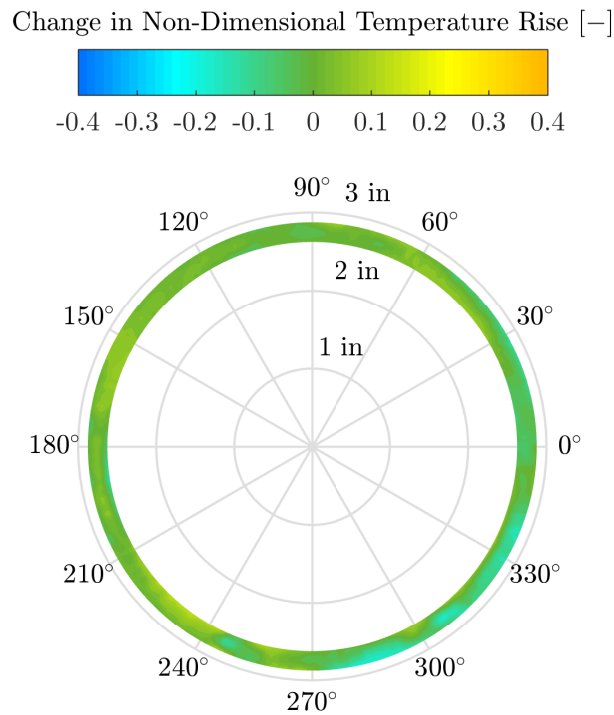


Figure 5.8: Change in Exit Temperature Profile, Even and +4% LD.

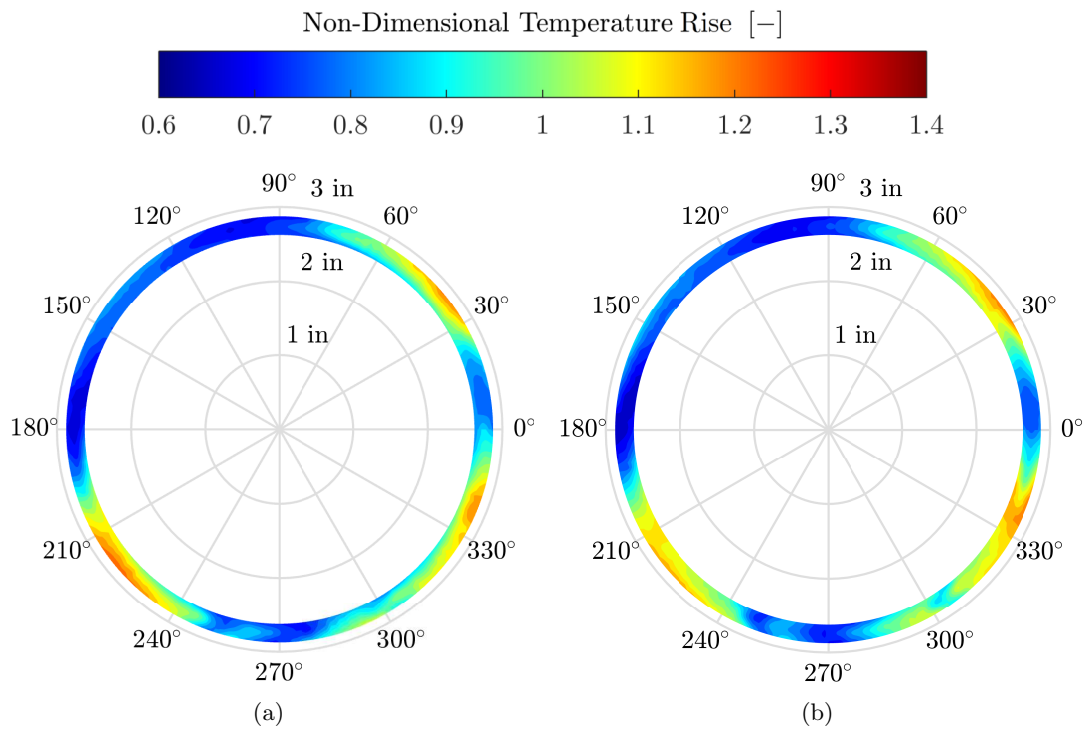


Figure 5.9: Exit Temperature Profile for the New Combustion Chamber for (a) Even, (b) +4% RD.

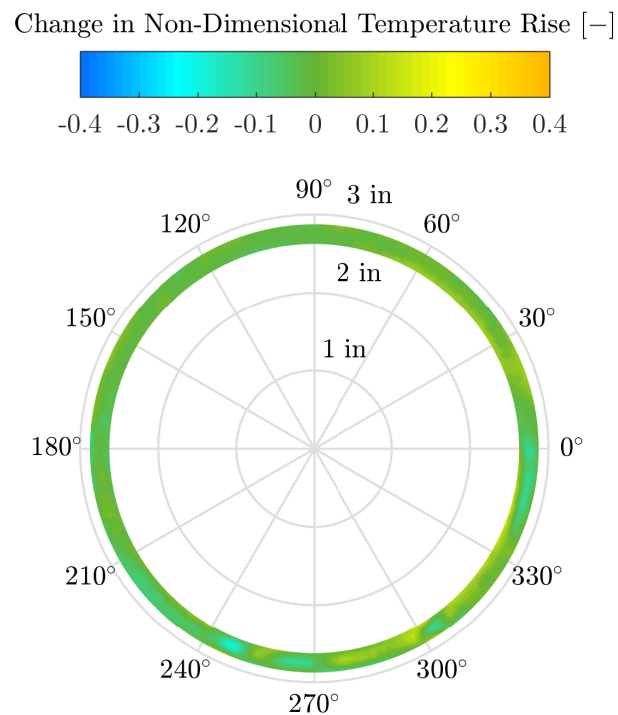


Figure 5.10: Change in Exit Temperature Profile, Even and +4% RD.

In all test cases, the locations of the hot regions were consistent. Between each test case, there was no significant circumferential expansion of the hot regions. There were increases in temperature on either side of the outlet due to the change in inlet flow. These increases in temperature occurred mostly on the inner radius of combustion chamber outlet. Inlet flow distortion did not have a significant effect on the outlet temperature profile.

The locations of the cold regions were also consistent for each test case. The location of the cold regions are at approximately 5° , 95° , 185° , and 275° and were not significantly affected by inlet distortion. These cold regions are at the locations of four of the eight dilution zone holes. The small cold spots near 250° and 305° are caused by the struts in the NGV shield which can be seen in Fig. 5.3.

5.3 Average Temperature and Pattern Factor

The non-dimensional temperature rise for each data point was calculated with Eqn. 5.1. The pattern factor was then calculated by first converting the average non-dimensional temperature to the average temperature and then using Eqn. 2.39. The results are shown in Tab. 5.3. The non-dimensional temperature uncertainty, $u_{\theta_{\text{avg}}}$, is also listed.

Table 5.3: Average Non-dimensional Temperature Rise and Pattern Factor

Test Case	θ_{avg}	Pattern Factor	$u_{\theta_{\text{avg}}}$
Original Even Baseline	0.943	0.273	0.006
New +4% LD	0.912	0.389	0.006
New Even	0.906	0.379	0.006
New +4% RD	0.920	0.335	0.006

The average non-dimensional temperature rise at the outlet of the combustion chamber was lower than the desired temperature rise for all test cases. This can be attributed to heat losses in the combustion chamber like the cooling of the NGV shield and losses to the surroundings. The average non-dimensional temperature rise was consistent across all test cases.

The average temperature rise and pattern factor for the original liner baseline test was comparable to the results of Maqsood [30]. For the new combustion chamber the even test case had the lowest temperature rise, while +4% LD had the highest pattern factor. For the the even and +4% LD cases, the maximum temperature occurred in the hot region at 220° . With the decrease in temperature on the left side for +4% RD, the maximum temperature occurred in the hot region at 330° , however, this temperature was lower than the maximum temperature for the other test cases resulting in a lower pattern factor.

No significant change in average non-dimensional temperature rise was observed between the three test cases. For both inlet distortion test cases, the maximum change in temperature from the even test case was recorded along the inner radius, showing that the inner radius was effected more significantly than the middle and outer radii. The lack of change in temperature at the outer radius is the reason for the minimal change in pattern factor between the even and +4% LD cases and the decrease in +4% RD. Referring to Figs. 5.8 and 5.10, most of the temperature profile remained unchanged, only changing significantly in the hotter regions in the middle and inner radii.

6 Discussion

The results obtained from the tests of the new combustion chamber offer further understanding of the behaviour of the M250 combustion chamber. Hot spots were still present in the outlet temperature profile, close to the same position as in the original combustion chamber suggesting the problem is not related to the liner but with the entire combustion chamber.

In this chapter, the results of the combustion chamber with the redesigned liner are analyzed and compared to the results from the original combustion chamber, the geometry of the redesigned liner is compared to the original liner, and the effects of the outlet temperature profile on the engine are discussed. The effects of inlet flow distortion on the new liner are also discussed.

6.1 Temperature Profiles

Four regions of relatively higher temperature were observed at 40° , 150° , 220° , and 330° . The presence of these four hot regions are not caused by the liner but by the casing. The hot spots at the outlet of the combustion chamber are caused by the flow from the diffuser to the annulus. The transition from the diffuser tubes to the annulus is a series of holes in the casing wall. The flow from the diffuser tubes enters the casing at the two inlets indicated in Fig. 6.1. The air enters the annulus through 12 holes around the casing where it is then distributed around the liner. The inside of the casing with the hole layout is also shown in Fig. 6.1.

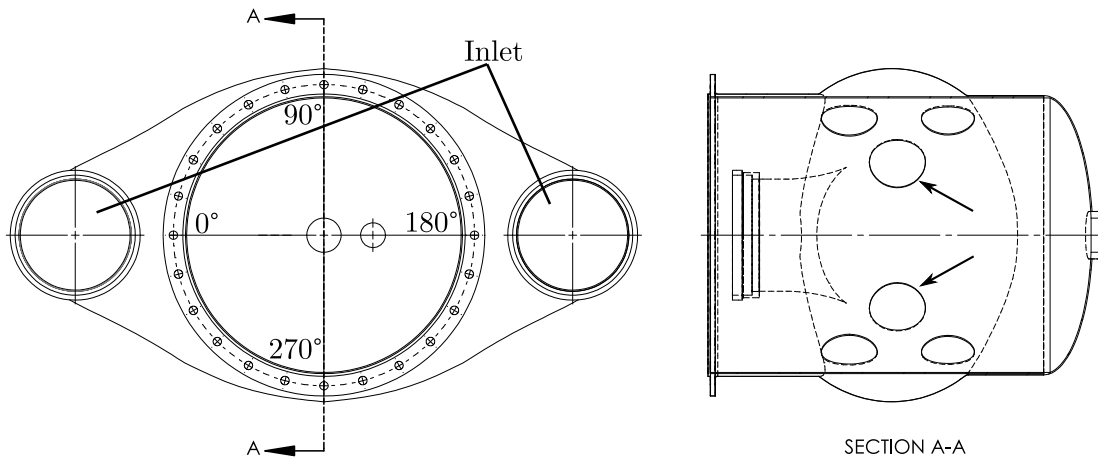


Figure 6.1: Sketch of Casing Inner Wall.

Instead of uniformly entering the casing through the 12 holes, the air entered mostly through the holes closest to 0° and 180° indicated by the arrows in Fig. 6.1. This caused more air to enter the liner through holes near 40° , 150° , 220° , and 330° . The equivalence ratio in the recirculation zone is approximately 1.2 for this operating condition. By adding more air in this region, the mixture approaches stoichiometric and the local temperature will increase. This relationship is shown in Fig. 6.2.

The regions with less air are richer, resulting in lower local temperatures. This corresponds to the cold spots in the exit temperature profile. The uneven distribution of air in the recirculation zone caused by the casing air distribution resulted in local hot regions and carried on through the combustion chamber to the outlet.

The region near 150° was expected to be at the same temperature as the regions at 40° , 220° , and 330° , however, the igniter and dome film cooling device at 180° are the reason for the low temperature. Since the igniter is at this location, the dome film cooling splash strip did not surround the entire circumference. This resulted in the discontinuous splash strip at 180° to accommodate the igniter.

During manufacturing the sleeve for the igniter was not installed completely straight. As a result, the igniter hole was not positioned correctly and the igniter could not be inserted into the liner. To fix this, a small amount of the sleeve was ground off to

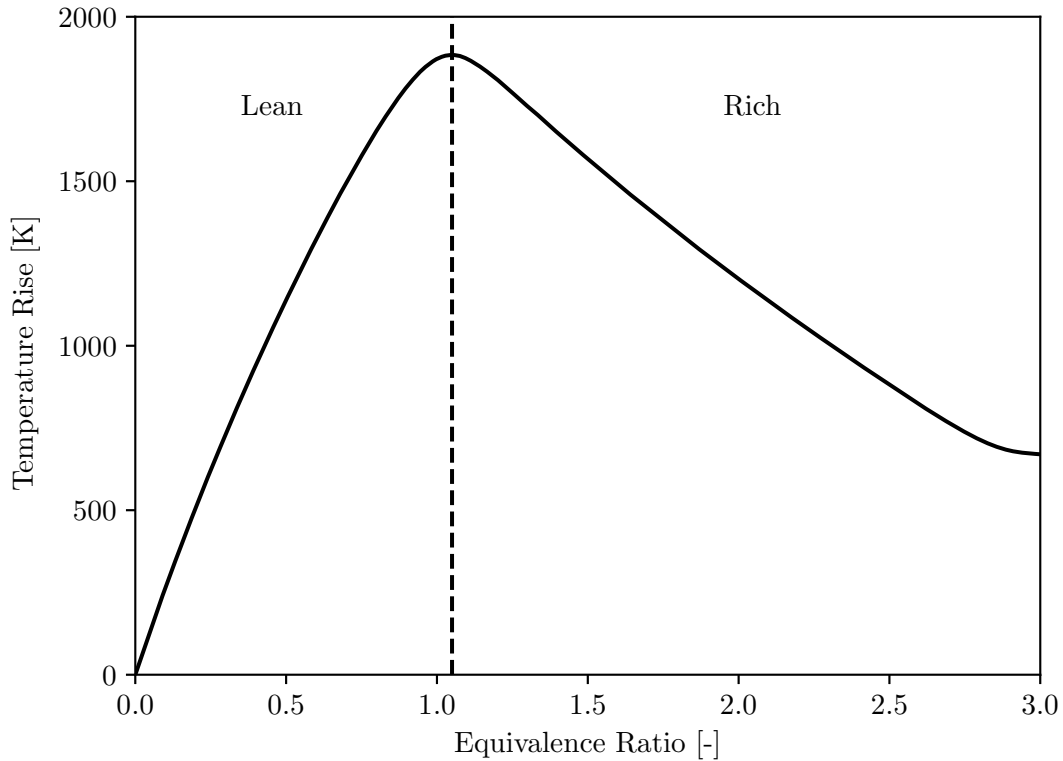


Figure 6.2: Plot of Temperature Rise as a Function of Equivalence Ratio.

increase the size of the hole so that the igniter could be inserted correctly. This resulted in a slightly larger hole than intended.

It is possible that the hole for the igniter in the dome was too large and air entered at this point. The air would have disrupted the toroidal vortex in this location causing further non-uniformity in the primary zone. The additional air from the igniter holes in addition to air from the casing hole near 150° could have also resulted in lean conditions, $\phi < 1$, lowering the temperature. The soot deposited at this location is also different than the rest of the splash strip, giving further evidence that there was not as much fuel in this region. The air exiting the swirler around 180° is directed along the splash resulting in the pattern shown in Fig. 6.3.

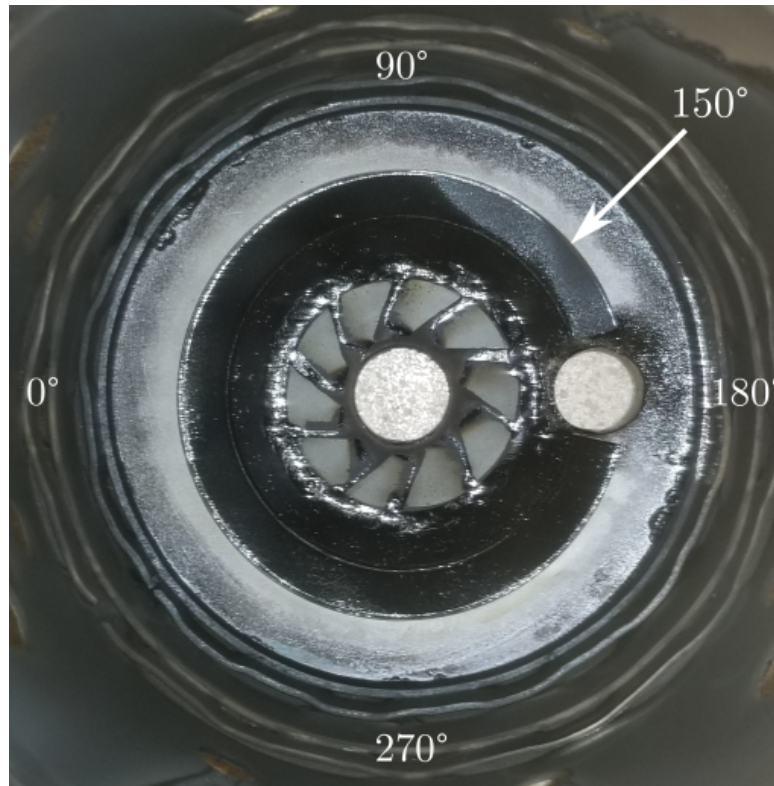


Figure 6.3: Soot Deposit on Splash Strip After Test.

The entire splash strip is covered in a shiny coating of soot except for the region from 100° to 170° . This inconsistency from the rest of the splash strip strongly connects the theory of lean conditions at this location to the deviation from the expected temperature rise at the outlet of the combustion chamber at 150° .

6.1.1 Performance Comparison

The temperature profile from the new combustion chamber tests were compared to the temperature profile of the original combustion chamber which was tested by Maqsood [30]. To compare each temperature profile, Eqn. 5.4 was used. Graphical comparisons between the new and the original combustion chamber for each test case are shown in Figs. 6.6 through 6.9.

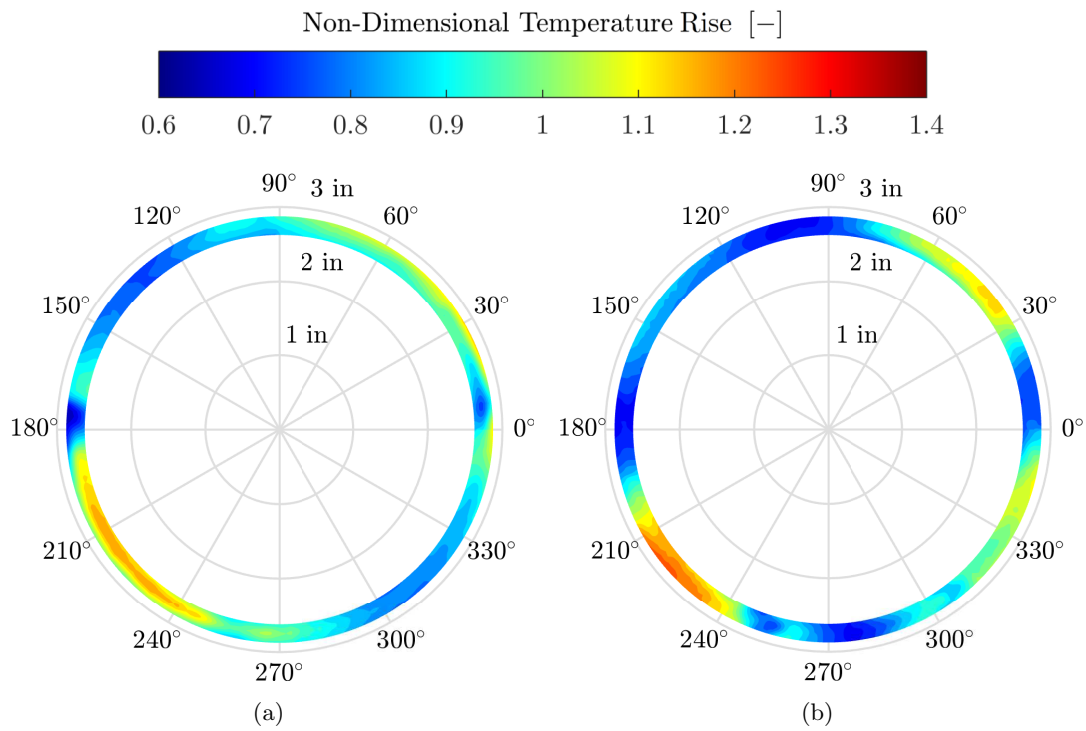


Figure 6.4: Exit Temperature Profile for +4% LD with (a) Original Liner from Maqsood [30], (b) New Liner.

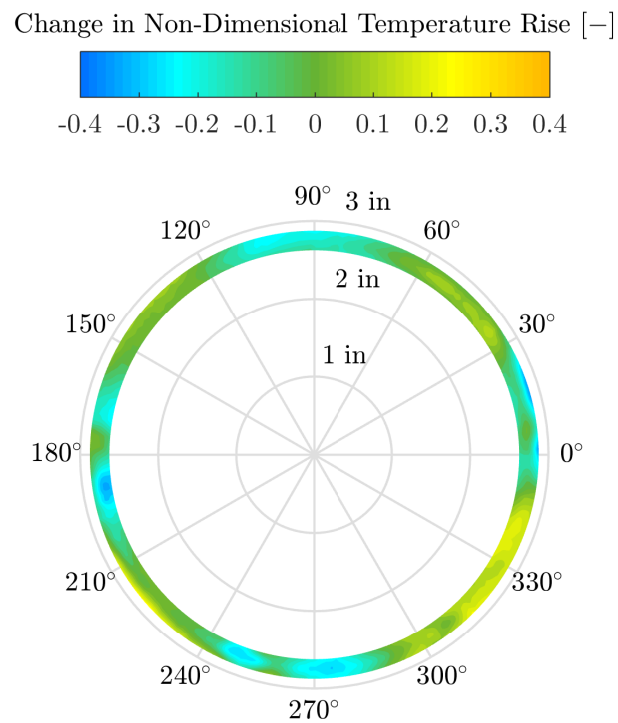


Figure 6.5: Change in Exit Temperature Profile - New and Original Liners, +4% LD.

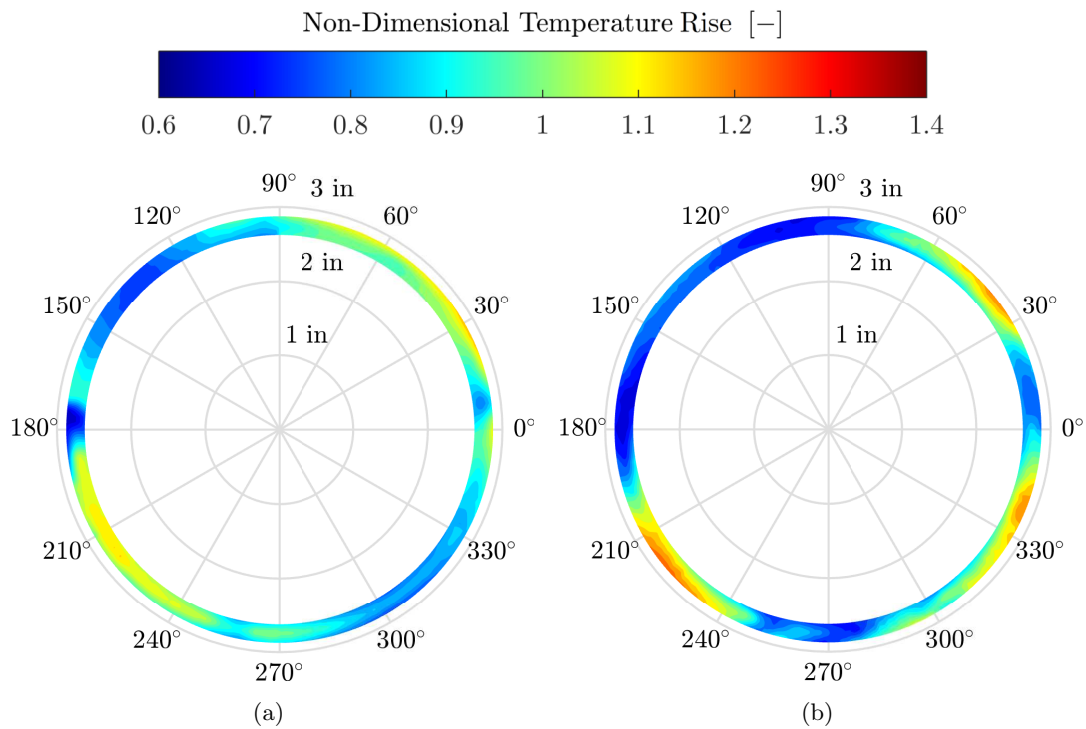


Figure 6.6: Exit Temperature Profile for Even Inlet Flow with (a) Original Liner from Maqsood [30], (b) New Liner.

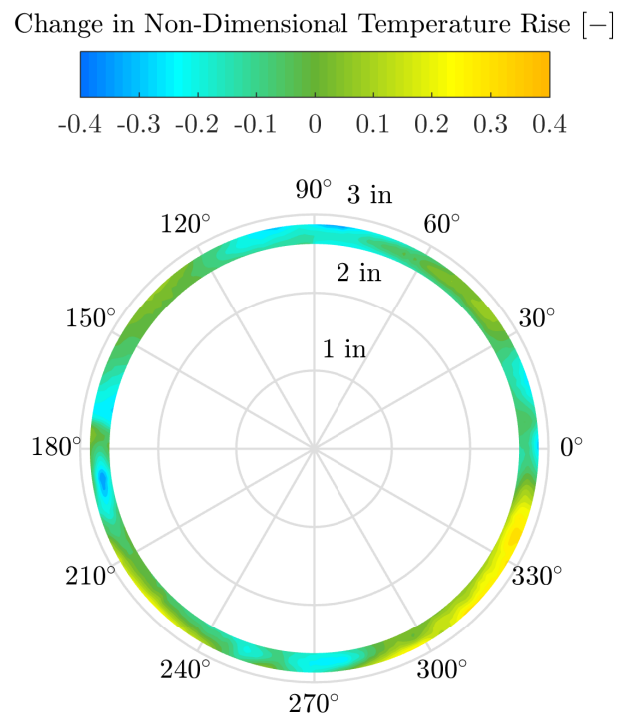


Figure 6.7: Change in Exit Temperature Profile - New and Original Liners, Even.

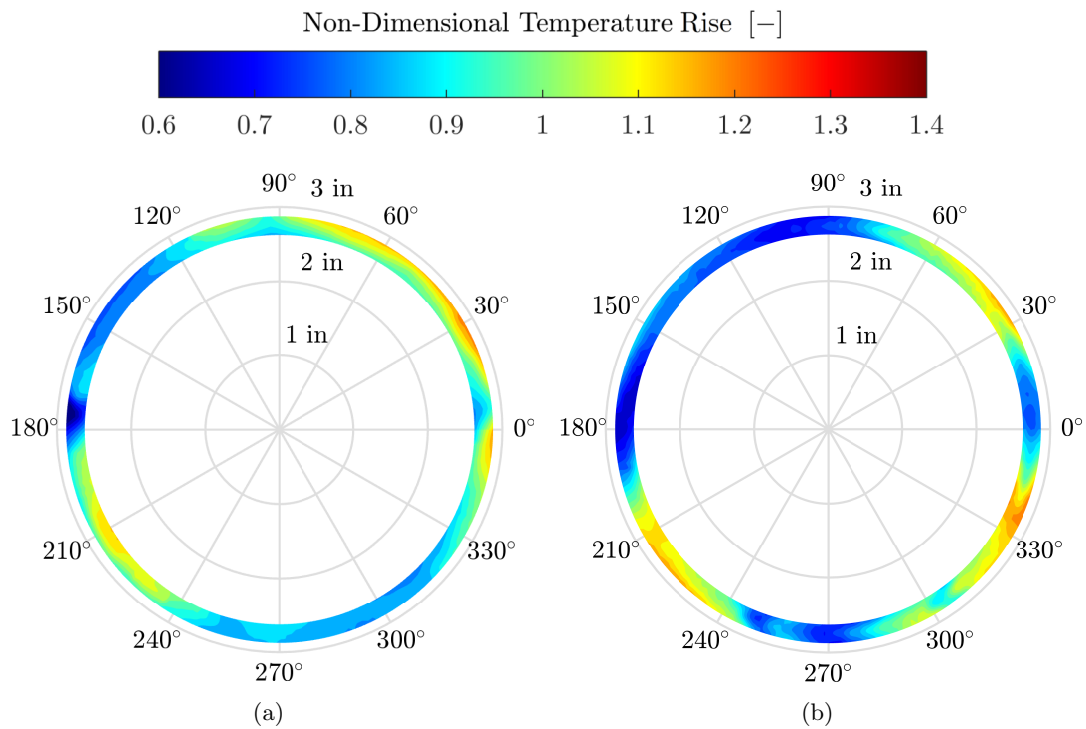


Figure 6.8: Exit Temperature Profile for +4% RD with (a) Original Combustion Chamber from Maqsood [30], (b) New Combustion Chamber.

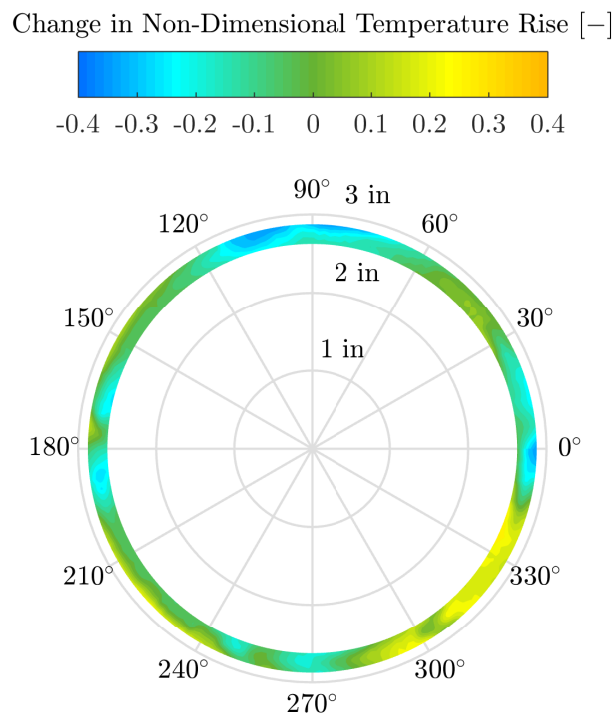


Figure 6.9: Change in Exit Temperature Profile - New and Original Liners, +4% RD.

The original combustion chamber had two regions of relatively high temperature at approximately 45° and 225° . The new liner did not reduce the magnitude of these hot spots, but instead increased them. An additional regions of higher temperature when compared to the original liner was also identified. The regions near 40° and 220° are slightly hotter, however, the most noticeable change is in the region between 290° to 345° . This is due to the new hot spot that was produced in this region that was not present in the original combustion chamber. There is also an increase in temperature rise along the outer radius from 120° to 240° .

Maqsood [30] calculated the average non-dimensional temperature with an image processing software *Matrox*, however, the values could not be replicated with the provided data so the average non-dimensional temperature was calculated with Eqn. 5.2. The average non-dimensional temperature and pattern factor for the original combustion chamber and the new combustion chamber are shown in Tab. 6.1.

Table 6.1: Average Non-dimensional Temperature Rise and Pattern Factor Comparison to Tests by Maqsood [30].

Test Case	New Liner		Original Liner	
	θ_{avg}	Pattern Factor	θ_{avg}	Pattern Factor
New +4% LD	0.912	0.389	0.935	0.279
New Even	0.906	0.379	0.931	0.256
New +4% RD	0.920	0.335	0.943	0.308

The average temperature rise of the new liner is lower than the average temperature rise with the original liner. This may be attributed to the increased soot deposition on the inner wall of the liner due to the rich conditions in the primary zone. The difference in average temperature rise is quite small and likely due to testing configuration. On the original liner there is a lip which is used to mount the liner onto the NGV shield at the outlet of the combustion chamber. There is a small gap outside of the NGV shield for the outer lip of the liner. While the liner is installed the gap should be plugged during operation on the test rig. The NGV shield and liner lip are shown in Fig. 6.10.

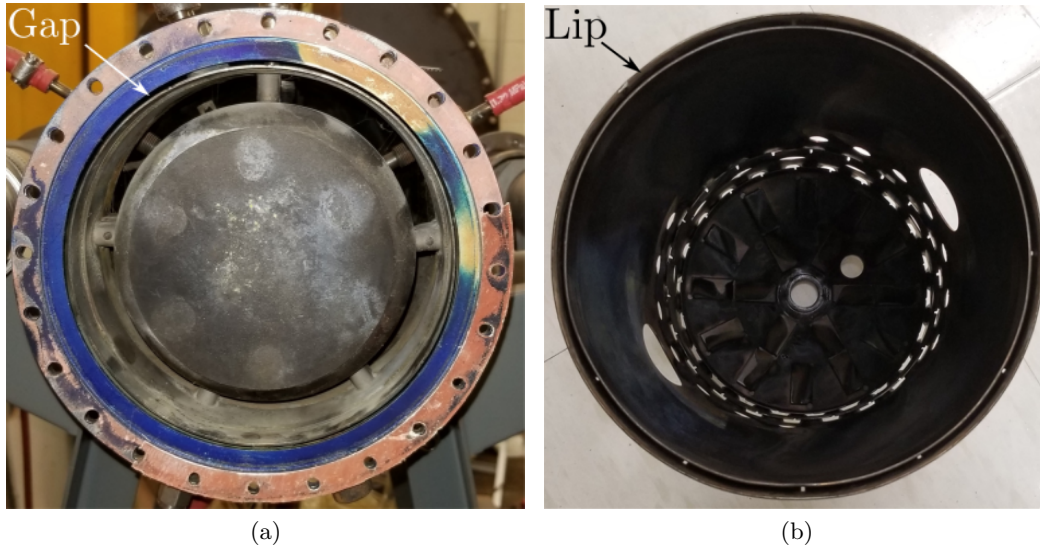


Figure 6.10: (a) Outer Gap Around the NGV Shield, (b) Liner Lip.

The new liner did not have the outer lip to plug this gap. To ensure no air escaped through the gap, it was covered with a piece of sheet metal. It is possible that during tests on the original liner a small amount of air leaked around the outer lip of the liner. This would result in a higher equivalence ratio in the combustion chamber raising the adiabatic flame temperature resulting in a higher average temperature. This would have been a small amount of air which would not have a notable change in the flow in the combustion chamber.

The pattern factor for all three cases is also significantly higher with the new liner than with the original liner. This higher pattern factor is partially due to the lower average temperature rise, as pattern factor is the deviation from average temperature rise, however, it is mainly a result of the local hot regions in the primary zone.

A drawback of the pattern factor is that it does not take into account the area of the temperature deviation. Upon inspection of the temperature profiles shown in Figs. 5.6, 5.7, and 5.9, the regions of high temperature are small. These regions are surrounded by larger regions close to the desired temperature rise. Although the maximum temperature deviation is higher, the area of these high temperatures are small.

6.1.2 Effects of Inlet Distortion

The effects of inlet distortion on the exit temperature profile were present in the new liner and were consistent with the original liner results presented by Maqsood [30]. It was found that the side with higher inlet flow increased in temperature, which was also observed in the original combustion chamber. An observation from the cases with inlet distortion showed an increase in temperature rise along the inner radius for both cases, shown in Figs. 5.8 and 5.10. A more uniform radial temperature profile is seen in the hot regions for both cases with inlet distortion when compared to the even inlet flow case. The reason for is likely from improved mixing due to the increased flow rate on the affected side.

The maximum temperature did not change significantly due to inlet distortion. This is the reason there was no notable increase in pattern factor like in the original liner. The maximum temperature for each case was measured on the outer radius, however, the majority of the increased temperature with inlet distortion was found along the inner radius. The temperature along the outer radius was mostly unchanged along the hotter side. This can be seen in Figs. 5.8 and 5.10.

This result shows that the new liner had a smaller change in temperature profile under uneven inlet flow conditions when compared to the original liner. The change in pattern factor for the new liner was minimal and lower than with the original liner. For the cases with inlet distortion, the maximum temperature did not significantly increase as with the original liner. For 4% higher left inlet flow, the change in maximum temperature in the hot region near 220° was 49 K for the original liner, and 15 K for the new liner. For 4% higher right inlet flow, the change in maximum temperature in the hot region near 40° was 56 K for the original liner, and 12 K for the new liner. Although the pattern factor was higher for all cases with the new liner, the change in both pattern factor and maximum temperature was not as significant.

The observations with the new liner are also consistent with the results of Bruan [22] shown in Fig. 3.3. For those tests the effects of inlet distortion were not fully investi-

gated, however, it was noted that with higher inlet flow rate at one side of the combustion chamber, the temperature increased on that side.

6.2 Combustion Chamber Design Comparison

The design of the new combustion chamber varies in many ways from the original design specifically in air distribution and geometry. The new liner was made of stainless steel rather than an advanced material due to manufacturing limitations. To accommodate the lower temperature limit of steel, the film cooling air was increased. No other special considerations to facilitate the choice of material needed to be made. A comparison between the design of the two liners shows the difference in the design methodology for each combustion chamber.

6.2.1 Geometry

The diameter of the new liner was sized based on the correlations based on aerodynamics (Eqns. 2.12 – 2.14) which produced a much smaller primary zone diameter than the original. From this diameter, the size of each zone was determined. Using this method, compromises had to be made in order for the liner to fit in the existing casing.

The length of the liner was constrained to the length of the original liner, therefore, the small diameter was necessary. A longer primary zone would have been preferred, however, space constraints did not allow it. The length of the primary zone was as short as Eqn. 2.16 allowed in order for the total length to match the original liner. The length of each zone for the two liners is comparable, however, the length to diameter ratio for each zone in the new liner is much higher than for the original liner.

The smaller primary zone diameter meant that the diameter of the liner would need to increase along the length of the liner to achieve the correct exit diameter. This was achieved with the conical section in the dilution zone. The cone angle is acceptable due to the exit geometry of the combustion chamber. At the outlet is the NGV shield which

directs the flow to the exit annulus, meaning the flow will follow the conical shape of the dilution zone wall.

The length of the dilution zone is similar on both liners. The new liner diameter increases in the dilution zone so a ratio of length to diameter is difficult to estimate. Odgers and Kretschmer [4] provide Eqn. 2.18 to estimate the dilution zone length based on maximum pattern factor and primary zone diameter. Since the liner diameter increases along the length of the liner, this may underestimate the required length of the dilution zone.

The correlation in Eqn. 2.43 was used to estimate the pattern factor for the new liner. This resulted in a pattern factor of 0.17. By this calculation, the length of the liner is appropriate, however, the experimental results deviate considerably from this value due to the non-uniform air distribution by the casing. This equation does not take into account the increasing liner diameter in the dilution zone. It is possible that the use of this conical section requires a longer dilution zone to adequately mix the air. A longer dilution zone could have helped to provide a more uniform exit temperature profile.

After testing the dome cooling splash strip was fully coated in soot. The splash strip stuck out into the recirculation zone and acted as an obstruction for the fuel droplets in the toroidal vortex. Most of the fuel was unaffected but as shown in Fig. 6.3, shiny layer is a result of some fuel droplets in the recirculation zone coating the splash strip in addition to soot from combustion. The preferred configuration would have been a cooling device that did not change the geometry of the dome.

The new liner has one film cooling device in the dome and four along the length of the liner wall. The original liner uses the dome swirlers as cooling devices for the dome and has two additional film cooling devices to cool to the rest of the liner. The new liner is made of stainless steel while the original liner is likely made from another material with a higher operating temperature allowing fewer film cooling devices to be used. Fewer film cooling devices would have allowed for more air to be used for

the holes for each zone. This would allow for a higher number of holes to be used improving mixing while maintaining appropriate jet penetration. Due to manufacturing limitations, wiggle strips were used. A more sophisticated method of wall cooling would have been beneficial, resulting in less air used for film cooling and more for the holes.

6.2.2 Air Distribution

The holes in the liner wall are evenly distributed around the liner for the new design, unlike the original liner. In addition to the evenly spaced holes, the sizes and number of holes in each zone differed significantly from the original liner. The number of holes as well as the total area for each set of holes are compared for the new liner and the old liner in Tab. 6.2. The total area of the holes along the liner are approximately equal, suggesting that the intended pressure drop and velocity through the holes are approximately equal.

Table 6.2: Liner Hole Comparison

Zone	Number of Holes	New Liner		Original Liner		
		Diameter d_{hole} [mm]	Total Area ΣA_{hole} [mm ²]	Number of Holes	Diameter d_{hole} [mm]	Total Area ΣA_{hole} [mm ²]
Primary	8	9.4	550	6/6	14.3/12.7	1720
Secondary	6	13.2	820	14	9.5	1000
Dilution	8	21.3	2860	2	31.8	1580

The largest difference is noticed in the primary zone and the dilution zone. For the new liner, the addition of the swirler and dome cooling splash strip resulted in a small proportion of air through the primary zone holes, and therefore, fewer and smaller holes. The eight dilution zone holes are evenly spaced around the liner as opposed to the original liner where there are only two holes, 180° apart. Both liners are shown in Fig. 6.11.

Eight dilution zone holes were chosen so that they could be staggered with the primary zone holes. This resulted in a jet penetration slightly deeper than the centerline.



Figure 6.11: Hole Size and Placement (a) New Liner, (b) Original Liner.

During manufacturing the holes were not staggered, however, this was not identified until testing had begun. Rather than having eight dilution zone holes, twelve dilution zone holes could have been chosen to be offset with secondary zone holes. This would have resulted in a small degree of under penetration ($\frac{y}{d} = 0.45$), however, the increased number of holes would have resulted in better circumferential mixing. This may have reduced the temperature of the hot spots and raised the temperature of the cold spots. Since there were four hot spots and four cold spots, they likely correspond to the eight primary zone holes and eight dilution zone holes. Changing the dilution zone hole

pattern from eight to twelve could result in an exit temperature profile with six hot spots and six cold spots, each with a smaller deviation from the average temperature.

The hole size and placement in the original suggests the air distribution and the intended equivalence ratio in the original liner prior to the exit of the combustion chamber is much different than in the new liner. On the original liner, the area of the primary zone holes and the holes used for the dome cooling flaps and swirler is nearly one third of the total area for air to enter the liner. This results in a primary zone that should be slightly lean with rich regions as a result of local air distribution. Comparing this to the new liner, which is designed to be rich in this region, shows that the design philosophy of the original combustion chamber was completely different when it came to distributing the air for each zone.

Evidence of a rich primary zone was visible after testing. The proportion of air in the recirculation zone was calculated to be 19% of the total air, resulting in an equivalence ratio of 1.21 in the region. This is supported by the soot deposits on the dome cooling splash strip. Soot deposits on the splash strip suggest that the recirculation zone was very rich, as the splash strip was completely coated with soot, as shown by the shiny coating in Fig. 6.3.

The placement of the igniter in the dome causes it to protrude into the recirculation zone resulting in asymmetric flow in the region. If the dome cooling strip was a full ring and not interrupted by the igniter, it is likely that the colder region around 150° would produce similar temperatures and cover the same area as the rest of the hot regions.

The type of swirler was changed from a dome swirler to an axial swirler. This change was implemented to introduce a toroidal vortex to create a swirl-stabilized recirculation flow in the primary zone. The swirler in the new liner allows 6% of the total airflow into the liner to produce a toroidal vortex in the primary zone. In the original liner, there is likely no recirculation set up as a result of the counter rotating swirlers, any recirculation that is produced is due to the jets of the primary zone holes.

The swirler was successful in producing a toroidal vortex in the primary zone as all

soot deposits along the inner wall of the liner show no evidence of swirl unlike in the original liner. The deposits of soot on the wall of the new liner are generally in the axial direction, while the original liner had soot deposits with an angle of approximately 20° from axial. The lack of swirl downstream of the primary zone was the intended result. Since there was no evidence of swirl downstream of the primary zone, there was a complete transition from swirling flow to recirculating flow resulting in a strong vortex.

6.3 Effects on Engine

The presence of hot spots at the turbine inlet can lead to secondary flows. These secondary flows caused by thermal gradients in the turbine result in reduced performance. Thermal gradients at the outlet of the combustion chamber can introduce secondary flows in turbines, possibly larger in magnitude than secondary flows introduced by velocity gradients as demonstrated by Lakshminarayana [40].

Although the thermal gradients lead to secondary flows which affect the turbine performance, the more significant consequence is on the turbine life. The first row in the turbine consists of the NGVs. The NGVs experience the highest temperatures in the turbine, therefore, when the combustion chamber delivers temperatures higher than the design specifications, the NGVs can quickly degrade. The premature degradation of these parts leads to decreased service life and increased maintenance time and costs over the life of the engine.

The operating condition in the current tests was a cruise condition. This condition produces temperatures well below the temperatures at take off, however, the engine spends the majority of its time at cruise meaning the NGVs would experience the hot streaks for extended periods of time. This results in a non-uniform distribution of thermal stresses on the NGVs. Since NGVs are stationary, only the paths with the hot streaks will experience this increase in thermal stress. For the new liner this has

increased from two locations to three and could be of greater concern for conditions with higher turbine inlet temperatures like during takeoff. Additional tests would need to be performed to determine the temperature profile at these conditions.

Both hot and cold spots at the outlet of the combustion chamber affect the life of turbine blades. For turbine blades, the frequency at which the blades transition from relatively high temperature to low temperature must be considered. The amplitude of the fluctuations is approximately the same between the new and original liners. The frequency of the gas temperature fluctuations has increased for the new liner when compared to the original liner. Although the amplitude has remained the same and the frequency has increased for the gas temperature, the strain amplitude on the blades has likely decreased. The strain on the blades is driven by the heat transfer from the gas to the blades which results in the temperature change. Since the frequency of the temperature fluctuations has increased, it results in less time over which heat transfer to the blades occurs resulting in a smaller variation in the blade temperature. Further investigation into the thermal mechanical fatigue behaviour of turbine blades is needed to determine if the new liner reduces the life of turbine blades, however, that is beyond the scope of this project.

7 Conclusions and Recommendations

7.1 Conclusions

The objective of this research was to design a new combustion liner for the Rolls-Royce M250-C20B combustion chamber that produces a more uniform temperature profile than the original liner and also reduces the effects of uneven inlet air flow conditions. The new liner was designed using present-day design practices and tested on an atmospheric combustion test rig. The exit temperature profile of the new combustion chamber was measured and the performance was compared to the original combustion chamber.

A scaled cruise condition was used for the testing conditions on the atmospheric test rig. This was achieved by matching the quasi-non-dimensional Mach number and the equivalence ratio, and minimizing the Sauter mean diameter of the fuel droplets. Real engine parts were used to match the geometry of the combustion chamber on the engine. The airflow from the real operating condition was scaled using Mach number. The area in the combustion chamber and the gas properties were consistent between test rig and engine operation allowing for the use of the quasi-non-dimensional Mach number. The fuel droplet characteristics were matched by ensuring the Sauter mean diameter was below $120\ \mu\text{m}$.

A number of changes were made to the test rig. The fuel nozzle was replaced because

the original nozzle produced streaks. The water cooled chamber housing the stepper motor was also slightly modified to better protect the stepper motor from extreme temperatures. The O-ring grooves were re-machined and larger O-rings were used to provide a better seal. Compressed air was supplied to pressurize the chamber with the stepper motor to keep exhaust gas from entering and over heating the stepper motor.

The results of the tests showed that the temperature profile of the new combustion chamber contained hot spots in the same location as the two hot spots identified in the original combustion chamber. The hot spots in the new combustion chamber temperature profile were higher in temperature than the original liner. There was also one additional hot spot that was not present in the original liner. A fourth region of increased temperature was observed, however, the temperature in this region was significantly lower than the other three.

The consistency of the locations of the hot spots between the original and new combustion chamber resulted in further analysis of the entire combustion chamber rather than just the liner. This revealed that the reason for the hot spots in the temperature profile at the exit of the new combustion chamber was due to the air distribution in the casing. Regardless of liner design, the hot spots were still produced because of the inlet air flow from the diffuser tubes into the annulus surrounding the liner through a set of 12 holes in the casing.

The air did not enter the casing uniformly, and instead entered through 4 of the 12 holes in the transition from the diffuser tubes to the annulus. The air entering through these four holes did not surround the liner uniformly and entered the liner at four locations in line with the casing holes. This resulted in regions in the primary zone that were locally hotter than others. These hot regions were carried through the liner to the outlet where they were identified on the exit temperature profile.

The effect of inlet distortion was also investigated. The inlet air flow was varied for the two inlets of the combustion chamber. For these tests, the flow rate of air entering the combustion chamber was 4% higher on one side with tests conducted for uneven

air flow on both sides. This resulted in similar observations to the original liner and agreed with external research conducted on the engine. The temperature on the side of the combustion chamber with higher inlet flow rate increased.

The effect of inlet distortion for the new liner was not as significant as in the original liner. There was no significant change in maximum temperature, however, the area of the hot regions increased. The change in pattern factor was minimal for the inlet distortion cases and much smaller when compared to the original liner. This showed that the design of the new liner partially achieved the objective of improving the combustion chamber.

This was the first attempt to redesign part of the combustion chamber. The design can be further refined based on the experimental findings. It is difficult to predict outlet temperature distributions without experimentation, therefore, it is difficult for the first design to achieve all objectives. As an initial design, the new liner offered comparable performance to the original liner with improvements in overall temperature distribution around the outlet annulus and with inlet distortion but did create additional hot and cold spots.

7.2 Recommendations

The conclusions of the research suggest that the casing was the reason for the hot spots at the outlet of the combustion chamber. To investigate the effects of the casing air distribution, the casing should be redesigned to provide a uniform air distribution around the circumference of the liner and tested with both the redesigned liner, and the original liner.

If a second iteration of the liner is to be designed, a change in hole configuration may be useful. Changing the symmetry of the holes in liner, similar to what is done on the original liner, would be difficult and would require extensive testing with new designs based on the test results. Changing the number and size of the holes may be an

easier solution. Eight dilution zone holes were selected so that they could be staggered with the eight primary zone holes. Since the jet penetration was high for the dilution zone, a greater number of smaller holes could be used. A possible configuration is twelve dilution zone holes staggered with the six secondary zone holes.

The airflow in the primary zone is thought to be non-uniform around the circumference of the liner, however, the flow paths were not observed. Flow visualization through experimentation or simulation would be beneficial in further understanding the air distribution from the casing. The airflow without combustion would be sufficient to visualize the flow paths through the combustion chamber.

Additional tests should be conducted with the new liner to establish a more consistent average temperature rise and pattern factor. Further testing at different operating points should also be conducted to measure the performance of the combustion chamber at various conditions.

It is also recommended that the cooling system for the stepper motor be redesigned or enhanced. The temperature of the air in the water cooled chamber was measured during testing to monitor the condition of the stepper motor. The stepper motor stalled at high temperatures and was only operational if room temperature compressed air was delivered into the test section to keep the temperature from increasing rapidly.

Although no streaks were present in the second fuel nozzle spray pattern, spray patternation testing should be conducted for fuel nozzles to be used in future combustion research to establish a baseline for the state of the nozzle before testing. Preliminary testing proved that the outlet temperature profile is very sensitive to nozzle spray pattern, therefore, spray patternation testing should be performed to determine the state of fuel nozzles for future work.

References

- [1] H. I. H. Saravanamuttoo, G. Rogers, H. Cohen, and P. Straznicki, *Gas Turbine Theory*. Pearson Education Limited, Sixth ed., 2009.
- [2] W. S. Blazowski and R. E. Henderson, “A Review of Turbopropulsion Combustion, Part I. Fundamentals of Combustion. Part II. Turbopropulsion Combustion Technology,” Technical Report, Air Force Aeropropulsion Laboratory, 1977.
- [3] A. Kanury, *Introduction to Combustion Phenomena*. Gordon and Breach Science Publishers, 1975.
- [4] J. Odgers and D. Kretschmer, *The Design and Development of Gas Turbine Combustors*, vol. II - Design Methods and Development Techniques, ch. The Basic Design Method - Can Combustors. Northern Research and Engineering Corporation, 1980.
- [5] C. K. Law, *Combustion Physics*. Cambridge University Press, 2006.
- [6] A. H. Lefebvre and D. R. Ballal, *Gas Turbine Combustion: Alternative Fuels and Emissions*. CRC Press, Third ed., 2010.
- [7] Rolls Royce plc, *The Jet Engine*. Rolls-Royce plc, 1996.
- [8] R. K. Eckhoff, *Explosion Hazards in the Process Industries*. Gulf Publishing Company, Second ed., 2016.
- [9] D. Kretschmer and J. Odgers, “Modeling of gas turbine combustors- a convenient reaction rate equation,” *Journal of Engineering for Power*, vol. 94, pp. 173–180, 1972.

-
- [10] J. Odgers, "Design of a single gas turbine combustor." Unpublished.
- [11] N. A. Chigier and A. Chervinsky, "Experimental investigation of swirling vortex motion in jets," *Journal of Applied Mechanics*, vol. 34, pp. 443–451, 1967.
- [12] J. D. Mattingly, W. H. Heiser, and D. T. Pratt, *Aircraft Engine Design*. American Institute of Aeronautics and Astronautics, Inc., Second ed., 2002.
- [13] D. A. Nealy and S. B. Reider, "Evaluation of laminated porous wall materials for combustor liner cooling," *Journal of Engineering for Power*, vol. 102, pp. 268–276, 1980.
- [14] G. Cerri, A. Giovannelli, L. Battisti, and R. Fedrizzi, "Advances in effusive cooling techniques of gas turbines," *Applied Thermal Engineering*, vol. 27, pp. 692–698, 2007.
- [15] E. R. G. Eckert and J. N. B. Livingood, "Comparison of effectiveness of convection-, transpiration-, and film-cooling methods with air as coolant," Technical Note, Lewis Flight Propulsion Laboratory, 1953.
- [16] J. F. Carrotte and S. J. Stevens, "The influence of dilution hole geometry on jet mixing," *Journal of Engineering for Gas Turbines and Power*, vol. 112, pp. 73–79, 1990.
- [17] S. J. Stevens and J. F. Carrotte, "Experimental studies of combustor dilution zone aerodynamics," in *24th AIAA/ASME/SAE/ASEE Joint Propulsion Conference*, 1988.
- [18] A. Eroglu, "Turbulent mixing in accelerating transverse jets," in *21st AIAA Fluid Dynamics, Plasma Dynamics and Lasers Conference*, 1990.
- [19] R. Friedman and E. R. Carlson, "A polar-coordinate survey method for determining jet-engine combustion-chamber performance," Technical Note, Lewis Flight Propulsion Laboratory, 1955.
- [20] P. P. Walsh and P. Fletcher, *Gas Turbine Performance*. Blackwell Science, 1998.

-
- [21] C. Kotzer, M. LaViolette, W. Allan, and A. Asghar, "Effects of combustion chamber geometry deviations upon exit temperature profiles for populations with varied service limitations," *Journal of Engineering for Gas Turbines and Power*, vol. 133, pp. 111503–1 – 111503–7, 2011.
- [22] K. T. Bruan, "Improved Aerothermodynamic Instrumentation of an Allison T63-A-700 Gas Turbine Engine," Master's Thesis, Naval Postgraduate School, 2002.
- [23] B. G. A. Sjoblom, "Some aspects on increasing gas turbine combustor exit temperature," in *ASME Gas Turbine Conference and Products Show*, 1980.
- [24] A. H. Lefebvre, "Fuel effects on gas turbine combustion," Technical Report, Aero-propulsion Laboratory, 1983.
- [25] F. M. White, *Fluid Mechanics*. McGraw-Hill, Sixth ed., 2008.
- [26] J. Odgers, D. Kretschmer, and G. F. Pearce, "The combustion of droplets within gas turbine combustors: Some recent observations on combustion efficiency," *Journal of Engineering for Gas Turbines and Power*, vol. 115, pp. 522–532, 1993.
- [27] B. P. Eckerle, "Design and component integration of a T63-A-700 gas turbine engine test facility," Master's Thesis, Naval Postgraduate School, 1995.
- [28] D. W. Haas, "The Instrumentation Design and Control of a T63-A-700 Gas Turbine Engine," Master's Thesis, Naval Postgraduate School, 1996.
- [29] J. Ilott, "Characterization of the discharge flow of a dual volute axi-centrifugal compressor," Master's Thesis, Royal Military College of Canada, 2012.
- [30] O. Maqsood, "Effects of inlet distortion on gas turbine combustion chamber exit temperature profiles," Master's Thesis, Royal Military College of Canada, 2013.
- [31] Allison Engine, *Engine Training Manual for Model 250-C20B*, 1990.
- [32] C. A. Palmer, *Dynamic Simulation of a Solid Fuelled Gas Turbine System*. Ph.D. Thesis, University of Wisconsin - Madison, 1991.
- [33] StandardAero, "Model A250-C20B test data." Unpublished.

-
- [34] A. F. El-Sayed, *Aircraft Propulsion and Gas Turbine Engines*. CRC Press, 2017.
- [35] B. J. McBride, M. J. Zehe, and S. Gordon, “NASA Glenn Coefficients for Calculating Thermodynamic Properties of Individual Species,” technical report, Glenn Research Center, 2002.
- [36] J. D. Mattingly and K. M. Boyer, *Elements of Propulsion: Gas Turbines and Rockets*. American Institute of Aeronautics and Astronautics, Inc., Second ed., 2016.
- [37] S. Gordon and B. J. McBride, “Computer program for calculation of complex chemical equilibrium compositions and applications,” reference publication, NASA Lewis Research Center, 1994.
- [38] D. Kretschmer and J. Odgers, “A simple method for the prediction of wall temperature in gas turbines,” in *Transactions of the AMSE/IGTI TurboExpo*, 1972.
- [39] J. M. De Freitas, “POLAR3D: A 3-Dimensional Polar Plot Function in Matlab,” 2005. <https://www.mathworks.com/matlabcentral/mlc-downloads/downloads/submissions/7656/versions/1/previews/polar3d.m/index.html>. Accessed: 18-09-2018.
- [40] B. Lakshminarayana, “Effects of inlet temperature gradients on turbomachinery performance,” *Journal of Engineering for Power*, vol. 97, pp. 64–71, 1975.

A Calculations

A.1 Diameter Calculations

The calculations for the combustion chamber diameter are shown for condition 1.

A.1.1 Chemical Kinetics

The volume required for the reaction is calculated with Eqn. A.1. The diameter is calculated with this volume, assuming a cylindrical volume with equal length and diameter. The steps are shown in Eqns A.1 through A.6. The values for M , n , y , $\frac{E}{R}$, ϵ , and α were obtained from Kretschmer and Odgers [9].

$$\frac{\dot{M}}{VP_3^n} = \frac{4.76 K_{\text{coll}}}{1000^{n-1} \bar{R}^n} \frac{e^{-\frac{E}{R(T_3 + \epsilon \Delta T_{\text{PZ}})}}}{(T_3 + \epsilon \Delta T_{\text{PZ}})^{n-0.5}} \frac{1}{y\epsilon} \frac{[5(1-y\epsilon)]^\alpha [\phi_{\text{PZ}} - y\epsilon]^{n-\alpha}}{[23.8 + \phi_{\text{PZ}} + y\epsilon]^n} \quad (\text{A.1})$$

$$\frac{\dot{M}}{VP_3^n} = \frac{4.76 \left(12.9 \times 10^9 \frac{\text{mol}^{1-n} \text{m}^{3(n-1)}}{\text{K}^{0.5} \text{s}} \right)}{1000^{(1.49-1)} \left(8.314 \frac{\text{J}}{\text{mol K}} \right)^{1.49}} \frac{e^{-\frac{23900 \text{ K}}{575 \text{ K} + 0.851(1745 \text{ K})}}}{(575 \text{ K} + 0.851(1745 \text{ K}))^{1.49-0.5}} \quad (\text{A.2})$$

$$\times \frac{1}{1(0.851)} \frac{[5[1 - 1(0.851)]]^{0.746} [1.34 - 1(0.851)]^{1.49-0.746}}{[23.8 + 1.34 + 1(0.851)]^{1.49}}$$

$$\frac{\dot{M}}{VP_3^n} = 1.78 \times 10^{-3} \frac{\text{mol}}{\text{Pa}^{1.49} \text{m}^3 \text{s}} \quad (\text{A.3})$$

$$V = \frac{\dot{M}}{1.78 \times 10^{-3} \frac{\text{mol}}{\text{Pa}^{1.49} \text{m}^3 \text{s}} P_3^n} = \frac{\frac{\dot{m}}{M}}{1.78 \times 10^{-3} \frac{\text{mol}}{\text{Pa}^{1.49} \text{m}^3 \text{s}} P_3^n} \quad (\text{A.4})$$

$$V = \frac{\frac{1.78 \frac{\text{kg}}{\text{s}}}{0.0290 \frac{\text{kg}}{\text{mol}}}}{1.78 \times 10^{-3} \frac{\text{mol}}{\text{Pa}^{1.49} \text{m}^3 \text{s}}} (7.47 \text{ Pa})^{1.49} = 59.8 \text{ mm}^3 \quad (\text{A.5})$$

$$d = \sqrt[3]{\frac{4V}{\pi}} = \sqrt[3]{\frac{4(59.8 \text{ mm}^3)}{\pi}} = 42.4 \text{ mm} \quad (\text{A.6})$$

A.1.2 Mach Number Correlation

The diameter of the liner can be calculated with Eqn A.8. The Mach number in the combustion chamber is assumed to be 0.05. The Mach number is used to calculate the casing diameter which is proportional to the liner diameter. The liner diameter is 70 % of the diameter of the casing.

$$Ma = \left(14.3 \frac{\text{m}}{\text{s K}^{0.5}}\right) \frac{\dot{m}_3 \sqrt{T_3}}{A_D P_3} = 0.05 \quad (\text{A.7})$$

$$A_D = \left(14.3 \frac{\text{m}}{\text{s K}^{0.5}}\right) \frac{1.79 \frac{\text{kg}}{\text{s}} \sqrt{575 \text{ K}}}{0.5 (746\,000 \text{ Pa})} \quad (\text{A.8})$$

$$A_D = 16\,400 \text{ mm}^2 \quad (\text{A.9})$$

$$D = \sqrt{\frac{4A}{\pi}} = \sqrt{\frac{4(16\,400 \text{ mm}^2)}{\pi}} = 144 \text{ mm} \quad (\text{A.10})$$

$$d = 0.7D = 0.7(144 \text{ mm}) = 101 \text{ mm} \quad (\text{A.11})$$

A.1.3 Bragg Correlation

The correlation by Bragg, Eqn. A.13, can also be used to size the primary zone. The pressure loss across the combustion chamber, $\frac{\Delta P_{3-4}}{P_3}$, is assumed to be 5 %.

$$A_d = \left(0.0162 \frac{\text{m}^2 \text{ s}}{\text{kg K}^{0.5}}\right) \frac{\dot{m}_f \sqrt{T_3}}{\left(\frac{P_3}{P_2}\right)} \sqrt{\frac{1}{\left(\frac{\Delta P_{3-4}}{P_3}\right)}} \quad (\text{A.12})$$

$$A_d = \left(0.0162 \frac{\text{m}^2 \text{ s}}{\text{kg K}^{0.5}}\right) \frac{0.0344 \frac{\text{kg}}{\text{s}} \sqrt{575 \text{ K}}}{7.37} \sqrt{\frac{1}{0.05}} \quad (\text{A.13})$$

$$A_d = 8120 \text{ mm}^2 \quad (\text{A.14})$$

$$d = \sqrt{\frac{4A}{\pi}} = \sqrt{\frac{4(8120 \text{ mm}^2)}{\pi}} = 102 \text{ mm} \quad (\text{A.15})$$

A.1.4 Aerodynamic Groups

The area of the casing can be calculated with Eqn. A.16 and from there the liner diameter is determined. The values in Tab. A.1 are used in Eqn. A.16 to calculate the casing diameter.

$$A_D = \frac{\dot{m}}{P_3} \sqrt{\frac{RT_3}{2}} \sqrt{\frac{\Delta P_{3-4}}{q_{\text{ref}}} \frac{P_3}{\Delta P_{3-4}}} \quad (\text{A.16})$$

Table A.1: Typical Values Used in Eqn. A.16.

Type	$\frac{\Delta P_{3-4}}{q_{\text{ref}}}$	$\frac{\Delta P_{3-4}}{P_3}$	$\frac{\dot{m}\sqrt{T_3}}{A_D P_3}$
Can	40	0.053	0.0030
Can-annular	30	0.054	0.0035
Annular	20	0.060	0.0030

$$\frac{\Delta P_{3-4}}{q_{\text{ref}}} = \frac{\Delta P_{3-4}}{P_3} \left(\frac{2}{R} \right) \left(\frac{1}{\frac{\dot{m}\sqrt{T_3}}{A_D P_3}} \right)^2 \quad (\text{A.17})$$

$$\frac{\Delta P_{3-4}}{q_{\text{ref}}} = 0.053 \left(\frac{2}{287 \frac{\text{J}}{\text{kgK}}} \right) \left(\frac{1}{0.003} \right)^2 = 41.0 \quad (\text{A.18})$$

$$A_D = \frac{1.79 \frac{\text{kg}}{\text{s}}}{747\,000 \text{ Pa}} \sqrt{\frac{287 \frac{\text{J}}{\text{kgK}} (575 \text{ K})}{2}} \sqrt{41.0 \frac{1}{0.053}} \quad (\text{A.19})$$

$$A_D = 19\,000 \text{ mm}^2 \quad (\text{A.20})$$

$$D = \sqrt{\frac{4A}{\pi}} = \sqrt{\frac{4(19\,000 \text{ mm}^2)}{\pi}} = 156 \text{ mm} \quad (\text{A.21})$$

$$d = 0.7D = 0.7(156 \text{ mm}) = 109 \text{ mm} \quad (\text{A.22})$$

A.1.5 Greenhough-Lefebvre Correlation

The Greenhough-Lefebvre correlation, Eqn. A.24, estimates the size of the casing. The diameter of the liner is calculated from the volume of the cylinder calculated with this method. The volume is assumed to be of a cylinder with equal diameter and length. The value for the combustion efficiency parameter, Φ , is provided in Odgers [10].

$$\Phi = \frac{V^{0.75} P_3^{1.75} e^{\frac{T_3}{260\text{K}}}}{\dot{m}} \quad (\text{A.23})$$

$$V^{0.75} = \frac{\Phi \dot{m}_a}{P_3^{1.75} e^{\frac{T_3}{260\text{K}}}} \quad (\text{A.24})$$

$$V = \left(\frac{2.96 \times 10^9 \frac{\text{Pa}^{1.75} \text{m}^{2.25} \text{s}}{\text{kg}} \left(1.79 \frac{\text{kg}}{\text{s}} \right)}{(747\,000 \text{ Pa})^{1.75} e^{\frac{575\text{K}}{260\text{K}}}} \right)^{\frac{1}{0.75}} \quad (\text{A.25})$$

$$V = 9.50 \times 10^6 \text{ mm}^3 \quad (\text{A.26})$$

$$D = \sqrt[3]{\frac{4V}{\pi}} = \sqrt[3]{\frac{4(9.50 \times 10^6 \text{ mm}^3)}{\pi}} = 42.4 \text{ mm} \quad (\text{A.27})$$

$$d = 0.7 D = 161 \text{ mm} \quad (\text{A.28})$$

A.2 Dome Angle Equation Derivation

The dimensions of the primary zone are shown in Fig. A.1.

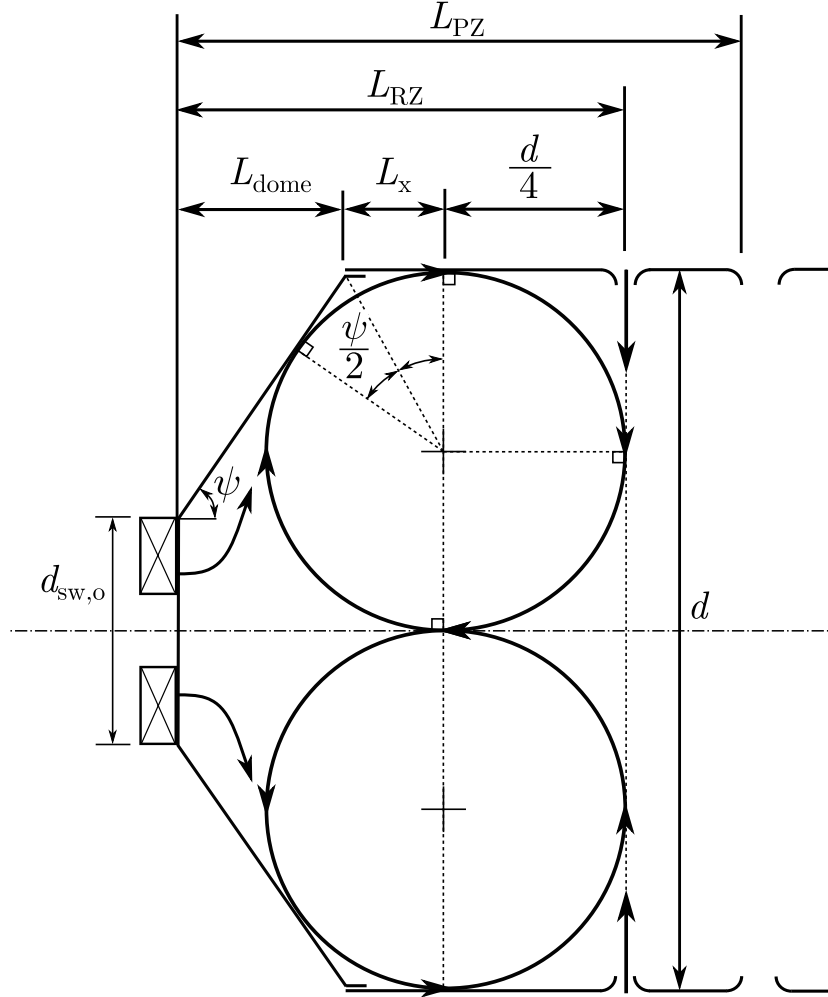


Figure A.1: Primary Zone Dimensions.

The length of the recirculation zone is the sum of the three lengths. The first is the length of the dome, L_{dome} . This is the horizontal length from the swirler to the end of the dome and is calculated with Eqn. A.29.

$$L_{\text{dome}} = \frac{d - d_{\text{sw},o}}{2 \tan \psi} \quad (\text{A.29})$$

The next length, L_x , is the length from the end of the dome to the point tangent to the magic circle on the liner wall. The arc on the magic circle between the point

tangent to the dome and the point tangent to the liner wall can be intersected at the midpoint by a line from the end of the dome to the center of the circle. This line creates two identical right angle triangles, each with one side equal to the radius of the magic circle and an angle of half the dome angle, as shown in Fig. A.1. This triangle is used to determine the length, L_x , as shown in Eqn. A.30.

$$L_x = \frac{d}{4} \tan\left(\frac{\psi}{2}\right) \quad (\text{A.30})$$

The third length is the radius of the magic circle, $\frac{d}{4}$. The length of the recirculation zone is shown in Eqn. A.32.

$$L_{\text{RZ}} = \frac{d - d_{\text{sw,o}}}{2 \tan \psi} + \frac{d}{4} \tan\left(\frac{\psi}{2}\right) + \frac{d}{4} \quad (\text{A.31})$$

$$L_{\text{RZ}} = \frac{1}{2} \left[\frac{d - d_{\text{sw,o}}}{\tan \psi} + \frac{d}{2} \tan\left(\frac{\psi}{2}\right) + \frac{d}{2} \right] \quad (\text{A.32})$$

A.3 Filming Cooling Device Placement

The temperature along the length of the combustion chamber was estimated to determine the heat transfer to the liner wall along the length of the combustion chamber. The method was developed by Odgers and Kretschmer [38]. The parameters for condition 1 are given in Tab. A.2.

Table A.2: Operating Conditions for Condition 1

Parameter	Value	Parameter	Value
P_3	747 000 Pa	\dot{m}_3	$1.78 \frac{\text{kg}}{\text{s}}$
T_3	575 K	$\frac{\dot{m}_{\text{RZ}}}{\dot{m}_3}$	0.19
T_4	1345 K	d	100 mm
T_{PZ}	2320 K	L_{RZ}	54 mm
T_{SZ}	2327 K	L_{PZ}	67 mm
$T_{\phi=1}$	2472 K	L_{SZ}	50 mm
ϕ	0.311	L_{DZ}	136 mm

The temperature rise through each zone is assumed to be linear. The calculations for condition 1 are shown. The first step is to estimate the recirculation zone exit temperature.

$$T_{\text{RZ,o}} = T_3 + \frac{2}{3}\eta_{\text{RZ}}(T_{\phi=1} - T_3) \quad (\text{A.33})$$

$$\eta_{\text{RZ}} = 0.56 + 0.44 \tanh [1.55 \times 10^{-3} (T_3 + 108 \ln P_3 - 1863)] \quad (\text{A.34})$$

$$\eta_{\text{RZ}} = 0.56 + 0.44 \tanh [1.55 \times 10^{-3} (575 + 108 \ln (747000) - 1863)] \quad (\text{A.35})$$

$$\eta_{\text{RZ}} = 0.676 \quad (\text{A.36})$$

$$T_{\text{RZ,o}} = 575 \text{ K} + \frac{2}{3} (0.676) (2472 \text{ K} - 575 \text{ K}) = 1430 \text{ K} \quad (\text{A.37})$$

The same approach is used to determine the temperature at the exit of the primary zone.

$$T_{\text{PZ,o}} = T_3 + \eta_{\text{PZ}}(T_{\text{PZ}} - T_3) \quad (\text{A.38})$$

$$\eta_{\text{PZ}} = 0.56 + 0.44 \tanh [1.55 \times 10^{-3} (T_3 + 108 \ln P_3 - 1863)] \quad (\text{A.39})$$

$$\eta_{\text{PZ}} = 0.71 + 0.29 \tanh [1.55 \times 10^{-3} (575 + 108 \ln (747000) - 1863)] \quad (\text{A.40})$$

$$\eta_{\text{PZ}} = 0.786 \quad (\text{A.41})$$

$$T_{\text{PZ,o}} = 575 \text{ K} + 0.786 (2320 \text{ K} - 575 \text{ K}) = 1946 \text{ K} \quad (\text{A.42})$$

Combustion is completed at the exit of the secondary zone, therefore, the temperature at the exit of the secondary zone is assumed to be $T_{\text{SZ}} = 2327 \text{ K}$. The temperature at the exit of the dilution is $T_4 = 1345 \text{ K}$. Thus, the temperature along the length of the combustion chamber is defined.

The liner wall temperature, T_w , is calculated by considering the heat transfer due to radiation and convection to and from the liner wall. Conduction is not considered in the calculation as the temperature difference across the liner wall is negligible due to the small wall thickness. The energy balance into the liner wall and out of the liner wall is shown in Eqn. A.43.

$$\dot{q}_{\text{rad},1} + \dot{q}_{\text{conv},1} = \dot{q}_{\text{cond}} = \dot{q}_{\text{rad},2} + \dot{q}_{\text{conv},2} \quad (\text{A.43})$$

A sample calculation is provided for condition 1 at 20 mm from the first cooling device at the end of the dome. The gas temperature, $T_{g,x}$, is calculated with Eqn. A.45.

$$T_{g,x} = T_3 + \frac{T_{\text{RZ,o}} - T_3}{L_{\text{RZ}}} x \quad (\text{A.44})$$

$$T_{g,20} = T_3 + \frac{T_{\text{RZ,o}} - T_3}{L_{\text{RZ}}} (20 \text{ mm} + L_{\text{dome}}) \quad (\text{A.45})$$

$$L_{\text{dome}} = \frac{d - d_{\text{sw,o}}}{2 \tan \psi} = \frac{100 \text{ mm} - 39.6 \text{ mm}}{2 \tan(69^\circ)} = 11.6 \text{ mm} \quad (\text{A.46})$$

$$T_{g,20} = 575 \text{ K} + \frac{1430 \text{ K} - 575 \text{ K}}{54 \text{ mm}} (20 \text{ mm} + 11.6) = 1080 \text{ K} \quad (\text{A.47})$$

The radiation from the combustion gas to the inner liner wall is calculated with Eqn. A.48.

$$\dot{q}_{\text{rad},1} = \frac{1}{2} \sigma (1 + \varepsilon_w) \varepsilon_g T_{g,x}^{1.5} (T_{g,x}^{2.5} - T_w^{2.5}) \quad (\text{A.48})$$

The emissivity of the wall, ε_w , is assumed to be 0.8. The emissivity of the gas is calculated with Eqn. A.49.

$$\varepsilon_g = 1 - \exp \left[-0.0746 Lu P_3 (0.6 d \phi_{\text{RZ}})^{0.5} T_{g,x}^{-1.5} \right] \quad (\text{A.49})$$

The luminosity factor Lu , calculated with Eqn. A.51. The fuel is Jet-A, $\text{C}_{12}\text{H}_{23}$, therefore, $a = 12$ and $b = 23$. The molar mass of carbon is $12.0 \frac{\text{g}}{\text{mol}}$. The molar mass of hydrogen is $23.0 \frac{\text{g}}{\text{mol}}$. The equivalence ratio in the recirculation zone is calculated with Eqn. A.53.

$$Lu = 0.0691 \left(\frac{a M_C}{b M_H} - 1.82 \right)^{2.71} \quad (\text{A.50})$$

$$Lu = 0.0691 \left(\frac{12 \left(12.0 \frac{\text{g}}{\text{mol}} \right)}{23 \left(1.01 \frac{\text{g}}{\text{mol}} \right)} - 1.82 \right)^{2.71} = 3.78 \quad (\text{A.51})$$

$$\phi_{\text{RZ}} = \frac{\phi}{\frac{\dot{m}_{\text{RZ}}}{\dot{m}_3}} = \frac{0.311}{0.19} = 1.64 \quad (\text{A.52})$$

$$\varepsilon_g = 1 - \exp \left[-0.0746 (3.78) (747\,000 \text{ Pa}) (0.6 (0.1 \text{ m}) (1.64))^{0.5} (1080 \text{ K})^{-1.5} \right] \quad (\text{A.53})$$

$$\varepsilon_g = 0.845 \quad (\text{A.54})$$

The luminosity factor is calculated for the gas in the recirculation zone, however, for gas in the primary, secondary, and dilution zones, the luminosity factor is 3, 2, and 1, respectively. The convective heat transfer from the gas to the inner liner wall is calculated with Eqn. A.55.

$$\dot{q}_{\text{conv},1} = 0.017 \left(\frac{\lambda_c}{\mu_c^{0.8}} \right) \left(\frac{\dot{m}_c}{A_c} \right)^{0.8} d_{h,c}^{-0.2} (T_{c,x} - T_{w1}) \quad (\text{A.55})$$

Where \dot{m}_c is the mass flow rate of air through the cooling device, A_c is the area of the cooling slot, $d_{h,c}$ is the hydraulic diameter of the slot, which is double the slot width, w , and $T_{c,x}$ is the temperature of the cooling gas along the wall. The width of the cooling slot is 2 mm. The conductivity and viscosity, $\frac{\lambda}{\mu^{0.8}}$, are represented by an empirical relation, calculated with Eqn. A.56.

$$\frac{\lambda}{\mu^{0.8}} = 74.8 + 1.67 T^{0.75} - 0.00816 T^{1.5} + 2.25 \times 10^{-5} T^{2.25} - 2.53 \times 10^{-8} T^3 \quad (\text{A.56})$$

The temperature of the cooling air near the wall increases and the efficiency of the cooling air on the the liner wall decreases further away from the cooling device. The cooling efficiency for a wiggle strip is plotted against an axial position parameter, X , in Fig. A.2. The position parameter is defined in Eqn. A.57.

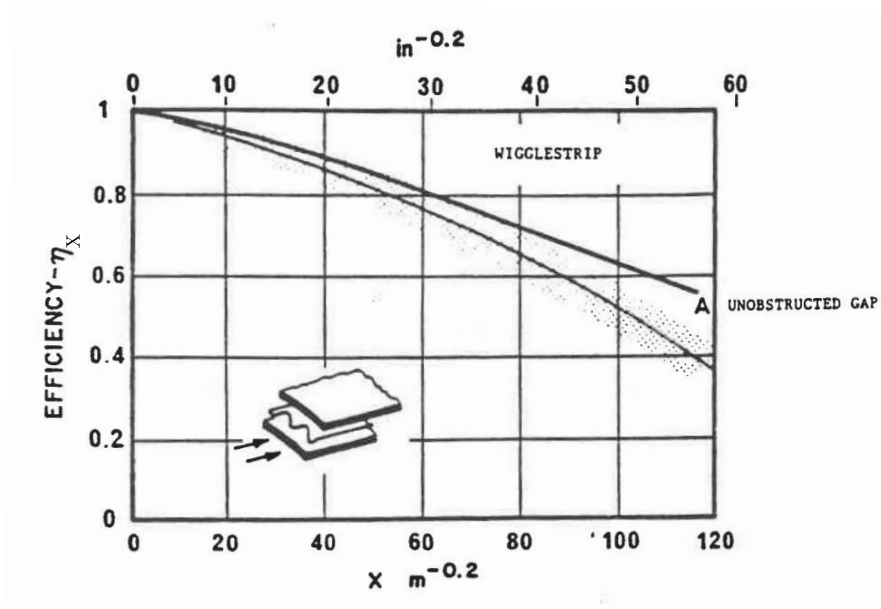


Figure A.2: Cooling Efficiency for a Wiggle Strip [10].

$$X = \left(\frac{\dot{m}_g A_c}{\dot{m}_c A_d} \right)^{0.8} \left(\frac{T_{g,avg}}{T_3} \right)^{0.6} \frac{x^{0.8}}{w} K_X \quad (\text{A.57})$$

Where \dot{m}_g is the mass flow rate of gas inside the liner, A_c is the area of the cooling slot, $T_{g,avg}$ is the average temperature of the gas at the entrance of the slot and the current position, x , and K_X is dependent on the velocity of gas in the liner and air in the slot as shown in Eqn. A.58.

$$K_X = \begin{cases} 1 & \text{for } \frac{u_g}{u_c} \geq 0.8 \\ \left(\frac{u_g}{u_c} + 0.2 \right)^{-1.25} & \text{for } 0 > \frac{u_g}{u_c} > 0.8 \end{cases} \quad (\text{A.58})$$

Where,

$$u_g = \frac{\dot{m}_g}{\rho_g A_d} \quad (\text{A.59})$$

$$u_c = \frac{\dot{m}_c}{\rho_c A_c} \quad (\text{A.60})$$

$$\frac{u_g}{u_c} = \frac{\dot{m}_g \rho_c A_c}{\dot{m}_c \rho_g A_d} \approx \frac{\dot{m}_g T_{g,\text{avg}} A_c}{\dot{m}_c T_3 A_d} \quad (\text{A.61})$$

The mass flow rate through the cooling slot is dependent on the effective area of the slot, the pressure drop across the slot, and the conditions of the air. The effective area of the slot is determined by the coefficient of discharge of the slot, C_D , 0.85 for wiggle strips, the area of the slot, A_c , and the area of material blocking the slot, A_B , such as a strip of material used to create a wiggle strip. The blockage for these wiggle strips is 65 % of the total area of the slot. The effective area, $A_{c,\text{eff}}$, is calculated with Eqn. A.63.

$$A_{c,\text{eff}} = C_D A_c \left(1 - \frac{A_B}{A_c}\right) \quad (\text{A.62})$$

$$A_{c,\text{eff}} = C_D \frac{\pi}{4} ((d + 2w)^2 - d^2) \left(1 - \frac{A_B}{A_c}\right) \quad (\text{A.63})$$

$$A_{c,\text{eff}} = 0.85 \left(\frac{\pi}{4}\right) ((100 \text{ mm} + 2(2 \text{ mm}))^2 - (100 \text{ mm})^2) (1 - 0.65) \quad (\text{A.64})$$

$$A_{c,\text{eff}} = 181 \text{ mm}^2 \quad (\text{A.65})$$

The pressure drop through the slot is equal to the pressure loss across the swirler. The pressure loss is calculated with Eqn. A.67.

$$\frac{\Delta P_c}{P_3} = \frac{\Delta P_{\text{sw}}}{P_3} = \frac{\Delta P_{\text{sw}}}{q_{\text{ref}}} \left(\frac{q_{\text{ref}}}{P_{3-4}}\right) \left(\frac{\Delta P_{3-4}}{P_3}\right) \quad (\text{A.66})$$

$$\frac{\Delta P_c}{P_3} = 32.0 \left(\frac{1}{41.0}\right) (0.05) = 0.039 \quad (\text{A.67})$$

The mass flow rate through the film cooling device is calculated with Eqn. A.69.

$$\dot{m}_c = \sqrt{\frac{\Delta P_c}{P_3} \frac{2 P_3^2 A_{c,\text{eff}}^2}{R T_3}} \quad (\text{A.68})$$

$$\dot{m}_c = \sqrt{0.039 \frac{2 (747\,000 \text{ Pa})^2 (0.000181 \text{ m}^2)^2}{287 \frac{\text{J}}{\text{kg K}} (575 \text{ K})}} = 0.092 \frac{\text{kg}}{\text{s}} \quad (\text{A.69})$$

$$\frac{\dot{m}_c}{\dot{m}_3} = \frac{0.092 \frac{\text{kg}}{\text{s}}}{1.78 \frac{\text{kg}}{\text{s}}} = 0.052 \quad (\text{A.70})$$

The cooling efficiency of the film, η_X , can be determined with Fig. A.2 after calculating X .

$$T_{g,\text{avg}} = \frac{T_{g,0} + T_{g,20}}{2} = \frac{759 \text{ K} + 1080 \text{ K}}{2} = 919 \text{ K} \quad (\text{A.71})$$

$$\frac{u_g}{u_c} = \frac{0.19 (919 \text{ K}) (641 \text{ mm}^2)}{0.052 (575 \text{ K}) (7850 \text{ mm}^2)} = 0.477 \quad (\text{A.72})$$

$$K_X = \left(\frac{u_g}{u_c} + 0.2 \right)^{-1.25} = (0.477 + 0.2)^{-1.25} = 1.63 \quad (\text{A.73})$$

$$X = \left(\frac{0.19 (641 \text{ mm}^2)}{0.052 (7850 \text{ mm}^2)} \right)^{0.8} \left(\frac{919 \text{ K}}{575 \text{ K}} \right)^{0.6} \left(\frac{(0.02 \text{ m})^{0.8}}{0.002 \text{ m}} \right) (1.63) \quad (\text{A.74})$$

$$X = 17.9 \frac{1}{\text{m}^{0.2}} \quad (\text{A.75})$$

The efficiency of the cooling film is 0.95. The temperature of the cooling air 20 mm from the cooling device is then calculated with Eqn. A.77.

$$T_{c,x} = T_{g,\text{avg}} - \eta_X (T_{g,\text{avg}} - T_3) \quad (\text{A.76})$$

$$T_{c,20} = 919 \text{ K} - 0.95 (919 \text{ K} - 575 \text{ K}) = 592 \text{ K} \quad (\text{A.77})$$

The radiation and convective heat transfer away from the liner to the annulus is calculated with Eqns. A.78 and A.79.

$$\dot{q}_{\text{rad},2} = 0.4\sigma (T_{w2}^4 - T_3^4) \quad (\text{A.78})$$

$$\dot{q}_{\text{conv},2} = 0.02 \left(\frac{\lambda_3}{\mu_3^{0.8}} \right) \left(\frac{\dot{m}_{\text{an}}}{A_{\text{an}}} \right)^{0.8} d_{h,\text{an}}^{-0.2} (T_w - T_3) \quad (\text{A.79})$$

Inserting all values into the appropriate equations yields the following.

$$\dot{q}_{\text{rad},1} = \frac{1}{2} \left(5.67 \times 10^{-8} \frac{\text{W}}{\text{m}^2 \text{K}^4} \right) (1 + 0.8)(0.848) \quad (\text{A.80})$$

$$\times (1080 \text{ K})^{1.5} \left((1080 \text{ K})_{\text{g},x}^{2.5} - T_{\text{w}}^{2.5} \right) \quad (\text{A.81})$$

$$\dot{q}_{\text{rad},1} = 0.00154 \frac{\text{W}}{\text{m}^2 \text{K}^{2.5}} (38.3 \times 10^6 \text{ K}^{2.5} - T_{\text{w}}^{2.5}) \quad (\text{A.82})$$

$$\dot{q}_{\text{conv},1} = 0.017 \left(192 \frac{\text{kg}^{0.2} \text{m}^{1.8}}{\text{s}^{2.2} \text{K}} \right) \left(\frac{0.052(1.78 \frac{\text{kg}}{\text{s}})}{0.000641 \text{ m}^2} \right)^{0.8} (2(0.002 \text{ m}))^{-0.2} \quad (\text{A.83})$$

$$\times (592 \text{ K} - T_{\text{w}}) \quad (\text{A.84})$$

$$\dot{q}_{\text{conv},1} = 526 \frac{\text{W}}{\text{m}^2 \text{K}} (592 \text{ K} - T_{\text{w}}) \quad (\text{A.85})$$

$$\dot{q}_{\text{rad},2} = 0.4 \left(5.67 \times 10^{-8} \frac{\text{W}}{\text{m}^2 \text{K}^4} \right) (T_{\text{w}}^4 - 109 \times 10^9 \text{ K}^4) \quad (\text{A.86})$$

$$\dot{q}_{\text{conv},2} = 0.02 \left(191 \frac{\text{kg}^{0.2} \text{m}^{1.8}}{\text{s}^{2.2} \text{K}} \right) \left(\frac{0.75 \left(1.78 \frac{\text{kg}}{\text{s}} \right)}{0.0176 \text{ m}^2} \right)^{0.8} (0.08 \text{ m})^{-0.2} \quad (\text{A.87})$$

$$\times (T_{\text{w}} - 575 \text{ K})$$

$$\dot{q}_{\text{conv},2} = 202 \frac{\text{W}}{\text{m}^2 \text{K}} (T_{\text{w}} - 575 \text{ K}) \quad (\text{A.88})$$

An iterative solver would be used to solve for T_{w} , however, for demonstration, a wall temperature of 644 K is inserted into Eqn. A.89.

$$0.00154 \frac{\text{W}}{\text{m}^2 \text{K}^{2.5}} (38.3 \times 10^6 \text{ K}^{2.5} - T_{\text{w}}^{2.5}) + 526 \frac{\text{W}}{\text{m}^2 \text{K}} (592 \text{ K} - T_{\text{w}}) \quad (\text{A.89})$$

$$= 0.4 \left(5.67 \times 10^{-8} \frac{\text{W}}{\text{m}^2 \text{K}^4} \right) (T_{\text{w}}^4 - 109 \times 10^9 \text{ K}^4) + \left(202 \frac{\text{W}}{\text{m}^2 \text{K}} \right) (T_{\text{w}} - 575 \text{ K})$$

$$0.00154 \frac{\text{W}}{\text{m}^2 \text{K}^{2.5}} (38.3 \times 10^6 \text{ K}^{2.5} - (644 \text{ K})^{2.5}) + \left(526 \frac{\text{W}}{\text{m}^2 \text{K}} \right) (592 \text{ K} - 644 \text{ K}) \quad (\text{A.90})$$

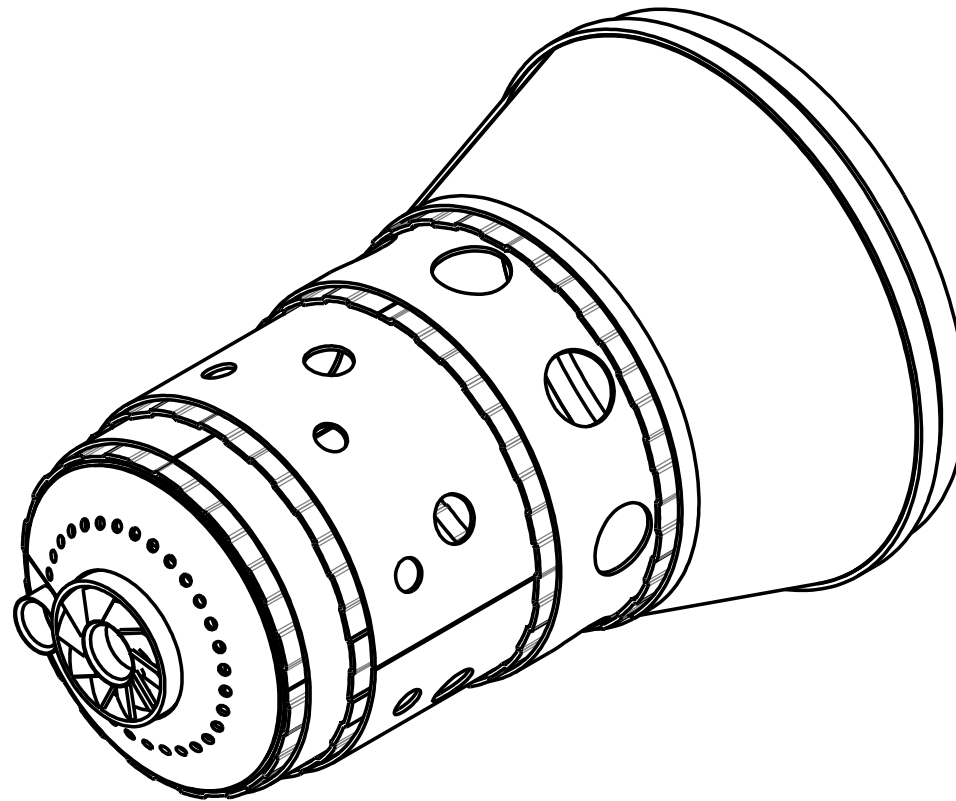
$$= 0.4 \left(5.67 \times 10^{-8} \frac{\text{W}}{\text{m}^2 \text{K}^4} \right) \left((644 \text{ K})^4 - 109 \times 10^9 \text{ K}^4 \right) + \left(202 \frac{\text{W}}{\text{m}^2 \text{K}} \right) (644 \text{ K} - 575 \text{ K})$$

$$42\,800 \frac{\text{W}}{\text{m}^2} - 27\,400 \frac{\text{W}}{\text{m}^2} = 1\,430 \frac{\text{W}}{\text{m}^2} + 13\,900 \frac{\text{W}}{\text{m}^2} \quad (\text{A.91})$$

$$15\,400 \frac{\text{W}}{\text{m}^2} \approx 15\,330 \frac{\text{W}}{\text{m}^2} \quad (\text{A.92})$$

The wall temperature is 644 K.

B Engineering Drawings



MATERIAL MATIÈRE	WEIGHT MASSE	lbs
CREATED DATE DATE DE CRÉATION	June-21-18 2:07:51 PM	
SAVED SAUVÉGARDE	May-13-19 1:47:09 PM	
FOLDER DOSSIER	C:\Users\katz\Documents\Thesis\Design\models\chamberv5\Assemblies\	

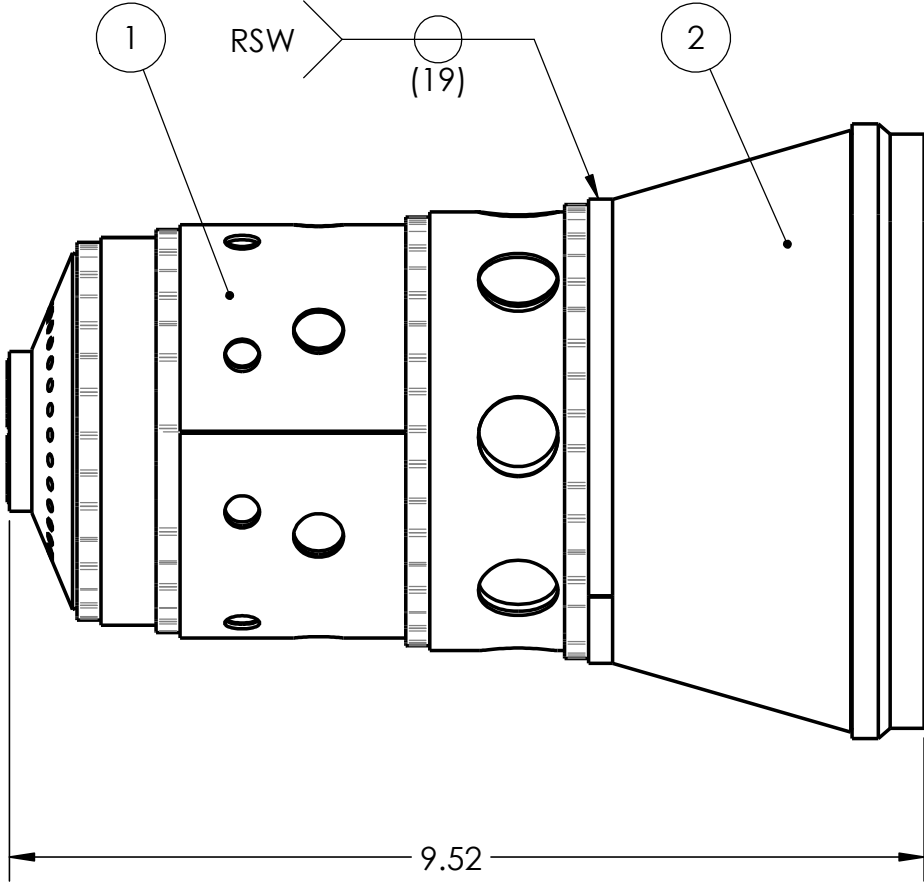


**RMCC
ENGINEERING
FACULTY**
CMRC
FACULTÉ
D'INGÉNIÉRIE

INCH / POUCE  SCALE ÉCHELLE 1:2
DECIMAL TOLERANCE UNLESS OTHERWISE SPECIFIED /
TOLÉRANCE DÉCIMALE SAUF SI SPÉCIFICATION DIFFÉRENTE
X.X = ± 0.05
X.XX = ± 0.005
X.XXX = ± 0.001

TITLE TITRE	M250 COMBUSTION CHAMBER		DWG # / DESSIN#
NAME NOM	CURTIS KAATZ	NUMBER NUMÉRO	G7456
FILE NAME NOM FICHIER	M250 COMBUSTION CHAMBER V2	SHEET PAGE	1 OF 41 DE
			1

ITEM NO.	DRAWING NUMBER	QTY.
1	1.2	1
2	1.1	1



MATERIAL MATIÈRE	WEIGHT MASSE	lbs
CREATED DATE DATE DE CRÉATION	June-21-18 2:07:51 PM	
SAVED SAUVÉ/GARDÉ	May-13-19 1:47:09 PM	
FOLDER DOSSIER	C:\Users\katz\Documents\Thesis\Design\models\chamberv5\Assemblies\	

**RMCC
ENGINEERING
FACULTY**

**CMRC
FACULTÉ
D'INGÉNIÉRIE**

INCH /
POUCE

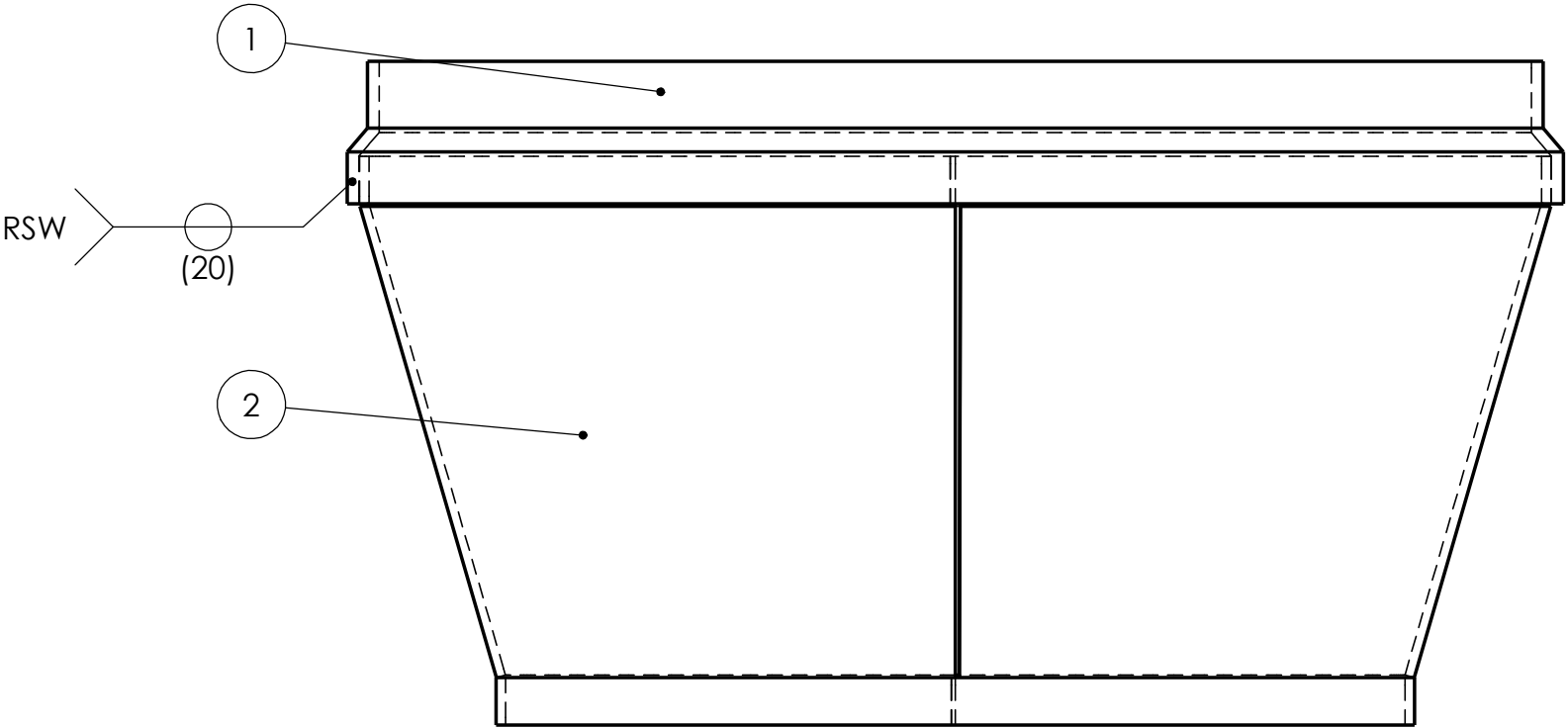
SCALE
ÉCHELLE 1:2

DECIMAL TOLERANCE UNLESS OTHERWISE SPECIFIED/
TOLÉRANCE DÉCIMALE SAUF SI SPÉCIFICATION DIFFÉRENTE

X.X = ± 0.05
X.XX = ± 0.005
X.XXX = ± 0.001

TITLE TITRE		M250 COMBUSTION CHAMBER	
NAME NOM	CURTIS KAATZ	NUMBER NUMÉRO	G7456
FILE NAME NOM FICHIER	M250 COMBUSTION CHAMBER V2	SHEET PAGE	2 OF 41 DE
			DWG # / DESSIN# 1

ITEM NO.	DRAWING NUMBER	QTY.
1	1.1.1	1
2	1.1.2	1



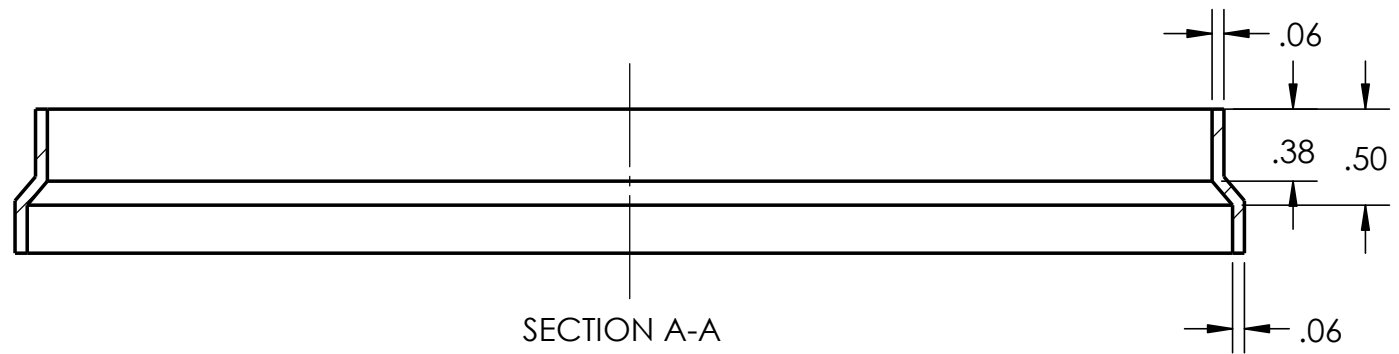
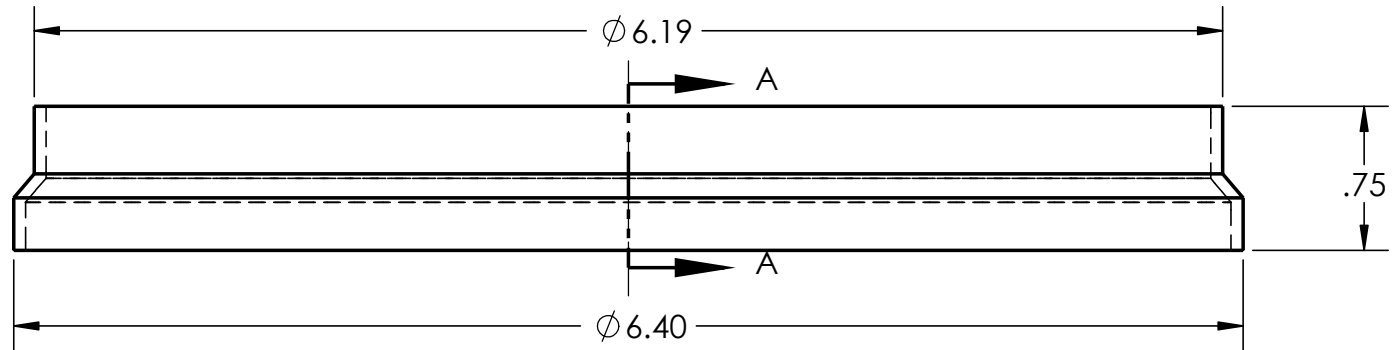
MATERIAL MATIÈRE	WEIGHT MASSE	lbs
CREATED DATE DATE DE CRÉATION	June-21-18 1:59:28 PM	
SAVED SAUVÉGARDE	August-31-18 10:04:48 AM	
FOLDER DOSSIER	C:\Users\katz\Documents\Thesis\Design\models\chamberv5\Assemblies\	


**RMCC
ENGINEERING
FACULTY**
**CMRC
FACULTÉ
D'INGÉNIÉRIE**

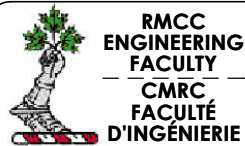
INCH / POUCE  SCALE ÉCHELLE 1:1
DECIMAL TOLERANCE UNLESS OTHERWISE SPECIFIED /
TOLÉRANCE DÉCIMALE SAUF SI SPÉCIFICATION DIFFÉRENTE
 X.X = ± 0.05
 X.XX = ± 0.005
 X.XXX = ± 0.001

TITLE TITRE	SECTION 4-SLOT ASSEMBLY		DWG # / DESSIN
NAME NOM	CURTIS KAATZ		NUMBER NUMÉRO G7456
FILE NAME NOM FICHIER	SECTION 4-SLOT V2	SHEET PAGE 3 OF DE 41	1.1

PART NAME	DESCRIPTION	QTY.	MATERIAL
SLOT V2	MACHINED	1	316L STAINLESS STEEL



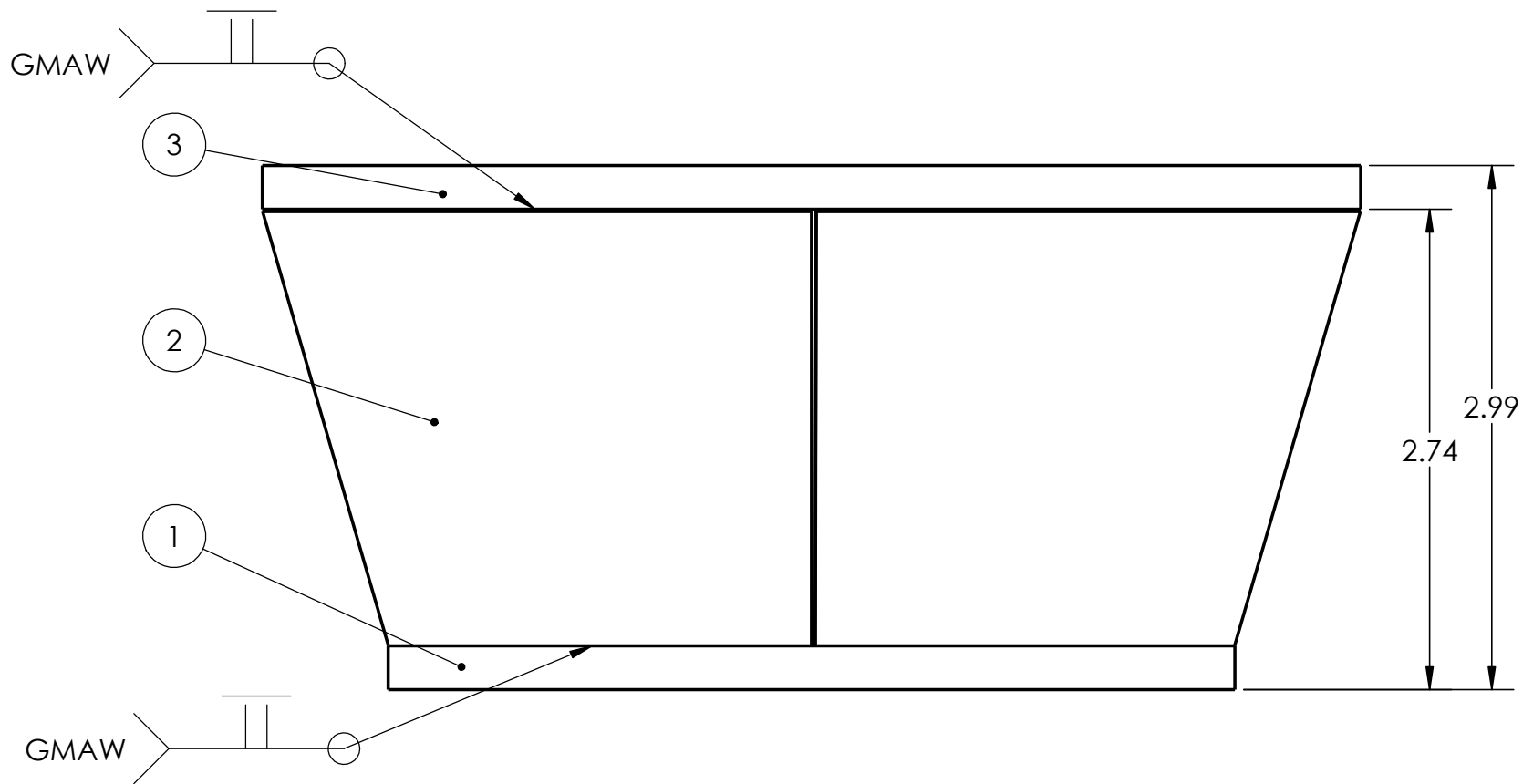
MATERIAL MATIÈRE	WEIGHT MASSE	lbs
CREATED DATE DATE DE CRÉATION	August-30-18 2:43:44 PM	
SAVED SAUVÉ/GARDÉ	August-30-18 3:51:44 PM	
FOLDER DOSSIER	C:\Users\kaatz\Documents\Thesis\Design\models\chamberv5\Parts\	



INCH / POUCE  SCALE ÉCHELLE 1:1
DECIMAL TOLERANCE UNLESS OTHERWISE SPECIFIED /
 TOLÉRANCE DÉCIMALE SAUF SI SPÉCIFICATION DIFFÉRENTE
 X.X = ± 0.05
 X.XX = ± 0.005
 X.XXX = ± 0.001

TITLE TITRE	SLOT		DWG # / DESSIN#
NAME NOM	CURTIS KAATZ	NUMBER NUMÉRO	G7456
FILE NAME NOM FICHIER	SLOT V2	SHEET PAGE	4 OF DE 41
			1.1.1

ITEM NO.	DRAWING NUMBER	QTY.
1	1.1.2.1	1
2	1.1.2.2	1
3	1.1.2.3	1



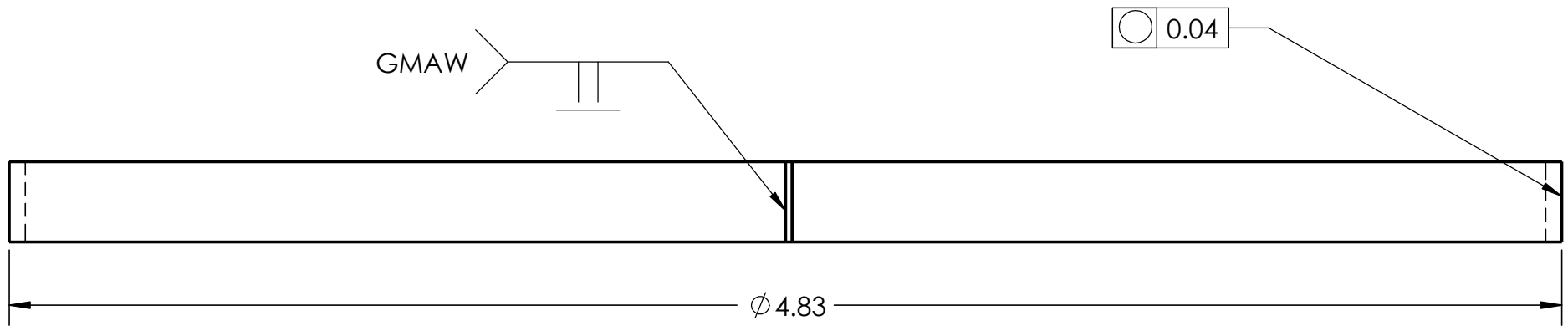
MATERIAL MATIÈRE	WEIGHT MASSE	lbs
CREATED DATE DATE DE CRÉATION	June-20-18 6:26:36 PM	
SAVED SAUVÉGARDE	August-31-18 10:04:50 AM	
FOLDER DOSSIER	C:\Users\katz\Documents\Thesis\Design\models\chamberv5\Assemblies\	


**RMCC
ENGINEERING
FACULTY**
**CMRC
FACULTÉ
D'INGÉNIÉRIE**

INCH / POUCE  SCALE ÉCHELLE 1:1
DECIMAL TOLERANCE UNLESS OTHERWISE SPECIFIED /
TOLÉRANCE DÉCIMALE SAUF SI SPÉCIFICATION DIFFÉRENTE
 X.X = ± 0.05
 X.XX = ± 0.005
 X.XXX = ± 0.001

TITLE TITRE	SECTION 4 ASSEMBLY	
NAME NOM	CURTIS KAATZ	NUMBER NUMÉRO G7456
FILE NAME NOM FICHIER	SECTION 4 ASSEMBLY V2	SHEET PAGE 5 OF DE 41
		DWG # / DESSIN# 1.1.2

PART NAME	DESCRIPTION	QTY.	MATERIAL
SECTION 4-1	ROLLED 18 GAUGE SHEET	1	316L STAINLESS STEEL



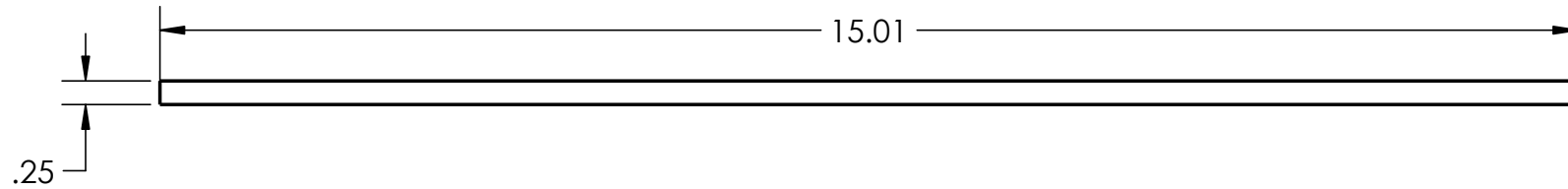
MATERIAL MATIÈRE	WEIGHT MASSE	lbs
CREATED DATE DATE DE CRÉATION	June-20-18 6:15:02 PM	
SAVED SAUVÉGARDE	July-09-18 10:46:04 AM	
FOLDER DOSSIER	C:\Users\kaatz\Documents\Thesis\Design\models\chamberv5\Parts\section4	


**RMCC
ENGINEERING
FACULTY**
**CMRC
FACULTÉ
D'INGÉNIÉRIE**

INCH / POUCE  SCALE ÉCHELLE 2:1
DECIMAL TOLERANCE UNLESS OTHERWISE SPECIFIED /
TOLÉRANCE DÉCIMALE SAUF SI SPÉCIFICATION DIFFÉRENTE
 X.X = ± 0.05
 X.XX = ± 0.005
 X.XXX = ± 0.001

TITLE TITRE	SECTION 4-1	
NAME NOM	CURTIS KAATZ	NUMBER NUMÉRO G7456
FILE NAME NOM FICHIER	SECTION 4-1	SHEET PAGE 6 OF DE 41
		DWG # / DESSIN 1.1.2.1

PART NAME	DESCRIPTION	QTY.	MATERIAL
SECTION 4-1	18 GAUGE SHEET	1	316L STAINLESS STEEL



MATERIAL MATIÈRE	WEIGHT MASSE	lbs
CREATED DATE DATE DE CRÉATION	June-20-18 6:15:02 PM	
SAVED SAUVÉGARDE	July-09-18 10:46:04 AM	
FOLDER DOSSIER	C:\Users\kaatz\Documents\Thesis\Design\models\chamberv5\Parts\section4	

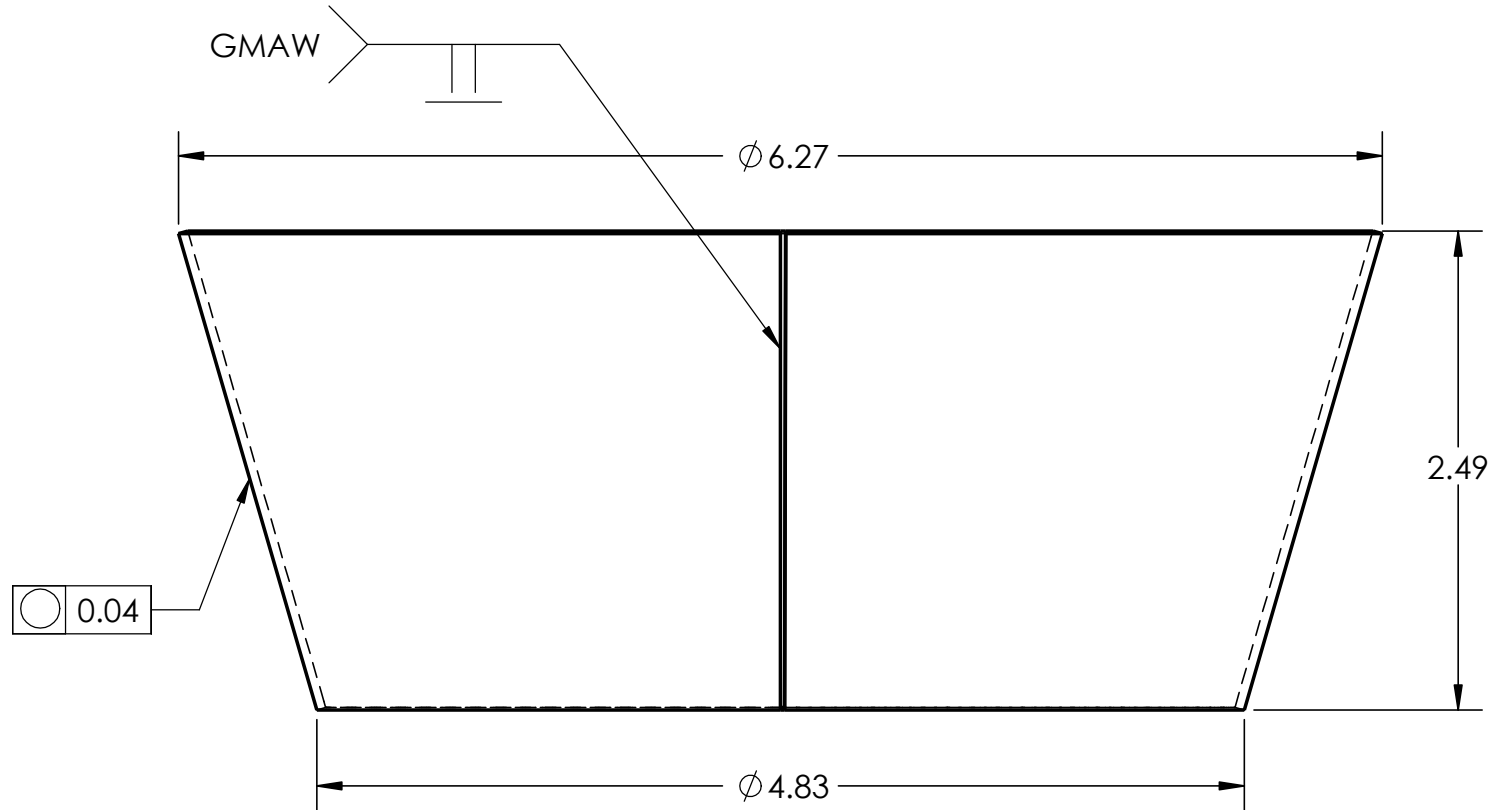


**RMCC
ENGINEERING
FACULTY**
**CMRC
FACULTÉ
D'INGÉNIÉRIE**

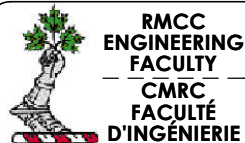
INCH / POUCE  SCALE / ÉCHELLE 1:2
DECIMAL TOLERANCE UNLESS OTHERWISE SPECIFIED /
TOLÉRANCE DÉCIMALE SAUF SI SPÉCIFICATION DIFFÉRENTE
X.X = ± 0.05
X.XX = ± 0.005
X.XXX = ± 0.001

TITLE TITRE	SECTION 4-1		DWG # / DESSIN
NAME NOM	CURTIS KAATZ	NUMBER NUMÉRO	G7456
FILE NAME NOM FICHIER	SECTION 4-1	SHEET PAGE	7 OF DE 41
			1.1.2.1

PART NAME	DESCRIPTION	QTY.	MATERIAL
SECTION 4-2 V2	ROLLED 18 GAUGE SHEET	1	316L STAINLESS STEEL



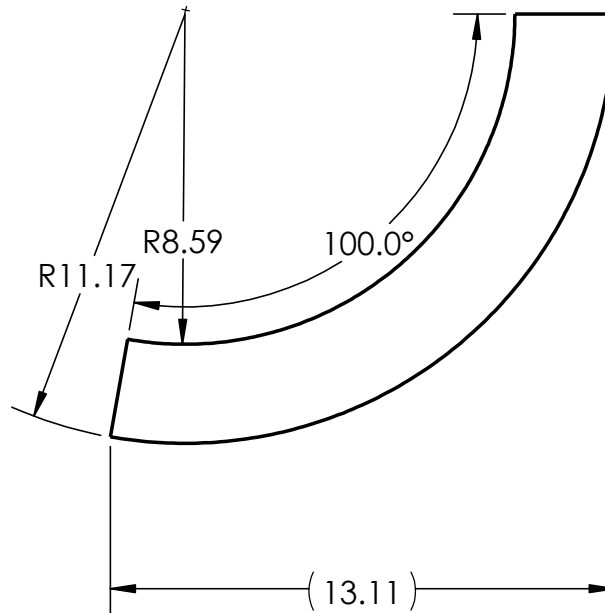
MATERIAL MATIÈRE	WEIGHT MASSE	lbs
CREATED DATE DATE DE CRÉATION	June-20-18 6:19:22 PM	
SAVED SAUVÉGARDE	August-31-18 10:04:50 AM	
FOLDER DOSSIER	C:\Users\kaatz\Documents\Thesis\Design\models\chamberv5\Parts\section4	



INCH / POUCE		SCALE ÉCHELLE	1:2
DECIMAL TOLERANCE UNLESS OTHERWISE SPECIFIED/ TOLÉRANCE DÉCIMALE SAUF SI SPÉCIFICATION DIFFÉRENTE			
X.X = ± 0.05			
X.XX = ± 0.005			
X.XXX = ± 0.001			

TITLE TITRE	SECTION 4-2		DWG # / DESSIN
NAME NOM	CURTIS KAATZ	NUMBER NUMÉRO	G7456
FILE NAME NOM FICHIER	SECTION 4-2 V2	SHEET PAGE	8 OF DE 41
			1.1.2.2

PART NAME	DESCRIPTION	QTY.	MATERIAL
SECTION 4-2 V2	18 GAUGE SHEET	1	316L STAINLESS STEEL



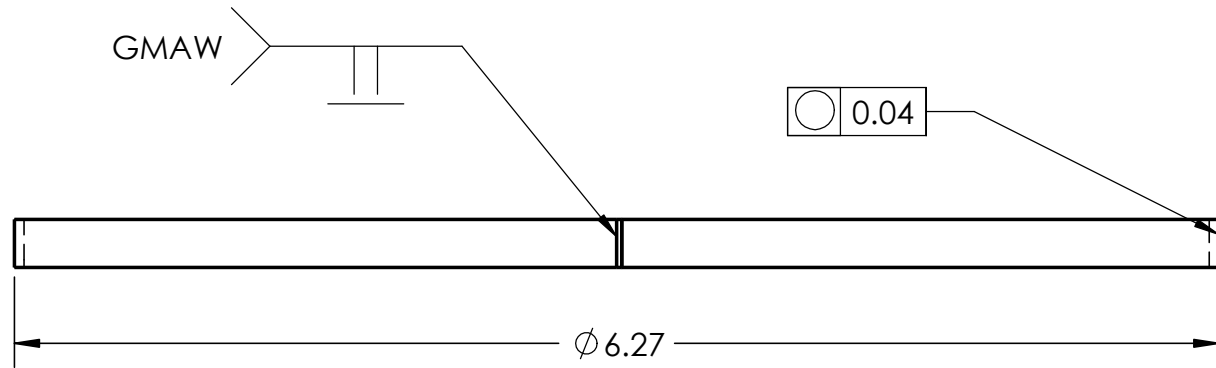
MATERIAL MATIÈRE	WEIGHT MASSE	lbs
CREATED DATE DATE DE CRÉATION	June-20-18 6:19:22 PM	
SAVED SAUVÉ/GARDÉ	August-31-18 10:04:50 AM	
FOLDER DOSSIER	C:\Users\kaatz\Documents\Thesis\Design\models\chamberv5\Parts\section4	


**RMCC
ENGINEERING
FACULTY**
**CMRC
FACULTÉ
D'INGÉNIÉRIE**

INCH / POUCE  SCALE ÉCHELLE 1:5
DECIMAL TOLERANCE UNLESS OTHERWISE SPECIFIED /
TOLÉRANCE DÉCIMALE SAUF SI SPÉCIFICATION DIFFÉRENTE
 X.X = ± 0.05
 X.XX = ± 0.005
 X.XXX = ± 0.001

TITLE TITRE		SECTION 4-2	
NAME NOM	CURTIS KAATZ	NUMBER NUMÉRO	G7456
FILE NAME NOM FICHIER	SECTION 4-2 V2	SHEET PAGE	9 OF 41 DE
			DWG # / DESSIN 1.1.2.2

PART NAME	DESCRIPTION	QTY.	MATERIAL
SECTION 4-3 V2	ROLLED 18 GAUGE SHEET	1	316L STAINLESS STAIN



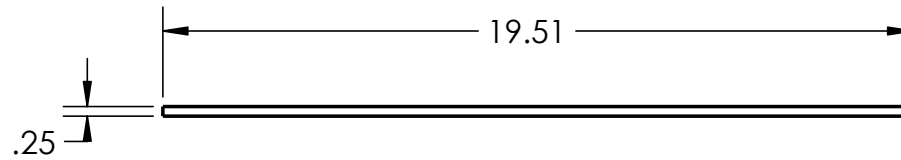
MATERIAL MATIÈRE	WEIGHT MASSE	lbs
CREATED DATE DATE DE CRÉATION	June-20-18 6:24:13 PM	
SAVED SAUVÉGARDE	August-30-18 4:05:24 PM	
FOLDER DOSSIER	C:\Users\kaatz\Documents\Thesis\Design\models\chamberv5\Parts\section4	


**RMCC
ENGINEERING
FACULTY**
**CMRC
FACULTÉ
D'INGÉNIÉRIE**

INCH / POUCE  SCALE ÉCHELLE 1:2
DECIMAL TOLERANCE UNLESS OTHERWISE SPECIFIED /
TOLÉRANCE DÉCIMALE SAUF SI SPÉCIFICATION DIFFÉRENTE
 X.X = ± 0.05
 X.XX = ± 0.005
 X.XXX = ± 0.001

TITLE TITRE		SECTION 4-3	
NAME NOM	CURTIS KAATZ	NUMBER NUMÉRO	G7456
FILE NAME NOM FICHIER	SECTION 4-3 V2	SHEET PAGE	10 OF DE 41
			DWG # / DESSIN 1.1.2.3

PART NAME	DESCRIPTION	QTY.	MATERIAL
SECTION 4-3 V2	18 GAUGE SHEET	1	316L STAINLESS STEEL



MATERIAL MATIÈRE	WEIGHT MASSE	lbs
CREATED DATE DATE DE CRÉATION	June-20-18 6:24:13 PM	
SAVED SAUVÉGARDE	August-30-18 4:05:24 PM	
FOLDER DOSSIER	C:\Users\kaatz\Documents\Thesis\Design\models\chamberv5\Parts\section4	

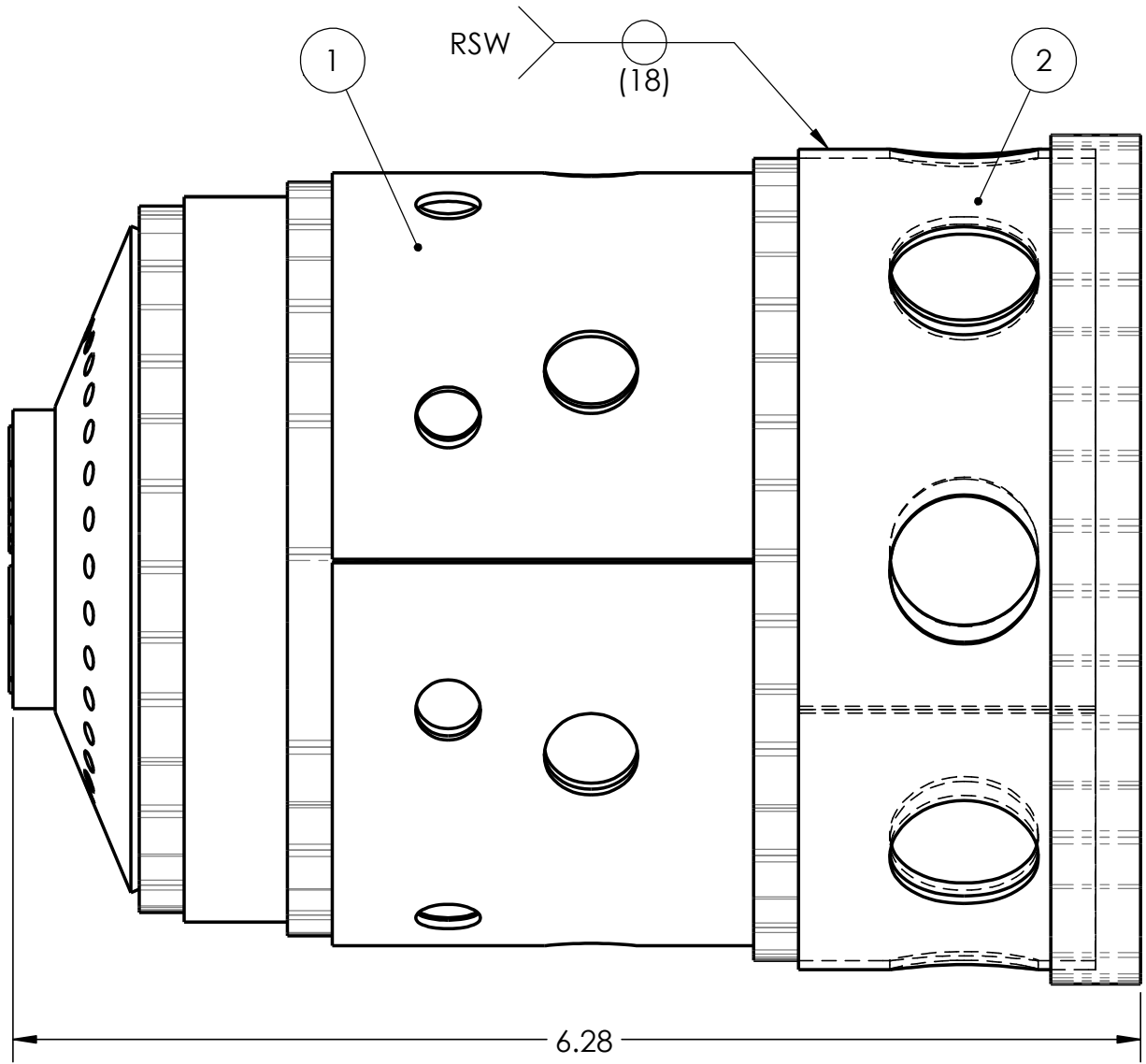


**RMCC
ENGINEERING
FACULTY**
**CMRC
FACULTÉ
D'INGÉNIÉRIE**

INCH /
POUCE  SCALE
ÉCHELLE 1:5
DECIMAL TOLERANCE UNLESS OTHERWISE SPECIFIED/
TOLÉRANCE DÉCIMALE SAUF SI SPÉCIFICATION DIFFÉRENTE
X.X = ± 0.05
X.XX = ± 0.005
X.XXX = ± 0.001

TITLE TITRE	SECTION 4-3 FLAT	
NAME NOM	CURTIS KAATZ	NUMBER NUMÉRO G7456
FILE NAME NOM FICHIER	SECTION 4-3 V2	SHEET PAGE 11 OF DE 41
		DWG # / DESSIN 1.1.2.3

ITEM NO.	DRAWING NUMBER	QTY.
1	1.2.2	1
2	1.2.1	1



MATERIAL MATIÈRE	3	WEIGHT MASSE	lbs
CREATED DATE DATE DE CRÉATION	June-21-18 2:06:20 PM		
SAVED SAUVÉGARDE	August-30-18 2:25:59 PM		
FOLDER DOSSIER	C:\Users\katz\Documents\Thesis\Design\models\chamberv5\Assemblies\		

**RMCC
ENGINEERING
FACULTY**
**CMRC
FACULTÉ
D'INGÉNIÉRIE**

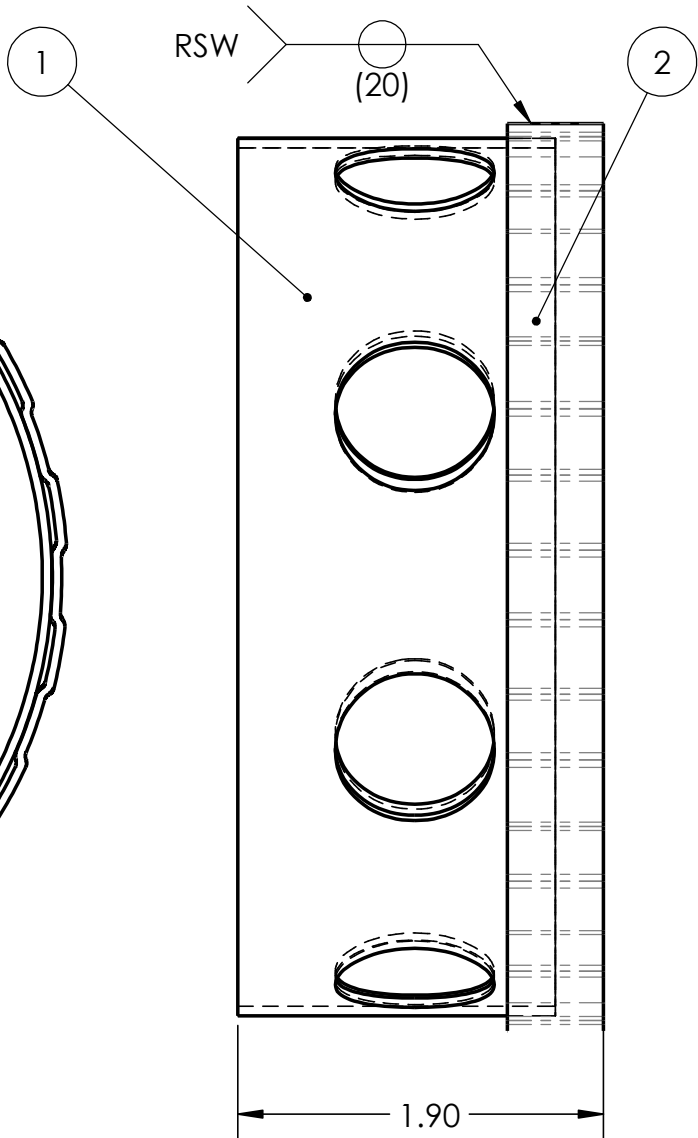
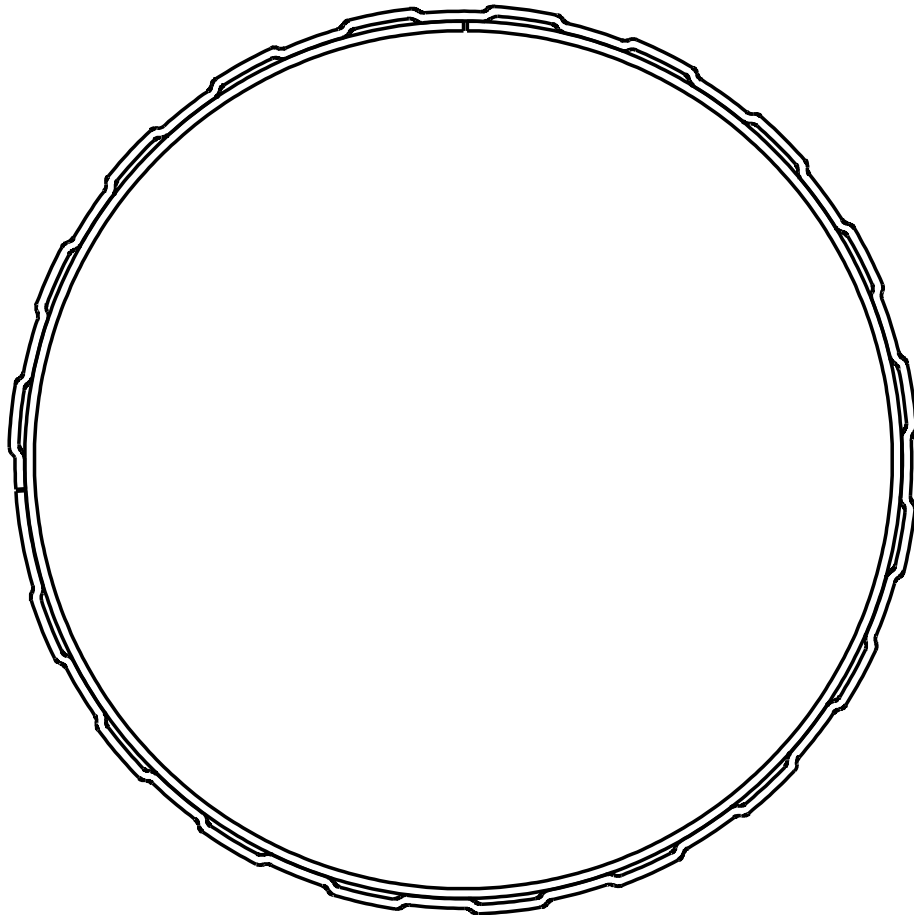
INCH / POUCE SCALE ÉCHELLE 1:1

DECIMAL TOLERANCE UNLESS OTHERWISE SPECIFIED /
TOLÉRANCE DÉCIMALE SAUF SI SPÉCIFICATION DIFFÉRENTE

X.X = ± 0.05
X.XX = ± 0.005
X.XXX = ± 0.001

TITLE TITRE	SUBASSEMBLY 3	
NAME NOM	CURTIS KAATZ	NUMBER NUMÉRO G7456
FILE NAME NOM FICHIER	SUBASSEMBLY 1	SHEET PAGE 12 OF 41 DE 41
		DWG # / DESSIN 1.2

ITEM NO.	DRAWING NUMBER	QTY.
1	1.2.1.1	1
2	1.2.1.2	1



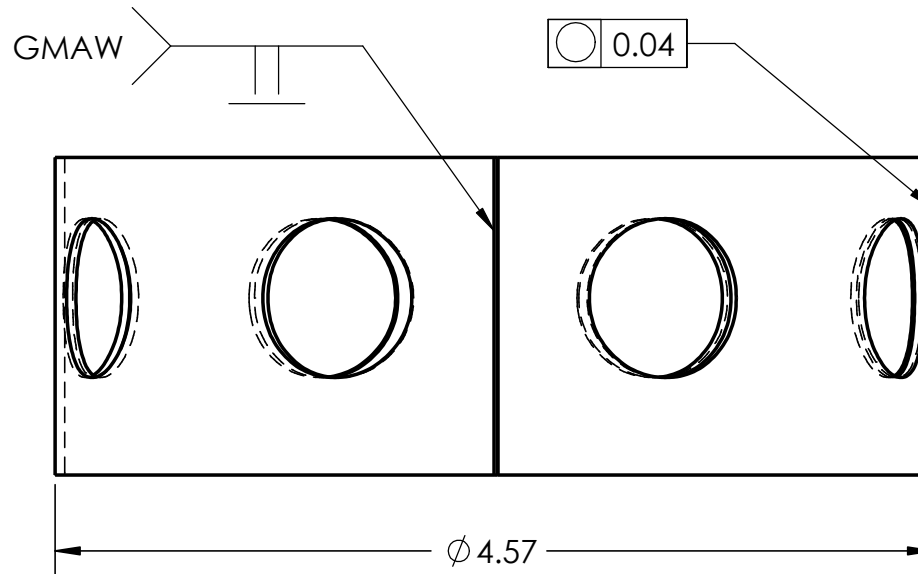
MATERIAL MATIÈRE	WEIGHT MASSE	lbs
CREATED DATE DATE DE CRÉATION	June-21-18 1:57:10 PM	
SAVED SAUVÉGARDE	August-30-18 2:25:58 PM	
FOLDER DOSSIER	C:\Users\katz\Documents\Thesis\Design\models\chamberv5\Assemblies\	


**RMCC
ENGINEERING
FACULTY**
**CMRC
FACULTÉ
D'INGÉNIÉRIE**

INCH / POUCE  SCALE ÉCHELLE 1:1
DECIMAL TOLERANCE UNLESS OTHERWISE SPECIFIED /
TOLÉRANCE DÉCIMALE SAUF SI SPÉCIFICATION DIFFÉRENTE
 X.X = ± 0.05
 X.XX = ± 0.005
 X.XXX = ± 0.001

TITLE TITRE		SECTION 3-WIGGLE 4	
NAME NOM	CURTIS KAATZ	NUMBER NUMÉRO	G7456
FILE NAME NOM FICHIER	SECTION 3-WIGGLE 4	SHEET PAGE	13 OF 41 DE 41
			DWG # / DESSIN 1.2.1

PART NAME	DESCRIPTION	QTY.	MATERIAL
SECTION 3	ROLLED 18 GAUGE SHEET	1	316L STAINLESS STEEL



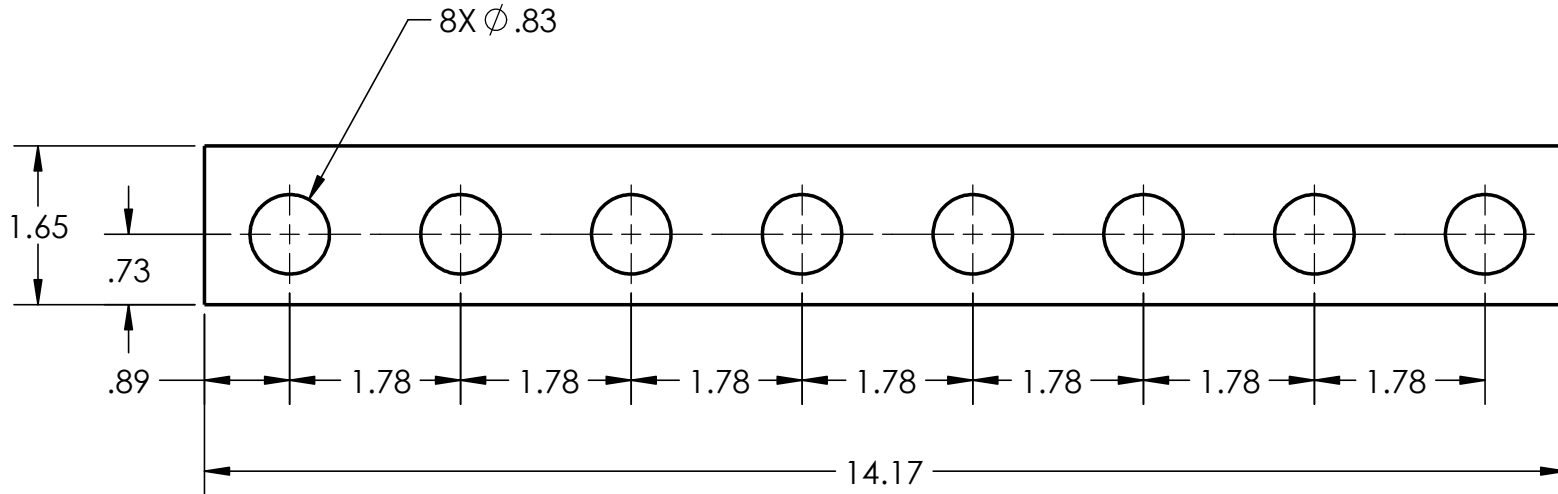
MATERIAL MATIÈRE	316L STAINLESS STEEL	WEIGHT MASSE	lbs
CREATED DATE DATE DE CRÉATION	June-05-18 3:07:21 PM		
SAVED SAUVÉGARDE	July-23-18 10:59:09 AM		
FOLDER DOSSIER	C:\Users\kaatz\Documents\Thesis\Design\models\chamberv5\Parts\		


**RMCC
ENGINEERING
FACULTY**
**CMRC
FACULTÉ
D'INGÉNIÉRIE**

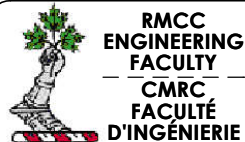
INCH / POUCE  SCALE ÉCHELLE 1:1
DECIMAL TOLERANCE UNLESS OTHERWISE SPECIFIED /
TOLÉRANCE DÉCIMALE SAUF SI SPÉCIFICATION DIFFÉRENTE
 X.X = ± 0.05
 X.XX = ± 0.005
 X.XXX = ± 0.001

TITLE TITRE	SECTION 3		DWG # / DESSIN
NAME NOM	CURTIS KAATZ	NUMBER NUMÉRO	G7456
FILE NAME NOM FICHIER	SECTION 3	SHEET PAGE	14 OF DE 41
			1.2.1.1

PART NAME	DESCRIPTION	QTY.	MATERIAL
SECTION 3	WATER JET 18 GAUGE SHEET	1	316L STAINLESS STEEL



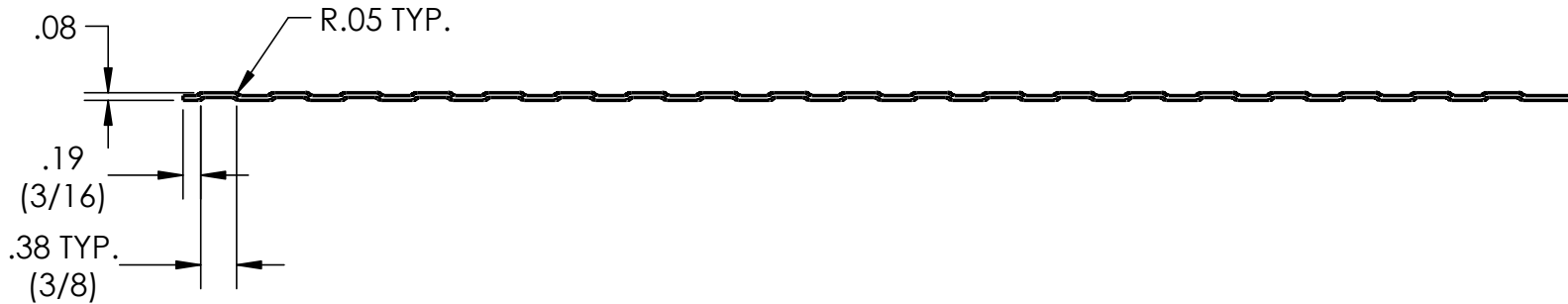
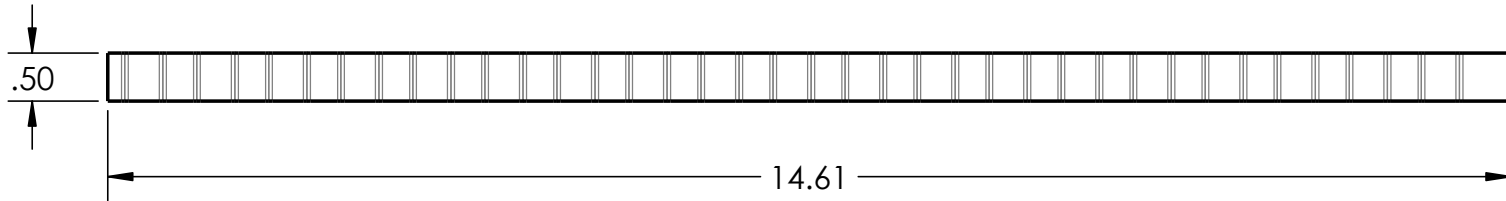
MATERIAL MATIÈRE	WEIGHT MASSE	lbs
CREATED DATE DATE DE CRÉATION	June-05-18 3:07:21 PM	
SAVED SAUVÉGARDE	July-23-18 10:59:09 AM	
FOLDER DOSSIER	C:\Users\kaatz\Documents\Thesis\Design\models\chamberv5\Parts\	



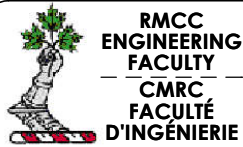
INCH / POUCE		SCALE ÉCHELLE	1:2
DECIMAL TOLERANCE UNLESS OTHERWISE SPECIFIED/ TOLÉRANCE DÉCIMALE SAUF SI SPÉCIFICATION DIFFÉRENTE			
X.X = ± 0.05			
X.XX = ± 0.005			
X.XXX = ± 0.001			

TITLE TITRE		SECTION 3 FLAT	
NAME NOM	CURTIS KAATZ	NUMBER NUMÉRO	G7456
FILE NAME NOM FICHIER	SECTION 3	SHEET PAGE	15 OF 41 DE 41
			DWG # / DESSIN 1.2.1.1

PART NAME	DESCRIPTION	QTY.	MATERIAL
WIGGLE STRIP 4	18 GAUGE SHEET	1	316L STAINLESS STEEL



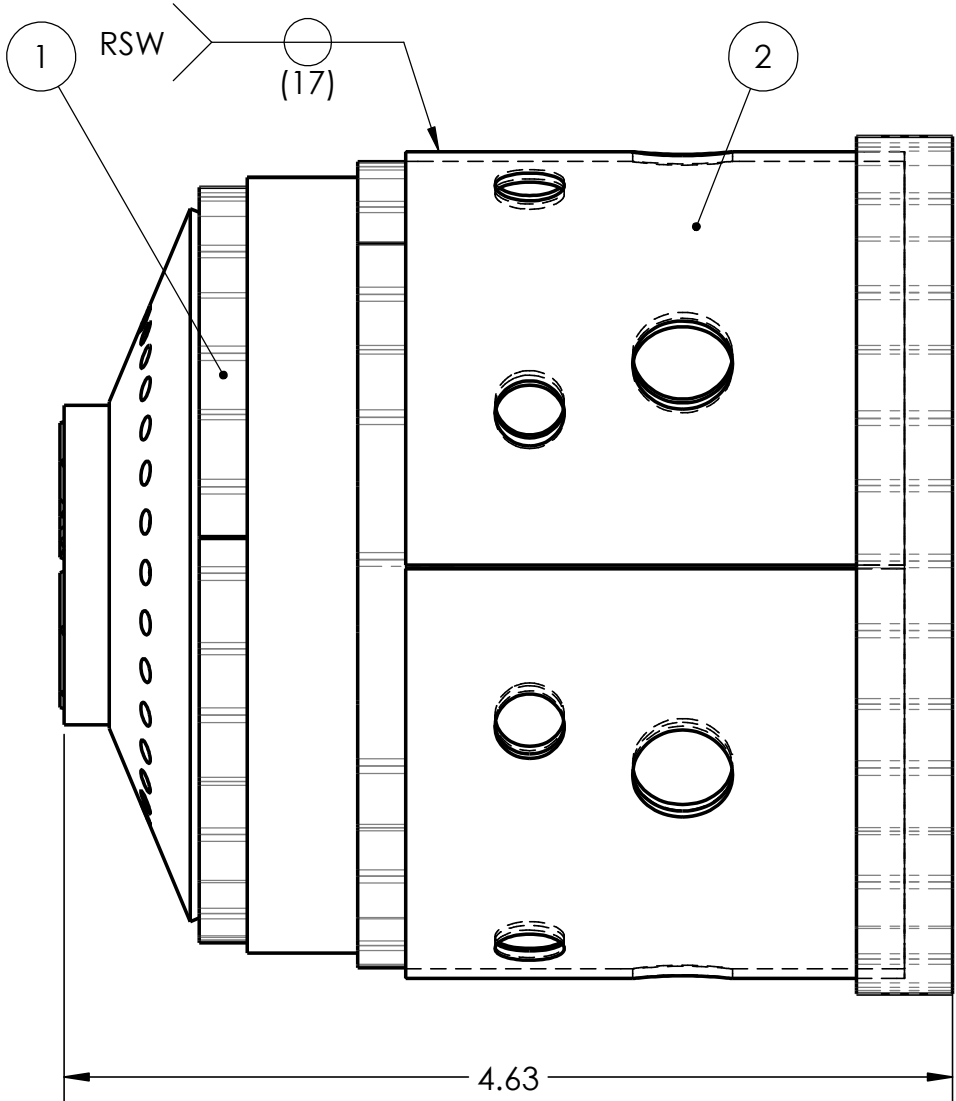
MATERIAL MATIÈRE	WEIGHT MASSE	lbs
CREATED DATE DATE DE CRÉATION	June-29-18 10:24:01 AM	
SAVED SAUVÉGARDE	July-09-18 10:55:08 AM	
FOLDER DOSSIER	C:\Users\kkaatz\Documents\Thesis\Design\models\chamberv5\Parts\wobble strips\	



INCH / POUCE	SCALE ÉCHELLE	1:2
DECIMAL TOLERANCE UNLESS OTHERWISE SPECIFIED/ TOLÉRANCE DÉCIMALE SAUF SI SPÉCIFICATION DIFFÉRENTE		
X.X = ± 0.05		
X.XX = ± 0.005		
X.XXX = ± 0.001		

TITLE TITRE		WIGGLE STRIP 4	
NAME NOM	CURTIS KAATZ	NUMBER NUMÉRO	G7456
FILE NAME NOM FICHIER	W4 straight	SHEET PAGE	16 OF 41 DE
			DWG # / DESSIN# 1.2.1.2

ITEM NO.	DRAWING NUMBER	QTY.
1	1.2.2.2	1
2	1.2.2.1	1



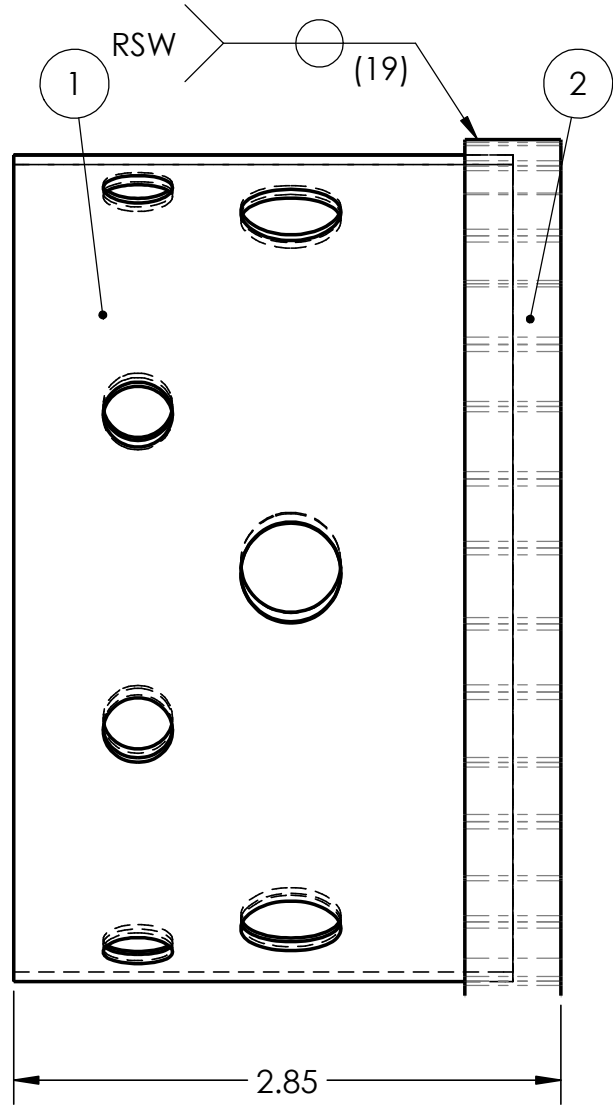
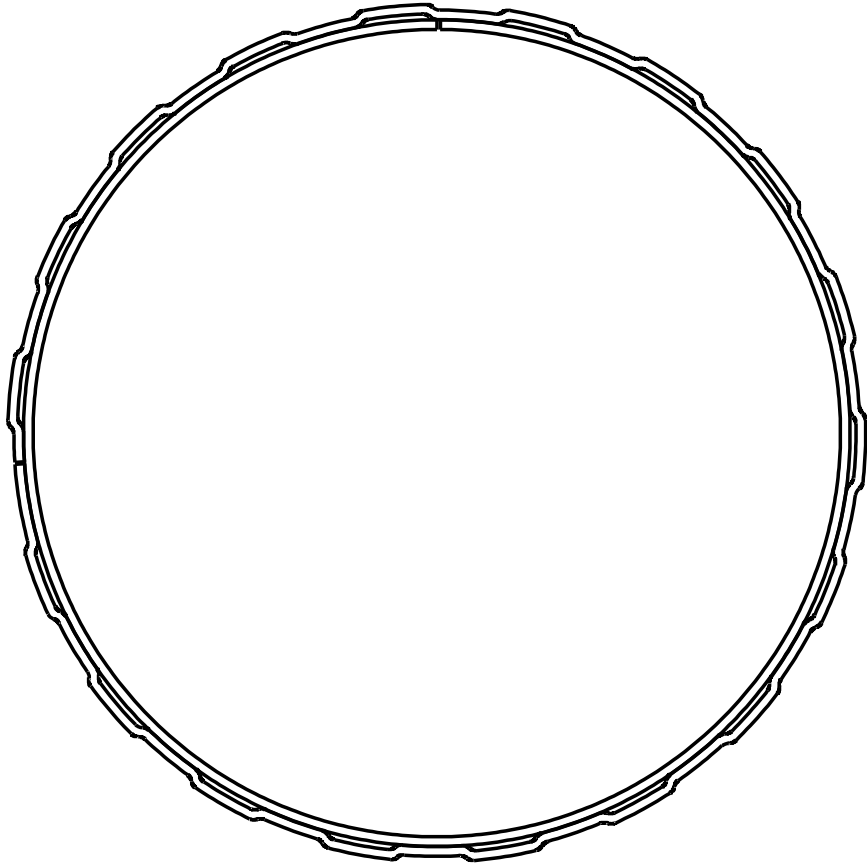
MATERIAL MATIÈRE	WEIGHT MASSE	lbs
CREATED DATE DATE DE CRÉATION	June-21-18 2:04:53 PM	
SAVED SAUVÉGARDE	July-24-18 1:42:06 PM	
FOLDER DOSSIER	C:\Users\katz\Documents\Thesis\Design\models\chamberv5\Assemblies\	


RMCC ENGINEERING FACULTY
CMRC FACULTÉ D'INGÉNIERIE

INCH / POUCE  SCALE ÉCHELLE 1:1
DECIMAL TOLERANCE UNLESS OTHERWISE SPECIFIED / TOLÉRANCE DÉCIMALE SAUF SI SPÉCIFICATION DIFFÉRENTE
 X.X = ± 0.05
 X.XX = ± 0.005
 X.XXX = ± 0.001

TITLE TITRE		SUBASSEMBLY 2	
NAME NOM	CURTIS KAATZ	NUMBER NUMÉRO	G7456
FILE NAME NOM FICHIER	SUBASSEMBLY 2	SHEET PAGE	17 OF 41 DE
			DWG # / DESSIN 1.2.2

ITEM NO.	DRAWING NUMBER	QTY.
1	1.2.2.1.1	1
2	1.2.2.1.2	1



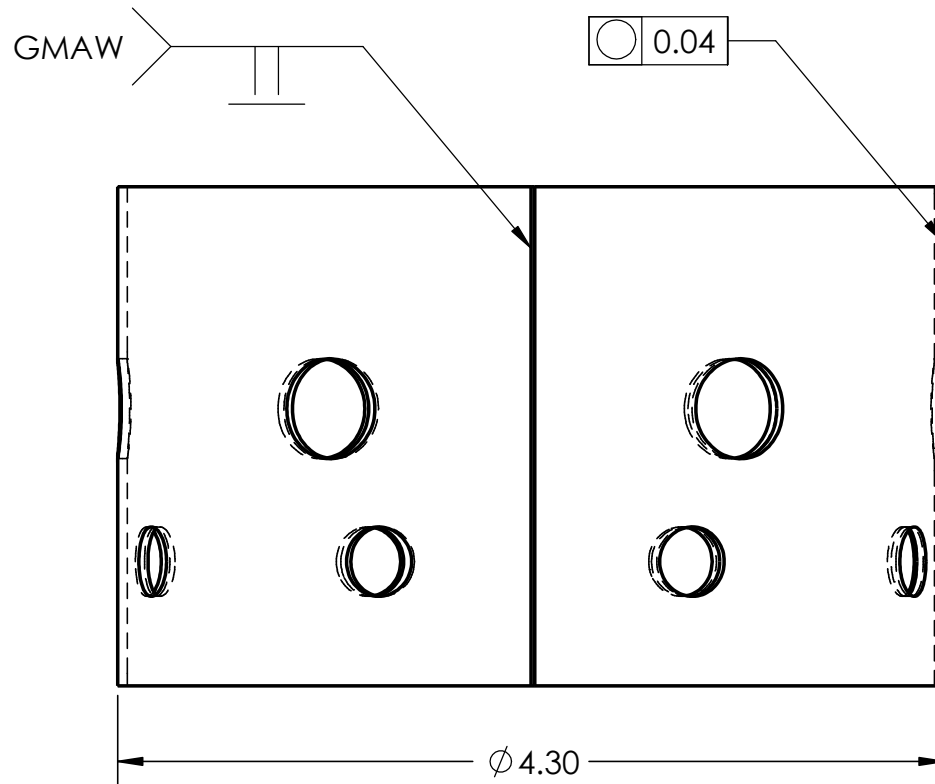
MATERIAL MATIÈRE	WEIGHT MASSE	lbs
CREATED DATE DATE DE CRÉATION	June-21-18 1:56:05 PM	
SAVED SAUVÉGARDE	July-24-18 1:42:01 PM	
FOLDER DOSSIER	C:\Users\katz\Documents\Thesis\Design\models\chamberv5\Assemblies\	


**RMCC
ENGINEERING
FACULTY**
**CMRC
FACULTÉ
D'INGÉNIÉRIE**

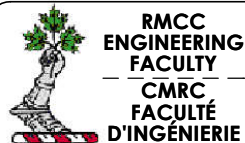
INCH / POUCE  SCALE ÉCHELLE 1:1
DECIMAL TOLERANCE UNLESS OTHERWISE SPECIFIED /
TOLÉRANCE DÉCIMALE SAUF SI SPÉCIFICATION DIFFÉRENTE
 X.X = ± 0.05
 X.XX = ± 0.005
 X.XXX = ± 0.001

TITLE TITRE		SECTION 2-WIGGLE 3	
NAME NOM	CURTIS KAATZ	NUMBER NUMÉRO	G7456
FILE NAME NOM FICHIER	SECTION 2-WIGGLE 3	SHEET PAGE	18 OF 41 DE
			DWG # / DESSIN 1.2.2.1

PART NAME	DESCRIPTION	QTY.	MATERIAL
SECTION 2	ROLLED 18 GAUGE SHEET	1	316L STAINLESS STEEL



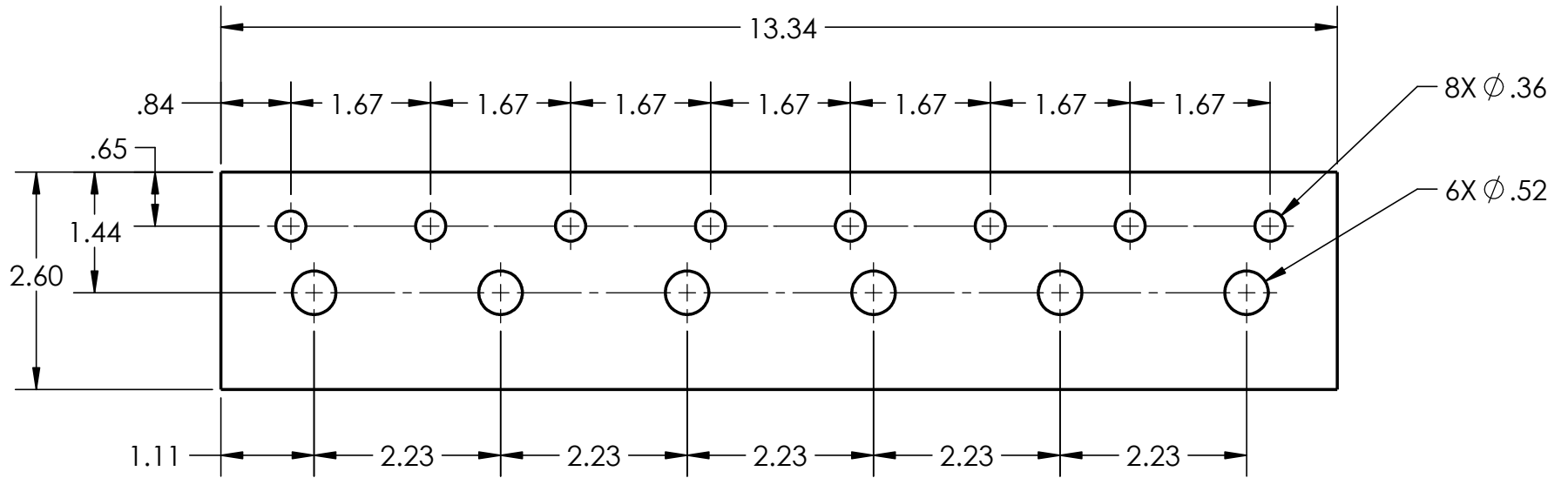
MATERIAL MATIÈRE	WEIGHT MASSE	lbs
CREATED DATE DATE DE CRÉATION	June-20-18 3:13:46 PM	
SAVED SAUVÉGARDE	July-23-18 10:59:09 AM	
FOLDER DOSSIER	C:\Users\kaatz\Documents\Thesis\Design\models\chamberv5\Parts\	



INCH / POUCE	SCALE ÉCHELLE	1:1
DECIMAL TOLERANCE UNLESS OTHERWISE SPECIFIED/ TOLÉRANCE DÉCIMALE SAUF SI SPÉCIFICATION DIFFÉRENTE		
X.X = ± 0.05		
X.XX = ± 0.005		
X.XXX = ± 0.001		

TITLE TITRE		SECTION 2	
NAME NOM	CURTIS KAATZ	NUMBER NUMÉRO	G7456
FILE NAME NOM FICHIER	SECTION 2	SHEET PAGE	19 OF DE 41
			DWG # / DESSIN# 1.2.2.1.1

PART NAME	DESCRIPTION	QTY.	MATERIAL
SECTION 2	WATER JET 18 GAUGE SHEET	1	316L STAINLESS STEEL



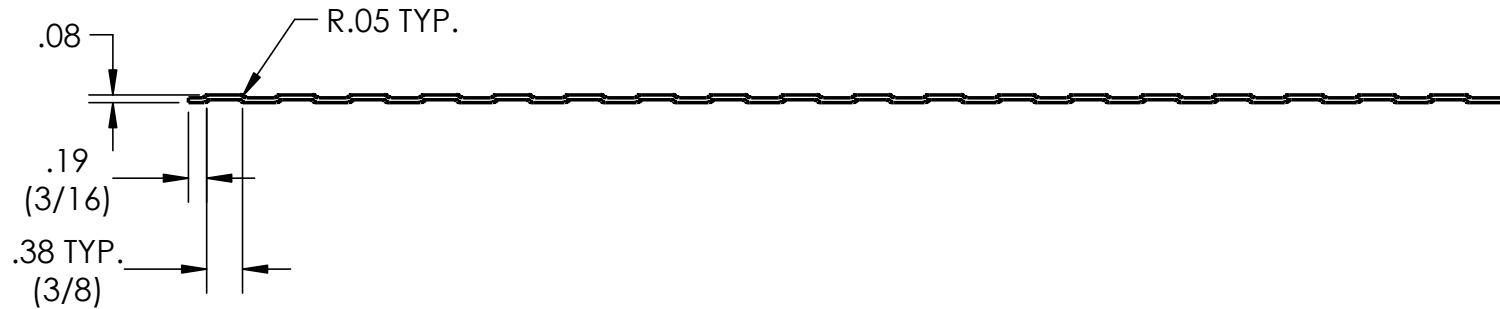
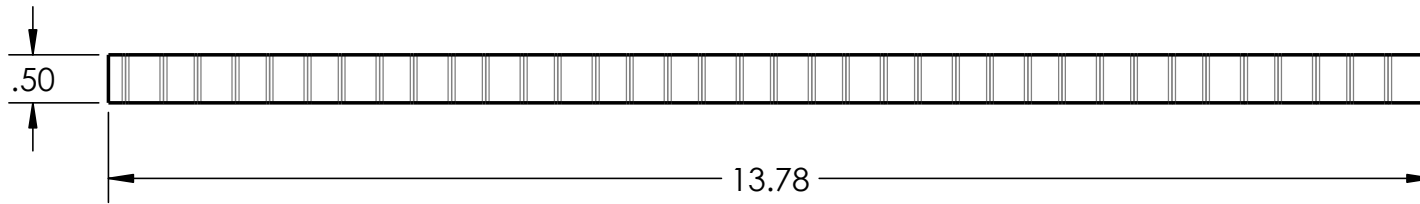
MATERIAL MATIÈRE	WEIGHT MASSE	lbs
CREATED DATE DATE DE CRÉATION	June-20-18 3:13:46 PM	
SAVED SAUVÉGARDE	July-23-18 10:59:09 AM	
FOLDER DOSSIER	C:\Users\kaatz\Documents\Thesis\Design\models\chamberv5\Parts\	


**RMCC
ENGINEERING
FACULTY**
**CMRC
FACULTÉ
D'INGÉNIÉRIE**

INCH / POUCE  SCALE ÉCHELLE 1:2
DECIMAL TOLERANCE UNLESS OTHERWISE SPECIFIED /
TOLÉRANCE DÉCIMALE SAUF SI SPÉCIFICATION DIFFÉRENTE
 X.X = \pm 0.05
 X.XX = \pm 0.005
 X.XXX = \pm 0.001

TITLE TITRE		SECTION 2 FLAT	
NAME NOM	CURTIS KAATZ	NUMBER NUMÉRO	G7456
FILE NAME NOM FICHIER	SECTION 2	SHEET PAGE	20 OF 41 DE
			DWG # / DESSIN# 1.2.2.1.1

PART NAME	DESCRIPTION	QTY.	MATERIAL
WIGGLE STRIP 3	18 GAUGE SHEET	1	316L STAINLESS STEEL



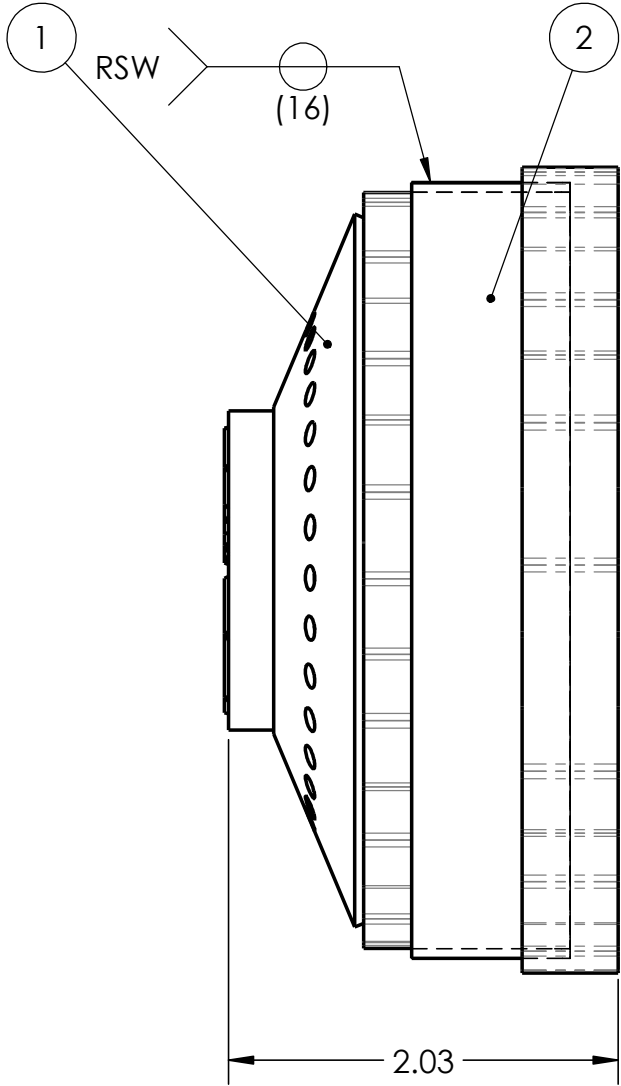
MATERIAL MATIÈRE	WEIGHT MASSE	lbs
CREATED DATE DATE DE CRÉATION	June-29-18 10:24:01 AM	
SAVED SAUVÉGARDE	July-09-18 10:56:04 AM	
FOLDER DOSSIER	C:\Users\kaatz\Documents\Thesis\Design\models\chamberv5\Parts\wobble strips\	


**RMCC
ENGINEERING
FACULTY**
**CMRC
FACULTÉ
D'INGÉNIÉRIE**

INCH / POUCE  SCALE ÉCHELLE 1:2
DECIMAL TOLERANCE UNLESS OTHERWISE SPECIFIED /
TOLÉRANCE DÉCIMALE SAUF SI SPÉCIFICATION DIFFÉRENTE
 X.X = ± 0.05
 X.XX = ± 0.005
 X.XXX = ± 0.001

TITLE TITRE		WIGGLE STRIP 3	
NAME NOM	CURTIS KAATZ	NUMBER NUMÉRO	G7456
FILE NAME NOM FICHIER	W3 straight	SHEET PAGE	21 OF DE 41
			DWG # / DESSIN# 1.2.2.1.2

ITEM NO.	DRAWING NUMBER	QTY.
1	1.2.2.2	1
2	1.2.2.1	1



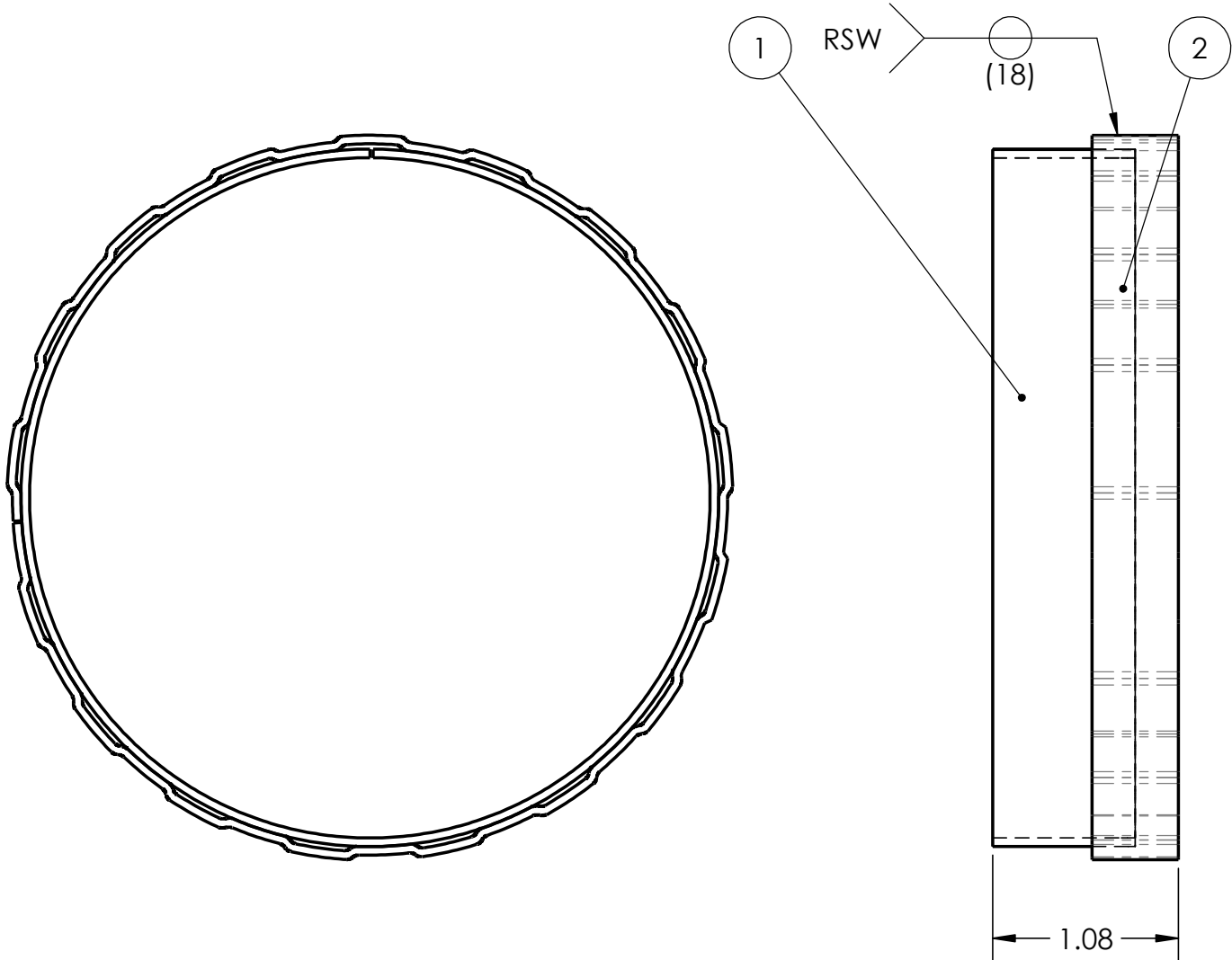
MATERIAL MATIÈRE	WEIGHT MASSE	lbs
CREATED DATE DATE DE CRÉATION	June-21-18 2:03:37 PM	
SAVED SAUVÉGARDE	July-12-18 2:06:24 PM	
FOLDER DOSSIER	C:\Users\katz\Documents\Thesis\Design\models\chamberv5\Assemblies\	


RMCC ENGINEERING FACULTY
CMRC FACULTÉ D'INGÉNIÉRIE

INCH / POUCE  SCALE ÉCHELLE 1:1
DECIMAL TOLERANCE UNLESS OTHERWISE SPECIFIED /
 TOLÉRANCE DÉCIMALE SAUF SI SPÉCIFICATION DIFFÉRENTE
 X.X = ± 0.05
 X.XX = ± 0.005
 X.XXX = ± 0.001

TITLE TITRE		SUBASSEMBLY 2	
NAME NOM	CURTIS KAATZ	NUMBER NUMÉRO	G7456
FILE NAME NOM FICHIER	SUBASSEMBLY 3	SHEET PAGE	22 OF 41 DE
			<small>DWG # / DESSIN</small> 1.2.2.2

ITEM NO.	DRAWING NUMBER	QTY.
1	1.2.2.2.1.1	1
2	1.2.2.2.1.2	1



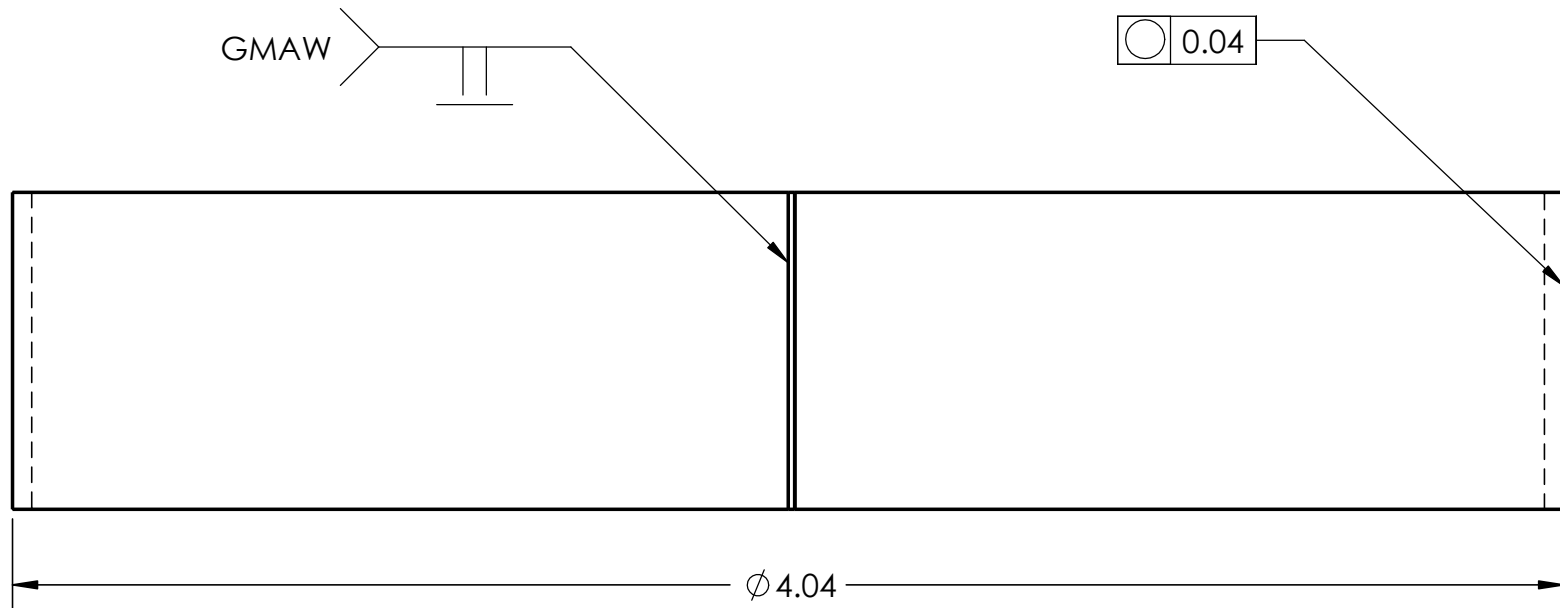
MATERIAL MATIÈRE	WEIGHT MASSE	lbs
CREATED DATE DATE DE CRÉATION	June-21-18 1:47:04 PM	
SAVED SAUVÉGARDE	July-24-18 1:42:02 PM	
FOLDER DOSSIER	C:\Users\katz\Documents\Thesis\Design\models\chamberv5\Assemblies\	


**RMCC
ENGINEERING
FACULTY**
**CMRC
FACULTÉ
D'INGÉNIÉRIE**

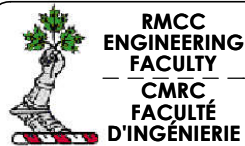
INCH / POUCE  SCALE ÉCHELLE 1:1
DECIMAL TOLERANCE UNLESS OTHERWISE SPECIFIED /
TOLÉRANCE DÉCIMALE SAUF SI SPÉCIFICATION DIFFÉRENTE
 X.X = ± 0.05
 X.XX = ± 0.005
 X.XXX = ± 0.001

TITLE TITRE		SECTION 1-WIGGLE 2	
NAME NOM	CURTIS KAATZ	NUMBER NUMÉRO	G7456
FILE NAME NOM FICHIER	SECTION 1-WIGGLE 2	SHEET PAGE	23 OF 41 DE
			DWG # / DESSIN 1.2.2.2.1

PART NAME	DESCRIPTION	QTY.	MATERIAL
SECTION 1	ROLLED 18 GAUGE SHEET	1	316L STAINLESS STEEL



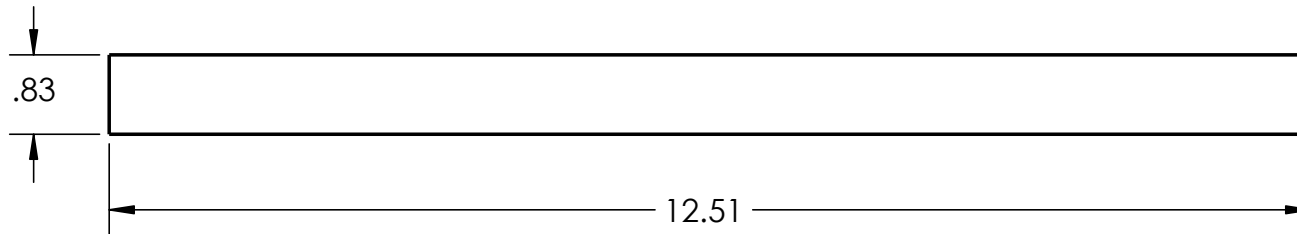
MATERIAL MATIÈRE	WEIGHT MASSE	lbs
CREATED DATE DATE DE CRÉATION	June-20-18 3:08:22 PM	
SAVED SAUVÉGARDE	July-10-18 5:00:55 PM	
FOLDER DOSSIER	C:\Users\kaatz\Documents\Thesis\Design\models\chamberv5\Parts\	



INCH / POUCE		SCALE ÉCHELLE	2:1
DECIMAL TOLERANCE UNLESS OTHERWISE SPECIFIED/ TOLÉRANCE DÉCIMALE SAUF SI SPÉCIFICATION DIFFÉRENTE			
X.X = ± 0.05			
X.XX = ± 0.005			
X.XXX = ± 0.001			

TITLE TITRE	SECTION 1		DWG # / DESSIN
NAME NOM	CURTIS KAATZ	NUMBER NUMÉRO	G7456
FILE NAME NOM FICHIER	SECTION 1	SHEET PAGE	24 OF DE 41
			1.2.2.2.1.1

PART NAME	DESCRIPTION	QTY.	MATERIAL
SECTION 1	18 GAUGE SHEET	1	316L STAINLESS STEEL



MATERIAL MATIÈRE	WEIGHT MASSE	lbs
CREATED DATE DATE DE CRÉATION	June-20-18 3:08:22 PM	
SAVED SAUVÉGARDE	July-10-18 5:00:55 PM	
FOLDER DOSSIER	C:\Users\kaatz\Documents\Thesis\Design\models\chamberv5\Parts\	

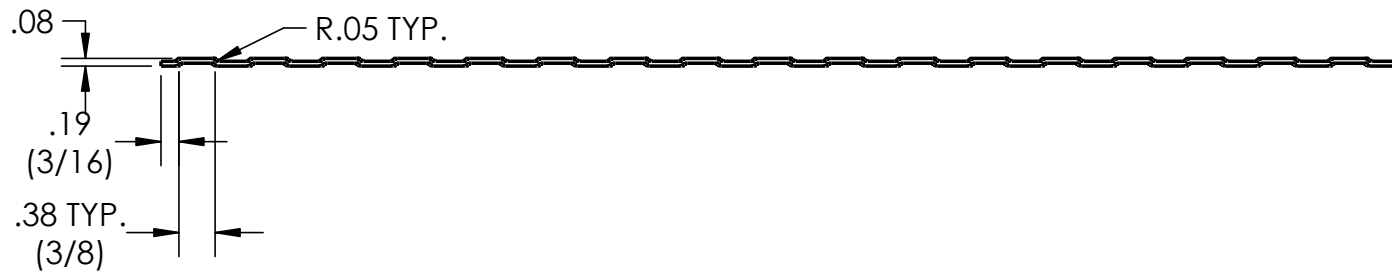
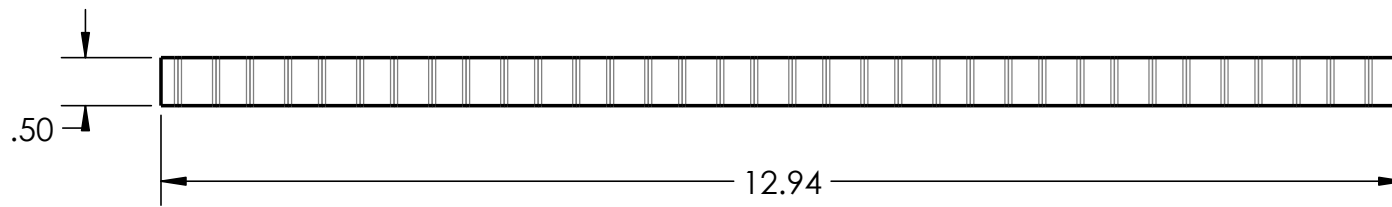


**RMCC
ENGINEERING
FACULTY**
**CMRC
FACULTÉ
D'INGÉNIÉRIE**

INCH /
POUCE  SCALE
ÉCHELLE 1:2
DECIMAL TOLERANCE UNLESS OTHERWISE SPECIFIED/
TOLÉRANCE DÉCIMALE SAUF SI SPÉCIFICATION DIFFÉRENTE
X.X = ± 0.05
X.XX = ± 0.005
X.XXX = ± 0.001

TITLE TITRE		SECTION 1 FLAT	
NAME NOM	CURTIS KAATZ	NUMBER NUMÉRO	G7456
FILE NAME NOM FICHIER	SECTION 1	SHEET PAGE	25 OF DE 41
			DWG # / DESSIN 1.2.2.2.1.1

PART NAME	DESCRIPTION	QTY.	MATERIAL
WIGGLE STRIP 2	18 GAUGE SHEET	1	316L STAINLESS STEEL



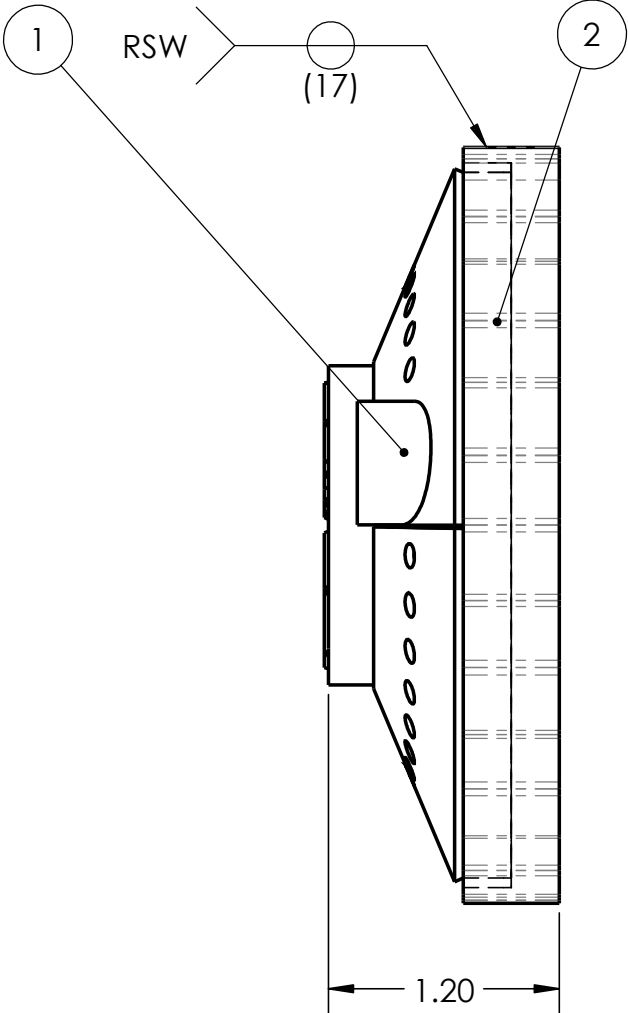
MATERIAL MATIÈRE	WEIGHT MASSE	lbs
CREATED DATE DATE DE CRÉATION	June-29-18 10:24:01 AM	
SAVED SAUVÉGARDE	July-09-18 10:57:07 AM	
FOLDER DOSSIER	C:\Users\kaatz\Documents\Thesis\Design\models\chamberv5\Parts\wobble strips\	


**RMCC
ENGINEERING
FACULTY**
**CMRC
FACULTÉ
D'INGÉNIÉRIE**

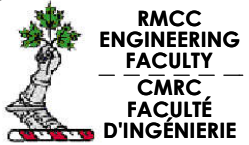
INCH / POUCE  SCALE ÉCHELLE 1:2
DECIMAL TOLERANCE UNLESS OTHERWISE SPECIFIED /
TOLÉRANCE DÉCIMALE SAUF SI SPÉCIFICATION DIFFÉRENTE
 X.X = ± 0.05
 X.XX = ± 0.005
 X.XXX = ± 0.001

TITLE TITRE		WIGGLE STRIP 2	
NAME NOM	CURTIS KAATZ	NUMBER NUMÉRO	G7456
FILE NAME NOM FICHIER	W2 straight	SHEET PAGE	26 OF 41 DE
			DWG # / DESSIN 1.2.2.2.1.2

ITEM NO.	DRAWING NUMBER	QTY.
1	1.2.2.2.2	1
2	1.2.2.2.1	1



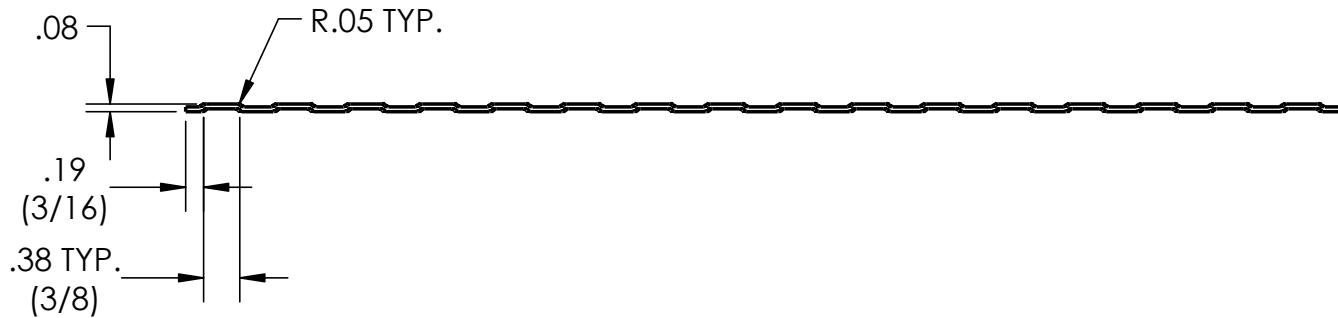
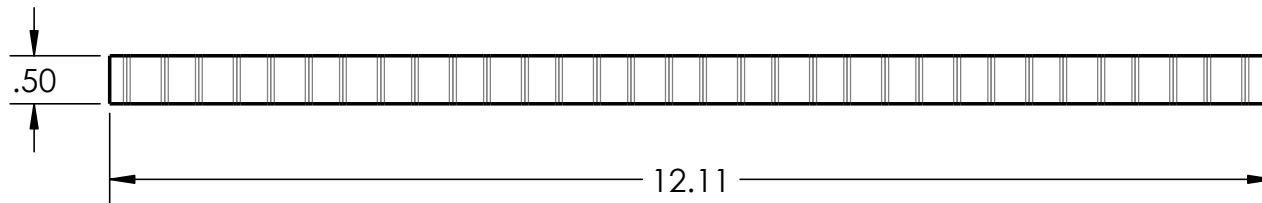
MATERIAL MATIÈRE	WEIGHT MASSE	lbs
CREATED DATE DATE DE CRÉATION	June-21-18 1:45:34 PM	
SAVED SAUVÉGARDE	July-24-18 1:42:05 PM	
FOLDER DOSSIER	C:\Users\katz\Documents\Thesis\Design\models\chamberv5\Assemblies\	



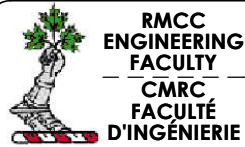
INCH / POUCE SCALE ÉCHELLE 1:1
DECIMAL TOLERANCE UNLESS OTHERWISE SPECIFIED /
 TOLÉRANCE DÉCIMALE SAUF SI SPÉCIFICATION DIFFÉRENTE
 X.X = ± 0.05
 X.XX = ± 0.005
 X.XXX = ± 0.001

TITLE TITRE		SUBASSEMBLY 1	
NAME NOM	CURTIS KAATZ	NUMBER NUMÉRO	G7456
FILE NAME NOM FICHIER	SUBASSEMBLY 4	SHEET PAGE	27 OF 41 DE 41
			DWG # / DESSIN 1.2.2.2.2

PART NAME	DESCRIPTION	QTY.	MATERIAL
WIGGLE STRIP 1	18 GAUGE SHEET	1	316L STAINLESS STEEL



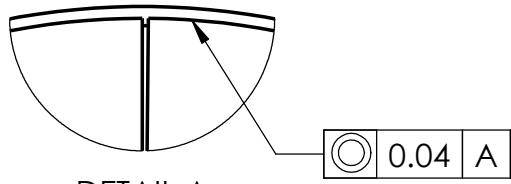
MATERIAL MATIÈRE	WEIGHT MASSE	lbs
CREATED DATE DATE DE CRÉATION	June-29-18 10:24:01 AM	
SAVED SAUVÉGARDE	July-09-18 10:57:38 AM	
FOLDER DOSSIER	C:\Users\kaatz\Documents\Thesis\Design\models\chamberv5\Parts\wobble strips\	



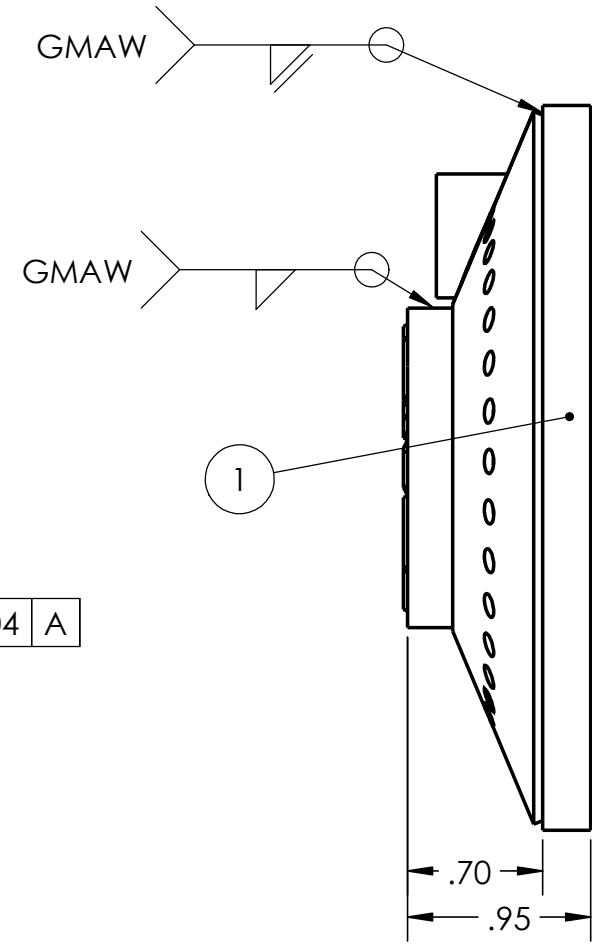
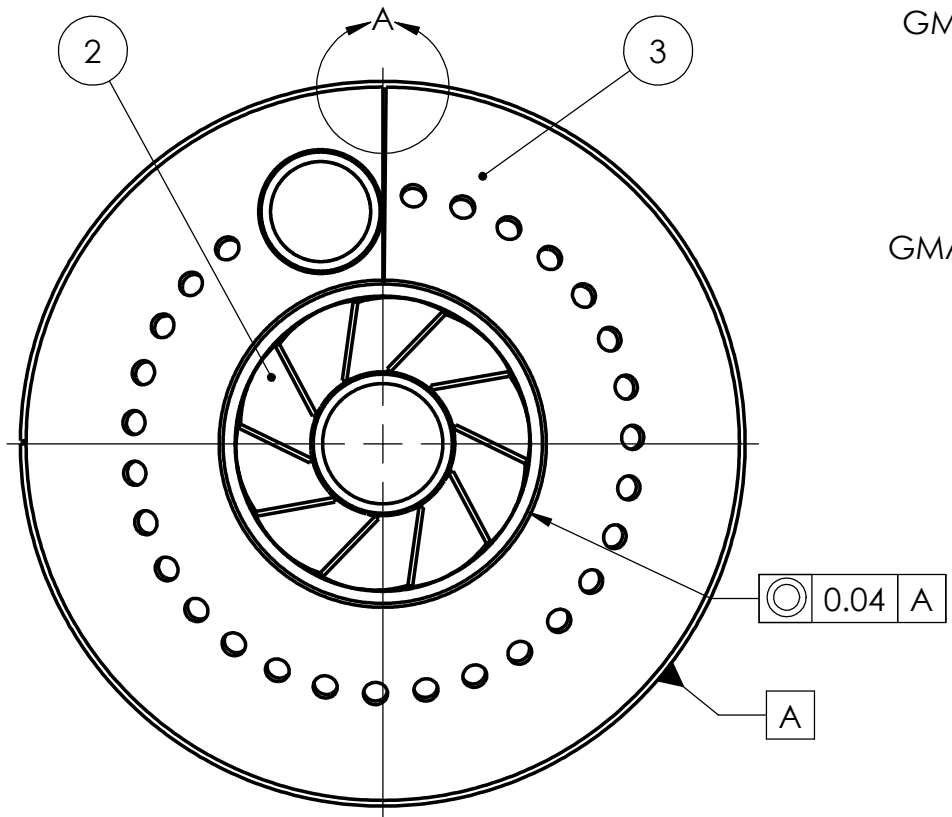
INCH / POUCE		SCALE ÉCHELLE	1:2
DECIMAL TOLERANCE UNLESS OTHERWISE SPECIFIED/ TOLÉRANCE DÉCIMALE SAUF SI SPÉCIFICATION DIFFÉRENTE			
X.X = ± 0.05			
X.XX = ± 0.005			
X.XXX = ± 0.001			

TITLE TITRE	WIGGLE STRIP 1		DWG # / DESSIN
NAME NOM	CURTIS KAATZ	NUMBER NUMÉRO	G7456
FILE NAME NOM FICHIER	W1 straight	SHEET PAGE	28 OF DE 41
			1.2.2.2.1

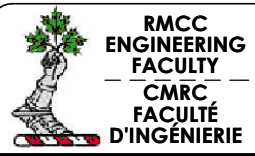
ITEM NO.	DRAWING NUMBER	QTY.
1	1.2.2.2.2.1	1
2	1.2.2.2.2.3	1
3	1.2.2.2.2.2	1



DETAIL A
SCALE 2:1



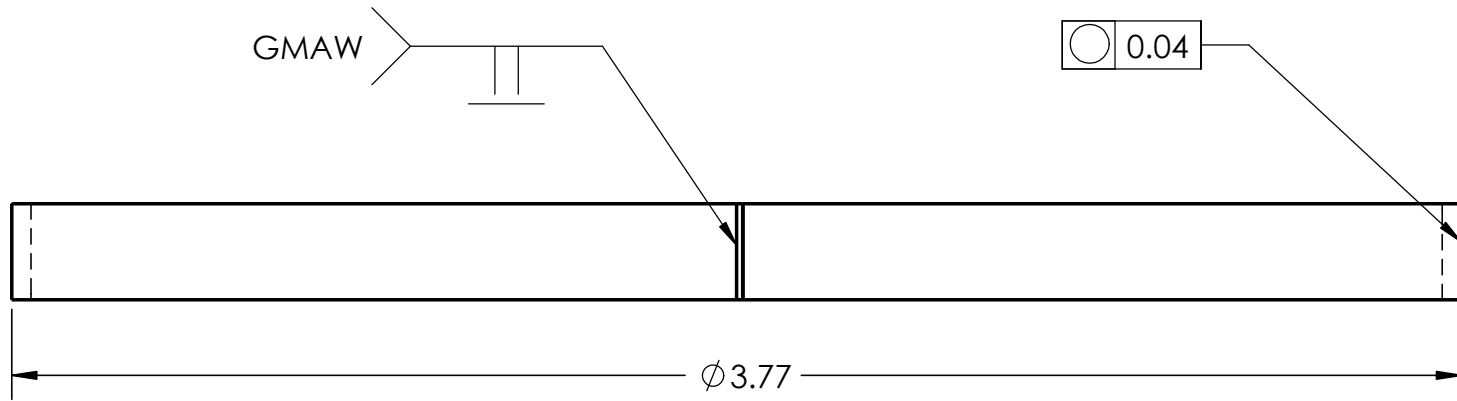
MATERIAL MATIÈRE	316L STAINLESS STEEL	WEIGHT MASSE	lbs
CREATED DATE DATE DE CRÉATION	June-08-18 10:43:04 AM		
SAVED SAUVÉGARDE	July-24-18 1:42:05 PM		
FOLDER DOSSIER	C:\Users\katz\Documents\Thesis\Design\models\chamberv5\Assemblies\		



INCH / POUCE		SCALE ÉCHELLE	1:1
DECIMAL TOLERANCE UNLESS OTHERWISE SPECIFIED/ TOLÉRANCE DÉCIMALE SAUF SI SPÉCIFICATION DIFFÉRENTE			
X.X = ± 0.05			
X.XX = ± 0.005			
X.XXX = ± 0.001			

TITLE TITRE		INLET ASSEMBLY	
NAME NOM	CURTIS KAATZ	NUMBER NUMÉRO	G7456
FILE NAME NOM FICHIER	SWIRLER-DOME ASSEMBLY	SHEET PAGE	29 OF 41 DE 41
			DWG # / DESSIN 1.2.2.2.2

PART NAME	DESCRIPTION	QTY.	MATERIAL
DOME SLEEVE	ROLLED 18 GAUGE SHEET	1	316L STAINLESS STEEL



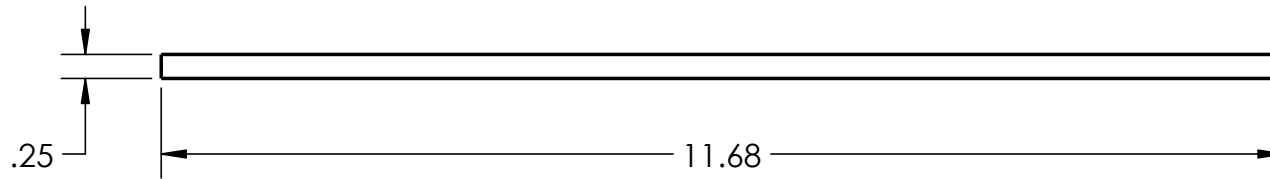
MATERIAL MATIÈRE	316L STAINLESS STEEL	WEIGHT MASSE	lbs
CREATED DATE DATE DE CRÉATION	June-07-18 3:21:30 PM		
SAVED SAUVÉGARDE	July-09-18 10:46:06 AM		
FOLDER DOSSIER	C:\Users\kaatz\Documents\Thesis\Design\models\chamberv5\Parts\swirler_folder\		


**RMCC
ENGINEERING
FACULTY**
**CMRC
FACULTÉ
D'INGÉNIÉRIE**

INCH / POUCE  SCALE ÉCHELLE 2:1
DECIMAL TOLERANCE UNLESS OTHERWISE SPECIFIED /
TOLÉRANCE DÉCIMALE SAUF SI SPÉCIFICATION DIFFÉRENTE
 X.X = ± 0.05
 X.XX = ± 0.005
 X.XXX = ± 0.001

TITLE TITRE	DOME SLEEVE	
NAME NOM	CURTIS KAATZ	NUMBER NUMÉRO G7456
FILE NAME NOM FICHIER	DOME SLEEVE	SHEET PAGE 30 OF DE 41
		DWG # / DESSIN# 1.2.2.2.2.1

PART NAME	DESCRIPTION	QTY.	MATERIAL
DOME SLEEVE	18 GAUGE SHEET	1	316L STAINLESS STEEL



MATERIAL MATIÈRE	WEIGHT MASSE	lbs
CREATED DATE DATE DE CRÉATION	June-07-18 3:21:30 PM	
SAVED SAUVÉGARDE	July-09-18 10:46:06 AM	
FOLDER DOSSIER	C:\Users\kaatz\Documents\Thesis\Design\models\chamberv5\Parts\swirler_f older\	

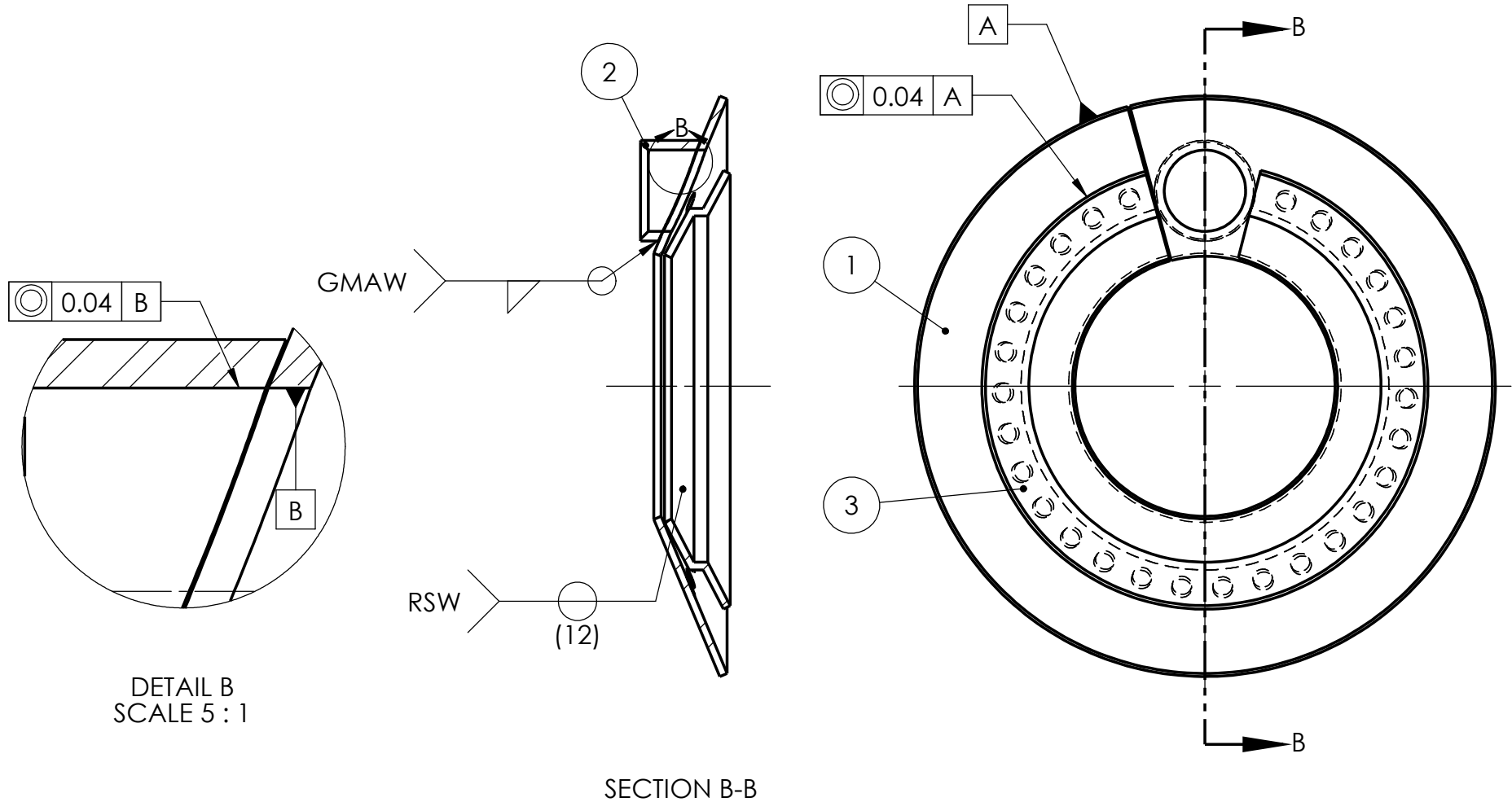


**RMCC
ENGINEERING
FACULTY**
**CMRC
FACULTÉ
D'INGÉNIÉRIE**

INCH /
POUCE  SCALE
ÉCHELLE 1:2
DECIMAL TOLERANCE UNLESS OTHERWISE SPECIFIED/
TOLÉRANCE DÉCIMALE SAUF SI SPÉCIFICATION DIFFÉRENTE
X.X = ± 0.05
X.XX = ± 0.005
X.XXX = ± 0.001

TITLE TITRE	DOME SLEEVE FLAT	
NAME NOM	CURTIS KAATZ	NUMBER NUMÉRO G7456
FILE NAME NOM FICHIER	DOME SLEEVE	SHEET PAGE 31 OF DE 41
		DWG # / DESSIN# 1.2.2.2.2.1

ITEM NO.	DRAWING NUMBER	QTY.
1	1.2.2.2.2.2.1	1
2	1.2.2.2.2.2.3	1
3	1.2.2.2.2.2.2	1



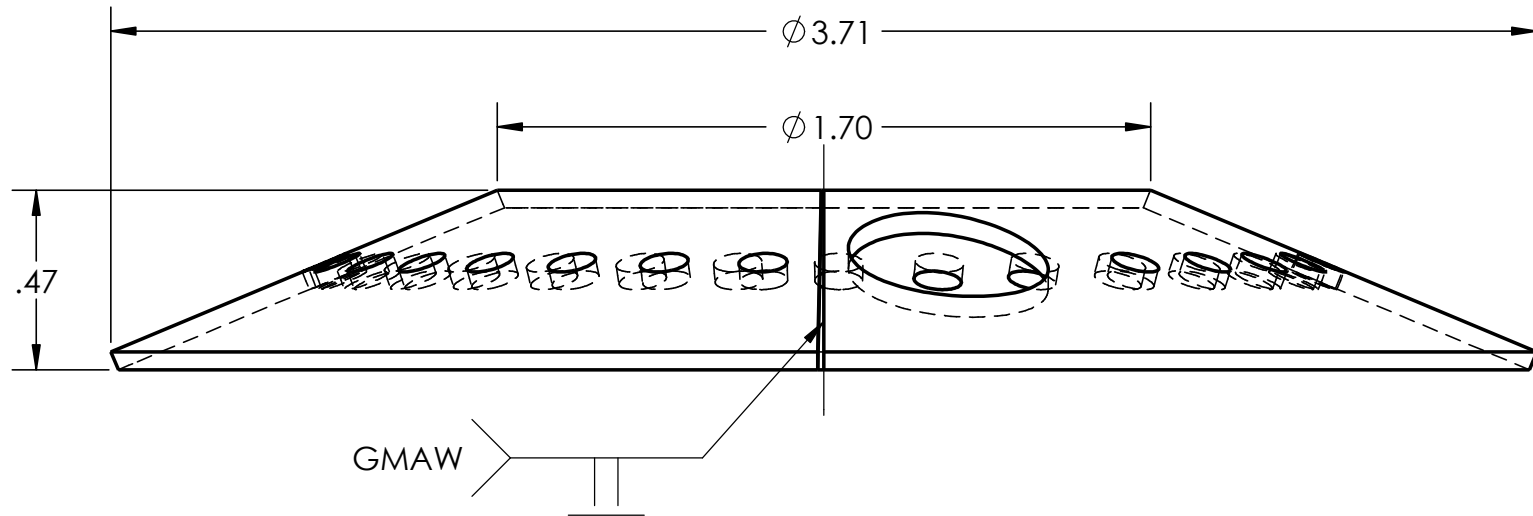
MATERIAL MATIÈRE	WEIGHT MASSE	lbs
CREATED DATE DATE DE CRÉATION	July-01-18 4:58:14 PM	
SAVED SAUVÉGARDE	July-24-18 1:42:03 PM	
FOLDER DOSSIER	C:\Users\katz\Documents\Thesis\Design\models\chamberv5\Assemblies\	


**RMCC
ENGINEERING
FACULTY**
**CMRC
FACULTÉ
D'INGÉNIÉRIE**

INCH / POUCE  SCALE
 ÉCHELLE 1:1
DECIMAL TOLERANCE UNLESS OTHERWISE SPECIFIED /
 TOLÉRANCE DÉCIMALE SAUF SI SPÉCIFICATION DIFFÉRENTE
 X.X = ± 0.05
 X.XX = ± 0.005
 X.XXX = ± 0.001

TITLE TITRE		DOME ASSEMBLY	
NAME NOM	CURTIS KAATZ	NUMBER NUMÉRO	G7456
FILE NAME NOM FICHIER	DOME-SPLASH-PORT ASSEMBLY	SHEET PAGE	32 OF 41 DE
		DWG # / DESSIN# 1.2.2.2.2.2.2	

PART NAME	DESCRIPTION	QTY.	MATERIAL
DOME	ROLLED 18 GAUGE SHEET	1	316L STAINLESS STEEL



MATERIAL MATIÈRE	316L STAINLESS STEEL	WEIGHT MASSE	lbs
CREATED DATE DATE DE CRÉATION	June-07-18 1:37:39 PM		
SAVED SAUVÉGARDE	July-12-18 1:35:14 PM		
FOLDER DOSSIER	C:\Users\kaatz\Documents\Thesis\Design\models\chamberv5\Parts\swirler_folder\		

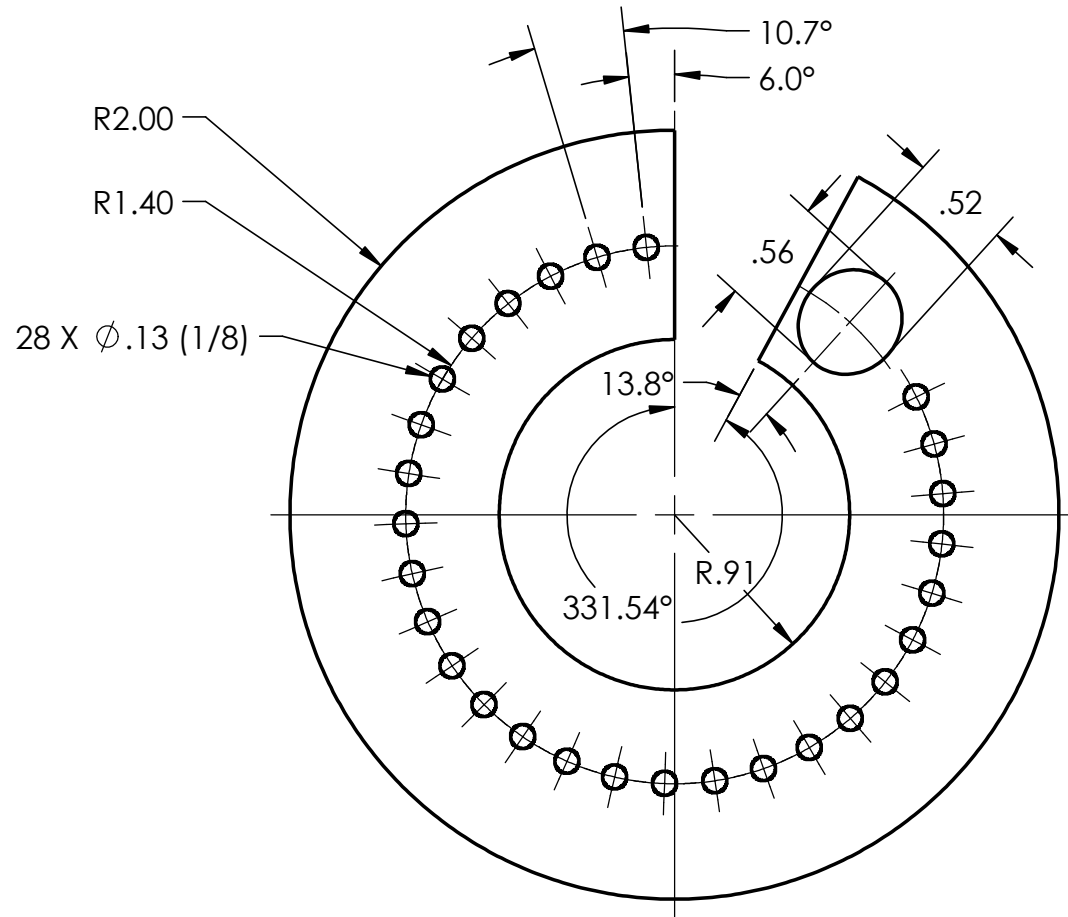


**RMCC
ENGINEERING
FACULTY**
**CMRC
FACULTÉ
D'INGÉNIÉRIE**

**INCH /
POUCE**  **SCALE
ÉCHELLE 2:1**
DECIMAL TOLERANCE UNLESS OTHERWISE SPECIFIED/
TOLÉRANCE DÉCIMALE SAUF SI SPÉCIFICATION DIFFÉRENTE
X.X = ± 0.05
X.XX = ± 0.005
X.XXX = ± 0.001

TITLE TITRE		DOME	
NAME NOM	CURTIS KAATZ	NUMBER NUMÉRO	G7456
FILE NAME NOM FICHIER	DOME	SHEET PAGE	33 OF 41 DE
			DWG # / DESSIN
			1.2.2.2.2.2.1

PART NAME	DESCRIPTION	QTY.	MATERIAL
DOME	WATER JET 18 GAUGE SHEET	1	316L STAINLESS STEEL



MATERIAL MATIÈRE	WEIGHT MASSE	lbs
CREATED DATE DATE DE CRÉATION	June-07-18 1:37:39 PM	
SAVED SAUVÉGARDE	July-12-18 1:35:14 PM	
FOLDER DOSSIER	C:\Users\kaatz\Documents\Thesis\Design\models\chamberv5\Parts\swirler_f older\	

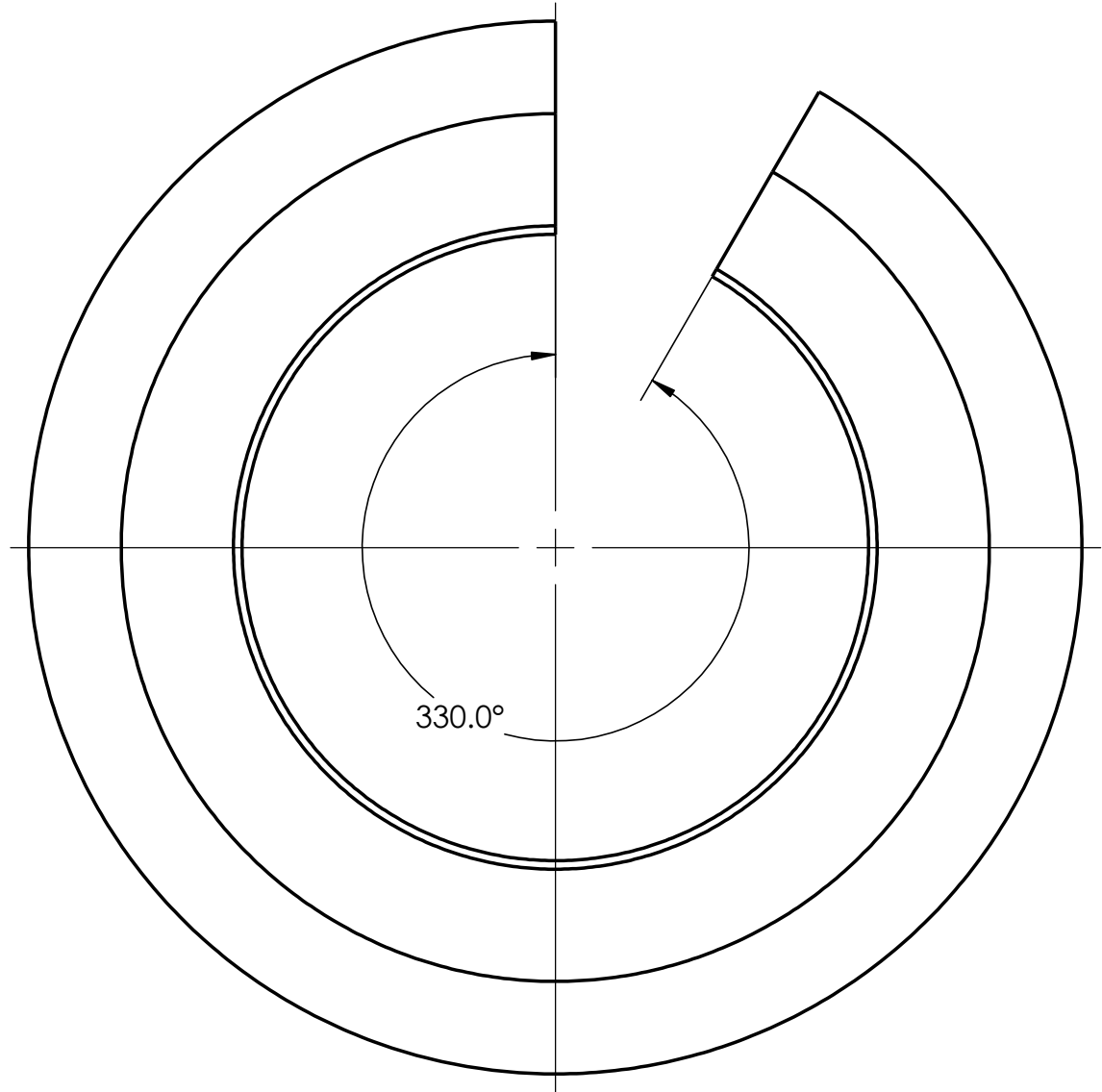
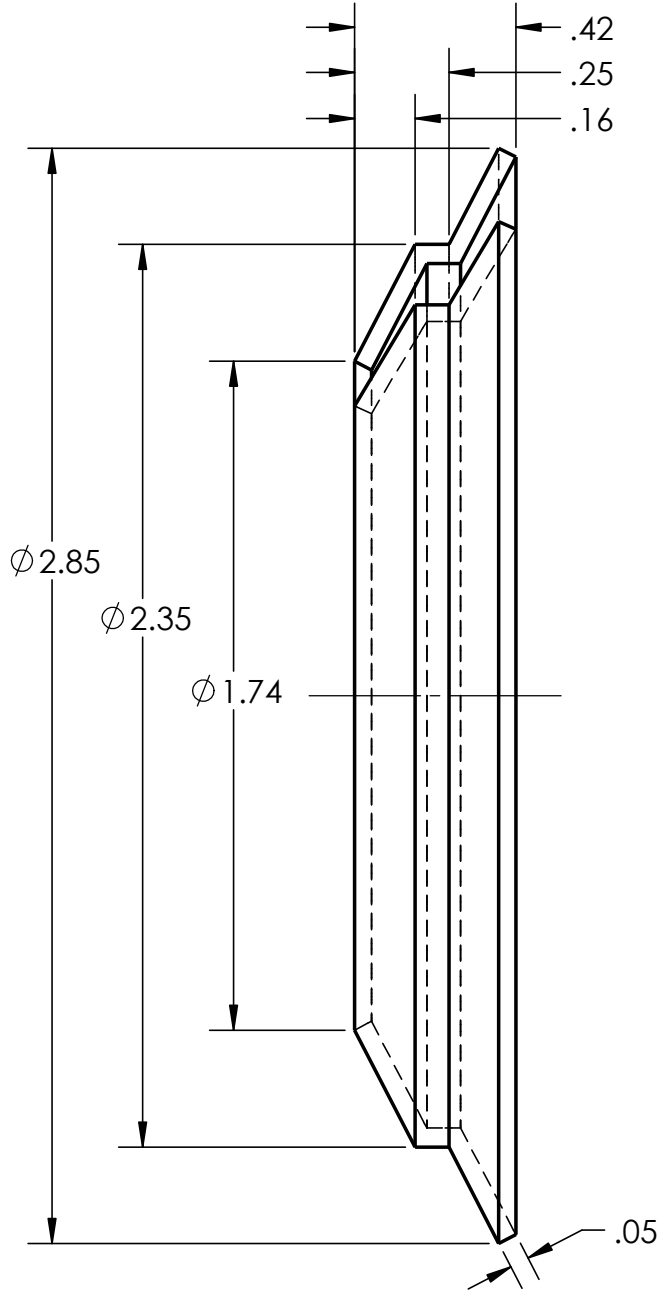


**RMCC
ENGINEERING
FACULTY**
**CMRC
FACULTÉ
D'INGÉNIÉRIE**

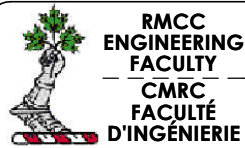
**INCH /
POUCE** **SCALE
ÉCHELLE** 1:1
DECIMAL TOLERANCE UNLESS OTHERWISE SPECIFIED/
TOLÉRANCE DÉCIMALE SAUF SI SPÉCIFICATION DIFFÉRENTE
X.X = ± 0.05
X.XX = ± 0.005
X.XXX = ± 0.001

TITLE TITRE		DOME FLAT	
NAME NOM	CURTIS KAATZ	NUMBER NUMÉRO	G7456
FILE NAME NOM FICHIER	DOME	SHEET PAGE	34 OF 41 DE
			DWG # / DESSIN
			1.2.2.2.2.2.1

PART NAME	DESCRIPTION	QTY.	MATERIAL
SPLASH STRIP	MACHINED	1	316L STAINLESS STEEL



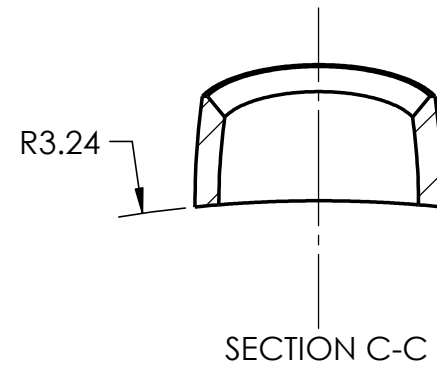
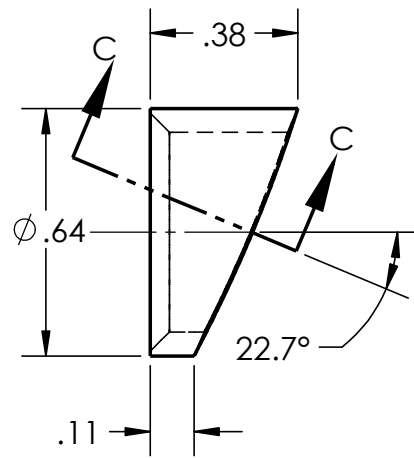
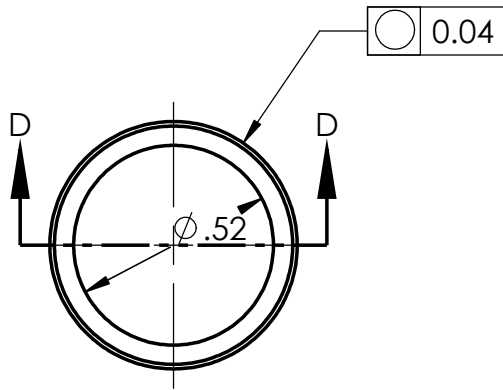
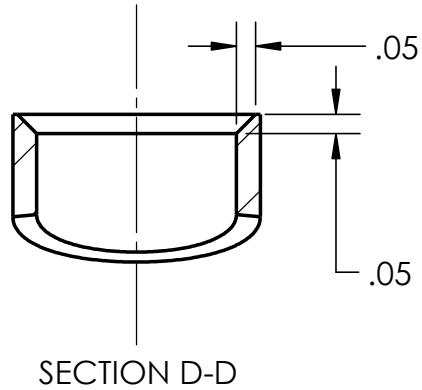
MATERIAL MATIÈRE	316L STAINLESS STEEL	WEIGHT MASSE	lbs
CREATED DATE DATE DE CRÉATION	June-06-18 3:37:12 PM		
SAVED SAUVÉGARDE	July-12-18 1:44:52 PM		
FOLDER DOSSIER	C:\Users\kaatz\Documents\Thesis\Design\models\chamberv5\Parts\swirler_folder\		



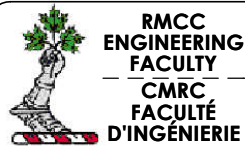
INCH / POUCE		SCALE ÉCHELLE	2:1
DECIMAL TOLERANCE UNLESS OTHERWISE SPECIFIED/ TOLÉRANCE DÉCIMALE SAUF SI SPÉCIFICATION DIFFÉRENTE			
X.X = ± 0.05			
X.XX = ± 0.005			
X.XXX = ± 0.001			

TITLE TITRE		SPLASH STRIP	
NAME NOM	CURTIS KAATZ	NUMBER NUMÉRO	G7456
FILE NAME NOM FICHIER	SPLASH STRIP	SHEET PAGE	35 OF 41
		DWG # / DESSIN#	
		1.2.2.2.2.2.2.2	

PART NAME	DESCRIPTION	QTY.	MATERIAL
IGNITER PORT	MACHINED	1	316L STAINLESS STEEL



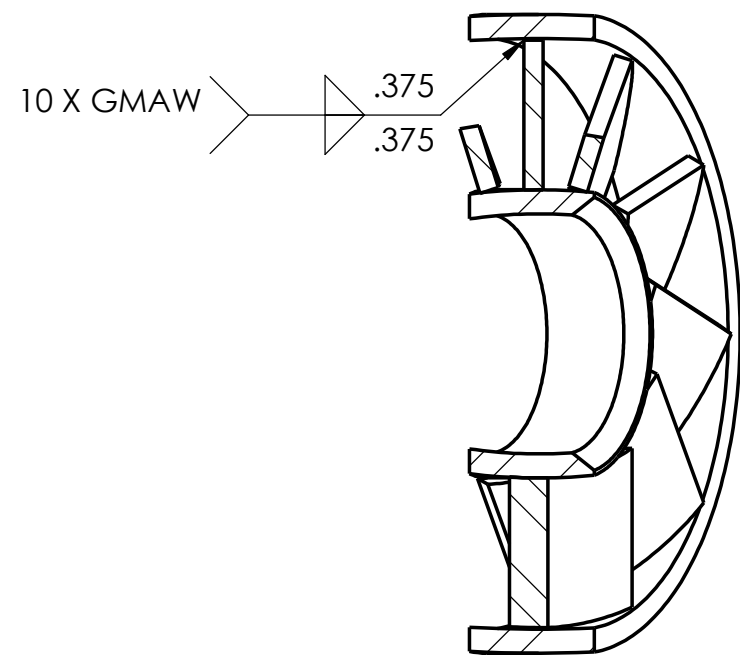
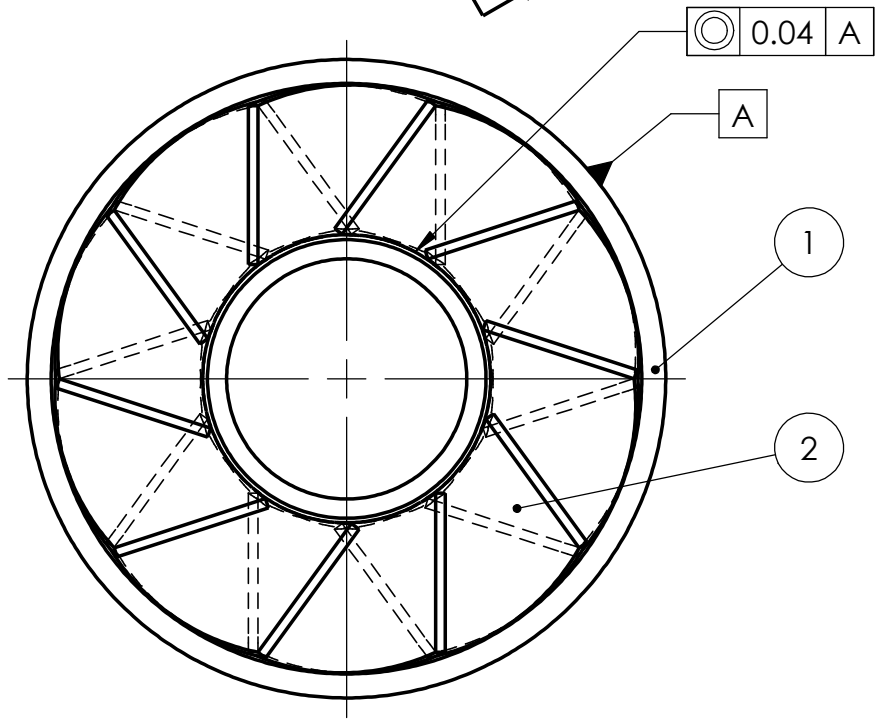
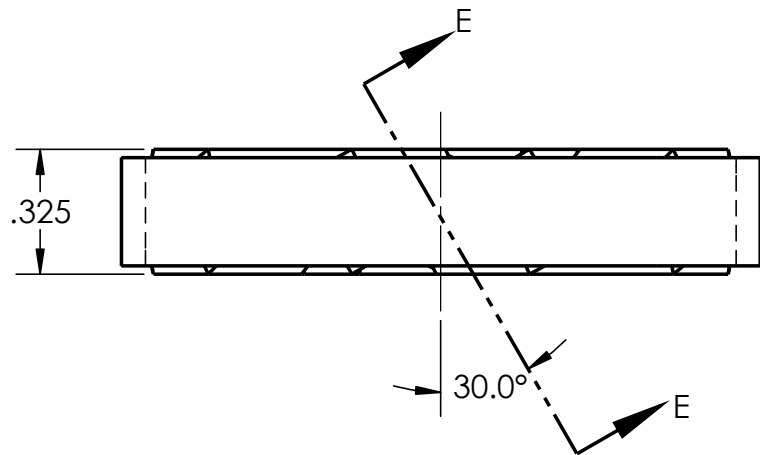
MATERIAL MATIÈRE	316L STAINLESS STEEL	WEIGHT MASSE	lbs
CREATED DATE DATE DE CRÉATION	June-16-18 6:38:36 PM		
SAVED SAUVÉGARDE	July-11-18 10:45:35 AM		
FOLDER DOSSIER	C:\Users\kaatz\Documents\Thesis\Design\models\chamberv5\Parts\swirler_folder\		



INCH / POUCE		SCALE ÉCHELLE	2:1
DECIMAL TOLERANCE UNLESS OTHERWISE SPECIFIED/ TOLÉRANCE DÉCIMALE SAUF SI SPÉCIFICATION DIFFÉRENTE			
X.X = ± 0.05			
X.XX = ± 0.005			
X.XXX = ± 0.001			

TITLE TITRE		IGNITER PORT	
NAME NOM	CURTIS KAATZ	NUMBER NUMÉRO	G7456
FILE NAME NOM FICHIER	IGNITER PORT	SHEET PAGE	36 OF DE 41
			DWG # / DESSIN 1.2.2.2.2.2.3

ITEM NO.	DRAWING NUMBER	QTY.
1	1.2.2.2.2.3.1	1
2	1.2.2.2.2.3.2	1



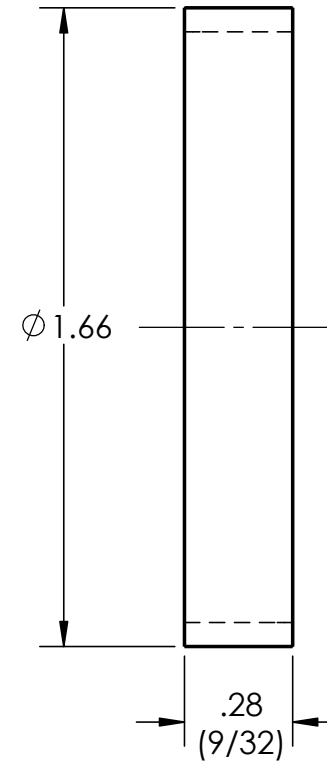
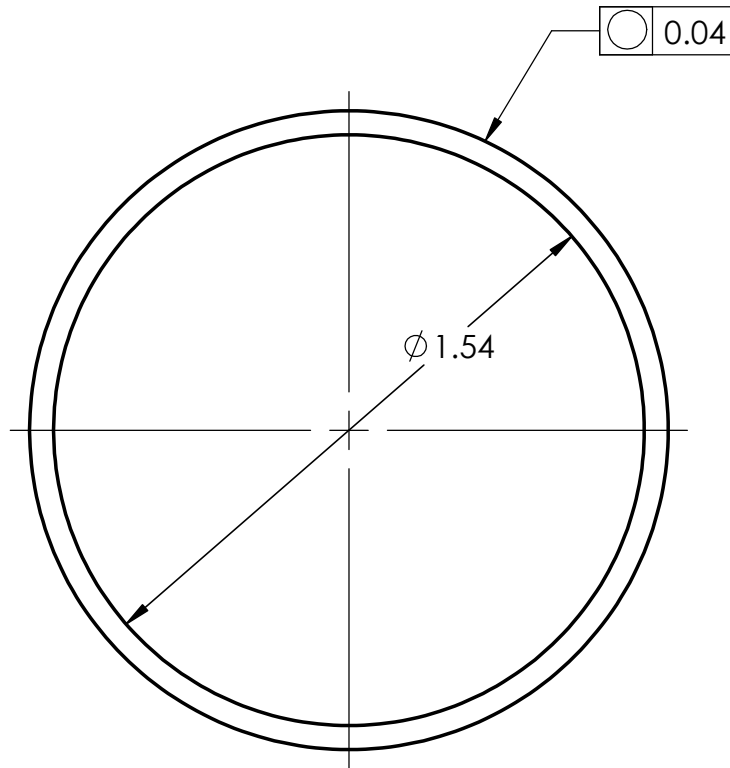
SECTION E-E

MATERIAL MATIÈRE	316L STAINLESS STEEL	WEIGHT MASSE	lbs
CREATED DATE DATE DE CRÉATION	June-14-18 11:30:45 AM		
SAVED SAUVÉGARDE	July-24-18 1:42:04 PM		
FOLDER DOSSIER	C:\Users\kaatz\Documents\Thesis\Design\models\chamberv5\Assemblies\		

INCH / POUCE		SCALE ÉCHELLE	2:1
DECIMAL TOLERANCE UNLESS OTHERWISE SPECIFIED / TOLÉRANCE DÉCIMALE SAUF SI SPÉCIFICATION DIFFÉRENTE			
X.X = ± 0.05			
X.XX = ± 0.005			
X.XXX = ± 0.001			

TITLE TITRE		SWIRLER ASSEMBLY	
NAME NOM	CURTIS KAATZ	NUMBER NUMÉRO	G7456
FILE NAME NOM FICHIER	SWIRLER ASSEMBLY	SHEET PAGE	37 OF 41 DE
			DWG # / DESSIN # 1.2.2.2.2.3

PART NAME	DESCRIPTION	QTY.	MATERIAL
OUTER SWIRLER RING	MACHINED	1	316L STAINLESS STEEL



MATERIAL MATIÈRE	316L STAINLESS STEEL	WEIGHT MASSE	lbs
CREATED DATE DATE DE CRÉATION	June-07-18 12:42:55 PM		
SAVED SAUVÉGARDE	July-05-18 3:30:28 PM		
FOLDER DOSSIER	C:\Users\kaatz\Documents\Thesis\Design\models\chamberv5\Parts\swirler_folder\		



RMCC
ENGINEERING
FACULTY
CMRC
FACULTÉ
D'INGÉNIÉRIE

INCH / POUCE  SCALE ÉCHELLE 2:1
DECIMAL TOLERANCE UNLESS OTHERWISE SPECIFIED /
TOLÉRANCE DÉCIMALE SAUF SI SPÉCIFICATION DIFFÉRENTE
X.X = ± 0.05
X.XX = ± 0.005
X.XXX = ± 0.001

TITLE
TITRE

OUTER SWIRLER RING

NAME
NOM

CURTIS KAATZ

NUMBER
NUMÉRO

G7456

FILE NAME
NOM FICHIER

OUTER SWIRLER RING

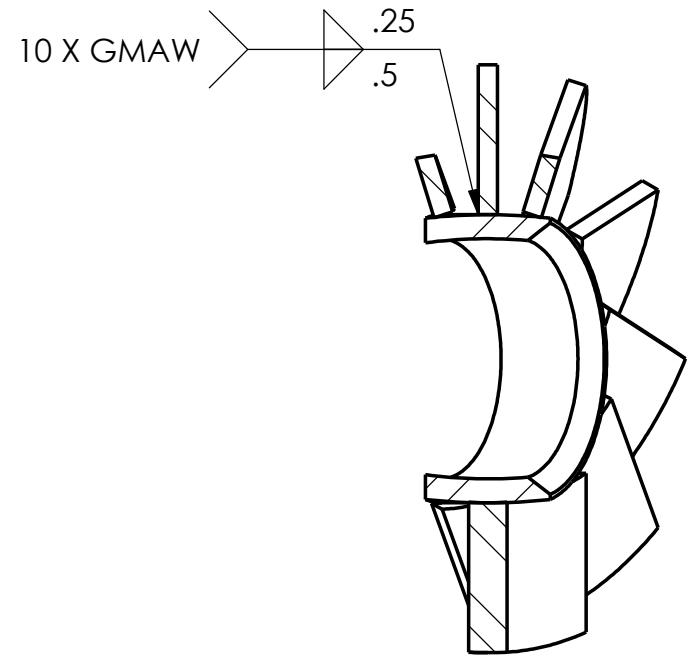
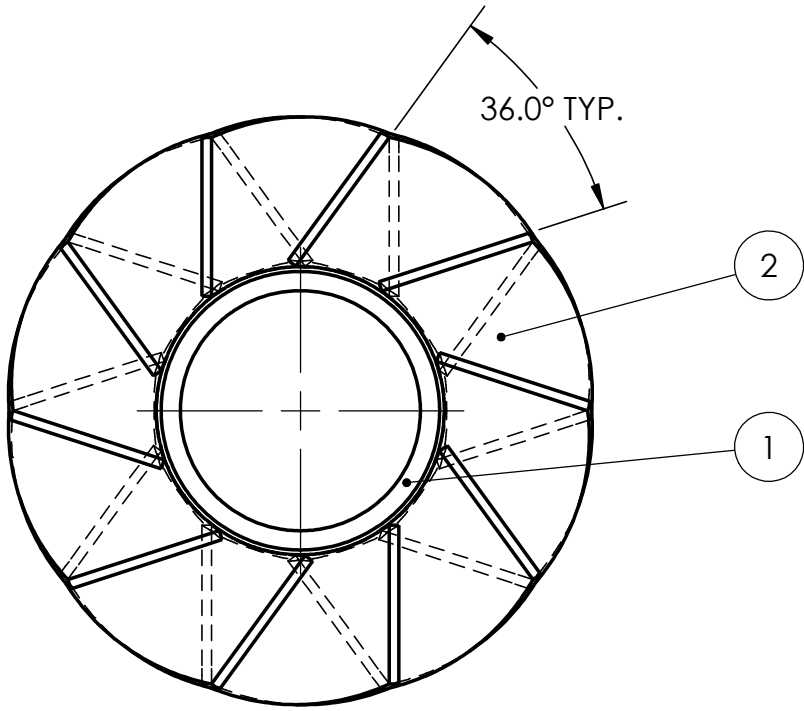
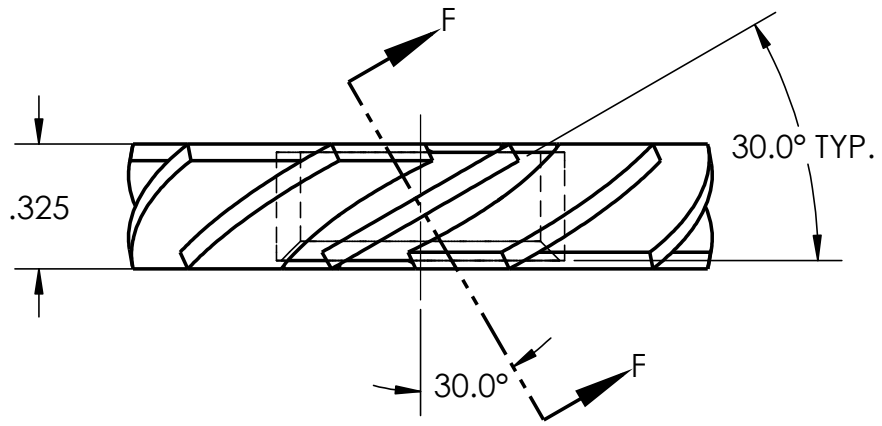
SHEET
PAGE

38 OF 41
DE

DWG # /
DESSIN #

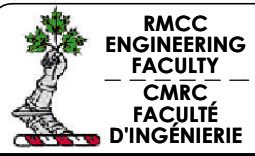
1.2.2.2.2.3.1

ITEM NO.	DRAWING NUMBER	QTY.
1	1.2.2.2.2.3.2.1	1
2	1.2.2.2.2.3.2.2	10



SECTION F-F

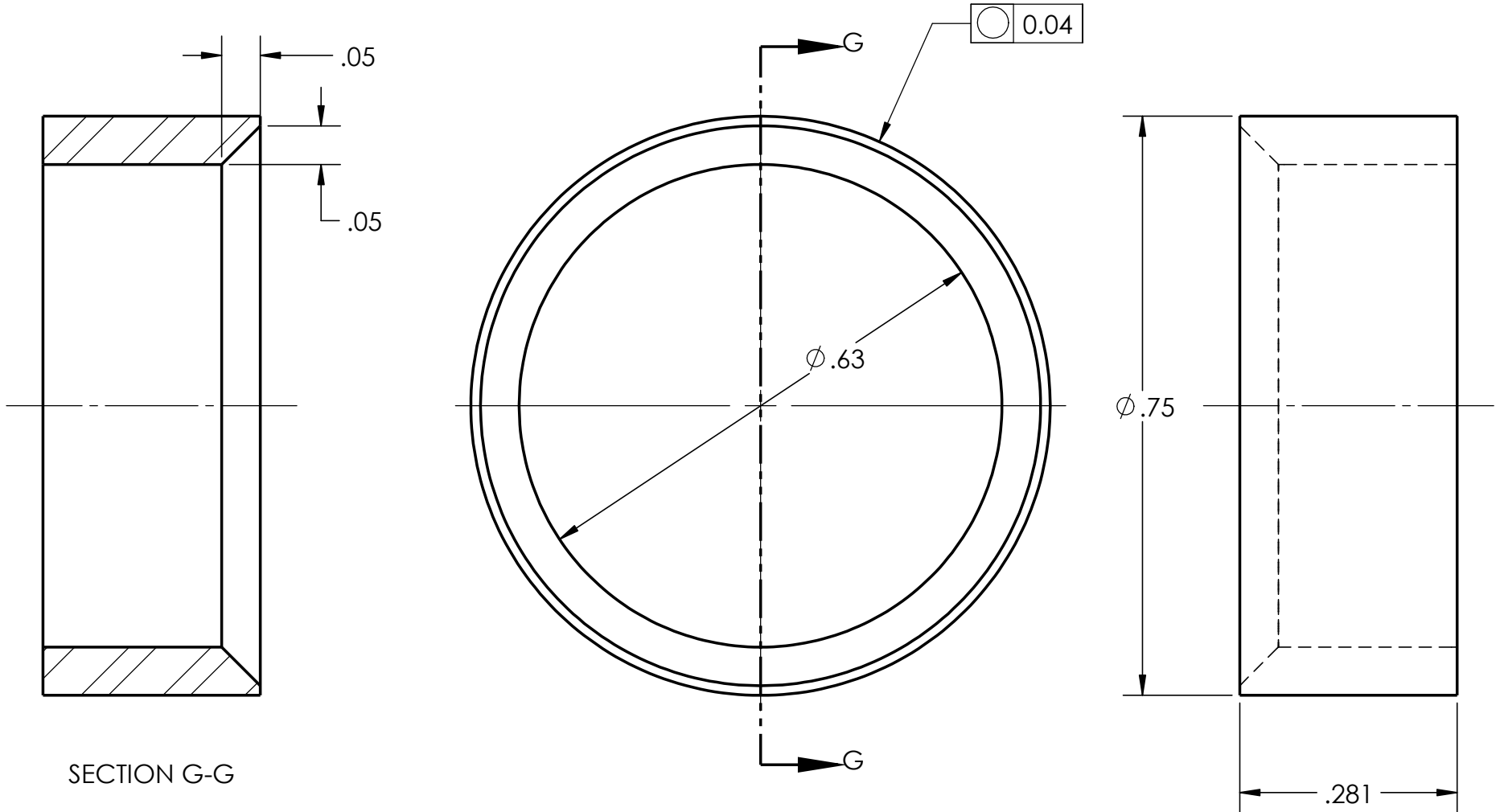
MATERIAL MATIÈRE	316L STAINLESS STEEL	WEIGHT MASSE	lbs
CREATED DATE DATE DE CRÉATION	June-14-18 11:30:45 AM		
SAVED SAUVÉGARDE	July-24-18 1:42:04 PM		
FOLDER DOSSIER	C:\Users\kaatz\Documents\Thesis\Design\models\chamberv5\Assemblies\		



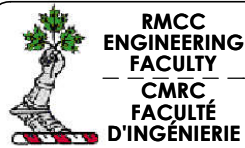
INCH / POUCE SCALE ÉCHELLE 2:1
DECIMAL TOLERANCE UNLESS OTHERWISE SPECIFIED /
 TOLÉRANCE DÉCIMALE SAUF SI SPÉCIFICATION DIFFÉRENTE
 X.X = ± 0.05
 X.XX = ± 0.005
 X.XXX = ± 0.001

TITLE TITRE	INNER SWIRLER ASSEMBLY		
NAME NOM	CURTIS KAATZ	NUMBER NUMÉRO	G7456
FILE NAME NOM FICHIER	INNER SWIRLER ASSEMBLY	SHEET PAGE	39 OF 41 DE 41
			DWG # / DESSIN 1.2.2.2.2.3.2

PART NAME	DESCRIPTION	QTY.	MATERIAL
INNER SWIRLER RING	MACHINED	1	316L STAINLESS STEEL



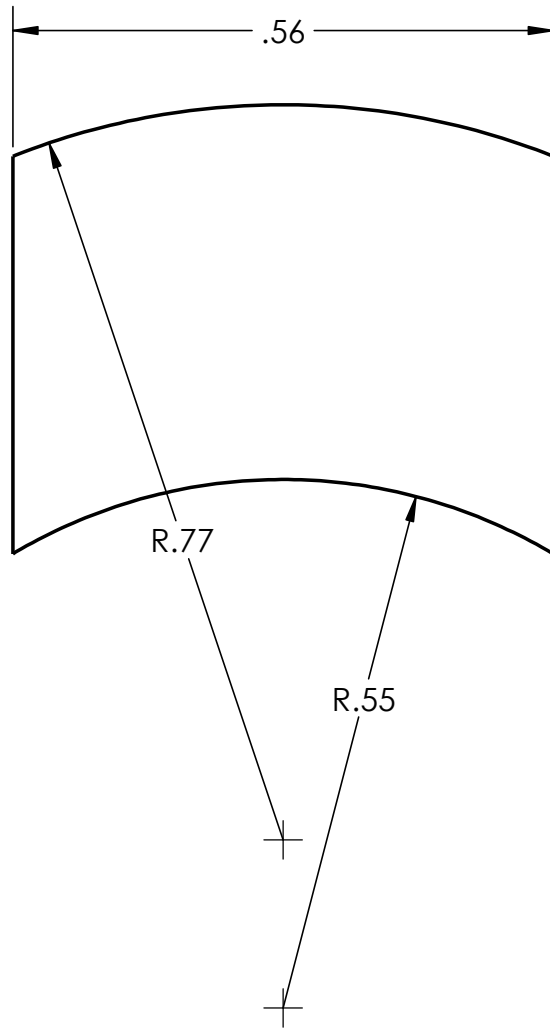
MATERIAL MATIÈRE	316L STAINLESS STEEL	WEIGHT MASSE	lbs
CREATED DATE DATE DE CRÉATION	June-07-18 12:38:02 PM		
SAVED SAUVÉGARDE	July-11-18 11:06:31 AM		
FOLDER DOSSIER	C:\Users\kaatz\Documents\Thesis\Design\models\chamberv5\Parts\swirler_folder\		



INCH / POUCE		SCALE ÉCHELLE	5:1
DECIMAL TOLERANCE UNLESS OTHERWISE SPECIFIED/ TOLÉRANCE DÉCIMALE SAUF SI SPÉCIFICATION DIFFÉRENTE			
X.X = ± 0.05			
X.XX = ± 0.005			
X.XXX = ± 0.001			

TITLE TITRE		INNER SWIRLER RING	
NAME NOM	CURTIS KAATZ	NUMBER NUMÉRO	G7456
FILE NAME NOM FICHIER	INNER SWIRLER RING	SHEET PAGE	40 OF 41 DE 41
			1.2.2.2.2.3.2.1

PART NAME	DESCRIPTION	QTY.	MATERIAL
SWIRLER BLADE	WATER JET 18 GAUGE SHEET	10	316L STAINLESS STEEL



MATERIAL MATIÈRE	316L STAINLESS STEEL	WEIGHT MASSE	lbs
CREATED DATE DATE DE CRÉATION	June-14-18 2:02:27 PM		
SAVED SAUVÉGARDE	July-12-18 2:05:00 PM		
FOLDER DOSSIER	C:\Users\kaatz\Documents\Thesis\Design\models\chamberv5\Parts\swirler_f older\		



RMCC
ENGINEERING
FACULTY
CMRC
FACULTÉ
D'INGÉNIERIE

INCH / POUCE  SCALE ÉCHELLE 5:1
DECIMAL TOLERANCE UNLESS OTHERWISE SPECIFIED /
TOLÉRANCE DÉCIMALE SAUF SI SPÉCIFICATION DIFFÉRENTE
X.X = ± 0.05
X.XX = ± 0.005
X.XXX = ± 0.001

TITLE
TITRE

SWIRLER BLADE

NAME
NOM

CURTIS KAAZ

NUMBER
NUMÉRO

G7456

FILE NAME
NOM FICHIER

SWIRLER BLADE

SHEET
PAGE

41 OF 41
DE

DWG # /
DESSIN #

1.2.2.2.2.3.2.2